https://doi.org/10.15388/vu.thesis.735
https://orcid.org/0009-0006-7373-180X

VILNIUS UNIVERSITY
CENTER FOR PHYSICAL SCIENCES AND TECHNOLOGY

Matas Tartėnas

Supermassive Black Hole Feeding and Feedback

DOCTORAL DISSERTATION

Natural Sciences,
Physics (N 002)

VILNIUS 2025

This dissertation was written between 2020 and 2024 at the Department of Fundamental Research, Center for Physical Sciences and Technology.
The research was supported by the Research Council of Lithuania.

Academic supervisor:
Dr. Kastytis Zubovas (Center for Physical Sciences and Technology, Natural Sciences, Physics – N 002)

Dissertation Defense Panel:

Chairman - Prof. Dr. Vladas Vansevičius (Center for Physical Sciences and Technology, Natural Sciences, Physics – N 002)

Members:
Dr. Vidas Dobrovolskas (Vilnius University, Natural Sciences, Physics – N 002).
Dr. Mindaugas Karčiauskas (Center for Physical Sciences and Technology, Natural Sciences, Physics – N 002).
Dr. Alessandro Lupi (Paris Institute of Astrophysics, Sorbonne University, France, Natural Sciences, Physics – N 002).
Dr. Rima Stonkutė (Center for Physical Sciences and Technology, Natural Sciences, Physics – N 002).

The dissertation shall be defended at a public meeting of the Dissertation Defense Panel at 14:00 on 2025-03-28 in Room D401 of the Center for Physical Sciences and Technology.
Address: Saulėtekio av. 3, NFTMC, Room D401, Vilnius, Lithuania.
Tel. +370 645 15550; email: office@ftmc.lt.

The text of this dissertation can be accessed at the Vilnius University Library, as well as on the Center for Physical Sciences and Technology Library: https://www.ftmc.lt/renginiai-ir-skelbimai.

https://doi.org/10.15388/vu.thesis.735
https://orcid.org/0009-0006-7373-180X

VILNIAUS UNIVERSITETAS
FIZINIŲ IR TECHNOLOGIJOS MOKSLŲ CENTRAS

Matas Tartėnas

Supermasyvių juodųjų skylių maitinimas ir grįžtamasis ryšys

DAKTARO DISERTACIJA

Gamtos mokslai,
Fizika (N 002)

VILNIUS 2025

Disertacija rengta 2020 – 2024 metais Fizinių ir technologijos mokslų centro Fundamentinių tyrimų skyriuje.
Mokslinius tyrimus rėmė Lietuvos mokslo taryba.

Mokslinis vadovas:
dr. Kastytis Zubovas (Fizinių ir technologijos mokslų centras, gamtos mokslai, fizika – N 002).

Gynimo taryba:

Pirmininkas – Prof. dr. Vladas Vansevičius (Fizinių ir technologijos mokslų centras, gamtos mokslai, fizika – N 002).

Nariai:
dr. Vidas Dobrovolskas (Vilniaus universitetas, gamtos mokslai, fizika – N 002).
dr. Mindaugas Karčiauskas (Fizinių ir technologijos mokslų centras, gamtos mokslai, fizika – N 002).
dr. Alessandro Lupi (Paryžiaus astrofizikos institutas, Sorbonos universitetas, Prancūzija, gamtos mokslai, fizika – N 002).
dr. Rima Stonkutė (Fizinių ir technologijos mokslų centras, gamtos mokslai, fizika – N 002).

Disertacija ginama viešame Gynimo tarybos posėdyje 2025 m. kovo mėn. 28 d. 14:00 val. Nacionalinio fizinių ir technologijos mokslų centro D401 konferencijų salėje. Adresas: Saulėtekio al. 3, NFTMC, D401 aud., Vilnius, Lietuva.
Tel. +370 645 15550; el. paštas: office@ftmc.lt.

Disertaciją galima peržiūrėti Vilniaus universiteto bibliotekoje Vilniaus universiteto bibliotekoje ir Fizinių ir technologijos mokslų centro bibliotekoje https://www.ftmc.lt/renginiai-ir-skelbimai.

Acknowledgements

I would like to begin by thanking my supervisor, Kastytis Zubovas, for his invaluable guidance, enduring support and for patience deciphering the difficult *prose* which I often too eagerly present without edit.

I would also like to thank the maintainers of freely available packages extensively used in this work, especially `matplolib` (Hunter 2007), `pygadgetreader` (Thompson 2014), `numba` (Lam et al. 2015), `numpy` (Harris et al. 2020), `splash` (Price 2011). Their contributions have been instrumental in enabling the research presented here. I also acknowledge the assistance of OpenAI's ChatGPT in providing technical suggestions in refining LaTeX formatting of this dissertation (OpenAI 2025).

Finally, I would like to thank my family, friends and especially my wife Greta Tartėnė whose love and warmth held me together as the world seemingly tried to end itself over the last few years.

Contents

List of abbreviations

ADP	Accretion Disc Particle
AGN	Active Galactic Nucleus
BH	Black Hole
BLR	Broad Line Region
CND	Circumnuclear Disc
CNR	Circumnuclear Ring
CMZ	Central Molecular Zone
CPU	Central Processing Unit
EHT	Event Horizon Telescope
FB	Feedback
GC	Galactic Centre
GR	General Relativity
IR	Infrared
ISCO	Innermost Stable Circular Orbit
ISM	Interstellar Medium
KDK	Kick-Drift-Kick Leapfrog Variant
LIGO	Laser Interferometer Gravitational-Wave Observatory
MAD	Magnetically Arrested Disc
MC	Molecular Cloud
MHD	Magnetohydrodynamics
MRI	Magneto-rotational Instability
MW	Milky Way
NGC	New General Catalogue
NIR	Near-Infrared
NLR	Narrow Line Region
NSC	Nuclear Stellar Cluster
SANE	Standard and Normal Evolution
SMBH	Super-Massive Black Hole
SPH	Smoothed Particle Hydrodynamics
SPHS	Smoothed Particle Hydrodynamics with a Higher Order Dissipation Switch
UFO	Ultra-fast Outflow
UV	Ultraviolet
PT	Paukščių Takas (santraukoje)

Introduction

Motivation

The large galactic scales (tens of kilo-parsecs) are connected to the much smaller supermassive black hole (SMBH) influence scales (parsecs or less) by irregular cycles of feeding and feedback from the resultant active galactic nucleus (AGN) (Gaspari et al. 2020). This is due to the fact that accretion onto the SMBH can drive winds and/or jets that push a significant portion of the surrounding gas outward in powerful outflows, shaping the evolution of the bulge and beyond (King & Pounds 2015). Accretion itself is sustained by material infalling in from larger galactic scales.

One of the key channels of SMBH feeding is gas transportation towards the centre via galactic bars (Sellwood & Wilkinson 1993). With new observations, it is possible to measure the associated gas inflow rates. For example, Sormani & Barnes (2019) estimated the amount of gas feeding the Central Molecular Zone (CMZ) of our Galaxy, finding a time-averaged inflow rate of $\sim 3\ \mathrm{M_\odot\ yr^{-1}}$ over ~ 10 Myr. More recently, Sormani et al. (2023) find a time-averaged value of mass inflow in NGC 1097 $\sim 3\ \mathrm{M_\odot\ yr^{-1}}$ over 40 Myr. Interestingly, both mass inflow rates vary by a factor of a few over timescales of 10 Myr. The gas moving in via dust lanes lingers in the hundred-parsec scale star-forming rings (Combes 2019), however these rings are now seen as highly dynamic systems connected to the SMBH scales. Numerous trailing spirals detected by high-resolution observations (Combes et al. 2014; Audibert et al. 2019, 2021) indicate that the gas quickly (one rotation, ~ 10 Myr) loses its angular momentum and thus is driven further in towards the SMBH (Combes 2019), the finding further reinforced by detailed simulations taking into account more of the complexity (stellar feedback, gas self-gravity, magnetic fields etc.) (eg.; Tress et al. 2020, 2024; Moon et al. 2023). In our own Galaxy, the Milky Way (MW), we find that the CMZ, the hundred-parsec scale ring, is connected to the central couple parsecs, by a complex network of filaments and clouds where the Circumnuclear ring (CNR) acts as a pit stop for inflowing material intermittently feeding the SMBH resulting in phases of nuclear activity (Hsieh et al. 2017; Bryant & Krabbe 2021).

Evidence for these intermittent phases of galactic activity is etched in the surrounding ISM on various scales. An activity episode that happened ~ 6 Myr ago is likely responsible for the formation of the *Fermi* and the *eRosita* bubbles (Zubovas & Nayakshin 2012) - the huge bipolar structures stretching for 10 kpc and 15 kpc respectively from the Galactic Centre, perpendicular to the Galactic plane (Su et al. 2010; Predehl et al. 2020). A more recent episode occurred ~ 0.1 Myr ago (Takekawa et al. 2024) and could have produced the hundred-parsec scale X-ray chimneys and 430-pc radio bubbles (Ponti et al. 2019; Heywood et al. 2019) and X-ray echoes hint at a period of heightened activity as recently as few hundred years ago (Koyama et al. 1996; Revnivtsev et al. 2004; Ponti et al. 2013a). Taken together these findings suggest that MW, while currently inactive, is still uniquely well suited for studies of intermittent nuclear activity (Zubovas & Nayakshin 2012).

Unfortunately, we cannot directly follow the dynamical evolution of a single galaxy over ~ 10 Myr. To further investigate episodic feeding and feedback, we must use hydrodynamical simulations. The galactic bar model by Tress et al. (2020, 2024) shows good agreement with estimated feeding rates for the Central Molecular Zone (CMZ) (Sormani & Barnes 2019; Su et al. 2024). It also shows that stellar feedback and gas self-gravity are important factors when driving gas further in toward the SMBH. A more idealized CMZ model by Salas et al. (2021) indicated that turbulence may also play a role. Simulations of the central 10 pc show that the capture of infalling gas may produce rings similar to the currently observed CNR (Mapelli & Trani 2015; Trani et al. 2018). In Chapter 3 we show that further infalling gas, depending on the collision angle, may result in rapid SMBH feeding due to the cancellation of angular momentum and a strong AGN episode, or transient disruption of the CNR-like ring and its growth. The same material that would contribute towards the AGN episode may also fuel star formation. However, to meaningfully address the subject of the interplay between feeding and feedback, we argue that the prescription for accretion should be sufficiently detailed to provide the correct timing and scope of the resultant feedback, which we explore in Chapter 4. The coupling between AGN wind and ISM is not straightforward and is usually based on simple spherical wind models, neglecting the impact of inhomogeneous gas distribution and increased energy dissipation in dense clumps due to cooling - effects that are sometimes missed in large-scale simulations, which cannot resolve the necessary detail. We show how these complications affect outflows on kilo-parsec scales and should not be neglected in observational estimates in Chapter 5.

In this work I aim to improve our understanding about the interplay between feeding and feedback, and its effect on the morphology of the central gas reservoirs surrounding the SMBH, using purpose-made small-to-medium scale simulations. To do this I had to fulfil the following tasks:

- Investigate how gas morphology in the central few parsecs depends on the properties of the infalling material by creating an idealised model of the CNR region.
- Develop a more realistic prescription for tracking SMBH accretion in hydrodynamical simulations and determine how corrected timing and extent of activity affect the surrounding dense material.
- Develop a computationally efficient method for AGN feedback injection.
- Investigate the AGN outflow expansion into a cool and clumpy ISM and how this added complexity affects the coupling efficiency between the AGN wind and the ISM.

Statements to be defended

1. The build-up of gas rings on several parsec scales in galactic centres, referred to as the CNR-limit cycle in the context of the Milky Way, is a viable explanation for episodic galactic activity.
2. Whether or not a specific collision event results in nuclear activity depends on the impact parameters of the feeding material, resulting in a power-law-like relationship between their strength and likelihood; up to half of the initial gas mass may be swallowed by the SMBH after a retrograde collision.
3. We developed a prescription for SMBH accretion that improves the realism and timing of the AGN event by incorporating a one-dimensional standard thin accretion disc.
4. AGN wind can produce large-scale outflows while not significantly disrupting the densest structures within the central few parsecs, therefore simultaneous outflows, SMBH feeding and star formation can occur in all but the most luminous AGN.
5. Gas clumpiness and cooling reduce the efficiency of wind-ISM coupling, resulting in 1-2 orders of magnitude lower momentum and energy loading factors and smaller outflows than predicted by a naïve application of spherical AGN wind theory.

Layout of the dissertation

This dissertation is composed of five chapters. Chapter 1 outlines the literature on black hole feeding and feedback where Section 1.2 deals with both population and individual object studies on SMBH-galaxy connection and in Section 1.3

special attention is given to the Milky Way galaxy as a model AGN. In Chapter 2 we provide a basic overview of the numerical methods used. The following chapters are based on authors' own published works. In Chapter 3 implications from the idealised model of collision between a gaseous ring and a molecular cloud in the galactic centre are explored. The method, while simple, clearly illustrates that feeding of the central region results in either the growth of the central ring or an AGN phase which is in line with the CNR limit-cycle theory. In Chapter 4 we focus on improving the sub-grid prescriptions of accretion in small-medium scales simulations, that resolve the outskirts of the accretion disc. There we argue, that simple Bondi-like or viscosity timescale, angular momentum-based container methods are not sufficient for the correct timing of feedback - which might be pivotal when modelling the interplay between feeding, feedback and star formation in the vicinity of the SMBH. Chapter 5 deals with the complexities of feedback-ISM coupling on kilo-parsec scales. Using idealised controlled spherical models we show, that gas clumpiness and cooling, significantly affect the coupling efficiency. We close the thesis with a summary of key results in Conclusions.

Contribution of the author

The author developed the novel sub-grid prescriptions for following SMBH accretion and wind feedback, in addition to various technical improvements. The author set up all the simulations used in this work and processed/analysed the resultant data. The author wrote the papers that form the basis of Chapter 3 and Chapter 4 and significantly contributed to the writing of the paper which is the basis of Chapter 5.

List of publications

On the dissertation topic

TZ1 Feeding of active galactic nuclei by dynamical perturbations, **M. Tartėnas**, K. Zubovas, Mon. Not. Roy. Astron. Soc.**492**(1), 603-614 (2020)

TZ2 Improving black hole accretion treatment in hydrodynamical simulations, **M. Tartėnas**, K. Zubovas, Mon. Not. Roy. Astron. Soc.**516**(2), 2522-2539 (2022)

ZTB The complex effect of gas cooling and turbulence on AGN-driven outflow properties, K. Zubovas, **M. Tartėnas**, M. Bourne, Astronomy & Astrophysics, **691**, A151 (2024)

Conference presentations

C1 **M. Tartėnas** (presented), K. Zubovas. Improving black hole accretion and feedback in numerical simulations, ISM2021: Structure, characteristic scales, and star formation, Beirut (virtual), 2021, (flash presentation).

C2 **M. Tartėnas** (presented), K. Zubovas. Improving black hole accretion and feedback in numerical simulations, KooGiG-21, Peking (virtual), 2021, (poster presentation).

C3 **M. Tartėnas** (presented), K. Zubovas. Improving black hole the realism of accretion and feedback in numerical simulations, EAS annual meeting 2021, Leiden (virtual), 2021, (poster presentation).

C4 **M. Tartėnas** (presented), K. Zubovas. Juodųjų skylių akrecijos ir grįžtamojo ryšio skaitmeninio modeliavimo tobulinimas, 44-oji Lietuvos Nacionalinė Fizikos Konferencija, Vilnius, 2021, (oral presentation).

C5 **M. Tartėnas** (presented), K. Zubovas. A more realistic black hole accretion treatment for hydrodynamical simulations, EAS annual meeting 2022, Valencia, 2022, (poster presentation).

C6 **M. Tartėnas** (presented), K. Zubovas. Accretion disc-mediated SMBH feeding in hydrodynamical simulations, What Drives the Growth of Black Holes: A Decade of Reflection, Reykjavík, 2022, (poster presentation).

C7 **M. Tartėnas** (presented), K. Zubovas. Stacionaraus eulerinio gardelės panaudojimas greitai grįžtamojo ryšio injekcijai SPH aktyviųjų galaktikų modeliuose, 44-oji Lietuvos Nacionalinė Fizikos Konferencija, Vilnius, 2023 (stendinis).

C8 **M. Tartėnas** (presented), K. Zubovas. A fast grid-based feedback injection method in SPH AGN simulations, EAS annual meeting 2023, Krakow, 2023, (poster presentation).

C9 **M. Tartėnas** (presented), K. Zubovas, T. Costa. SMBH feeding by parsec-scale chaotic accretion over millions of years, EAS annual meeting 2024, Padova, 2024, (oral presentation).

Chapter 1

Super massive black hole feeding and feedback - connecting the big with the huge

Black holes (BHs) have long captivated the interest of astrophysicists. Over the past century, they have transitioned from theoretical concepts to concrete astrophysical objects. Stellar physics has demonstrated that BHs are the final stage in the life cycle of certain massive stars and their presence in binary systems is confirmed by distinct X-ray signatures and gravitational wave observations. This work focuses on a different and, in some ways, less understood class of black holes: supermassive black holes (SMBHs) and their connection to galaxy evolution. These colossal entities are found at the centres of nearly every galaxy. Setting aside the intriguing mystery of SMBH origins[1], the feeding and feedback emerged as one of the key factors in galaxy evolution, making them an indispensable element of the modern understanding of the Universe.

In this introductory chapter, I will first describe how SMBH became an integral element of the modern astrophysics (Section 1.1). I will show the SMBH-galaxy connection, where feeding accretion and resultant feedback likely play a pivotal role (Section 1.2). I will finish this chapter by arguing, that our Galaxy, the Milky Way, shows clear evidence for episodic activity and therefore may serve as a laboratory for AGN research (Section 1.3).

[1] The origin of these SMBH remains a mystery to this day. They appear at relatively high redshift $z > 7$, young enough that they could not have had time to accrete enough material to grow up to the observed masses by conventional means. There are a number of suggestions including super-Eddington accretion, mergers in extremely dense stellar clusters or direct collapse of extremely homogeneous primordial gas cloud (Smith & Bromm 2019; Inayoshi et al. 2020; Zubovas & King 2021).

1.1 Towards the reality of black holes

The modern understanding of BH began to take shape in the early years of the theory of General Relativity (GR) when Karl Schwarzschild discovered an exact solution to Einstein's field equations only a year after their publication in Einstein (1915). The Schwarzschild (1916) solution, which describes the space-time geometry surrounding a spherically symmetric, stationary, non-rotating mass is now known as the Schwarzschild metric and is given by:

$$\mathrm{d}s^2 = \left(1 - \frac{r_\mathrm{s}}{r}\right) c^2\,\mathrm{d}t^2 - \left(1 - \frac{r_\mathrm{s}}{r}\right)^{-1} \mathrm{d}r^2 - r^2 \mathrm{d}\Omega^2, \tag{1.1}$$

where t and r are time and radial coordinates respectively; $\mathrm{d}\Omega^2 = \mathrm{d}\theta^2 + \sin^2\theta\,\mathrm{d}\phi^2$ is the solid angle and r_s is the critical radius known as the Schwarzschild radius[2]:

$$r_\mathrm{s} = \frac{2GM_\mathrm{BH}}{c^2}, \tag{1.2}$$

where G is the gravitational constant, and c is the speed of light. There are two special points in the metric described by eq. (1.1). The point at $r = 0$ corresponds to a physical singularity, where the (known) laws of physics cease to be applicable (Penrose 1965)[3]. The point at $r = r_\mathrm{s}$ corresponds to a coordinate singularity. It differs from the physical singularity at 0 in that it is possible to get rid off $r = r_\mathrm{s}$ singularity by formulating alternative coordinates (eg. Lemaître 1933; Kruskal 1960). However, the r_s is still significant as it marks a surface called the event horizon (Rindler 1956; Finkelstein 1958). A particle can cross the event horizon towards the singularity; within the event horizon all future time paths can only bring the particle closer in.

Later other solutions of the Einstein Field Equations were discovered, allowing, in addition to BH mass, to account for rotation (the Kerr metric; Kerr 1963) and electric charge (the Reissner–Nordström and the Kerr-Newman; Reissner 1916; Nordström 1918; Newman et al. 1965). This culminated in the formulation of the *no-hair* conjecture (Carter 1971; Misner et al. 1973), which asserts that all black holes can be fully described by just three externally observable parameters: mass, angular momentum, and electric charge. In an astrophysical context, it is generally assumed that black holes do not maintain a significant electric charge, as any excess charge would quickly neutralise by accretion of oppositely charged particles (Eardley & Press 1975) and currently the non-negligibly charged black holes remain elusive (eg. Gong et al. 2019;

[2] Interestingly, black holes, as hypothetical objects massive enough that even light could not escape their gravity were already considered in the context of Newtonian mechanics. In the 18th century Michell and Laplace estimated the sizes of such objects by equating escape velocity for the speed of light and arrived at the expression for radius identical to the r_s (Montgomery et al. 2009)

[3] One of the pioneers of the theoretical black hole research doubts the *realness* of physical BH singularities (Kerr 2023)

Gu et al. 2024).

1.1.1 Astrophysical black holes

Even with increased theoretical understanding, BHs remained a mere mathematical curiosity for decades. The scales implied by the Schwarzschild radius ($r_{\mathrm{s}} \sim 3M_{\mathrm{BH}}/\mathrm{M}_{\odot}$ km) are exceedingly small compared to any astrophysical object known at the time. Peers remained sceptical when Chandrasekhar (1931) calculated the critical mass, now called the Chandrasekhar mass, above which the electron degeneracy pressure of electrons cannot prevent a white dwarf from collapsing into a black hole. Eddington was especially critical, calling for a new law of nature that would prevent stars from acting in such an absurd way (Stratton et al. 1935). In some sense this early criticism was correct as it was later found that the quantum pressure of neutrons could stop the collapse, forming a neutron star first observed by Hewish et al. (1968). Later calculations for the Tolman–Oppenheimer–Volkoff limit, the limit over which the neutron star should collapse into a BH (Tolman 1939; Oppenheimer & Volkoff 1939) were greeted with a similar pattern of scepticism and invocations of new physical processes (Bambi 2020). Now, however, *a new law of nature* is not presenting itself.

A very gradual shift towards not necessarily confirmation, but acceptance of BHs, occurred in the second half of the century. On the theoretical side, Penrose (1965) showed that BH can form without assuming very idealised initial conditions. Others focused not on the BHs themselves, but on their influence on the surrounding environment. The first source to be accepted as a BH was Cygnus X-1, due to the fact that the companion mass exceeded that of a neutron star (Webster & Murdin 1972; Bolton 1972). Currently, there are more than 20 X-ray binaries with confirmed massive, likely black hole, companions (Bambi 2020). In addition, the now classic paper by Shakura & Sunyaev (1973) suggested a robust description of accretion flows from a companion to the black hole. These may form a thin accretion disc with distinct spectral features, like X-ray emission and variability timescales, which were also applied to Cygnus X-1 (Rothschild et al. 1974). The more concrete model gave credence to earlier work by Zel'dovich (1964) and Salpeter (1964) suggesting that accretion onto massive central object may power the quasi-stellar objects, or more commonly now - quasars. These ideas were built upon the observations of 3C 287 (Schmidt 1963; Matthews & Sandage 1963) and the realisation that quasars are extremely powerful distant sources. Early investigations culminated with the paper by Soltan (1982), which suggested that given the luminosity density of quasars, they are likely powered by accretion onto SMBH in galaxy centres and that the amount of matter required to power the observed quasars, would result in a 'dead quasar' at the centre of nearly every galaxy. Similar claims were made earlier by (Lynden-Bell 1969).

Over the last few decades, observations found many distinct signatures of the extreme environment surrounding the SMBHs. For example, a combination of techniques like reverberation mapping (Blandford & McKee 1982; Peterson 2006) and gravitational microlensing (Yonehara et al. 1999) allow to peer in to AGN variability and put constraints on accretion disc properties and their timescales (Hawkins 2002; Burke et al. 2021). Microlensing specifically was used to establish the $M_{\rm SMBH} - R_{\rm acc.disc}$ relation, which predicts slightly larger accretion discs than expected from the standard thin accretion disc model (Morgan et al. 2010, 2018). Another canonical example is the Fe Kα line. This intrinsically narrow line at ~ 6.4 keV is emitted by the SMBH accretion disk and appears broadened due to relativistic Doppler effects, beaming and gravitational red-shift - a distinct profile that allows for detailed probes into the physics of the accretion disc (Fabian et al. 2000). As one of the strongest emission features it is also important in population studies (Ricci et al. 2014; Elías-Chávez et al. 2024). High-resolution gas and stellar kinematic studies (Harms et al. 1994; Kormendy & Richstone 1995) are also consistent with the presence of extremely compact SMBH-like objects in many galaxies. The extreme distortions of space-time due to BHs also left an opportunity to open a new field of gravitational wave observations, with a merger between two stellar mass BHs (~ 30 $\rm M_{\odot}$) detected for the first time in 2015 (Abbott et al. 2016a). Continued observations slowly populate the intermediate mass BH sample (Abbott et al. 2020). However, current-generation gravitational wave observatories cannot detect individual SMBH mergers (Wang et al. 2022) although such mergers may contribute to the gravitational wave background that is detected using pulsar timing arrays (Sato-Polito & Zaldarriaga 2024). The existence of an SMBH in our own Galactic Centre (GC), Sgr A*(Balick & Brown 1974) was confirmed by various methods. These include emission spectrum and variability (Witzel et al. 2018; Do et al. 2019), as well as its compact size confirmed with interferometry (Issaoun et al. 2019). The most substantial and long-lasting observations are probably the monitoring of the so-called S-stars in the central parsec, which allowed to precisely recreate their extreme orbits (Eckart & Genzel 1996; Schödel et al. 2002; Gillessen et al. 2009; Jovanović et al. 2024). Today, these observations are somewhat overshadowed by the most direct observation to date, made by the Event Horizon Telescope (EHT) collaboration. Using a very-long-baseline interferometry approach EHT can probe down to the scales of, as the name suggests, the event horizon of a SMBH. The long-anticipated first image of the shadow of a supermassive black hole was revealed in 2019 and appears consistent with the Kerr metric BH (Event Horizon Telescope Collaboration et al. 2019). An image of Sgr A*followed a couple of years later (Event Horizon Telescope Collaboration et al. 2022).

As a result of observations outlined above (and many others), the existence of BHs is now rarely debated. While BHs may sometimes stretch our thinking about what a direct observation is, they do create an extreme environment with specific observable traits. And as we will highlight in the next section, SMBHs have an outsized influence on their host galaxies, even outside their immediate environment.

1.2 SMBH - galaxy connection

It is now more or less accepted that the majority, if not all, of massive galaxies have SMBH at the centre (Soltan 1982; Kormendy & Richstone 1995; Magorrian et al. 1998; Merritt & Ferrarese 2001a). The link between SMBHs and their host galaxies was further reinforced by the discovery of scaling relations between the SMBH and host properties. Magorrian et al. (1998) using data from 36 nearby galaxies established a linear relation between the masses of the SMBHs and the bulges of their host galaxies, now referred to as the Magorrian relation, $M_{\rm BH}/M_{\rm b} \approx 0.006$. A tighter and probably more fundamental relationship was established between SMBH mass and velocity dispersion in the central spheroid - the $M - \sigma$ relation (Gebhardt et al. 2000; Ferrarese & Merritt 2000; Merritt & Ferrarese 2001b; McConnell & Ma 2013).

At first glance, however, the fact that SMBHs have any effect on the global evolution of galaxies, beyond their immediate surroundings, might seem far-fetched. And despite the words *super massive* in their name, they are still significantly less massive than their host galaxies. In practice, this means that SMBH gravity dominates just in the very centre of its host galaxy. For example, the radius of influence of Sgr A* can be estimated using (Peißker et al. 2024):

$$r_{\rm inf} \sim \frac{GM_{\rm SgrA^*}}{\sigma_\star^2} \sim 1.7 \left(\frac{M_{\rm SgrA^*}}{4 \times 10^6 {\rm M}_\odot}\right) \left(\frac{\sigma_\star}{100\,{\rm km\,s^{-1}}}\right)^{-2} {\rm pc}, \tag{1.3}$$

where $M_{\rm SgrA^*}$ is the mass of Sgr A*, and $\sigma_\star$ is the velocity dispersion of the stars within the central parsec. This could imply the evolutionary link between SMBHs and their host galaxies is very weak, or, worded significantly more strongly by Jahnke & Macciò (2011), non-causal. They showed that galaxy merging alone, without invoking any causal connection between SMBH and host galaxies, could establish and reinforce the linear $M_{\rm b} - M_{\rm BH}$ scaling relation from arbitrary initial distribution of $M_{\rm b}$ and $M_{\rm BH}$ values (Peng 2007; Jahnke & Macciò 2011). However, the more established view is that the existence of the previously mentioned scaling relations implies coevolution (Kormendy & Ho 2013) and that is made possible by the fact that quasar feedback is powerful enough to affect galaxies in a multitude of other observable ways non-trivially Silk & Rees (1998); Harrison et al. (2018); Harrison & Ramos Almeida (2024). For example, feedback may drive the ISM enrichment, trigger star formation, or drive high velocity ($v > 100$ km s^{-1}) outflows expelling/destroying molecular gas (Ikeuchi 1981; Sanders et al. 1988; Natarajan et al. 1998; Harrison et al. 2018). Over time these considerations led to a movement away from disparate observational categories like *quasar*, *radio galaxy*, *Seyfert*, etc., towards a more general category of Active Galactic Nuclei (AGN), where these different objects are grouped in a unifying scheme (Rowan-Robinson 1977; Antonucci 1993; Urry & Padovani 1995; Mickaelian 2015). The modern unified AGN model (Netzer 2015; Padovani et al. 2017; Ramos Almeida & Ricci 2017; Hickox & Alexander 2018) successfully explains many of the observed properties of an AGN and is still instructive today. In this picture, any given galaxy spends $\sim 5\%$ of its lifetime in the active state (Shankar et al. 2013). This is why some suggest that AGN are better understood as *events*, not as *objects* (Harrison & Ramos Almeida 2024). In addition to the central accreting SMBH, the model AGN consists of (according to Ramos Almeida & Ricci (2017)): a broad-line region (BLR), a narrow-line region (NLR), a (obscuring) torus and (possibly) a jet. BLR is the region closest to the SMBH ($\sim 100 r_\mathrm{s}$). Here a large number ($> 10^7$) of gas clouds are affected by both ionising radiation and extreme gravitation. Rapid movement of many dense cloudlets produces non-forbidden emission lines with spectral width $\Delta v \geq 2000\ \mathrm{km\,s^{-1}}$. In the more distant and less dense NLR, both effects gradually diminish resulting in emission lines with $\Delta v \leq 1000\ \mathrm{km\,s^{-1}}$. The more extensive NLR is more or less always observable, but the BLR may be obscured by the dense dusty torus, depending on its orientation towards the observer. Although the exact shape of a *torus* is uncertain; Hönig (2019) suggests a *torus* is shaped like an conical shell, motivated by the MIR emission (Asmus 2019), leaving the in-plane disc to feed the SMBH. A jet formed by the interaction of a rotating SMBH and a magnetised accretion disk may also be present and visible in the radio (Blandford & Znajek 1977; Blandford et al. 2019). Winds can also produce similar emissions and multiple mechanisms may work at the same time, so there is no neat delineation between different objects (Chen et al. 2024; Harrison & Ramos Almeida 2024). The unified AGN model, sometimes (not necessarily fondly) referred to as *the AGN zoo* (Mickaelian 2015; Padovani et al. 2017), does not fully describe the huge diversity of objects. However, it is still a powerful paradigm that helps to establish a somewhat clearer picture out of the many discrete observables. For our current purposes, the most important fact is that AGNs arise because of rapid feeding of the SMBH, which results in powerful feedback affecting the surrounding ISM - sufficient to ultimately push galactic scale outflows.

1.2.1 Wind as AGN feedback

The potential for AGN feedback to create large-scale outflows is well illustrated by King & Pounds (2015). Assuming that SMBH grows via luminous accretion, i.e. the accreted material releases fraction $\eta \approx 0.1$ of its rest mass energy as radiation, (Soltan 1982), the energy liberated is

$$E_{\rm acc} \approx \eta M_{\rm BH} c^2 \approx 2 \times 10^{61} \frac{M_{\rm BH}}{10^8 {\rm M}_\odot} \,{\rm erg} \tag{1.4}$$

is far larger than the binding energy of the host bulge:

$$E_{\rm bulge} \sim 8 \times 10^{58} \frac{M_{\rm BH}}{10^8 {\rm M}_\odot} \left(\frac{\sigma}{200\,{\rm km\,s^{-1}}} \right)^2 {\rm erg}. \tag{1.5}$$

In fact, this suggests, that the feedback process cannot be overly efficient. If it were, i.e. most of the released energy would be absorbed by the gas in the bulge, the black hole could potentially disrupt the host galaxy significantly or, at the very least, remove a substantial fraction of its gas, long before the SMBH grew to the observed masses.

In this work, we assume AGN feedback take the form of a small-scale wind launched from a thin accretion disc; this is one possible outcome of accretion (see Section 1.2.2). Observations of blue-shifted high-ionisation iron absorption lines reveal fast quasi-spherical winds reaching speeds up to $\sim 0.1c$ (c is the speed of light) (Pounds et al. 2003a,b) present in a large fraction of nearby active galaxies (Tombesi et al. 2010a,b). In the case of the radiatively efficient accretion flow, as is the case with the thin disc (Shakura & Sunyaev 1973), luminosity

$$L = \eta \dot{M}_{\rm BH} c^2, \tag{1.6}$$

is determined by the rate of accretion onto the SMBH, $\dot{M}_{\rm BH}$, and the radiative efficiency η, which is between $0.035 - 0.42$ depending on the rotation of the SMBH, but is typically assumed to be ~ 0.1 (King & Pounds 2015). It is often assumed, that accretion is Eddington-limited - that luminosity may not exceed $L_{\rm Edd}$ by much, else the feeding sustaining activity would seise due to the disruption caused by feedback itself. It is calculated by requiring that the radiation pressure force on the electrons in an accretion flow would compensate for the gravitational attraction of the SMBH (Frank et al. 2002):

$$L_{\rm Edd} = \frac{4\pi G M_{\rm BH} m_{\rm p} c}{\sigma_{\rm T}} \approx 1.3 \times 10^{46} \frac{M_{\rm BH}}{10^8 {\rm M}_\odot} {\rm erg\,s^{-1}}. \tag{1.7}$$

Here $\sigma_{\rm T}$ is the Thomson cross section and $m_{\rm p}$ the proton mass.

The winds have mass outflow rates comparable with the Eddington accretion rate $\dot{M}_{\rm w} = \dot{M}_{\rm Edd}$(King 2003); assuming the wind is spherical results in momentum and energy outflow rates similar to

$$\dot{p}_{\rm w} \approx \dot{M}_{\rm w} v_{\rm w} \approx \frac{L_{\rm Edd}}{c} \tag{1.8}$$

and

$$\dot{E}_{\rm w} = \frac{1}{2}\dot{M}_{\rm w} v_{\rm w}^2 \approx \frac{\eta}{2} L_{\rm Edd}, \tag{1.9}$$

respectively, where $v_{\rm w}$ is the wind velocity. Given this, the velocity of the launched wind should be extremely fast $v_{\rm w} \sim \eta c$ (Costa et al. 2014). The so-called ultra-fast outflows (UFO) are more or less in line with this expectation, with the spread of wind velocities between $\sim 0.03c$ and $\sim 0.3c$ (Pounds et al. 2003a; Tombesi et al. 2010a,b). We assume that wind is launched due to local luminosity in the accretion disc exceeding the local Eddington limit and that this occurs at a radius smaller than $r < 0.01$ pc, however, some recent work suggests that at least in some AGN launch radii is closer to tens of parsecs via alternative mechanisms (Laha et al. 2021; He et al. 2022; Naddaf et al. 2023). The way this small-scale quasi-spherical wind couples to the surrounding ISM depends crucially on whether it is in the so-called momentum- or energy-driven regime. In the first case, only ram-pressure force is communicated to the ISM, due to efficient cooling in the shocked wind. Conversely, in the energy-driven case, shock is unable to cool resulting in adiabatic, $P\mathrm{d}V$, expansion of the hot bubble. For a strong shock in monatomic gas the temperature is given by(Faucher-Giguère & Quataert 2012)

$$T_{\rm shock} = \frac{3\mu}{16k} m_{\rm p} v_{\rm shock}^2 \approx 1.2 \times 10^{10} \left(\frac{v_{\rm shock}}{30000\,{\rm km\,s^{-1}}}\right)^2 {\rm K}, \tag{1.10}$$

where μ is the mean molecular weight, depends quadratically on shock velocity $v_{\rm shock}^2$. So if the wind is fast enough it is possible to reach high temperatures $T > 10^9$ K. In this case, the temperatures of electrons and protons decouple. The weak coupling between the protons and the electrons becomes the limiting factor significantly slowing the cooling of protons and in effect trapping the thermal energy in the proton plasma, allowing it to sustain high pressure (Faucher-Giguère & Quataert 2012; King et al. 2011).

Following King (2003, 2005) and Costa et al. (2014), in the case of momentum-driven outflow in an isothermal halo, with velocity dispersion σ the expanding thin shell with the mass $M_{\rm shell}$ equation:

$$\frac{\mathrm{d}M_{\rm shell}(R)\dot{R}}{\mathrm{d}t} = \frac{L_{\rm Edd}}{c} - \frac{GM_{\rm shell}(R)M_{\rm tot}(<R)}{R^2}, \tag{1.11}$$

can be recast to

$$\frac{\mathrm{d}R\dot{R}}{\mathrm{d}t} = -2\sigma^2\left(1 - \frac{M_{\rm BH}}{M_\sigma}\right) - \frac{GM_{\rm BH}}{R}, \tag{1.12}$$

where $M_\sigma = \frac{f_{\rm gas}\kappa}{\pi G^2}\sigma^4$. If the initial launching velocity is higher than the escape velocity for the SMBH point mass, the final term can be neglected. An unbound solution in this case is only possible with $M_{\rm BH} > M_\sigma$, at which point further efficient feeding of the SMBH should be impossible. This gives the remarkable result, given the simplicity of the model, that the expected mass of a given SMBH tends to

$$M_{\mathrm{SMBH}} \approx M_\sigma = \frac{f_{\mathrm{gas}}\kappa}{\pi G^2}\sigma^4, \tag{1.13}$$

close to the observed $M-\sigma$ relation scaling of $M_{\mathrm{SMBH}} \propto \sigma^{4.3}$ (Kormendy & Ho 2013). It is however important to note, that there are suggestions that even this tight relation does not imply a causal relation between growth and feedback or that self-regulation does not occur, that is, the inflow is not limited by resultant feedback (Jahnke & Macciò 2011; Anglés-Alcázar et al. 2013). Buchner (2024) argues that feedback is important in regulating the growth of SMBH, but jets and stellar feedback are the key drivers. In the case, SMBH masses were energy-driven regime limited, a much steeper relation would be expected (Costa et al. 2014)

$$M_{\mathrm{SMBH}} \approx \frac{11 f_{\mathrm{gas}}\kappa}{0.5\eta\pi G^2 c}\sigma^5. \tag{1.14}$$

This highlights that while the SMBH mass is regulated by the momentum-driven regime, even an undermassive SMBH may produce large-scale outflow if conditions for this regime are met. In a more realistic, non-isotropic ISM, an energy-driven outflow takes the path of least resistance, as we explore further in Chapter 5 using hydrodynamical models.

1.2.2 Accretion flows

As shown in Section 1.2.1, the power of the outflow depends on the accretion rate onto the SMBH, which in turn is determined by the properties of the accretion flow. The simplest case of steady, spherically symmetric accretion of gas is commonly referred to as Bondi, or sometimes Bondi–Hoyle–Lyttleton, accretion (Hoyle & Lyttleton 1939; Bondi & Hoyle 1944; Bondi 1952). Here, the accretion rate on to the compact object (we will assume it to be an SMBH going forward) is expressed as

$$\dot{M}_{\mathrm{B}} = \frac{4\pi G^2 M_{\mathrm{BH}}^2 \rho_\infty}{(c_{\mathrm{s},\infty}^2 + v_\infty^2)^{3/2}}, \tag{1.15}$$

where ρ_∞, $c_{s,\infty}$ and v_∞ are ambient gas properties: density, speed of sound and velocity respectively[4]. This dependence of the accretion rate only on the ambient parameters makes it very attractive, and still extensively used in large-scale simulations, where the hopes of resolving the accretion disc scales are non-existent (eg; Dubois et al. 2014; Sijacki et al. 2015; Pillepich et al. 2018). It is, however, too simplistic to describe the full picture in the case of SMBH

[4]Other authors may use the term 'Bondi' accretion to refer to different forms of (1.15); for review see Edgar (2004). Our choice is motivated by the similarity to (2.33)

accretion, where flows rarely have zero angular momentum and the inflow is unlikely to be isotropic even far from the SMBH.

When angular momentum is not neglected, the accretion flow generally forms a rotating structure, more loosely - a disc. A robust understanding of these structures came about in the second half of the 20th century, after a seminal paper on accretion by Shakura & Sunyaev (1973), which gave a concrete description of a steady thin Keplerian accretion disc. The model was quickly generalised to the relativistic case by Novikov & Thorne (1973) and a diffusion equation-based description of the disc surface density (Σ) evolution quickly followed (Lynden-Bell & Pringle 1974; Pringle 1981):

$$\frac{\partial \Sigma}{\partial t} = \frac{3}{R}\frac{\partial}{\partial R}\left(R^{1/2}\frac{\partial}{\partial R}\left[\nu \Sigma R^{1/2}\right]\right) \tag{1.16}$$

here, ν is the effective kinematic viscosity and R is the radial distance from the centre. One of the key innovations of Shakura & Sunyaev (1973) was the introduction of the α parametrisation for ν

$$\nu = \alpha c_{\mathrm{s}} H, \tag{1.17}$$

where H is the height of the disc, c_{s} is the local speed of sound and α is a dimensionless parameter close to unity. This is a simple parametrisation is based on dimensional analysis; the model transports angular momentum outwards, while mass is transported inwards and at the same time, producing a temperature profile $T(R) \propto R^{-3/4}$ independently of the actual angular momentum loss mechanism (King 2012) and results in radiative efficiency of 5.7% with the Schwarzschild metric (up to 42% for a rotating Kerr BH)(Beckwith et al. 2006). The actual source of stresses in the disc is turbulence due to magneto-rotational instability (MRI) (Balbus & Hawley 1991; Frank et al. 2002; Abramowicz & Fragile 2013). With the development of this framework, steady-state solutions for thin accretion discs became feasible (Czerny & Naddaf 2018). With a few assumptions and refinements, the standard thin disc model successfully reproduced UV/optical spectra, including the characteristic *Big Blue Bump* observed in AGN spectra (e.g., Malkan 1983; Capellupo et al. 2015). However, this model is not sufficient to fully reproduce the entire spectral energy distribution. To address its limitations, additional components are often introduced, not calculated *ab initio* but incorporated empirically to account for specific spectral features. For instance, Kubota & Done (2018) extended the relativistic Novikov-Thorne thin disc model (Novikov & Thorne 1973) to include an inner hot/warm Comptonisation region and a hot corona, which explains well the X-ray emission. A model more suited to describing moderately super-Eddington accretion flows was introduced by Abramowicz et al. (1988) and is better known as a slim disc, due to its increased thickness. In this regime heat advection becomes important — a significant fraction of the locally generated energy is carried inward with the flow and is lost to the SMBH rather than being radiated away. As the accretion rate increases, the fraction of energy advected into the black hole grows, further decreasing the radiative efficiency (Czerny 2019).

Until relatively recently, parametrised solutions dominated the field, as hydrodynamical models including radiative transfer, magnetism and general relativity were prohibitively computationally expensive to run. The increased availability of computing power, together with recent observations with gravitational wave detector LIGO (Abbott et al. 2016b, 2017) and the previously-mentioned EHT invigorated the field of hydrodynamical accretion disc modelling. While the simpler models rely on multiple parametrised solutions to model observables, current full GR-MHD simulations are edging closer to reproducing at least some of them from well-defined initial and boundary conditions (see Porth et al. 2019, for comparison of many modern GRMHD codes). These models confirm the importance of magnetic fields in accretion flows, with large enough magnetic flux resulting in a so-called magnetically arrested disk (MAD) (Bisnovatyi-Kogan & Ruzmaikin 1976; Narayan et al. 2003) in contrast to the Standard and Normal Evolution (SANE), where accretion is largely unaffected by the black hole magnetosphere. It is suggested that MAD discs can produce jets (Begelman et al. 2022) and X-ray/IR flares observed in Sgr A*(Dexter et al. 2020; Porth et al. 2021), although jets can form in super-Eddington SANE discs as well (Curd et al. 2023). Typically such detailed accretion disc models are not directly used in large scale simulation modelling more than accretion disc themselves, but Hopkins et al. (2024c,b) arrived at a Magnetically-Dominated accretion disc by continuously refining the resolution in a galaxy model generated from cosmological initial conditions. However, the author himself stresses the need for further studies before reaching any strong conclusions about the plausibility of such discs, as they are distinct from both standard thin discs and MAD discs in that they are much more stable, and likely not driven by MRI.

For this work however, the standard α-prescription accretion disc is sufficient as the total luminosity of the accretion disc is the singular parameter defining the properties of feedback. I describe the accretion disc model used in my work in detail in Section 4.2.

1.2.3 Sustaining an AGN

As discussed in Section 1.2, the engine powering an AGN is an accreting SMBH (Netzer 2015); this implies that accretion is also responsible for a significant fraction of the overall growth of the SMBH mass. The amount of material available for SMBH consumption has to be enormous to sustain singular AGN episodes typically lasting ~ 0.1 Myr (Zubovas et al. 2022). Assuming Eddington limited accretion we get

$$
\begin{aligned}
L_{\mathrm{Edd}} &\approx 1.3 \times 10^{38} \, (M_{\mathrm{BH}}/\mathrm{M}_{\odot}) \, \mathrm{erg\,s^{-1}} \\
\dot{M}_{\mathrm{Edd}} &= \frac{L_{\mathrm{Edd}}}{c^2 \eta} \approx 2.4 \times 10^{-8} \, (M_{\mathrm{BH}}/\mathrm{M}_{\odot}) \, \mathrm{M_{\odot} yr^{-1}},
\end{aligned}
\tag{1.18}
$$

with the typical $\eta \sim 0.1$ we find that even the modestly sized SMBH Sgr A*, requires $\sim 10^5\,\mathrm{M}_{\odot}$ to fall on to the accretion disc on scales of $r < 0.01$ pc to produce a significant AGN episode. Understanding how this gas supply is sustained is the second half of the quest to understand the effectiveness of AGN feedback and SMBH-galaxy co-evolution (Kormendy & Ho 2013; Heckman & Best 2014).

Recent works have shown that the majority of SMBH growth occurs via secular (merger-free) mechanisms (Martin et al. 2018; McAlpine et al. 2020; Smethurst et al. 2021, 2022). This means, that mergers are not the primary drivers of the relationships known to exist between SMBHs and their host galaxies (Garland et al. 2024), although that does not mean that mergers could not have an effect, especially in the early Universe (eg.: Lin et al. 2023). Simulations show that material can be transferred from kiloparsec to hundred-parsec scales with the help of processes like bars or similar dynamic instabilities (Sellwood & Wilkinson 1993; Maciejewski et al. 2002; Tress et al. 2020) which is confirmed by observations (Sormani & Barnes 2019; Sormani et al. 2023). This result is corroborated by population studies showing the increased proportion of AGN in barred galaxies (Agüero et al. 2016; Garland et al. 2023, 2024). A bar is also present in MW (Clarke et al. 2019). Gas feeding the central ten-parsec scales is more directly observed in multiple galaxies. For example, Audibert et al. (2019) observed gas in NGC 613 moving down to ~ 10 pc, with clear trailing spirals, *the smoking gun* for AGN fuelling and feedback (Combes 2019) and indications that gas loses their angular momentum in the radius between the torus and the circumnuclear ring. Similar spirals were also likely found in the inner 100 pc of NGC 1808 (Busch et al. 2017), while spirals connecting hundreds- to tens-parsec scales were detected in Circinus and NGC 1097 (Izumi et al. 2018; Prieto et al. 2019a; Kolcu et al. 2023).

Intermittent feeding of the central few parsecs is inevitably required to sustain an AGN. Mapelli & Trani (2016) and Trani et al. (2018) show that clouds with even relatively small impact parameters tend to form several-parsec scale rings unless they come within the influence radius of the SMBH (see (1.3)). Similar rings are observed in MW, referred to as the Circumnuclear ring (CNR)[5] (Oka et al. 2011; Ferrière 2012) and appear to be stable and only

[5]Two remarks concerning (confusing) nomenclature. First, CNR only refers to a couple of parsec scale rings in the context of MW, in other galaxies, circumnuclear rings may refer to significantly larger structures (eg. Audibert et al. 2019; Prieto et al. 2019). Second, CNR

marginally feed the Sgr A*at the rate of $\sim 10^{-6}\,\mathrm{M}_\odot\,\mathrm{yr}^{-1}$ (Cuadra et al. 2008; Ponti et al. 2013b). These central rings can be perturbed by further collisions with inflowing material, resulting in intermittent AGN activity which I will detail in Chapter 3. This lends some credence to the CNR *limit cycle* theory, where the CNR itself is continuously reformed and disrupted by newly inflowing gas on its way to feed the Sgr A*(Morris & Serabyn 1996; Bryant & Krabbe 2021). There is no reason to think that similar thin events happen exclusively in MW. For example, two separate collisions are also invoked when explaining the detection of two discs rotating in opposite directions in prototypical Type 2 AGN NGC 1068 (García-Burillo et al. 2019), consistent with the chaotic accretion scenario (King & Pringle 2007), posing that efficient growth of the SMBH is possible when it is fed by an intermittent inflow of clumpy gas not aligned to its spin. Taking all this together, both observations and theoretical work underscore the complexity as fueling of the AGNs is neither uniform, nor continuous.

1.3 Milky Way centre as a model AGN

Our Galaxy, The Milky Way (MW), is currently inactive, with Sgr A* average luminosity comfortably below par for an AGN ($2 \times 10^{-9} L_{\mathrm{Edd}}$; Ponti et al. 2010). A small cool accretion disc surrounds Sgr A* (Murchikova et al. 2019; Event Horizon Telescope Collaboration et al. 2022) with daily variability in X-ray and infrared (Genzel et al. 2010). However, MW also has an established AGN history the most clear evidence of which is the ten-kiloparsec-scale bubbles emanating from the centre (Su et al. 2010; Predehl et al. 2020). In this section, I provide a brief overview of the Galactic Centre (GC) environment (Section 1.3.1) and MW AGN history (Section 1.3.2). A detailed overview can be found in a number of reviews (eg.: Genzel et al. 2010; Ferrière 2012; Ponti et al. 2013a; Bryant & Krabbe 2021; Sarkar 2024).

1.3.1 Galactic centre environment

MW has a pronounced bar (Clarke et al. 2019; Li et al. 2022; Sormani et al. 2022) that feeds the Central Molecular Zone (CMZ) via dust lanes (Sormani & Barnes 2019; Su et al. 2024). Binney et al. (1991) showed that due to the galactic bar potential, which dominates in the central $\sim$ 2.5 kpc, gas is transferred from the x1 (elongated along the bar) to the smaller x2 (elongated perpendicular to the bar) orbit family. The dense gas that makes up the CMZ is distributed within the central $r \sim 250$ pc(Henshaw et al. 2016), it contains a total of $M_{\mathrm{cmz}} \sim 3 \times 10^7\,\mathrm{M}_\odot$ (Morris & Serabyn 1996; Molinari et al.

is sometimes referred to as the Circumnuclear disc (CND). I will however stick to the CNR, as I find the name more appropriate.

2011). According to Molinari et al. (2011), the Sgr A*complex is offset from the dynamical centre of the CMZ orbit by around 24 pc. Sormani et al. (2018) used a 3d hydrodynamical simulation in agreement with the general morphology of the CMZ to argue that this asymmetry is a product of the unsteady inflow of gas. Using an improved model Tress et al. (2020) performed more detailed simulations of the CMZ and found the inflow in the central 200 pc of $\dot{M}_{200\mathrm{pc}} \approx 1\mathrm{M}_\odot$, which is consistent with observation-motivated estimates of about $\dot{M}_{\mathrm{infow}} \approx 1 - 2\mathrm{M}_\odot$ (Sormani & Barnes 2019; Su et al. 2024). From the observational side, CMZ is modelled as two spirals (Sofue 1995), a closed elliptical (Molinari et al. 2011) or orbit open stream (Kruijssen et al. 2015). Henshaw et al. (2016) compared these models and found an open stream to be the best description.

A complex network of filaments and clouds connects the CMZ to the CNR and the SgrA* complex (Montero-Castaño et al. 2009; Hankins et al. 2020). The CNR is best understood as a clumpy ring with an inner radius of about ~ 1.5 pc and an outer radius of about ~ 4 pc (Genzel et al. 1985; Lau et al. 2013; Iserlohe et al. 2019; Bryant & Krabbe 2021; Paumard et al. 2022). Following the description from Ferrière (2012), the CNR is mainly composed of 150 K molecular gas and a photodissociated inner region gas with temperature $T \sim$ 300 K. The CNR itself is likely not self-gravitating. The current minimum rate of CNR replenishment is $0.002\,\mathrm{M}_\odot\ \mathrm{yr}^{-1}$ (Liu et al. 2012; Hsieh et al. 2017), at which pace it would take between 2 and 200 million years to reach the estimated CNR mass between $\sim 10^4\,\mathrm{M}_\odot$ (Genzel et al. 1985) and $\sim 10^6\,\mathrm{M}_\odot$ (Christopher et al. 2005). Significantly higher intermittent feeding rates are shown to be possible in the previously mentioned detailed model by Tress et al. (2020). The model produces a complex network of infalling filaments and clouds that is in line with Hsieh et al. (2017). By comparing with the previous iteration of the CMZ model (Sormani et al. 2018), they argue that self-gravity and stellar feedback drive material inwards at an order of magnitude greater average rate of $\sim 0.03\,\mathrm{M}_\odot\ \mathrm{yr}^{-1}$. In the more recent iteration of the same simulation, Tress et al. (2024) found the inclusion of magnetic fields results in a similar amount of inflow due to turbulence supported via MRI, without including self-gravity. It is unclear which process dominates in this case and it is also possible that both interact in a non-linear way. A more idealised MHD simulation of two gas streams colliding to form a CMZ-like ring was also performed by Moon et al. (2023); they also found material inflow towards the centre.

At about the influence radius of Sgr A*, ~ 1.5 pc, we reach the central cavity, populated by diffuse gas, transient cloudlets (Goicoechea et al. 2018) and the minispiral (Zhao et al. 2010; Tsuboi et al. 2016). Recent magnetic field measurements seem to suggest that the minispiral is in the same plane as the CNR (Hsieh et al. 2018; Guerra et al. 2023). A strong magnetic field might also provide stabilising support against gravity as was suggested by Gaburov et al. (2012).

Another notable feature of the central parsec is some 200 young stars (formed ≈ 6 Myr ago Paumard et al. 2006; von Fellenberg et al. 2022). The existence of such a population was deemed unlikely at first and even referred to as 'the paradox of youth' (Ghez et al. 2003) since extreme tidal forces 'should' prevent star formation in the 'usual manner' (Genzel et al. 2010). One hint to their origin was found by investigating kinematics and distribution. The young stars form two distinct discs rotating in opposite directions and therefore referred to as the clockwise and the counter-clockwise disc Paumard et al. (2006). The counter-clockwise feature is difficult to confirm and is somewhat controversial, with e.g. Yelda et al. (2014) doubting its existence, while von Fellenberg et al. (2022) confirms it and adds an additional feature, composed of more eccentric stars. An ex-situ scenario, where a previously formed cluster is captured is out of favour precisely due to this rich complexity of identified orbits. An in-situ or mixed scenario, where an already star-forming infalling cloud is captured is investigated in a large number of works (eg. Nayakshin et al. 2007; Wardle & Yusef-Zadeh 2008, 2014; Generozov et al. 2022). A now classic paper by (Bonnell & Rice 2008) showed that a star-forming accretion disc would also produce a top-heavy initial mass function, consistent with observations (Bartko et al. 2010). Hobbs & Nayakshin (2009) showed that some complexity could be explained by an, admittedly somewhat far-fetched, two-cloud collision in close proximity to the Sgr A*. Trani et al. (2018) showed that ring formation is expected outside the sphere of influence of the SMBH, while discs form within the influence radius. Star formation in the CNR-like gas rings would be consistent with the recent finding that high-mass stars might migrate from the CNR inwards on on timescales of ~ 0.3 Myr (Peißker et al. 2024). In Chapter 3 I show that the cloud capture and cloud-cloud collision scenarios can be combined - an already present CNR could be disrupted by a collision with a newly infalling cloud, and, depending on the collision angle, resulting in a range of gas morphologies. While I did not track star formation explicitly, I show that star formation would be possible in resultant warped discs and CNR-like rings. As this scenario requires a significant amount of gas to come within the sphere of influence of the SMBH, it naturally results in at least some accretion, and thus SMBH feedback. Intriguingly, the resultant feedback may not be strong enough to disrupt the dense structures, allowing for simultaneous star and outflow formation.

1.3.2 History of Galactic activity

As mentioned previously, currently Sgr A* is not active. Its bolometric luminosity is $L_{\rm bol} \sim 10^{36}$ erg s^{-1} (Narayan et al. 1996) sit some 3 order of magnitude below luminosity threshold defined by Netzer (2015) as $L_{\rm AGN}/L_{\rm Edd} > 10^{-5}$, where the Eddington luminosity for Sgr A*is $L_{\rm Edd} \sim 5\times10^{44}$ erg s^{-1}. There is daily variability and flaring, where X-ray luminosity may climb from the quiescent $L_{10-79\rm keV} L_{\rm Edd} 3\times10^{34}$ erg s^{-1} up a few hundred times, with a corresponding increase in NIR, however, these are short lived events and do not result in substantial enough rise in continuum emission to be considered AGN events (Ponti et al. 2013a; von Fellenberg et al. 2024; Michail et al. 2024)[6]. However, the aforementioned *Fermi* (Su et al. 2010) and *eRosita* (Predehl et al. 2020) bubbles are likely results of past AGN activity (Ponti et al. 2013a; Zubovas & Nayakshin 2012; Fabian 2012) and would be a clear example of the so-called *fossil outflows* (Zubovas et al. 2022; Zubovas & Maskeliūnas 2023).

The Fermi bubbles - the huge gamma-ray emitting bipolar structures, stretching from the centre for about 10 kpc perpendicular to the Galactic plane were discovered by Su et al. (2010). A decade later, even larger, X-ray bubbles were detected (Predehl et al. 2020). Sections of these even larger bubbles were known before, but these were not confirmed to form the single bipolar $\sim$ 15 kpc structure. While at the moment, the origins of these objects are still not completely certain, an AGN event is a favoured explanation for the formation of these striking features (Yang et al. 2018; Sarkar 2024). The main alternative scenario is that star formation in the GC might release enough energy. Miller & Bregman (2016) and Sarkar et al. (2015) showed resultant feedback can produce similarly shaped bubbles with correct spectra over $\sim$ 30 Myr. However, observations of the northern bubble, specifically, UV absorption in quasar spectra, constrained their age to $6-9$ Myr (Bordoloi et al. 2017). AGN wind-based models by Zubovas & Nayakshin (2012) produce similar bubbles in $\sim$ 6 Myr - a time that would make the origin of the bubbles temporally coincide with a known period of significant star formation in GC. Conveniently, both processes require a significant amount of gas to be present. Alternatively, AGN wind might be replaced by a jet (Yang et al. 2022; Chang & Kiang 2024). These simulations also reproduce the expected morphology and some spectral features, but not the convenient timing, as the bubbles form over 2.6 Myr or less.

The more modest in size 'X-ray chimneys', channels from GC to the *Fermi* bubbles (Ponti et al. 2019), and almost entirely overlapping 430-parsec-tall bipolar 'radio bubbles' (Heywood et al. 2019) could have resulted from a more recent and significantly more modest activity. This hypothesis was reinforced recently with the detection of a parabolic-like trend in the SiO enhancement of the CMZ clouds by (Takekawa et al. 2024), a trend easily explained by an Sgr A*outburst occurring $\sim$ 0.1 Myr ago. X-ray echoes were previously detected on smaller scales as a prominent fluorescent iron line at 6.4 keV in

[6] These flaring events are still very interesting in their own right. For example, the extreme increase in near-infrared radiation observed by Do et al. (2019) was predicted by Kawashima et al. (2017) as a delayed consequence of the close passage of the G2 object in 2014.

the Sgr B complex, and were attributed to a more recent low-luminosity AGN phase that happened ~ 100 yr ago (Koyama et al. 1996; Revnivtsev et al. 2004; Marin et al. 2023). Signs of intermittent activity are also present in the MW surroundings. Bland-Hawthorn et al. (2013, 2019) took into account both travel time and recombination time, and showed that the excess ionization observed in the Magellanic stream can be explained by an AGN event reaching at least $0.1 L_{\rm Edd}$ that happened $1-3$ Myr ago. Fox et al. (2020) showed that kinematic analysis of the UV metal-line absorption in 31 background AGN spectra is consistent with the previous interpretation.

Taken together, the combined observations of kiloparsec- and 100-parsec-scale bubbles, echoes and the excess ionization of the Magellanic stream are essentially indisputable evidence of intermittent feeding and feedback in the centre of our Galaxy. These are consistent with the CNR *limit Cycle* outlined in the previous Section 1.2.3 and are the paradigm in which we analyse our results.

Chapter 2

Hydrodynamical modeling of galactic centres

Astrophysical systems, from galaxies to solar systems, are inherently complex and often, even the simple-looking problems, exemplified by the famous three-body problem, elude complete analytical description. Consequently, numerical modelling has become indispensable in our understanding of astrophysical systems. These range from cosmological simulations, for example, the Illustris and IliustrisTNG (Nelson et al. 2015, 2019b), Fire (Hopkins et al. 2014), Simba (Davé et al. 2019), Romulus (Tremmel et al. 2017) and others, enabled by the ever-growing computational power, to significantly more modest in scale and more idealised simulations aimed at some particular problem that are possible to model on a desktop computer.

In this thesis, we present the results of several idealised numerical simulations where we aim to clarify specific problems like sustaining intermittent AGN or how the propagation depends on the properties of a galactic bulge. For this, we use hydrodynamical simulations. In this work specifically - the hybrid N-body/smoothed particle hydrodynamics (SPH) code `Gadget-3`, an extended version of `Gadget-2` (Springel 2005). Therefore in Section 2.1 we will summarise the general principle of this hydrodynamical modeling approach. We also describe sub-grid prescriptions generally referred to throughout this work in Section 2.2, however, we will leave the more detailed descriptions of the modules we developed for accretion, `ringcode`, and for feedback injection, `gridWind`, for their respective chapters: Section 4.2 and Section 5.2.3.

2.1 General principles of Smoothed particle hydrodynamics

Smoothed particle hydrodynamics (SPH) is a particle-based numerical method for solving hydrodynamic equations. Paraphrasing Price (2012), it is one of the possible (good) answers to a question *how to compute density from randomly distributed points.* SPH was invented by Lucy (1977) and Gingold & Monaghan (1977). It uses a large set of interpolation points, called (somewhat confusingly) particles, to sample an underlying density field. The key principle differentiating this from 'just' an N-body method is that the influence of each particle diminishes within some radius, known as the smoothing length, h_i, defined such that some desired number of particles - the neighbours - are within this radius. All these influences are then combined to produce a smooth density (or other) field for any arbitrary position. In SPH literature, this is usually written as follows:

$$\rho_i(\mathbf{r}_i) = \sum_{j \neq i}^{N_{\mathrm{ngb}}} m_j W(\mathbf{r}_j - \mathbf{r}_i, h_i) \tag{2.1}$$

Here, the density ρ_i is calculated at a certain point in space by summing the masses of neighbouring particles m_j multiplied by a certain weighting function $W(\mathbf{r}, h)$, called the smoothing kernel. $W(\mathbf{r}, h)$ determines the influence of a particle depending on the distance from the point $\mathbf{r}_i$ and the smoothing length h_i. This can be understood as each discrete particle contributing a certain amount to the overall density field at a given point, proportional to the mass of the particle and $W(\mathbf{r}, h)$ which ensures that, as the distance from the centre of the particle increases, the particle's contribution to the overall fields, such as mass, density, etc., gradually decrease. The smoothing length is related to particle number and density. For example in `Gadget-3` the smoothing length for each particle h_i is defined in a way to keep the mass within the h_i radius of the particle approximately constant (Springel 2005):

$$h_i = \left(\frac{3 N_{\mathrm{ngb}} \bar{m}}{4 \pi \rho_i} \right)^{1/3}, \tag{2.2}$$

where N_{ngb} is the number of neighbours, $\bar{m}$ the average particle mass. At distances greater than the smoothing length h_i, the particle's influence is set equal to zero.

As mentioned, any scalar field, not only density, can be computed in a similar manner. Following Cossins (2010), we have the identity:

$$f(\mathbf{r}) = \int_V f(\mathbf{r}') \delta(\mathbf{r} - \mathbf{r}') \mathrm{d}^3 \mathbf{r}', \tag{2.3}$$

where the function $f(\mathbf{r})$ is defined in three dimensions $\mathbf{r}$, within the volume V of a single element. By replacing $\delta(\mathbf{r})$ with the smoothing kernel and expanding in a Taylor series, we get:

$$f(\mathbf{r}) = \int_V f(\mathbf{r}')W(\mathbf{r}-\mathbf{r}', h)\mathrm{d}^3\mathbf{r}' + O(h^2) \tag{2.4}$$

We can multiply the integrand by $\rho(\mathbf{r})/\rho(\mathbf{r})$ and, using $m/\mathrm{d}^3\mathbf{r}' = \rho(\mathbf{r}')$, discretize this integral over a finite number of neighbours. Then, the approximate discretized scalar field can be written as the sum of each particle contributions within the volume:

$$f(\mathbf{r}) \approx \sum_i \frac{m_i}{\rho_i} f(\mathbf{r}_i)W(\mathbf{r}-\mathbf{r}_i, h_i) \tag{2.5}$$

Here, $f(r_i)$, m_i, ρ_i are the value of the function $f(r)$ at the i-th particle, its mass, and its density. Equation (2.5) is the basis of SPH (Price 2012), where if we were calculating density $f(r_i) = \rho(r_i)$, (2.5) reduces to (2.1). The parameter value at a certain point in space is calculated by summing over the particles whose smoothing kernels reach that part of space. Cossins (2010) shows, that this approach is also valid for the discretization of the gradient of a scalar field $\nabla f(\mathbf{r})$ and the divergence of a vector field $\nabla \cdot \mathbf{F}(\mathbf{r})$:

$$\nabla f(\mathbf{r}) \approx \sum_i \frac{m_i}{\rho_i} f(\mathbf{r}_i)\nabla W(\mathbf{r}-\mathbf{r}_i, h) \tag{2.6}$$

$$\nabla \cdot \mathbf{F}(\mathbf{r}) \approx \sum_i \frac{m_i}{\rho_i} \mathbf{F}(\mathbf{r}_i)\cdot\nabla W(\mathbf{r}-\mathbf{r}_i, h) \tag{2.7}$$

This result is important because it shows that by calculating the gradient of the smoothing kernel ∇W and the field value f, it is possible to approximate the field gradient $\nabla f(\mathbf{r})$ without having to calculate it sequentially for each particle (Cossins 2010). Similarly, $\nabla \times \mathbf{F(r)}$ can be found; this result is important for models involving magnetic phenomena.

The approximate equations (2.5), (2.6) and (2.7) naturally have errors. Part of this arises because, in the discretization, only the integral part was considered, ignoring the $O(h^2)$ term left out of the integral. Intuitively, we can see that the former error term would be reduced by reducing the smoothing length h and the discretisation error would diminish with more complete sampling i.e. - an increased number of particles. Therefore, the most accurate results are achieved with a large number of particles in a small h - there is a trade-off between computation speed and accuracy. In addition, not all kernels support large particle numbers, so the properties of the kernel function also need to be carefully considered (Read et al. 2010).

The smoothing kernel $W(\mathbf{r}, h)$ must be a normalized function that behaves like the Dirac delta function as h approaches 0 (Cossins 2010):

$$\int_V W(\mathbf{r}, h)\mathrm{d}^3\mathbf{r} = 1 \tag{2.8}$$

$$\lim_{h\to 0} W(\mathbf{r}, h) = \delta(\mathbf{r}). \tag{2.9}$$

The smoothing kernel must be symmetric and ideally should have as many continuous higher-order derivatives as possible (Rosswog 2009; Price 2012). Some commonly used functions include spline and Gaussian-based functions (Monaghan 1992), spline-based (Monaghan & Lattanzio 1985; Lahiri et al. 2020), HOCT (Read et al. 2010) and others. In the models presented in this thesis, we use the Wendland C^2 kernel (Wendland 1995; Dehnen & Aly 2012):

$$W(l) = \frac{21}{2\pi h^3}(1-l)^4_+(1+4l), \tag{2.10}$$

where $l = \mathbf{r}/h$ is the normalised distance from the particle and $(1-l)^4_+$ is $\max(0,\ (1-l)^4)$. Our chosen kernel allows us to use more particles than the perhaps more standard cubic spline and matches the more complex HOCT and spline kernels in accuracy (Dehnen & Aly 2012).

The basis of SPH used in this work is the entropy-conserving SPH formulation described in Springel & Hernquist (2003). Starting with the Lagrangian (Read et al. 2010)

$$L = \int \left(\frac{1}{2}\rho v^2 - \rho u\right) \mathrm{d}V \approx \sum_j m_j(\frac{1}{2}v_j^2 - u_j), \tag{2.11}$$

where v is the velocity and u is the specific internal energy volume $\mathrm{d}V$ was swapped for volume per discrete particle $m_j/\mathrm{d}V_j \approx \rho_j$, we get the usual SPH equation of motion:

$$\frac{\mathrm{d}v_i}{\mathrm{d}t} = -\sum_{j=1}^{N} m_j \left(\frac{P_i}{\rho_i^2} + \frac{P_j}{\rho_j^2} + \Pi_{ij}\right) \nabla_i \bar{W}_{ij}, \tag{2.12}$$

where P is the pressure given by

$$P = A(s)\rho^\gamma \tag{2.13}$$

where $A(s)$ is the entropy function and s is the entropy, γ is the adiabatic index and $\bar{W}_{ij} = W(\mathbf{r}_{ij}, h_i)/2 + W(\mathbf{r}_{ji}, h_j)/2$. Π_{ij} is the artificial viscosity term, which helps to prevent fluid quantities from becoming multivalued as discrete SPH particles come very close to (or even cross) each other. This is needed in the presence of shocks, but it is not desired everywhere else. The specific SPH flavour we are using, SPHS, where the additional "S" stands for

"Switch", employs a spatial derivative of the velocity convergence $\nabla \cdot v$ in order to detect the flow convergence in advance. Read & Hayfield (2012) define a dimensionless dissipation switch $\alpha_{\mathrm{loc,i}}$:

$$\alpha_{\mathrm{loc},i} := \begin{cases} \frac{h_i^2 |\nabla(\nabla\cdot\mathbf{v}_i)|}{h_i^2|\nabla(\nabla\cdot\mathbf{v}_i)|+h_i|\nabla\cdot\mathbf{v}_i|+n_s c_s}\alpha_{\max} & \nabla\cdot\mathbf{v}_i < 0, \\ 0 & \text{otherwise,} \end{cases} \tag{2.14}$$

where $n_s = 0.05$ is a *noise* parameter describing the scale of velocity fluctuations in terms of the local speed of sound c_s, which smoothly decays into zero if particles are not converging.

$$\Pi_{ij} = \begin{cases} -\frac{\bar{\alpha}_{ij}}{2}\frac{v_{\mathrm{sig},ij} w_{ij}}{\rho_{ij}} & \text{if } \mathbf{v}_{ij}\cdot\mathbf{r}_{ij} < 0, \\ \\ 0 & \text{otherwise,} \end{cases} \tag{2.15}$$

where $v_{\mathrm{sig},ij} = c_{s,i} + c_{s,j} - 3w_{ij}$, $w_{ij} = (v_{ij} \cdot r_{ij})/|r_{ij}|$ and $c_{s,i}, c_{s,j}$ is the local speed of sound. $\bar{\alpha}_{ij} = \frac{1}{2}(\alpha_i + \alpha_j)$ where the specific values of α are related to α_{loc} so that they smoothly decay when not needed. This must then generate entropy to ensure energy conservation:

$$\dot{A}_{\mathrm{diss},i} = -\frac{1}{2}\frac{\gamma - 1}{\rho_i^{\gamma-1}}\sum_j^N m_j \bar{\alpha}_{ij}\Pi_{ij}\mathbf{v}_{ij}\cdot\nabla_i\bar{W}_{ij}. \tag{2.16}$$

In addition, a limit to viscosity parameter is applied in shear flows to prevent spurious angular momentum transfer (Balsara 1995; Cullen & Dehnen 2010):

$$f_{\mathrm{Balsara},i} = \frac{|\nabla\cdot\mathbf{v}|_i}{|\nabla\cdot\mathbf{v}|_i + |\nabla\times\mathbf{v}|_i + 0.0001 c_i/h_i}, \tag{2.17}$$

2.1.1 Gravity treatment

Gravitational interactions between particles in `Gadget-2` (Springel 2005) are followed using N-body algorithms, a broad class of numerical techniques designed to track the motions of particles under the influence of long-range forces. Specifically, `Gadget-2` employs the collisionless N-body formalism, which assumes that close encounters between particles are not significant. This approach allows for the softening of gravitational forces, meaning the attractive force between two particles becomes constant when their separation is less than the softening length ϵ. Gravitational softening is closely linked to the SPH smoothing length - $h = 2.8\epsilon$.

The unique problem gravity poses on the technical side is that while hydrodynamical parameters can be calculated locally, that is not strictly true for gravity where each particle affects each other particle in the entire volume, meaning that computation time increases with the number of particles N as

N^2. `Gadget-2` employs a commonly used tree algorithm, specifically, oct-tree, which also allows for efficient memory allocation, to speed up gravity calculations, improving the scaling with the number of particles to $N \log(N)$. The algorithm is based on the recursive subdivision of space. Initially, a cube encompassing all the material in the model is generated. This cube is repeatedly divided into 8 daughter nodes until each contains one particle. Now, consider that we have a particle A, which is affected by the gravity of a distant group of N other particles contained in some node, all of which have the same mass. One can estimate the effect this group would have on A if evaluated as a single entity or as separate particles. If this difference (error) is sufficiently small, we could use a single calculation instead of N separate ones. In practice, this check also costs resources, so the error is checked not with each separate particle in the node, but for the 8 smaller nodes. The error can be controlled by changing the expansion criterion, thus, with sufficient computational resources, it is possible to get very close to the correct force (Springel 2005).

2.1.2 Timestepping

`Gadget-2` uses the Kick-Drift-Kick (KDK) scheme of the Leapfrog algorithm for time integration. Springel (2005) shows in detail that nominally more accurate (and computationally expensive) higher order integrators, like Runge-Kutta, are significantly outperformed in this case. Here, a particle's step is split into two sections. The particle is then first kicked (acceleration is applied) for half a step, drifted (moved at the current velocity) for a full step, and then kicked again for half a step:

$$\begin{aligned} v_{i+1/2} &= v_i + a_i \frac{\Delta t}{2}, \\ x_{i+1} &= x_i + v_{i+1/2} \Delta t, \\ v_{i+1} &= v_{i+1/2} + a_{i+1} \frac{\Delta t}{2}. \end{aligned} \tag{2.18}$$

Using the same, sufficiently small, global timestep for all particles would represent a significant waste of resources and time. To this end, each particle is assigned a timestep dependent on their local properties on a timeline subdividing the total simulation time in powers of two, referred to as 'bins'. Hence, the highest bin is a multiple of lower bins, simplifying the synchronisation. The duration of a timestep of each particle is assigned by checking a set of conditions the choice of which is always a compromise between accuracy and practicality. For N-body systems, the earliest, and still rather common, constraint on timestep durations is the CFL condition (Courant et al. 1928), which states that the timestep cannot exceed a fraction $C < 1$ of the typical particle scale length divided by the typical signal velocity. The precise definitions of *particle scale length* and *signal velocity* vary between implementations, and so any given CFL condition does not by itself have a strictly defined numerical meaning. Typically `Gadget` employs a timestep condition

$$\Delta t_i = \min\left[\Delta t_{\max}, \left(\frac{2\eta\epsilon}{|a_i|}\right), \frac{Ch_i}{\max_j(v_{ij}^{\rm sig})}\right], \tag{2.19}$$

here, three conditions are applied. The first is just a simple global maximum timestep limit $\Delta t_{\max}$ set by the user. The middle term ensures that timesteps are sufficiently small based on gravitational acceleration, here η is the desired integration accuracy also set by the user, ϵ is the gravitational smoothing length, a_i is the acceleration; The final term is a hydrodynamical constraint based on SPH interactions, ensuring that timesteps respect the CFL-like condition. In this term, C is a user-defined CFL factor, h_i is the smoothing length of particle i, and $v_{ij}^{\rm sig}$ is the maximum signal velocity between particle i and its neighbours. However, additional limits are applied for specific sub-grid physics. Saitoh & Makino (2009) also show that additional limiting of particle timesteps is required as the criteria outlined here are insufficient to handle strong explosions and multiphase media. While one solution is to apply extremely stringent $\Delta t_{\max}$ to all particles, this would make a larger model unfeasible. Another approach is to disallow neighbouring particles to have significantly larger timesteps. Saitoh & Makino (2009) show that ensuring neighbours have at most 4 times larger timesteps is sufficient.

2.2 Subgrid prescriptions

Astrophysical modelling encompasses a multitude of spatial and time scales. For example, the Schwarzschild radius for Sgr A*

$$r_{\rm s} = \frac{2GM}{c^2} \sim 4\times 10^{-7}{\rm pc}, \tag{2.20}$$

while the size of the Fermi Bubbles, an outflow likely originating from the Galactic centre, $R_{\rm FB} \sim 10$ kpc (Su et al. 2010) - factor of $R_{\rm FB}/r_{\rm s} \sim 10^{10}$ difference in scales. A completely consistent simulation that includes all the relevant physics self-consistently derived from first principles would become unfeasible purely on practical terms. Due to limitations in computational resources, we have to rely on so-called sub-grid prescriptions. Here we describe the main prescriptions used in `Gadget-3` that are generally used throughout this work[1].

2.2.1 Gas cooling

Radiative cooling is included in an approximate manner by determining a specific heating or cooling rate for each particle, depending on their state. The

[1] Note, that not every prescription is active in all of the models.

simplest case is the enforcement of an isothermal state, that is, the gas temperature is kept constant. This is useful in specific cases, like convergence testing. Slightly more complex is the β-cooling prescription, which ties the cooling timescale to the dynamical/orbital timescale, $t_{\rm cool} = \beta t_{\rm dyn}$, where β is a free parameter. This simple one-parameter description allows model systems that are cooling quickly (high-density gas with various species) or slowly (assuming some kind of background heating e.g. AGN or stellar component). Setting β to very high values allows us to approximate adiabatic flows. So while this is a relatively crude approximation, the flexibility of this approach makes it very attractive and widely used in literature (eg. Gammie 2001; Cuadra et al. 2009; Bourne et al. 2024; Koudmani et al. 2024).

When more realism is desired, this simple approach is insufficient and in that case, the thermal properties of the gas particles are determined using *cooling functions*. These are usually empirically-derived functions that define both the amount of heating and the amount of cooling that occurs. In this work, we employ a combination of methods depending on the temperature of the gas.

For gas with temperatures between 20 K and 10^4 K an empirical function by Mashchenko et al. (2008) is used:

$$\log\left(\Lambda/n_{\rm H}^2\right) = -24.81 + 2.92x - 0.6982x^2 + \log(Z/Z_\odot), \tag{2.21}$$

where $x \equiv \log(\log(\log(T)))$, the cooling term $\Lambda/n_{\rm H}^2$ is in units of $\mathrm{erg\,s^{-1}cm^3}$, $n_{\rm H}$ is the number density of H (in $\mathrm{cm^{-3}}$), $\log(Z/Z_\odot)$ is the metallicity in solar units; we assume $Z = Z_\odot$, therefore the metallicity term disappears. This prescription is based on the assumption that radiative cooling occurs via fine structure and metastable lines of C, N, O, Fe, S, and Si and that the above elements are in ionization equilibrium maintained by locally produced cosmic rays.

For temperatures above $T \geq 10^4$ K we follow an approach from Sazonov et al. (2005) where the change in energy $\dot{E}$ is approximated by:

$$\dot{E} = n_{\rm H}^2(S_1 + S_2 + S_3). \tag{2.22}$$

Here, S_1, S_2 and S_3 correspond to the effect of different physical processes:

$$S_1 = -3.8 \times 10^{-27} T^{1/2} \tag{2.23}$$

is the bremsstrahlung cooling term,

$$S_2 = 4.1 \times 10^{-35}(1.9 \times 10^7 - T)\xi \tag{2.24}$$

is the Compton heating or cooling and

$$S_3 = 10^{-23}\frac{a + b(\xi/\xi_0)^c}{1 + (\xi/\xi_0)^c} \tag{2.25}$$

is a combination of photoionization heating and line and recombination continuum cooling. The parameters here are:

$$a = -\frac{48}{e^{25(\log T-4.35)^2}} - \frac{80}{e^{5.5(\log T-5.2)^2}} - \frac{17}{e^{3.6(\log T-6.5)^2}}, \tag{2.26}$$

$$b = \frac{1.7\times 10^4}{T^{0.7}}, \tag{2.27}$$

$$c = 1.1 - \frac{1.1}{\exp(\mathrm{T}/1.8\times 10^5)} + \frac{4\times 10^{15}}{T^4}, \tag{2.28}$$

$$\xi_0 = \frac{1}{1.5T^{-1/2} + 1.5\times 10^{12}T^{-5/2}} + \frac{4\times 10^{10}}{T^2}\left[1 + \frac{80}{e^{((T-10^4)/1.5\times 10^3)}}\right]. \tag{2.29}$$

To determine the ionization parameter ξ we use:

$$\xi = \frac{L_{\rm disc}}{n_{\rm H}r^2}, \tag{2.30}$$

where $L_{\rm disc}$ is the luminosity of the AGN.

For temperatures $T > 3\times 10^7$ K, the S_3 term is dropped from equation (2.22).

In addition to the above (mainly cooling) processes, background photoelectric heating from grains is taken into account. Using functions from Bakes & Tielens (1994), the photoelectric heating rate is given by:

$$\Gamma_{\rm pe} = 10^{-24}\epsilon\chi n_{\rm H}\,{\rm erg\,s^{-1}\,cm^{-3}}, \tag{2.31}$$

where ϵ is the heating efficiency and χ is the far-UV flux normalized to the Habing field appropriate for the Solar neighbourhood; $\chi = 100$ is appropriate for the Galactic Centre. An approximate expression for the heating efficiency is:

$$\epsilon = \frac{4.87\times 10^{-2}}{1 + 4\times 10^{-3}(\chi T^{1/2}/n_e)^{0.73}} + \frac{3.65\times 10^{-2}(T/10^4{\rm K})}{1 + 2\times 10^{-4}(\chi T^{1/2}/n_e)}, \tag{2.32}$$

where $n_{\rm e}$ is the electron number density defined in terms of an ionization fraction $f_{\rm ion} = n_{\rm e}/n_{\rm gas} = 10^{-3}$. The precise value of $n_{\rm e}$ has a negligible effect on our results.

2.2.2 Non-SPH particles, accretion and feedback

In general, compact, and usually unresolved, objects, like stars and black holes are modelled as non-SPH particles with somewhat custom behaviour (eg. Springel et al. 2005; Power et al. 2011a; Nayakshin et al. 2009). In our simulations we employ three types of non-SPH particles: sink particles representing the SMBH (and the accretion disc), collisionless star particles and virtual particles for feedback injection. The specific uses differ from model to model, therefore the details are left to the relevant Chapters. However, here we describe some more general points regarding their use.

The most significant non-SPH particle, used in all of our models, is a sink-type particle representing the SMBH. The SMBH particle has an initial mass and is fixed in place, to avoid spurious accelerations. Thus, in principle, this object acts as a fixed gravitational point potential. However, implementing it as a sink particle allows for easier tracking of its properties and simplifies the implementation of other modular extensions, like coupled accretion prescriptions and feedback.

Probably the most well-known sub-grid prescription for the process of accretion was proposed by Springel et al. (2005) and was based on the Bondi-Hoyle-Lyttleton accretion flow solution (Bondi method; Hoyle & Lyttleton 1939; Bondi & Hoyle 1944; Bondi 1952). Here, the Bondi accretion rate, $\dot{M}_{\rm B}$, (which usually corresponds to the accretion rate of the SMBH) is expressed as:

$$\dot{M}_{\rm B} = \frac{4\pi\alpha G^2 M_{\rm BH}^2 \rho}{(c_{\rm s}^2 + v^2)^{3/2}}, \tag{2.33}$$

where ρ and $c_{\rm s}$ are the density and sound speed of the gas, respectively, α is a dimensionless parameter, and v is the velocity of the black hole relative to the gas. This method is very convenient, especially in large-scale simulations, as the SMBH feeding depends entirely on gas properties *far away* from the black hole. In this case, once the SMBH accretion rate is determined using the ambient gas properties, SMBH mass is increased and particles are removed stochastically from the surrounding medium ensuring approximate conservation of mass. However, the standard Bondi approach does not provide a unique way to evaluate the ambient gas properties and the decision about what counts as *far away* and how exactly properties are calculated is somewhat arbitrary. It also requires the unrealistic assumption of the absence of angular momentum which may lead to an over- or underestimation of SMBH accretion in certain situations (Hobbs et al. 2012; Negri & Volonteri 2017). These issues are somewhat mitigated by introducing a numerical correction factor (Springel et al. 2005) and/or using other modifications/alternatives to the Bondi method that may include more physical parameters in the calculation (e.g., Booth & Schaye 2009; Rosas-Guevara et al. 2015; Schaye et al. 2015; Anglés-Alcázar et al. 2016).

However, these may require prior calibration (e.g., Davé et al. 2019).

Another, and in some ways more direct approach, is to first swallow the particles and then calculate accretion properties from the properties of the swallowed gas. That is, the rate of SMBH accretion is determined not (or at least not directly) by the ambient properties of gas surrounding the sink particle, but only by the particles that get swallowed after coming *close enough* and/or fulfilling some other accretion criteria (eg. low angular momentum, low internal energy, etc.). This method can be extended by coupling the SMBH to a gas reservoir that stores the accreted material and drip-feeds it to the SMBH (Power et al. 2011b; Hopkins 2015). These *two-stage* prescriptions allow the simulators to delay feedback injection and keep the black hole accretion rate close to some chosen accretion disc model.

In our simulations we opt for this *two-stage* approach since our simulations are small enough to resolve the outskirts of the accretion disc. In Chapter 3 we assume that the swallowed material joins the unresolved SMBH+accretion disc system. Here, we are not injecting feedback, therefore accretion rates can be post-processed using a separate accretion disc model. The main disadvantage of this sort of two-stage prescription is that the properties of the accretion flow are largely dependent on a set of freely chosen parameters - viscosity timescale, accretion efficiency, etc. In particular, the viscous timescale varies dramatically even in an $\alpha-$prescription accretion disc depending on the assumed accretion radius ($t_{\rm visc} \propto R^{3/2}$ (Pringle 1981)). This means that this single parameter may artificially increase or reduce the amount and significantly impact the timing of feedback injections in a given simulation, since $t_{\rm visc}$ can range between a few kyr and a few Myr inside a given accretion disc as shown in Section 3.2.3, although in practice some *reasonable number* in between the two extremes is often chosen. This may not be as important in large-scale simulations, where the temporal and spatial scales are significantly larger, but it may be critical if we want to, for example, isolate the impact that AGN wind has on star formation in the central ~ 100 pc. Motivated by this, we developed `ringcode` - a *two-stage* accretion prescription consisting of a full 1D α-accretion disc model coupled to the SMBH particle which is numerically solved on the on-the-fly. This allows us to more consistently determine the properties for of feedback injection and therefore more robustly determine its effect on the surrounding ISM. The method is described in detail in Section 4.2. Finally, in Chapter 5 the material is simply removed for numerical reasons thus accretion here adds very limited, if any, physical meaning.

The other two non-SPH particle types are star particles and virtual particles. In our models, SPH particles may be converted to star particles if they fail a somewhat typical Jeans stability test (eg. Nobels et al. 2024) in addition to surpassing a tidal density threshold. Since star formation reduces the number of hydrodynamical interactions it can also significantly boost performance of a simulation.

Virtual particles are used for feedback injection: they carry discrete packets of momentum and energy in a randomly-chosen direction outwards from a source. They then distribute said packets to the SPH particles along the way (Nayakshin et al. 2009). In Chapter 4 and Chapter 5 the SMBH particle acts as the source of feedback, however in Chapter 5 we use a somewhat different method of feedback injection, `gridWind`, which produces identical results to virtual particles but has a lower computational cost.

Chapter 3

Feeding the central SMBH by dynamical perturbations[1]

Observations of the interstellar medium (ISM) close to the Galactic Centre (GC) reveal a ring of molecular gas surrounding the Sgr A* radio source. Known as the Circum-nuclear ring (CNR), it has an inner radius of about $1.5-2\,\mathrm{pc}$ (Ferrière 2012; Lau et al. 2013). Hydrodynamical simulations (Mapelli & Trani 2015; Trani et al. 2018) show that the CNR-like feature can form if there is an infall of matter to the central region, for example from a tidally disrupted molecular cloud (MC), which is shown to be plausible by larger scale simulations (Tress et al. 2020, 2024). Further infall episodes would result in collisions with the then present CNR-like ring surrounding Sgr A*. Such a collision could initiate a period of nuclear activity in the Milky Way by transporting a large amount of gas toward the SMBH or increasing the total mass stored in the CNR. This would naturally result in intermittent AGN episodes of varying strength, potentially explaining the various past activity indicators observed at various scales (eg. the Fermi bubbles, 430-pc bubbles, echoes, etc. Su et al. 2010; Heywood et al. 2019; Takekawa et al. 2024).

Here we consider the collision between a gas cloud and a CNR-like gas ring and its effects on nuclear activity. We model the scenario using a set of idealised simulations run with `Gadget-3` (Springel 2005). The resultant SMBH feeding rates are used as input in a separate numerical accretion disc model. This approach allows us to produce a more realistic light-curve of the AGN episode than only using the accretion rate on to the SMBH in the hydrodynamic simulation, which in turn improves the calculation of the total released energy and the estimate of the episode duration.

We perform a set of simulations focused on investigating the dependence of the feeding of the SMBH and the morphology of the resultant system on

[1] The content of this chapter is based on M. Tartėnas, K. Zubovas, Mon. Not. Roy. Astron. Soc., **492**(1), 603-614 (2020)

the initial trajectory of the infalling cloud, defined by initial collision angle γ. Extreme values, $\gamma = 0$ and $\gamma = 180°$ corresponds to a prograde retrograde collisions respectively. We find that only the steepest angles result in significant mass transfer towards the centre; low-angle collisions produce a slightly perturbed, but more massive CNR-like system. We estimate that $\gamma > 150°$ are needed to produce an outflow similar in scope to the *Fermi* formatting bubbles, even for the highest physically plausible initial gas mass of a stable CNR $M_{\rm ring} \sim 10^6\,{\rm M}_\odot$ (Ferrière 2012). We estimate, using a toy model of the CMZ, that a collision of this scale occurs once per $60 - 140$ Myr. The total accreted mass has little dependence on the cloud-to-ring mass ratio or the radius of the cloud. We analyze the morphology of resulting structures and find that the mass and size of the present-day CNR can inform us about the likely properties of a past collision event. We also discuss the applicability of our results to other galaxies, where similar CNR-like gas rings are commonly observed.

3.1 Numerical setup

We set up an idealised collision between an already present CNR-like gas ring and an infalling molecular cloud. We are using `Gadget-3` Springel (2005) version utilising a higher order dissipation switch (SPHS; Read & Hayfield 2012). For SPHS, the appropriate smoothing kernel is a Wendland function C^2 (2.10) (Dehnen & Aly 2012) with neighbour number $N_{\rm neigh} = 100$. Our main set of models has $N_{\rm part} = 5 \times 10^5$ particles with mass $m_{\rm SPH} = 0.04\,{\rm M}_\odot$. The resolved mass is $M_{\rm res} = N_{\rm neigh} m_{\rm SPH} = 4{\rm M}_\odot$. The total number of particle numbers is increased/decreased proportionally when we vary CNR mass for testing purposes Section 3.3.1.

We use gravitational potential which is a sum of the SMBH point potential and an external isothermal potential:

$$\phi = -\frac{{\rm G}M_{\rm BH}}{r} + 2\sigma^2 \log\frac{r}{r_0}, \tag{3.1}$$

with velocity dispersion $\sigma = 100$ km s^{-1}; r_0 is an arbitrary large constant. The chosen potential corresponds to an enclosed mass $M_{\rm enc} = M_{\rm BH}$ at $R_{\rm enc} = 0.8$ pc. This is somewhat smaller than the $r_{\rm NSC} = 3.5$ pc radius of the Nuclear star cluster, which has a mass similar to $M_{\rm BH}$ (Fritz et al. 2016). However, our potential corresponds to stars, stellar remnants and dark matter, therefore must have a higher enclosed mass than just that of the stars.

In total, we simulate 52 collision scenarios with different cloud collision angles $0° < \gamma < 180°$, incrementing them by 15° steps (gray filled area in Fig. 3.1). This angle is the angle between the initial orbital angular momentum vectors of the cloud and the ring. Setting γ to 0 results in a prograde collision and $\gamma = 180°$ produces an ideally retrograde collision. For each value of γ we run

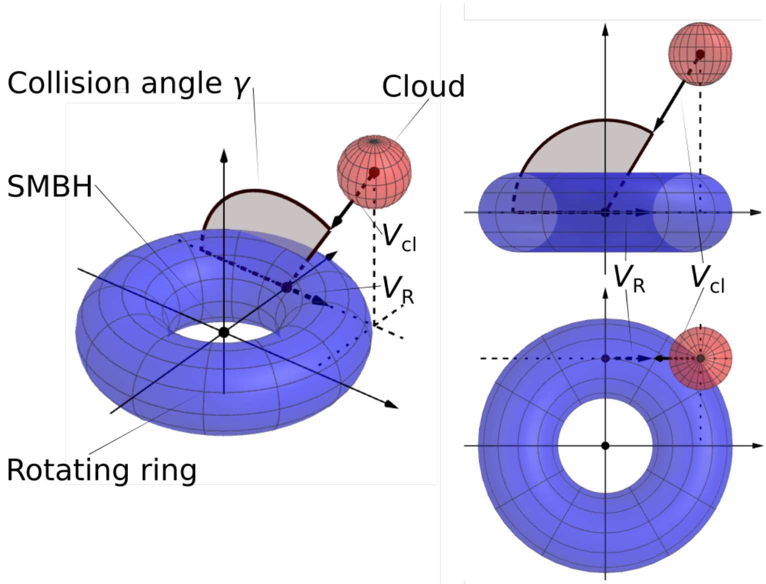

Figure 3.1: A schematic drawing of the initial system. The system is centred on the SMBH. The CNR-like gas ring is represented by the blue torus and the infalling cloud - as a red sphere. Vectors represent initial velocities: $V_{\rm cl}$ for cloud and $V_{\rm R}$ for the tangential component of rotation.

four simulations with stochastically different initial gas particle distributions in order to analyse variations due to possible chaotic aspects of the system's evolution.

A more detailed description of the initial conditions and the physics included in our simulations is given below.

3.1.1 Initial conditions

Our initial conditions consist of three main elements as shown in Fig. 3.1.

The supermassive black hole: the SMBH with an initial mass of $M_{\rm BH} = 4 \times 10^6\,{\rm M}_\odot$ is put at fixed central position. The chosen mass is similar to the SMBH mass at the centre of the Milky Way, determined from the orbits of S stars - $4.02 \pm 0.16 \pm 0.04 \times 10^6\,{\rm M}_\odot$ (Boehle et al. 2016). SMBH swallows gravitationally bound SPH particles if they fall inside $r_{\rm sink} = 0.01$ pc, which is approximately the minimal spatial resolution in the model.

The circumnuclear-like ring: The toroidal gas ring surrounds the SMBH. It has an inner radius $R_{\rm in} = 1.5$ pc, an outer radius $R_{\rm out} = 4$ pc, is similar to the currently observed CNR, but we set its mass to the lower bound of $M_{\rm ring} = 10^4{\rm M}_\odot$ (Christopher et al. 2005; Ferrière 2012). Ring particles move in circular orbits with speeds $v_{\rm R1.5} \sim 181$ km s^{-1} at the inner edge and $v_{\rm R4} \sim 160$ km s^{-1} at the outer edge.

The infalling molecular cloud: a molecular cloud with $M_{\rm cl} = M_{\rm ring} = 10^4 {\rm M}_\odot$, $r_{\rm cl} = 1$ pc is placed 6 pc away from the origin. The cloud is set on a collision course on a parabolic orbit set to pass through the middle of the ring at a point $(R_{\rm in} + R_{\rm out})/2 = 2.75$ pc away from the origin along the x-axis. The initial velocity of the centre of the cloud is $v_{\rm cl} = 220$ km s^{-1}. Clouds of similar size and mass have been observed in the GC (Kauffmann et al. 2017).

We exploit the fact that the CNR is likely not dominated by gas self-gravity by turning off the self-gravity completely. This leaves only external isothermal potential and SMBH point potential to influence the dynamical evolution of the system. In addition, we use the mass-independent β-cooling prescription (Meru & Bate 2011), where β is a constant coefficient that ties the cooling time-scale with dynamical time-scale: $t_{\rm cool} = \beta_{\rm cool} t_{\rm d}$, where the dynamical time is given by $t_{\rm d} = r/\sqrt{2}\sigma$. In our model $\beta = 0.1$, i.e. cooling is rather efficient. This means that results are insensitive to the actual masses of the ring and cloud. We show this explicitly in Section 3.3.1.

In addition to orbital velocities, all particles are given velocities from a turbulent velocity field. This is created based on the example of Dubinski et al. (1995), with velocity amplitude $\sigma_{\rm turb} \sim 37.5$ km s^{-1}. The Kolmogorov power spectrum of the velocity field for homogeneous and incompressible turbulence is

$$P_\nu \equiv \langle |v_k|^2 \rangle \propto k^{-11/3}, \tag{3.2}$$

where k is the wave number. The flow is divergence-free (i.e. turbulence is purely solenoidal) in incompressible fluid and so we can define a vector potential, $\mathbf{A}$. The components of $\mathbf{A}$ are described by a Gaussian random field, and velocity field can be derived by $\mathbf{v} = \nabla \times \mathbf{A}$. By dimensional arguments, the new power spectrum is

$$\langle |A_k|^2 \rangle \propto k^{-17/3}. \tag{3.3}$$

The dispersion of $|\mathbf{A}|$ for a field point diverges, so a cut-off wave number $k_{\rm min}$ is introduced to ensure convergence and power spectrum is redefined as

$$\langle |A_k|^2 \rangle = C(k^2 + k_{\rm min}^2)^{-17/6}, \tag{3.4}$$

where C is a normalisation constant. Since $k \propto 1/L$, the physical interpretation of $k_{\rm min}$ is that $R_{\rm max} \simeq k_{\rm min}^{-1}$ is the largest scale on which the turbulence is driven. The field is generated by first sampling the vector potential $\mathbf{A}$ in Fourier space, drawing amplitudes of each component at points (k_x, k_y, k_z) from a Rayleigh distribution with variance given by $\langle |A_k|^2 \rangle$ and assigning uniformly distributed phase angles between 0 and 2π. Then the curl is taken

$$\boldsymbol{v}_k = i\boldsymbol{k} \times \boldsymbol{A}_k \tag{3.5}$$

to obtain the velocity field components in Fourier space. Fourier transform is then taken to get the velocity field in real space. We use a grid of 64^3 cells when generating the statistical realization of the field. Finally, individual particle velocities are interpolated from nearby grid cell values.

Finally, we use a separate accretion disc model to determine the rate of SMBH accretion and therefore, the evolution and energetics of the induced AGN event. The model employs an Eulerian integration scheme to solve the thin-disc diffusion equation described in e.g., Chapter 5 of Frank et al. (2002):

$$\frac{\partial \Sigma}{\partial t} = \frac{3}{R}\frac{\partial}{\partial R}\left(R^{1/2}\frac{\partial}{\partial R}\left[\nu \Sigma R^{1/2}\right]\right), \tag{3.6}$$

where Σ is the surface density and R is the radial coordinate. The shear viscosity ν is parametrized by an α prescription (cf. Shakura & Sunyaev 1973): $\nu = \alpha c_{\rm s} H$, where $c_{\rm s}$ is the sound speed and H is the vertical scale height of the disc.

The disc consists of 151 of annuli rotating in Keplerian orbits around a central mass. We hold that the inner edge of the disc is the innermost stable orbit (ISCO) at $R_{\rm ISCO} = 3\,R_{\rm s}$ and set the outer edge at $R_{\rm out} = 26107\,R_{\rm s} = R_{\rm BH} = 0.01$ pc to correspond with the sink radius of the SMBH particle in the main simulation. The annuli have logarithmically increasing width: $l_{i+1}/l_i \simeq 1.06$. The width of the innermost annulus is $l_0 \approx 0.18\,R_{\rm s}$ and the outermost has $l_{150} \approx 1520\,R_{\rm s}$.

The material is transported through the disc toward the centre by the action of viscous torques, emitting thermal radiation. The mechanism of radiation emission is usually parameterised as being generated by the dissipation of viscous stress. We assume that each annulus is a separate black body for the purpose of luminosity calculation, so the full spectrum is given by the superposition of the spectra from each annulus and the luminosity at any given time is:

$$L = \sum_i L_i = \sigma_{\rm SB} \sum_i A_i T_i^4, \tag{3.7}$$

where $\sigma_{\rm SB}$ is the Stefan-Boltzmann constant and A_i and T_i are the surface area and temperature of the ith annulus, respectively. While this luminosity is calculated, it is not injected into the main simulation as feedback. This means, that the luminosity and duration of the AGN event is overestimated as we don't have the regulating influence of AGN wind. However, since the momentum of the AGN wind at its peak is still much smaller than the weight of the central disc (Section 3.3.6), the general morphology should not change by much. This is confirmed in the more detailed simulations with feedback shown in Chapter 4.

Lastly, since we only have the rate of acccretion, we calculate the parameters of the disc using five feeding radii (radii of the annuli into which the accreting material is initially deposited): $R_{\rm f}/R_{\rm s} = 300, 5725, 11150, 16575$ and 22000. In

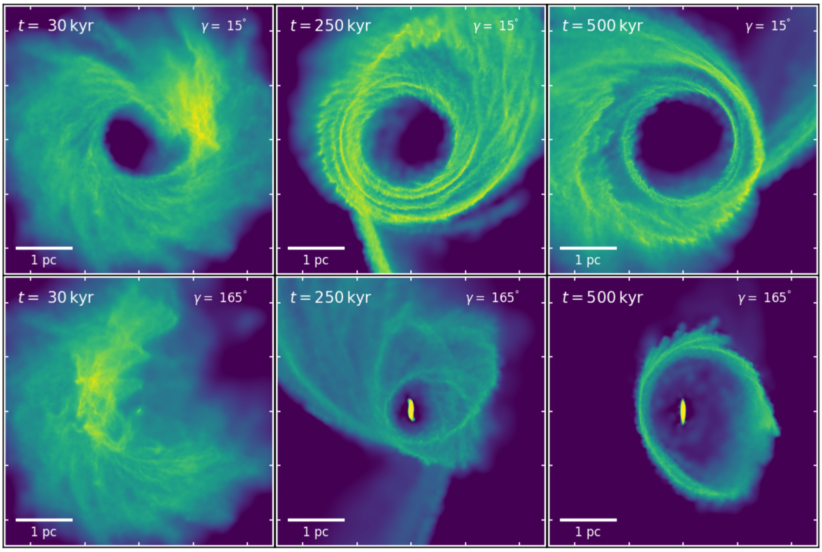

Figure 3.2: Evolution of models after prograde (top) and retrograde (bottom) collisions. From left to right we have the system's evolution in time, starting right after the initial collision at $t = 30$ kyr.

reality, there would be a spread of radii at which material falls on to the disc, but we expect that our method provides reasonable upper and lower limits to SMBH accretion rates. This is also checked more thoughtfully in our discussion on the application of the `ringcode` accretion prescription Section 4.2.3.

3.2 Results

3.2.1 Morphology of the resultant system

About 20 kyr into the simulation, the cloud collides with the ring. Both structures are somewhat patchy and filamentary, due to the effect of turbulence. In line with intuition, the effect of said collision depends strongly on the collision angle. The contrast between the post-collision morphologies is clearly noticeable in density maps (Fig. 3.2). Here we see that a shallow collision angle $\gamma = 15°$ (top) resulted in only a slight perturbation of the initial system, while a steep angle $\gamma = 165°$ (bottom) impact disrupted the initial system completely. In the first case, almost all the gas settles onto the perturbed initial ring, since the gas cloud does not oppose the rotation of the ring and even accelerates some of the ring particles. In the second case, the cloud opposes the rotation of the ring and the collision slows down some of the gas. Because of this, a large fraction of the initial gas mass is transported to the centre of

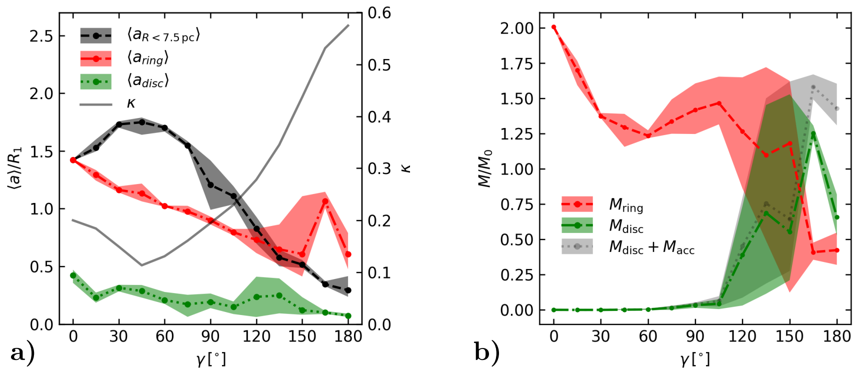

Figure 3.3: **a)** the average circularization radii of gas at $t = 0.5$ Myr in simulations with different initial collision angles. Black line: all gas within 7.5 pc; red line - the resultant rings, green line - the central disc. Shaded regions show the highest/lowest values among stochastically different models with the same collision angle. The grey line (scale on the right) shows the fraction κ of the ring contacted by the cloud during initial passage (eq. 3.8). **b)** average masses of the resultant rings (red) and central discs (green) in models with different initial collision angle γ expressed in ratio with the initial ring mass $M_0 = 10^4\,\mathrm{M}_\odot$. Grey line shows the sum of disc mass and mass accreted by the SMBH particle. Shaded areas show variations between models with the same γ.

the system, where it forms a central disc perpendicular to the rotation plane of the initial ring and the remaining matter settles into a somewhat smaller and significantly narrower ring.

For further analysis, we define two types of resultant structures: discs and rings. A disc is a structure that extends outward from the accretion radius $R_{\rm BH}$ and has a clear outer edge. A ring is a structure bounded by sudden density drops at both the inner and outer edges. To assign gas particles to either a disc, a ring, or neither, we analyse radial gas density profiles and density maps. In some cases, these distinctions are somewhat subjective, but they still provide a useful framework for studying the system's evolution. In fact, the formation of a distinct disc/ring system is expected as demonstrated by simulations performed by Trani et al. (2018), where discs tend to form inside the SMBH sphere of influence. We also note that we did not include tails of streams that did not yet settle onto the ring (e.g. Fig. 3.2, top) as contributing to the ring's mass.

Broadly speaking, large-angle collisions lead to formation of more compact systems; which we demonstrate by plotting the radius at which the structure should settle given the specific angular momentum, the average circularization radius, of the resultant structures - discs (green) and rings (red) Fig. 3.3(a).

All particles within the central < 7.5 pc are shown in black and include any particles that did not yet settle on to either a disc or a ring. The system is most compact after a retrograde collision ($\gamma = 180°$), but there is a striking peak at $\gamma = 45°$. Given the simplicity our idealised model, this is qualitatively explained by different *encounter lengths*, defined here as the fraction of ring material interacting with the cloud. This fraction can be roughly estimated analytically:

$$\kappa \approx \frac{v_{\rm enc} t_{\rm enc} + d_{\rm cloud}}{C}, \tag{3.8}$$

where $v_{\rm enc} \equiv v_{\rm cloud} \cos \gamma - v_{\rm orb}$ is the relative velocity of the cloud and ring material, $t_{\rm enc} \equiv l_\gamma / v_{\rm cloud}$ is the time required for the cloud to pass through the ring, l_γ is the length of the path of the cloud's orbit inside a spiric section of the toroidal ring for a given angle γ, $d_{\rm cloud}$ is the diameter of the cloud and C is the circumference at the midpoint of the torus. κ then shows the fraction of the ring circumference that the cloud travels while it stays in contact with the initial ring. $\kappa(\gamma)$ is plotted as a grey solid line in Fig. 3.3(a). Even though this is a very approximate estimate, its qualitative anti-correlation with the mean circularization radius is clearly evident. The stochastic variation of circularization radius is small for angles $30° \leq \gamma \leq 60°$, so this result is robust. The peak is only seen when we look at all the particles, including the ones that did not yet settle on to the central disc or rings. We interpret this as a consequence of the cloud carrying away some fraction of the ring material, which then stretches into elongated spiral orbits and has not settled into a ring-like structure by $t = 0.5$ Myr. The large variance of the disc and ring radii in simulations with $120° \leq \gamma \leq 150°$ is caused by the disc and ring having a very narrow gap in these simulations, so their relative sizes vary significantly due to stochastic differences; the variance disappears when we consider all the particles.

The peak in the circularization radius of the ring at $\gamma = 165°$ is explained better when we also consider the masses of the resultant structures shown in Fig. 3.3(b). At this angle, a significant majority of the system's gas mass is contained within the central disc and the low-mass rings are completely separated from the inner disc (Fig. 3.2). Almost all of the mass is contained in outer rings when $\gamma < 120°$. Central discs appear when $\gamma > 60°$. In simulations where $\gamma \geq 120°$ the mass of the discs becomes non-negligible and more and more of the material is transferred towards the centre as the angle increases; the amount that feeds the central BH accounted for as grey line and shaded region. In the most extreme retrograde collision more than half of the initial CNR mass is fed to the SMBH.

The central discs in our simulation are warped, which is clearly illustrated in Fig. 3.4(a). A warped disc with steep enough tilt is likely to break up (Nealon et al. 2016). However, in our simulations only a fraction of central

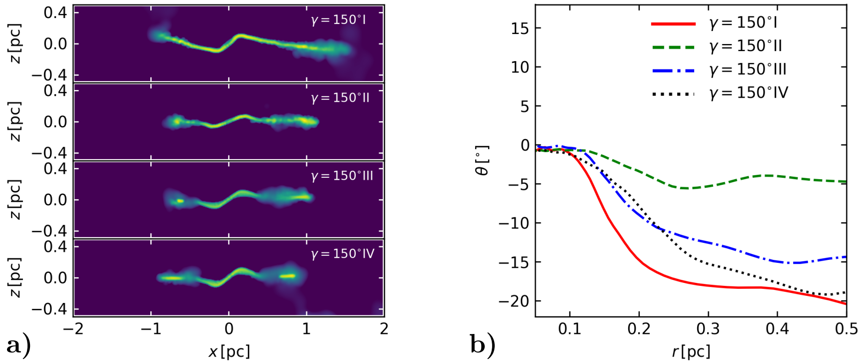

Figure 3.4: **a)** density wedge slices of the simulations with $\gamma = 150°$. **b)** the tilting of the central disc for simulations with $\gamma = 150°$. The tilt does not explain the breaking of the disc, as simulation I has the largest and steepest tilt but this did not result in a separate ring breaking off.

discs break up and this does not seem to be related to the tilt: Fig. 3.4(b) shows the tilt angle for the four simulations with $\gamma = 150°$; the central discs with the largest and the smallest tilts do not break up (I and II), while discs with intermediate tilts do (III, IV). The breaking up of the disc also appears to occur close to the radius at which the external potential starts to dominate over the SMBH (~ 0.8 pc), however, the largest and most tilted disc (I) is stable at even at larger radii. The specific appearance of these structures may also be mostly due to the stochastic differences in initial turbulent velocity field, as that is mostly responsible for the formation of specific clumps and filaments before the collision. In any case, the fact that the central disc is warped could be important for observation and the significance of narrow dense discs are explored further in Section 3.3.

3.2.2 Gas transport

Models with larger collision angles result in more gas moving into orbits closer to the black hole, increasing the number of particles crossing the $R_{\mathrm{BH}} = 0.01$ pc boundary. If these are also gravitationally bound to the SMBH we remove them from the hydrodynamical simulation and their mass is added onto the SMBH. We show the resultant SMBH accretion rate, scaled to the Eddington accretion rate $\dot{M}_{\mathrm{Edd}} = 9.5 \times 10^{-2}\,\mathrm{M}_{\odot}\ \mathrm{yr}^{-1}$, for three representative simulations with significant gas transfer rates in Fig. 3.5(a)[2]. The evolution of the gas transfer rate depends on the collision angle and can be grouped into three scenarios:

[2] To reduce noise, the curves are smoothed using a kernel $w = \{1/16, 4/16, 6/16, 4/16, 1/16\}$.

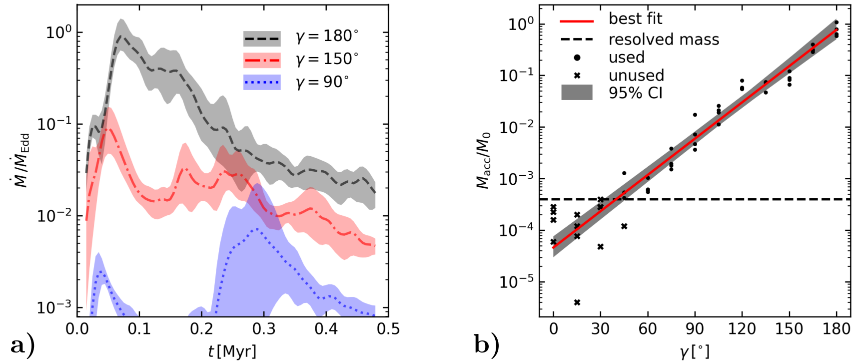

Figure 3.5: **a)** time evolution of the average accretion disc feeding rate, scaled to the Eddington mass accretion rate. Shaded regions show variations among stochastically different models with the same collision angles. The curves are smoothed by applying a weighting kernel to reduce spurious noise. **b)** the total mass transported to the central accretion disc over about 0.5 Myr. Red line is the best fit to the data of individual simulations (points; crosses indicate simulations that were not used for fitting, since the total transferred mass is smaller than the resolved mass limit), and the grey shaded area is the 95% confidence limit on the line parameters.

- **Low-angle collisions ($\gamma < 60°$):** The initial perturbation is weak, with negligible gas transfer to the system's centre.
- **Intermediate angles ($60° < \gamma < 120°$):** These collisions perturb the system enough to drive gas inward, increasing the feeding rate initially. Secondary collisions occur as some of the remnants of the cloud and ring interact with the newly forming central disc, producing a secondary accretion peak starting at $t \sim 0.22$ Myr, about 20 dynamical times of the initial ring.
- **High-angle collisions ($\gamma > 120°$):** Strong collisions significantly disrupt the system, sending large amounts of gas to the centre and potentially exceeding the Eddington limit. The secondary peak at $t \sim 0.22$ Myr diminishes with increasing angle, as more material falls directly inward rather than forming a stream that interacts with the ring.

Fig. 3.5(b) shows the total mass that feeds the BH (passes the 0.01 pc boundary) over 0.5 Myr. Each point represents a single simulation. The total accreted mass closely follows an exponential dependence on collision angle:

$$\log\left(M_{\mathrm{acc}}/M_0\right) \approx 2.34^{+0.14}_{-0.15} \times 10^{-2}\gamma - 4.34^{+0.22}_{-0.19} \tag{3.9}$$

When determining the parameters (slope and intercept), I disregarded the points where the total mass transfer to the SMBH particle was smaller than the mass resolution of our hydrodynamical simulation ($M_{\rm tot} < 100 m_{\rm SPH} < 4{\rm M}_\odot$); the cut-off is marked with a horizontal dashed line. The parameters were determined by fitting a line on a dataset generated by bootstrapping the simulation data. The best fit line is shown in Fig. 3.5(b) in red, with the shaded grey area encompassing a 95% confidence interval of possible slopes.

The fitted relation (eq. (3.9)) allows us to estimate the possible total energy output $E_{\rm tot}$ of the whole activity period given the angle of the collision and the initial mass of the system using:

$$E_{\rm tot} = \eta c^2 M_{\rm acc} = 1.8 \times 10^{57} \eta_{0.1} M_4 {\rm erg}, \tag{3.10}$$

where $\eta \equiv 0.1\eta_{0.1}$ is the radiative efficiency and $M_{\rm acc} \equiv 10^4 M_4\,{\rm M}_\odot$ is the total accreted mass.

3.2.3 Accretion and released energy

At face value, the hydrodynamical simulation results show that we have significant feeding of the SMBH. It is unrealistic, however, to assume that all the material feeds the SMBH instantaneously . Instead, material takes time travelling through the accretion disc due to viscous torques. We address this by post-processing the accretion rates with a separate accretion disc model (Section 3.1). Only the results of SPH simulations with the three largest resulting feeding rates were used as input: those with $\gamma = 150, 165$ and 180 degrees. Each input was used in five accretion disc simulations with different feeding radii, giving a total of 15 simulations.

Luminosity calculated using the feeding rates from SPH models with $\gamma = 180°$ is shown in Fig. 3.6(a) (left). Each disc simulation was run for 1.5 Myr. Here, delay and smoothness increases with larger feeding radii ($R_{\rm f}/R_{\rm s} = 300, 5725, 11150, 16575, 22000$, with $R_{\rm s}$ being the Schwarzschild radius of the SMBH, therefore the peaks of the luminosity curve move right due to delay and down due to the spreading over longer period. The delay increases because the material has to travel from $R_{\rm f}$ to ISCO to actually feed the SMBH. Perhaps less intuitively, the prolonged and somewhat diminished activity period occurs because not the entire injected mass, but only a diffused portion of it reaches the SMBH at any given time. If material is injected very near (or even directly into) the ISCO, we get instantaneous feeding of the SMBH, the same as we would get without the disc model. It is worth noting that if we take the usual AGN cut-off luminosity at $L > 0.01 L_{\rm Edd}$, the model with the smallest $R_{\rm f}$ gives a shorter AGN episode duration than models with $R_{\rm f}/R_{\rm s} = 5725, 11150, 16575$, since the accretion rate gets much more smoothed out in those cases. Finally, when $R_{\rm f} = 22000\ R_{\rm s}$, much of the matter escapes the accretion disc without producing significant luminosity. We will address accretion and the connection

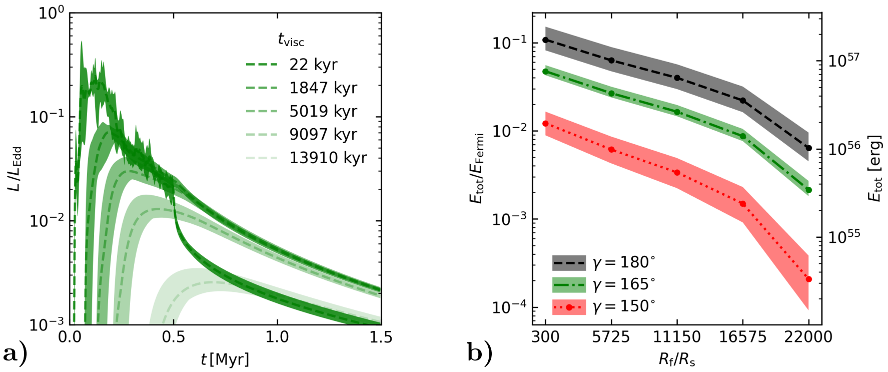

Figure 3.6: **a)** evolution of the luminosity of the accretion disc over time in the simulation with $\gamma = 180°$. A progression of lower peaks and longer delay correspond to the increasing disc feeding radii $R_{\rm f}/R_{\rm s} = 300, 5725, 11150, 16575, 22000$ ($t_{\rm visc} = 22, 1847, 5019, 9097, 13910$ kyr). **b)** the total energy released during the activity period (lines and points). Shaded regions show variations among models with the same γ.

between the accretion disc and the larger hydrodynamical model with significantly more detail in Chapter 4, where we introduce an accretion disc particle method (`ringcode`) to model accretion more consistently.

We calculate the total energy released during an induced activity period by integrating the luminosity over time. We show the result scaled to the energy required for *Fermi* bubble formation, in Fig. 3.6(b). The total energy release required for the inflation of the *Fermi* bubbles is estimated to be 1.6×10^{58} erg (Zubovas & Nayakshin 2012), therefore accretion of $< 10^5\,{\rm M}_\odot$ of gas is enough to produce them. We see that the total energy also decreases with increased $R_{\rm f}$. This happens because more of the gas leaves the system through the outer boundary as the feeding radius increases. But it's important to note, that these accretion rates are unlikely to reflect some *real* accretion rate, instead these should be taken as an indicator, that a more prudent approach to accretion modelling is required, especially when energy is injected back as feedback. Fig. 3.6(b) shows that models with collision angle of 180° generate on average about $\sim 10\%$ of the energy required to form *Fermi* bubbles if gas is injected into the disc close to the black hole; most simulations with $\gamma \geq 165°$ produce $> 1\%$ of the required energy.

We adopted the minimal mass estimated from observations of the CNR for our initial system, ensuring a lower limit for accretion. The initial mass could be up to two orders of magnitude larger and still consistent with the observational constraint, determined by the CNR self-gravity threshold $M_{\rm ring} \approx 10^6\,{\rm M}_\odot$ (Ferrière 2012). For the most massive possible system, the energy output could be up to 100 times greater than in our simulations. A cloud of this mass would likely also be significantly larger, $R_{\rm cl} \sim 5$ pc, even in the dense GC environment (Kauffmann et al. 2017), straining the validity of our setup. Models of retrograde collision (Chapter 4) show, that at least in that case a scaled-up cloud with $R_{\rm cl} \sim 3$ pc produces significant accretion. Notably, a cloud with a less massive than the ring by a factor of a few could still trigger a comparable accretion episode (see Section 3.3.1).

An additional complication is that our accretion disc model is not well suited to model systems with luminosity reaching $L > L_{\rm Edd}$ or to systems where the accretion rate is well below the Eddington accretion rate, where other types of accretion flows are more likely (Koudmani et al. 2024). Super-Eddington accretion causes some of the material to be shed before reaching the SMBH, therefore the difference in total released energy may not be as large as the increase in disc feeding rate. We return to this point in Section 3.3.6.

3.3 Discussion

We show that sufficiently retrograde collisions between a CNR-like gas ring and an infalling molecular cloud result in substantial gas transport to the system's centre and, in extreme cases, feeding of the central supermassive black hole. In contrast, prograde collisions increase the mass and extent of CNR-like ring, storing even more gas in the vicinity of the SMBH increasing the potential scope of a future AGN event.

Here we begin by discussing the impact that some chosen parameters - the gas cooling rate and the relative sizes/mass of the CNR and the MC - have on accretion (Section 3.3.1). In Section 3.3.2 we crudely estimate the expected frequency of collisions and the resulting AGN duty cycle. We discuss the implications of our findings for MW and other galaxies in Section 3.3.3 and Section 3.3.4. We discuss the dense, possibly star forming rings found in some of the simulations and the challenge they pose to our initial assumptions in Section 3.3.5. We address the possible effects of feedback and super-Eddington accretion, neglected in our simulations, in Section 3.3.6.

3.3.1 Varying the idealised setup

In our idealised setup, the initial mass of the CNR-like ring and the infalling MC are both the same. In order to investigate how relaxing this assumption effects our results, we performed several simulations of collisions with different ring masses. For practical reasons, simulations were performed only for the two most extreme collisions, $\gamma = 150°$ and $180°$, and for a reduced duration.

First, we ran simulations varying the mass ratios $M_{\rm cloud}/M_{\rm ring} = 0.4, 0.8, 1.2, 2.5$, while $M_{\rm cloud} = M_0 = 10^4 {\rm M}_\odot$ was kept the same as in the main simulations. Next, we similarly varied the radius of the cloud using

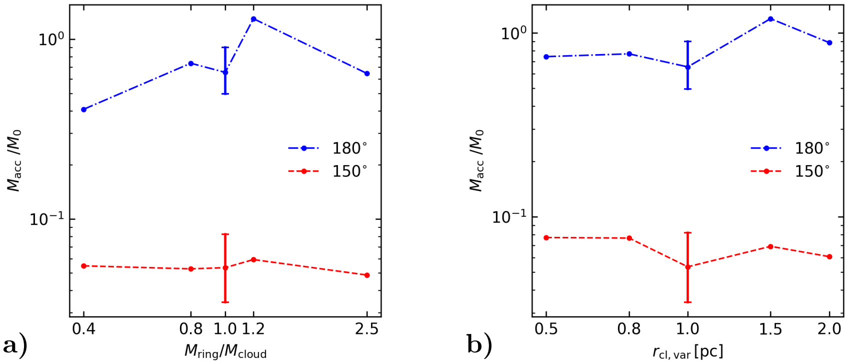

Figure 3.7: a) total accreted mass relative to total initial mass of the system after 0.2 Myr for varied initial ring/cloud mass. The average and the extent of the main set of models is shown at the point $M_{\rm ring} = M_{\rm cloud}$. **b)** total accreted mass relative to total initial mass of the system after 0.2 Myr for varied cloud radius. The average and the extent of the main set of models is shown at the point $R_{\rm ring} = 1$ pc.

$r_{\rm cl,var}/r_{\rm cl} = 0.5, 0.75, 1.5, 2$, keeping the mass constant. The total accreted mass as a function of mass ratios and as a function of cloud radius is shown in Fig. 3.7(a) and Fig. 3.7(b) respectively. Note that simulations with varied cloud parameters encompassed only 0.2 Myr; we did not continue them further because the evolution of the system was very similar to the main simulations in all cases. The central point in each case is the result from the main set of simulations, the error bar indicating the variation due to the stochastic particle positions/turbulence. We can clearly see that the changes in accretion due to the variation of parameters are comparable to the stochastic variations and have little to no systematic effect. However, we do not claim that this trend would hold for more extreme mass ratios or cloud radii.

Similarly contrived is our chosen cooling prescription, β-cooling (Meru & Bate 2011). This is a significant simplification of actual cooling processes, so in order to test the importance of cooling on our results, we ran several simulations varying the factor $\beta_{\rm c}$ from 10^{-3}, which makes the gas cool significantly faster, up to 10, which slows the cooling.

The results given in Fig. 3.8 show that longer cooling time for gas increases accretion up to a maximum factor ~ 3 higher than fiducial models. This happens because rapid cooling of gas results in narrower gas streams of due to the reduced pressure support as pressure P is directly proportional to the internal energy of the gas u. As a result, collisions become rarer, making it more difficult to cancel out angular momentum, which results in reduced gas transport to the central regions. It is also important to note that the stochastic variation in total accreted mass (error bars in Fig. 3.8) is as large as caused by

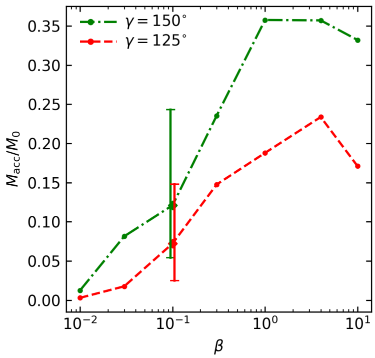

Figure 3.8: Relationship between the cooling parameter β and the total amount of accreted gas in units of $M_0 = 10^4 M_\odot$. The value of β_c used for the main set of models is marked with diamonds. The variation of accreted mass is shown as error bars.

a change of the value of β_c by a factor 3.

One piece of evidence for the activity period ~ 6 Myr ago is the ring of young stars around Sgr A*. They probably formed from a fragmenting gas disc and/or ring. It is known that fragmentation of rings in simulations requires the cooling parameter to be $< 4.5 - 6$ (Nayakshin et al. 2007). Therefore, the value of β_c chosen for our main set of models is rather conservative, since more efficient cooling allows for less accretion. The short cooling times also compensate, to some extent, for the lack of self-gravity in our simulations, by making the gas streams narrower than they might otherwise be. It is also notable that any heating is also neglected here and the more realistic simulations of a retrograde collision in Chapter 4 also use a more detailed cooling prescription and still produce significant accretion.

3.3.2 Frequency of collisions

Our hydrodynamical simulations follow only a single event. However, we assume that in our setup material intermittently flows towards the centre, which is how the initial CNR-like ring must have formed (Mapelli & Trani 2015; Trani et al. 2018). This matter flow could build up the CNR, only resulting in a significant activity episode once an extreme collision occurs. We can make a rough estimate of the timescales of these processes by looking at how many clouds might have orbits that take them closer than $r_t = 4$ pc to the BH ($\sim r_{out}$ of the CNR) and how likely that cloud is to come in at an angle that results in significant accretion. Given the mass spectrum of the MCs (Williams & Mckee 1997) and the mass of the CMZ ($M_{CMZ} \approx 3 - 5 \times 10^7$ M$_\odot$; Ponti et al. 2013a), we generate a random uniform distribution of clouds on elliptical orbits with semimajor axes 200 pc and 100 pc, which correspond to the sizes of the X$_1$ and x$_2$ orbit families of the Galactic bar potential The cloud velocity in the x-y plane is $v_{xy} = 165/\sqrt{2} \pm \sigma$ km $^{-1}$ and in the z direction $v_z = 0 \pm \sigma$ km/s. We test three values for the velocity dispersion $\sigma = 10, 20, 35$ km s^{-1}. The frequency of close encounters is computed based on the orbital period of clouds

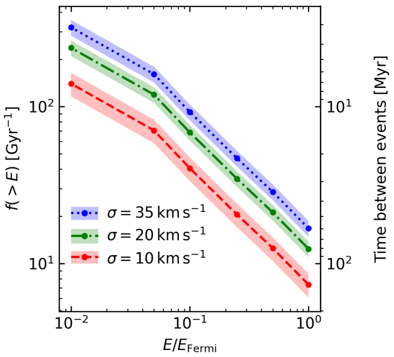

Figure 3.9: Estimated frequency of collisions that result in the energy release of at least the given fraction of $E_{\rm Fermi}$, scaled to CMZ mass of $5 \times 10^{7}\,\mathrm{M_{\odot}}$.

with the periapsis $r_{\rm peri} < r_{\rm t}$.

A cloud of certain mass produces substantial accretion only if the collision angle is steep enough; more massive clouds are more likely to produce substantial accretion, because the range of viable angles is greater, but they are also less numerous. This is taken into account using (3.9), which relates the total accreted mass and collision angle, and the mass spectrum of the MCs which gives a number of clouds in a given mass range. Frequency is weighted by the *viable* range of angles for a given cloud.

Our results after performing calculations with 100 random cloud distributions are shown in Fig. 3.9. We scale the energy released during an AGN event to the presumptive energy required for the inflation of the Fermi bubbles. We find that a smaller AGN event ($\sim 0.05 E_{\rm Fermi}$) could occur every $3.1 - 7.2$ Myr, while a much larger collision that could result in *Fermi* bubble formation occurs every $60 - 140$ Myr, for a CMZ with the mass of $5 \times 10^{7}\,\mathrm{M_{\odot}}$; the frequency of collisions scales linearly with CMZ mass.

This is a very simplistic calculation as we do not consider interactions between clouds and their orbital evolution. Also, equation (3.9) describes conditions where both CNR and MC are about the same mass. Based on the same assumptions as above, we estimate the CNR growth rate to be $\dot{M}_{\rm CNR} \sim (4.3 - 6.0) \times 10^{-2}\,\mathrm{M_{\odot}\,yr^{-1}}$, which is larger than the lower obeservational limit of the CNR mass growth given by$\dot{M}_{\rm min} \sim 2 \times 10^{-3}\,\mathrm{M_{\odot}\,yr^{-1}}$ (Hsieh et al. 2017), but only a factor of two bigger than the average feeding rate determined using detailed hydrodynamical model of the CMZ $\dot{M} \sim 0.03\mathrm{M_{\odot}}$ Tress et al. (2020). The fact that our toy calculation is close to agreement with much more sophisticated models give us some confidence that our simplistic model captures some interesting aspect of the system and works well enough for the purpose used here.

3.3.3 Evidence of past collisions in system morphology

Simulations of the formation of the CNR show that an infalling MC is a likely explanation of its origin (Trani et al. 2018). But the inflow of gas into the centre does not stop after the formation of the CNR; instead, it continues with other MCs and gas streams falling in, resulting in collisions between the CNR-like gas ring at the centre and the observed infalling matter from larger scales (Liu et al. 2012; Hsieh et al. 2017). This work also relies on an assumption that material falls in with random orientation. That is, the scales of the CNR are small enough that the trajectory of an infalling cloud will be in various random orientations; this is tangentially supported by both the orientation of the inclination of the current CNR of around 20° from Galactic disc and an even more inclined stellar rings (Hsieh et al. 2017; Paumard et al. 2006). That is, system as seen likely shows the effect of multiple collisions.

Our simulations show that these collisions do not necessarily result in significant nuclear activity - looking at the plot on the left in Fig. 3.3(b) we can see that for $\gamma \leq 105°$ almost all of the gas is still in the form of rings and its mass is larger than the initial mass of the CNR-like torus. The right of Fig. 3.3(a) shows that collisions with $90° < \gamma < 120°$ result in a system of similar extent to the initial ring. Collisions at larger angles leave rings that are smaller rings than the initial one. Thus it seems plausible that the CNR-analogue that existed > 6 Myr ago might have been more massive and larger than the present-day one, and was reduced in both mass and size following the extreme collision.

This process implies the existence of a cycle, where the ring system grows in mass, up until a collision feeds its mass to the black hole and/or star formation begins in the densest fragmenting regions. Additionally, star formation might not be confined to the central parsec. Dense filaments exist in the outer rings in our simulations. Provided that they are not disrupted by infalling matter, they could grow to be dense enough and create elongated stellar filaments. This could be contrasted with a single infalling cloud, which would result in star formation only in the central disc region (Bonnell & Rice 2008). More detailed simulations (Generozov et al. 2022) show that a low velocity cloud falling in from 10 pc could plausibly produce stars with highly elongated orbits to reproduce the young stellar disc (Levin & Beloborodov 2003).

In addition, the central cavity contains a minispiral (Ferrière 2012). Trani et al. (2018) hints that this central structure forms during the formation of the CNR. In this work we show that gas does naturally fill in the central region given a steep enough MC trajectory. There are also cloudlets observed in the central cavity which are possibly remnants of a smaller disrupted gas cloud (Goicoechea et al. 2018). These are short-lived structures, which suggest that there is somewhat regular inflow of clouds.

3.3.4 Qualitatively similar events in other galaxies

Our simplistic setup relies on comparisons to the surroundings of Sgr A*, and while it is true, that the mass of this SMBH is on the lower end, there is, however, little reason to think that similar intermittent cycles of feeding do not occur in other galaxies. On the contrary, in Section 1.2.3 we already outlined that our galaxy fits in inside the general picture where barred galaxies see increased activity (Ponti et al. 2013a; Storchi-Bergmann 2014; Agüero et al. 2016; Garland et al. 2023, 2024).

A CNR-like feature is often unresolved in other galaxies, but there seem to be examples of both central molecular discs and filaments transporting gas closer to the centre. For example, Audibert et al. (2019), combining ~ 17 pc resolution observations of both morphology and kinematics identified trailing spirals in the central region of the active galaxy NGC 613. The significant angular momentum loss in that region, between 25 pc and 100 pc, means that gas should move inwards. Similar spirals are observed in NGC 1808 (Busch et al. 2017; Audibert et al. 2021) and NGC 1566 (Combes et al. 2014; Smajić et al. 2015). There are also examples of both central molecular discs and filaments transporting gas closer to the centre (e.g., Izumi et al. 2018; Prieto et al. 2019b). ALMA observations also found a counter-rotating ~ 1 pc scale disc relative to the torus of the active galaxy NGC 1068 (Impellizzeri et al. 2019). This two-disc configuration suggests that the structure formed in more than one accretion event and is consistent with the chaotic accretion scenario (King & Pringle 2007). These observations suggest that CNR-like structures are closely connected to nuclear activity, perhaps through a cycle of growth and depletion via extreme collisions, as suggested by our simulations.

If we assume similarity between our Galaxy and others that contain CMZ-scale structures, we can speculate that gas inflow to the centre from this CMZ should first produce a CNR-like parsec-scale structure, with further collisions resulting in either a build-up of gas in the CNR-like structure or a larger activity event on a timescale similar to the one calculated in Section 3.3.2 above, linearly scaled to the mass of the CMZ-like rings. As seen in Fig. 3.3(b), the CNR-like ring is significantly depleted after a collision that results in significant accretion. But if we assume that new mass continuously enters the system it would take $0.2 - 2$ Myr for the CNR to grow to $10^4\,\mathrm{M}_\odot$. This is comparable to, but somewhat longer than, the timescale of the activity period (a few times 10^5 yr) (King & Nixon 2015; Schawinski et al. 2015). Therefore a CNR-like feature with a small mass could be an indicator of indicate recent nuclear activity.

3.3.5 Formation of stellar rings

The GC region contains a number of relatively young massive stars (Genzel et al. 2010). Most of the young stars located in the central $R \leq 0.5\,\mathrm{pc}$ formed

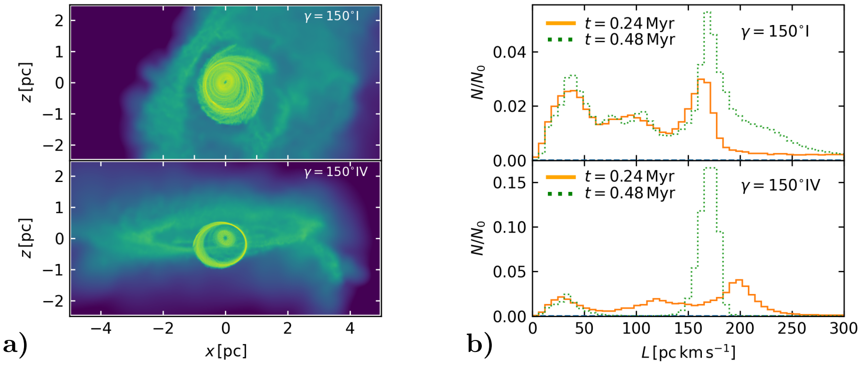

Figure 3.10: **a)** density maps of two simulations with $\gamma = 150°$ at $t = 0.48\,\mathrm{Myr}$. **b)** distribution of gas angular momentum per unit mass of the central region in the same simulations at times $t = 0.24\,\mathrm{Myr}$ and $t = 0.48\,\mathrm{Myr}$. A peak formed in both I and IV simulations, but the one in I did not detach from the central disc.

in a single episode $6 \pm 2\,\mathrm{Myr}$ ago (Paumard et al. 2006). This collection of stars is modelled as two co-eval (Bartko et al. 2009) discs rotating in clockwise and counter-clockwise directions, with a large angle between them (Genzel et al. 2010). The existence of the counter-clockwise disc is in doubt as more recent studies of the young star cluster kinematics did not detect a significant feature (Yelda et al. 2014).

A star formation episode could result from a fragmenting gas ring, possibly formed after a collision (Bonnell & Rice 2008; Hobbs & Nayakshin 2009). Possible star formation in two misaligned rings following a collision between a cloud and the CNR was the focus of Alig et al. (2013). They also found that such an event results in considerable accretion onto the SMBH. In our simulations gas self-gravity is turned off, so we cannot track gas fragmentation and star formation directly. Even so, some rings separate at the outer edge of the central disc at $\sim 1\,\mathrm{pc}$ (see fig. 3.10(a) and left panel of fig 3.4(a)), and most collisions form some rings that are narrower and denser than the initial one. The rings break apart as the particles travel closer to the centre, exchanging angular momentum with the faster-moving particles.

As the mass of these rings grows, so does their density, reaching values above the tidal density. The Toomre Q parameter (Toomre 1964),

$$Q = \left(\frac{GM}{r^3} + \frac{2\sigma^2}{r^2} \right) \frac{c_\mathrm{s}}{\pi G \Sigma}, \tag{3.11}$$

is smaller than unity ($Q < 1$) in some regions in simulations with $150° \leq \gamma \leq 165°$. Here self-gravity is important and our initial assumptions are somewhat challenged. The density within the discs themselves remain comfortably below the tidal density

$$\rho_{\text{tidal}} = \frac{3M_{\text{SMBH}}}{2\pi G r^3} \tag{3.12}$$

so our main results remain unaffected. However, increasing mass, and therefore density, may allow these rings to overcome tidal density and star formation could occur. While our rings form at about twice the distance (~ 1 pc) from the GC than the observed young stellar rings (< 0.5 pc) it is interesting that a single collision may result in a possibly star forming warped disc as well as a non-trivial amount of accretion giving more credence to the scenario where the birth of the young stars 6 Myr ago is linked with the *Fermi* bubble formation.

3.3.6 Effects of feedback

We do not account for feedback's effect on the surrounding ISM in this set of simulations, we investigate the effect of feedback calculated using a more robust accretion prescription in Chapter 4 and kilo-parsec-scale outflows in Chapter 5, however, we can estimate the effect a hypothetical spherical outflow would have. Following Zubovas et al. (2011) we compare the outward force of the outflow F_{out} to the weight of the central structures (Fig. 3.3(b)):

$$W_{\text{disc}} \sim g(R) M_{\text{disc}}(< R), \tag{3.13}$$

where $g(R)$ is the gravitational acceleration calculated at R from the potential of the system:

$$g\left(R\right) = \frac{\mathrm{G} M_{\text{BH}}}{R^2} + \frac{2\sigma^2}{R}. \tag{3.14}$$

The weight is $W_{\text{disc}} \sim 5.4 \times 10^{35} (M/10^4 \mathrm{M}_\odot)$ dyn at 1 pc from SMBH. We then estimate the outward force as:

$$F_{\text{out}} \sim \frac{H}{R} \frac{L_{\text{Edd}}}{c} = 1.37 \times 10^{32} \left(\frac{H/R}{0.01} \right) \text{dyn}, \tag{3.15}$$

where we take H/R to be the largest geometrical ratio for the chosen disc, which in most cases is about $0.06 - 0.09$.

We see that, in all cases, the weight of the disc is at least two orders of magnitude larger than the outward force. Importantly, scaling the mass of the system would make feedback even less disruptive, as weight grows linearly and luminosity only increases logarithmically above the Eddington limit. Thus we do not expect an AGN episode to completely clear out the central few parsecs - instead, the dense rings should help collimate the outflow as most of the energy-driven feedback would escape through the less dense opening perpendicular to the disc (Zubovas & Nayakshin 2014).

3.4 Conclusions

In this chapter we investigated circumstances under which a collision between a CNR-like gas ring and an infalling MC might initiate an AGN event. To do this, we set up an idealised system and varied the cloud collision trajectory between prograde and retrograde with respect to the CNR rotation. We show that a collision between the CNR and a MC can strongly perturb the initial system; its subsequent evolution strongly depends on the initial collision angle between the orbit of the cloud and the plane of the ring:

- Collisions with angles $\gamma \leq 105^\circ$ result in the CNR increasing in size and mass, with minimal mass transfer to the central part of the system.
- Collisions with steeper $\gamma > 105^\circ$ result in an increased transport of gas toward the Galactic centre, where it forms a warped disc and feeds the central SMBH.
- The steepest collisions, $\gamma > 150^\circ$, result in significant feeding of the SMBH; up to half of the initial gas mass is fed to the SMBH in the most extreme cases.
- A retrograde collision between a $10^5 \mathrm{M}_\odot$ cloud and similar mass CNR, would be sufficient to inflate the *Fermi* bubbles; the self-gravitating outskirts of the accretion disc may form stars, creating the observed stellar rings.

We estimate that a collision extreme enough to form the *Fermi* bubbles could happen once every $60-140$ Myr. Therefore, intermittent supply of matter from larger scales is a plausible explanation for the history of the accretion event that happened in our Galaxy ~ 6 Myr ago. Similar events may be occurring in other galaxies, leaving footprints visible for several Myr afterwards.

Chapter 4

SMBH accretion and feedback - connecting the super-massive black hole with its' surroundings[1]

As mentioned in Section 1.2, correlations between the properties of central SMBHs and their host galaxies indicate a strong link between galaxy and SMBH evolution (e.g., Silk & Rees 1998; King 2003; Ciotti & Ostriker 2007; Ciotti et al. 2007; Cattaneo et al. 2009; Novak et al. 2011; Kormendy & Ho 2013; Ciotti et al. 2017). There is almost no doubt that an episodic cycle of feeding and feedback plays a crucial role (Gaspari et al. 2020), however it is also challenging to study because SMBH scales (sub-parsec to a few parsecs) are orders of magnitude smaller than galactic scales (kiloparsecs) and as improvements in understanding require the integration of data from simulations and observations of many different spatial and temporal scales. For example, kilo-parsec-scale outflows are detected in many galaxies (McKinley et al. 2021; Laha et al. 2021) and observations at pc-scale resolution reveal an intricate picture of feeding and feedback in currently active galaxies (eg. García-Burillo et al. 2005, 2019; Audibert et al. 2019; Prieto et al. 2019a; Mingozzi et al. 2019; Nagai et al. 2019; García-Burillo et al. 2021, 2024) including UFOs reaching velocities of $0.1c$ (Pounds et al. 2003a; Tombesi et al. 2010a,b). Some of these features are also detected in our own Galaxy, which is currently inactive (Genzel et al. 2010). Large, kpc-scale, outflows (Su et al. 2010; Predehl et al. 2020) are linked to the Galactic Centre by a several-hundred-parsec bridge of X-ray chimneys and radio bubbles (Ponti et al. 2019; Heywood et al. 2019).

Cosmological and galactic-scale simulations are capable of recreating the observed scaling relations when AGN feedback is included (eg. Di Matteo et al. 2005; Filloux et al. 2010; Vogelsberger et al. 2014; Steinborn et al. 2015; Crain

[1]The content of this chapter is based on M. Tartėnas, K. Zubovas on. Not. Roy. Astron. Soc., **516**(2), 2522-2539 (2022)

et al. 2015; Anglés-Alcázar et al. 2016; Tremmel et al. 2017; Pillepich et al. 2019; Nelson et al. 2019a). In addition, the inclusion of feedback allows the simulations to recreate and explore the observed features such as *Fermi* bubble-like outflows (Pillepich et al. 2021) or the impact of AGN on the ISM (Davé et al. 2019; Torrey et al. 2020). While these models are relatively successful at recreating the large-scale features and observed relations, they are not capable, nor try to, accurately model the parsec-scale gas dynamics. In order to study SMBH feeding, AGN feedback and their impact on the local environment in more detail we still need to refer to smaller-scale simulations where gas dynamics in central parts of a galaxy can be resolved (eg. Bonnell & Rice 2008; Alig et al. 2013; Lucas et al. 2013; Hopkins et al. 2016; Shin et al. 2017; Tartėnas & Zubovas 2020; Tress et al. 2020; Moon et al. 2023; Tress et al. 2024); or utilize sub-resolution prescriptions to track unresolved physical processes (Negri & Volonteri 2017).

In this chapter, we present an accretion disc particle method (ADP) `ringcode` that improves the tracking of SMBH accretion in small-scale hydrodynamical simulations. `ringcode` could be considered an extension of the usual two-stage sink particle based accretion that instead of *drip-feeding* the SMBH from a single container following a somewhat arbitrary timescale, solves a diffusion equation for a 1D standard α accretion disc on the fly (Shakura & Sunyaev 1973; Pringle 1981; Frank et al. 2002). Feedback is directly determined by the properties of the accretion disc, with radiative efficiency naturally approaching $\eta \approx 0.0625$, which is correct for our chosen Paczyński-Wiita potential (Paczyński & Wiita 1980). We test the prescription in a smoothed-particle hydrodynamics (SPH) `Gadget-3` simulation (Springel 2005) of a retrograde cloud impacting a gas ring around an SMBH with a setup similar to the retrograde collision described in Chapter 3. We show that feedback has a significant effect on regulating the growth of the SMBH. Models with the accretion disc method produce a clear cavity in the centre, abruptly stopping any further accretion; this is not reproduced by models with instantaneous accretion. We argue that our result is more realistic than the alternative.

4.1 Numerical setup

As our accretion disc method is intended to improve simulations of the vicinity of an AGN, we test our approach with a set of simulations of retrograde collisions between a gas ring and a molecular cloud in an environment similar to that of the Milky Way centre. In the previous Chapter 3 we showed that similar configurations, without feedback, result in an AGN phase lasting $\gtrsim 100$ kyr.

We use the N-body/SPH code `Gadget-3` (Springel 2005) with the SPHS formulation (Read & Hayfield 2012) and the appropriate Wendland kernel function C^2 (Dehnen & Aly 2012) with neighbour number $N_{\rm neigh} = 100$. The

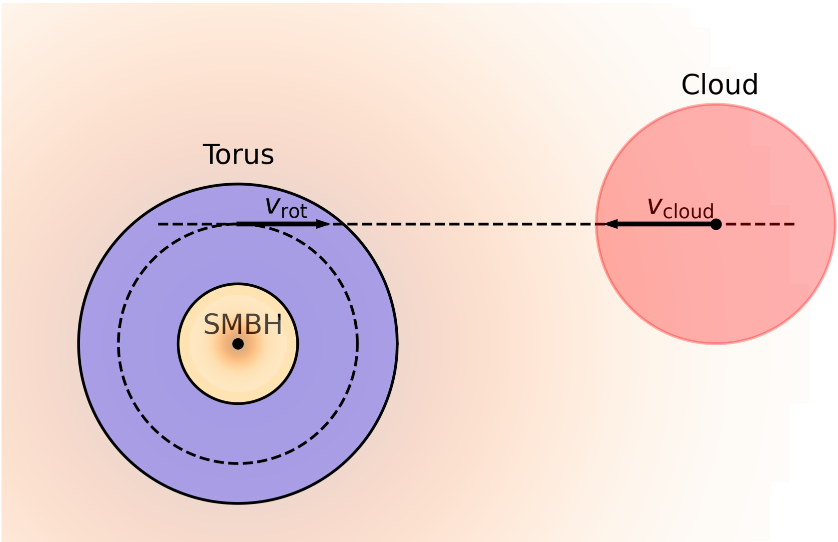

Figure 4.1: Elements of the model as seen along the z-axis: CNR-like torus (blue); the infalling molecular cloud (red); the background gas (orange); the SMBH (black dot). The cloud is placed on a collision course with the torus. All elements share the xy-midplane.

gas ring and cloud are each composed of $N_{\mathrm{part}} \approx 5 \times 10^5$ particles of mass $m_{\mathrm{SPH}} \approx 0.4\,\mathrm{M}_{\odot}$. The resolved mass is $M_{\mathrm{res}} = N_{\mathrm{neigh}} m_{\mathrm{SPH}} \approx 40\mathrm{M}_{\odot}$. The initial velocities are again determined using a potential given by (3.1). A more detailed description of the initial conditions and the physics included in our simulations is given below.

4.1.1 Initial Conditions

The supermassive black hole: Our model contains a SMBH with an initial mass of $M_{\mathrm{BH}} = 4 \times 10^6\,\mathrm{M}_{\odot}$. The chosen mass is similar to the SMBH mass at the centre of the Milky Way, determined from the orbits of S stars - $4.02 \pm 0.16 \pm 0.04 \times 10^6\,\mathrm{M}_{\odot}$ (Boehle et al. 2016). The SMBH is fixed at the centre of the system. The SMBH is coupled with a sub-resolution accretion disc. Particles may be accreted by this combined SMBH-accretion disc particle if they fall inside $r_{\mathrm{sink}} = 0.01$ pc, which is approximately the minimal volume spatial resolution in the model, and have orbits with circularization radius $r_{\mathrm{circ}} < r_{\mathrm{sink}}$. This excludes the accretion of particles with high angular momentum. Further evolution of this gas is followed using the accretion disc particle method (see Section 4.2).

The circumnuclear ring: The toroidal gas ring is similar in size and mass to the Circumnuclear Ring (CNR) found at the centre of the Milky Way (Ferrière 2012). It has an inner radius $R_{\mathrm{in}} = 1.5$ pc and an outer radius $R_{\mathrm{out}} = 4$ pc. The mass estimates of the current CNR vary by almost two orders of magnitude; for simplicity, we set the initial mass of the ring to $M_{\rm ring} = 10^5\,{\rm M}_\odot$ (Ferrière 2012) and set its density to a constant value. Ring particles move in circular orbits with speeds $v_{\rm R1.5} \sim 181$ km s^{-1} at the inner edge and $v_{\rm R4} \sim 160$ km s^{-1} at the outer edge.

The molecular cloud: An infalling molecular cloud is placed 12 pc away from the target (Fig. 4.1). The cloud initially has constant density and contains the same amount of gas as the CNR ($M_{\rm cloud} = 10^5\,{\rm M}_\odot$). We set the radius $r_{\rm cloud} = 3$ pc based on observational estimates of typical sizes of clouds of this mass in the Galaxy (Kauffmann et al. 2017). The cloud is set on a parabolic orbit that crosses the ring at a point 3 pc away from the origin along the Y axis. The initial velocity of the centre of the cloud is $v_{\rm cl} = 220$ km s^{-1}; this corresponds to a parabolic velocity at the position of the cloud's centre. While the molecular cloud in our simulations does not correspond to any particular feature currently observed in the Galactic Centre, an appearance of such a cloud over several million years seems likely given that both observations and simulations show an inflow of matter into the central few parsecs (Sormani & Barnes 2019; Tress et al. 2020). In fact, the CNR itself could have been formed by the capture of a similar cloud (Oka et al. 2011; Mapelli & Trani 2015; Trani et al. 2018).

Turbulence: In addition to orbital velocities, MC and CNR particles are given velocities from a turbulent velocity field. The velocity field is generated based on the example of Dubinski et al. (1995), with velocity amplitude $\sigma_{\rm turb} =$ 37.5 km s^{-1}; the same way as described in Section 3.1. Turbulence is only present initially and dissipates over time since there is no further turbulence driving. Nevertheless, it results in the formation of a turbulent density field, which is more realistic than smooth gaseous structures.

Background gas: In order to track the feedback energy input, especially in directions perpendicular to the CNR, we create/add a spherical background gas distribution. It contains $M_{\rm bg} = 1.2 \times 10^3 {\rm M}_\odot$ extending out to $r_{\rm bg} = 25$ pc and following an isothermal density profile. The background gas consists of $N_{\rm bg} \approx 3 \times 10^5$ particles; the mass of each particle is 100 times lower than that of particles in the cloud and the ring. The initial velocity of the background gas is set to zero.

Star formation: Our current model setup lacks the resolution to accurately simulate star formation in the vicinity of the SMBH (star formation near the SMBH is discussed further in section 4.4.3), but the removal of overly dense particles from hydrodynamical simulations helps speed up the simulation without sacrificing realism. Therefore, we introduce the following star formation prescription. Gas particles are probabilistically transformed to collisionless star particles if their density is higher than the tidal density and their Jeans mass is lower than the resolved mass. Star formation rate is related to the dynamical time of the particle:

$$t_{\rm dyn,i} = \sqrt{\frac{3\pi}{32 {\rm G} \rho_{\rm i}}} \tag{4.1}$$

which allows us to define the probability of the transformation, $P_{\rm sf,i}$, as:

$$P_{\rm sf,i} = 1 - \exp\left(-\frac{\eta_{\rm sf} \Delta t_i}{t_{\rm dyn,i}}\right), \tag{4.2}$$

here $\eta_{\rm sf} = 0.1$ is the star formation efficiency; Δt_i is the timestep of the particle.

4.1.2 Feedback

The physical basis of our feedback implementation is the AGN wind feedback model (for a review, see King & Pounds 2015). Numerically, we implement it with an improved version of the Monte Carlo radiation transfer method from Nayakshin et al. (2009). Here, the AGN wind is represented by a number of isotropically distributed discrete energy-momentum packets generated at the source location. The number of these is determined by the luminosity of the accretion disc particle. The momentum of a single packet is defined in relation to the SPH particle mass, $p_\gamma = m_{\rm sph} \times \sigma \approx 8 \times 10^{39} {\rm g\,cm\,s^{-1}}$. The momentum is defined using the higher-mass SPH particles making up MC and CNR. In principle, it would be better to use packet sizes defined by the smaller mass as larger packets may introduce artificial shocks in the low-mass background. However, this would make the computations prohibitively expensive. The diffuse background medium is there primarily for energy accounting purposes and has a negligible effect on the results.

An emitted packet moves steadily outwards with the velocity of $v_\gamma = 0.1c$. Once it comes close enough to some SPH particles it transfers its momentum and energy to them over several steps. The SPH density field is directly used to determine the amount of momentum passed to each particle:

$$\Delta \mathbf{p}_{\gamma,\rm i} = \frac{\rho_i(\mathbf{r})}{\rho(\mathbf{r})} \Delta \mathbf{p}_\gamma \tag{4.3}$$

here $\Delta \mathbf{p}_\gamma$ and $\Delta \mathbf{p}_{\gamma,\rm i}$ are the total amount of momentum transferred to the gas in a given step and the momentum transferred to the i-th particle, while $\rho(\mathbf{r})$ and $\rho_i(\mathbf{r})$ are the density field value at that point and the contribution of the i-th particle to that field. The radiation pressure force $\mathbf{f}_{\rm rad,i}$ on each particle then is:

$$\mathbf{f}_{\rm rad,i} = \frac{\sum_\gamma \Delta \mathbf{p}_{\gamma,\rm i}}{\Delta t_i}. \tag{4.4}$$

The same principle is applied when calculating the energy transfer, except that we replace $\Delta \mathbf{p}_\gamma$ with ΔE_γ, where $E_\gamma = \eta p_\gamma c/2$, where the radiative efficiency $\eta = L_{\rm disc}/\dot{M}_{BH} c^2$ is determined directly from the accretion disc model. The

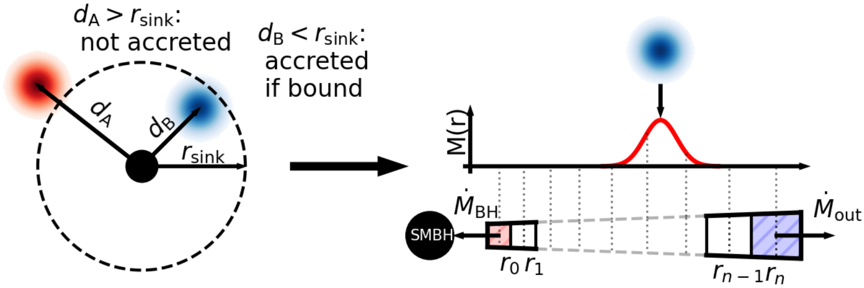

Figure 4.2: Visual representation of the accretion of the blue sph particle. When the particle crosses $r_{\rm sink}$ and its angular momentum is low enough it is marked for accretion. As the particle represents a gas parcel with nonzero dimensions, we distribute its mass over a number or rings of the accretion disc. The amount of matter added to each ring is weighted by the kernel used in the simulation. The red particle, conversely, is not accreted.

total energy injected to the gas approaches (King & Pounds 2015)

$$E_{\rm wind} = \frac{\eta^2}{2} M_{\rm acc} c^2. \tag{4.5}$$

4.2 Accretion disc particle

The core of our prescription is a one-dimensional thin accretion disc model which we couple to the SMBH sink particle in the hydrodynamical simulation. Here, we present the details of this model. First I describe the method in more general terms and show how it is connected to the main simulation (Section 4.2.1). I follow this up with a more detailed derivation of the main equations governing the disc evolution (Section 4.2.2) and various convergence tests for the disc model (Section 4.2.3).

4.2.1 Implementation

We assume that the accretion disc consists of concentric rings with logarithmically increasing radii R (Fig. 4.2, left). The innermost annulus lies within the innermost stable orbit, and the outermost extends beyond the sink radius, both acting as outflow boundaries. For simplicity, we assume the disc geometry remains fixed, as the SMBH mass growth is negligible compared to its initial mass, although this would become important if the method is applied more broadly.

As is usual for a two-stage approach, we define a set of accretion criteria and check them for any particles that cross the sink radius $r_{\rm sink}$. More precisely, we require that the following three conditions be met:

1. **Proximity:** the particle has to be within the accretion radius $r_{\rm sink}$ (also corresponding to the defined outer boundary of the accretion disc).

2. **Binding:** the particle has to be gravitationally bound to the sink particle

$$u_{\rm internal} + v_{\rm sph}^2/2 - GM_{\rm SMBH}/R < 0, \tag{4.6}$$

where $u_{\rm internal}$ is the internal energy per unit mass, which represents internal thermal motion and, therefore acts in opposition to accretion; $v_{\rm sph}$ is the velocity of the gas particle.

3. **Circularization:** the particle's circularization radius $R_{\rm circ} < r_{\rm sink}$. The circularization radius is calculated by

$$R_{\rm circ} = \frac{J_{\rm part}^2}{GM_{\rm SMBH}}, \tag{4.7}$$

where $J_{\rm part}$ is the angular momentum per unit mass.

The third, circularization, condition specifically excludes particles with high angular momentum. Those particles that pass the checks are removed from the simulation and added to the disc (Fig. 4.2, right). In SPH, the particles representing gas are not points, and they have spatial extent described by the smoothing length, h, and a kernel function $W(\mathbf{r}, h)$ (detailed in Section 2.1). Because the size of each annulus is very small when compared to SPH particles, $R_{i+1} - R_i < h$, in most cases SPH particles span multiple annuli, and sometimes are comparable in size to the entire disc. Therefore, we smoothly distribute the accreted material over the annuli spanned by the particle, as illustrated in (Fig. 4.2, right). We centre the distribution defined by the kernel of the SPH particle around the circularization radius $R_{\rm circ}$ of the accreted particle (4.7). Material outside the disc is assigned to the outer boundary, while material at the inner boundary is reflected. This method strikes a balance between a rigorous calculation and the simplicity of injecting mass into a single ring.

We evolve the disc using a pseudo-Newtonian Paczyński-Wiita (PW) potential (Paczyński & Wiita 1980):

$$\phi = \frac{-GM_{\rm BH}}{R - R_{\rm g}}, \tag{4.8}$$

where R is the distance from the SMBH and $R_{\rm g}$ is the Schwarzschild radius (1.2). The equation for the viscous evolution of the disc is then:

$$\frac{\partial \Sigma}{\partial t} = \frac{3}{R}\frac{\partial}{\partial R}\left[\frac{(R-R_{\rm g})^2}{R^{1/2}(R-3R_{\rm g})}\frac{\partial}{\partial R}\left(\nu \Sigma R^{3/2}\frac{R-\frac{1}{3}R_{\rm g}}{(R-R_{\rm g})^2}\right)\right]; \tag{4.9}$$

with viscosity defined as $\nu = \alpha c_{\rm s} H$, where $c_{\rm s}$ is the speed of sound, H is the height of the disc and $\alpha = 0.1$ (Shakura & Sunyaev 1973).

We solve the diffusion equation numerically, updating the surface density in each annulus comprising the accretion disc $\Sigma(R_i, t)$ after each timestep:

$$\Sigma(R_i, t + \Delta t) = \Sigma(R_i, t) + \frac{\partial \Sigma(R_i, t)}{\partial t}\Delta t; \tag{4.10}$$

Accretion disc evolution occurs after each sink particle step. The dynamical timescale of the accretion disc can be much smaller than that of the simulation as a whole so we use a different criterion to determine a timestep appropriate for the disc. An initial timestep estimate is calculated by:

$$\Delta t_{\mathrm{est}} = \mathrm{C} \min\left[\Delta t_i\right] = \mathrm{C} \min\left[\frac{\Delta R_i^2}{\nu_i}\right], \tag{4.11}$$

with an arbitrary Courant factor, in our case $\mathrm{C} = 0.01$ works well. The actual Δt is then defined in reference to the sink particle's timestep Δt_{sink}:

$$n_{\mathrm{steps}} = \mathrm{ceil}\left[\frac{\Delta t_{\mathrm{sink}}}{\Delta t_{\mathrm{est}}}\right] + 1, \tag{4.12}$$

$$\Delta t = \frac{\Delta t_{\mathrm{sink}}}{n_{\mathrm{steps}}}, \tag{4.13}$$

to ensure that both $\Delta t n_{\mathrm{steps}} = \Delta t_{\mathrm{sink}}$ and $\Delta t < \Delta t_{\mathrm{est}}$ conditions are met. Here $\mathrm{ceil}\left[x\right]$ is the ceiling function.

After a few steps, the properties of the accretion disc change. If it turns out that Δt is too large and leads to instability the timestep is halved, and iterations are redone with the corrected timestep. Only the viscous evolution of the accretion disc uses these smaller timesteps; processes like accretion onto the disc and feedback energy/momentum injection occur together with the sink particle updates.

The PW potential yields the following expression for the viscous dissipation per unit disc face area $D(R)$:

$$D(R) = \frac{3}{8}\frac{\dot{M}}{\pi}\frac{GM_{\mathrm{BH}}}{R}\left(\frac{1}{R - R_{\mathrm{g}}} - \frac{3^{3/2} R_{\mathrm{g}}^{1/2}}{2R^{3/2}}\right)\frac{\left(R - R_{\mathrm{g}}\right)^2}{R - \frac{1}{3}R_{\mathrm{g}}}, \tag{4.14}$$

which we use to calculate the luminosity of each annulus:

$$L(R) = 2\pi\left[D\left(R_{\mathrm{out}}\right)R_{\mathrm{out}} + D\left(R_{\mathrm{in}}\right)R_{\mathrm{in}}\right]\left(R_{\mathrm{out}} - R_{\mathrm{in}}\right) \tag{4.15}$$

here R_{in} and R_{out} are, respectively, the inner and outer radii of the i-th annulus. The total disc luminosity is obtained by summing over all annuli, and this value determines the energy and/or momentum injected into the surrounding gas. The radiative efficiency of accretion stays close to the expected value for the

PW potential $\eta \sim 6.25\%$ (Paczyński & Wiita 1980) throughout our simulation runs, which is somewhat higher than $\eta = 5.7\%$ appropriate for a Schwarzschild black hole.

4.2.2 Derivation

For completeness we provide a more detailed derivation of thin accretion disc equations, following Frank et al. (2002) but using the Paczyński & Wiita (1980); Abramowicz (2009) potential (PW). Equations (4.16)-(4.22) and (4.28)-(4.30) are included for posterity, as they are identical to the Newtonian case. For a more detailed description of the Newtonian case consult Pringle (1981) or Frank et al. (2002).

The disc is characterized by its surface density $\Sigma(R,t)$, which is obtained by integrating the gas density ρ in the z direction. The amount of matter contained in a single annulus between R and $R+\Delta R$ is $2\pi R\Delta R\Sigma$; similarly, the total angular momentum is $2\pi R\Delta R\Sigma R^2\Omega$, where Ω is the angular velocity. The rate of change of these quantities is determined by the net flow from neighbouring annuli:

$$\begin{aligned}\frac{\partial}{\partial t}(2\pi R\Delta R\Sigma) &= v_{\mathrm{R}}(R,t)2\pi R\Sigma(R,t) \\ &\quad - v_{\mathrm{R}}(R+\Delta R,t)2\pi(R+\Delta R)\Sigma(R+\Delta R,t) \\ &\approx -2\pi\Delta R\frac{\partial}{\partial R}(R\Sigma v_{\mathrm{R}}).\end{aligned} \tag{4.16}$$

As $\Delta R \to 0$, we get the mass conservation equation:

$$R\frac{\partial\Sigma}{\partial t} + \frac{\partial}{\partial R}\left(R\Sigma v_{\mathrm{R}}\right) = 0. \tag{4.17}$$

The conservation of angular momentum is constructed in the same way as the rate of change of angular momentum, but an additional transport term due to the viscous torques $G(R,t)$ is included:

$$\begin{aligned}\frac{\partial}{\partial t}(2\pi R\Delta R\Sigma R^2\Omega) &= v_{\mathrm{R}}(R,t)2\pi R\Sigma(R,t)R^2\Omega(R) \\ &\quad - v_{\mathrm{R}}(R+\Delta R,t)2\pi(R+\Delta R)\Sigma(R+\Delta R,t) \\ &\quad \times (R+\Delta R)^2\Omega(R+\Delta R) + \frac{\partial G}{\partial R}\Delta R \\ &\approx -2\pi\Delta R\frac{\partial}{\partial R}(R\Sigma v_{\mathrm{R}}R^2\Omega) + \frac{\partial G}{\partial R}\Delta R.\end{aligned} \tag{4.18}$$

again taking $\Delta R \to 0$ we arrive at the angular momentum conservation equation:

$$R\frac{\partial}{\partial t}(\Sigma R^2\Omega) + \frac{\partial}{\partial R}(R\Sigma v_R R^2\Omega) = \frac{1}{2\pi}\frac{\partial G}{\partial R}. \tag{4.19}$$

The expression for the torque includes the viscosity term $\nu = \alpha c_{\rm s} H$:

$$G(R) = 2\pi R \nu \Sigma R^2 \frac{\partial \Omega}{\partial R}. \tag{4.20}$$

Using (4.17) we can simplify (4.20):

$$R\Sigma v_{\rm R} \frac{\partial}{\partial R}\left(R^2\Omega\right) = \frac{1}{2\pi}\frac{\partial G}{\partial R}, \tag{4.21}$$

note that we assume that the $\partial\Omega/\partial t$ term can be safely neglected as the change in potential due to the increase in SMBH mass is negligible.

Combining (4.17) and (4.21) allows us to eliminate v_R.

$$R\frac{\partial \Sigma}{\partial t} = -\frac{\partial}{\partial R}\left(R\Sigma v_{\rm R}\right) = -\frac{\partial}{\partial R}\left[\frac{1}{2\pi\frac{\partial}{\partial R}\left(R^2\Omega\right)}\frac{\partial G}{\partial R}\right]. \tag{4.22}$$

We now introduce the PW potential

$$\phi = -\frac{{\rm G}M_{\rm BH}}{R - R_{\rm g}}, \tag{4.23}$$

from which a modified expression of orbital angular velocity of the gas, Ω, follows:

$$\Omega \equiv \left(\frac{1}{R}\frac{{\rm d}\phi}{{\rm d}R}\right)^{1/2} = \left(\frac{{\rm GM_{BH}}}{R^3}\right)^{1/2}\left(\frac{R}{R - R_{\rm g}}\right). \tag{4.24}$$

Inserting expressions for

$$\frac{\partial}{\partial R}\left(R^2\Omega\right) = \frac{R}{2}\frac{R - 3R_{\rm g}}{\left(R - R_{\rm g}\right)^2}\left(\frac{GM}{R^3}\right)^{1/2} \tag{4.25}$$

and

$$\begin{aligned}\frac{\partial G}{\partial R} &= \frac{\partial}{\partial R}2\pi R\nu\Sigma R^2\frac{\partial}{\partial R}\Omega \\ &= 2\frac{3}{2}\pi R\nu\Sigma R^2\left(\frac{GM}{R^3}\right)^2\left(\frac{R - R_{\rm g}/3}{\left(R - R_{\rm g}\right)^{1/2}}\right)\end{aligned} \tag{4.26}$$

to (4.22) and simplifying we arrive at the main diffusion equation:

$$\frac{\partial \Sigma}{\partial t} = \frac{3}{R}\frac{\partial}{\partial R}\left[\frac{\left(R - R_{\rm g}\right)^2}{R^{1/2}\left(R - 3R_{\rm g}\right)}\frac{\partial}{\partial R}\left(\nu\Sigma R^{3/2}\frac{R - R_{\rm g}/3}{\left(R - R_{\rm g}\right)^2}\right)\right]; \tag{4.27}$$

this is identical to eq. (4.9).

This is the main viscous evolution equation with the PW potential that our prescription solves by finite differences. Equation (4.27) reduces to the standard Newtonian form if we set $R_{\rm g} = 0$. To better illustrate how (4.27)

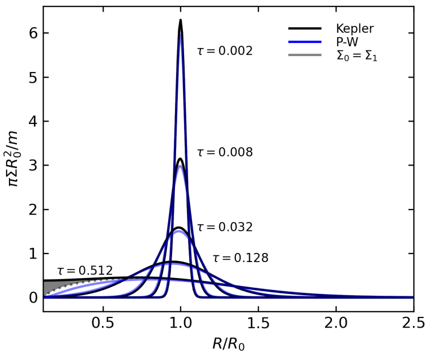

Figure 4.3: Diffusion of a one-off injection event, where a mass m is added to a single annulus at R_0. The blue curves correspond to evolution with eq. (4.27). Black lines correspond to the standard evolution equation, to which (4.27) reduces with $R_\mathrm{g} = 0$. $\tau = 12\nu t/R_0^2$ is the dimensionless time, where ν is a constant (Pringle 1981).

behaves we plot, in Fig. 4.3, how matter diffuses from a one-off injection into a single annulus. Results are shown for both PW (blue) and standard Newtonian (black) potentials. We recover the result shown in the example from Frank et al. (2002) by setting the boundary surface density to its neighbour's value artificially, that is $\Sigma(R_0, t) = \Sigma(R_1, t)$, however, we adopt the boundary value of zero in our simulations $\Sigma(R_0, t) = 0$ under the assumption that matter that passes the ISCO quickly feeds the SMBH. The effect of this change is highlighted as the grey region in Fig. 4.3. The key difference between the two potentials is that the PW potential results in somewhat faster diffusion. This is expected, because the PW potential effectively brings the material 'closer' to the origin of the potential, so its evolution is faster. Note, that since the definition of ISCO is that the orbits change from quasi-circular to ballistic, it is not necessarily clear what boundary conditions are 'right' at the inner-most edge.

Here we introduce another set of assumptions to derive the vertical structure of the disc. We assume that the disc is stable and thin and its parameters should tend to solutions for the steadily accreting disc. We treat each feeding cycle as a perturbation, while viscous diffusion distributes the matter to ever more closely resemble the ideal quasi-steady thin accretion disc. This assumption greatly simplifies the calculation of the disc parameters, allowing us to disregard the time derivative in the conservation equations (4.17) and (4.21). From these, we get:

$$\dot{M} = 2\pi R\Sigma(-v_\mathrm{R}), \tag{4.28}$$

where $\dot{M}$ is the accretion rate, and

$$R\Sigma v_\mathrm{R} R^2\Omega = \frac{G}{2\pi} + \frac{C}{2\pi}. \tag{4.29}$$

Here C is some constant. Inserting the expression (4.20) for G we get

$$-\nu\Sigma\frac{\partial\Omega}{\partial R} = \Sigma(-v_R)\Omega + \frac{C}{2\pi R^3}. \tag{4.30}$$

Equation (4.30) can be solved for C; applying $\partial\Omega/\partial R = 0$ at the innermost stable orbit ($R = 3R_{\rm g}$) we get:

$$C = -\frac{3}{2}\dot{M}(GM\cdot 3R_{\rm g})^{1/2}. \tag{4.31}$$

This allows us to get a useful expression:

$$\nu\Sigma = \frac{\dot{M}}{3\pi}\left(\frac{1}{R-R_{\rm g}} - \frac{3^{3/2}R_{\rm g}^{1/2}}{2R^{3/2}}\right)\left(\frac{(R-R_{\rm g})^2}{R-R_{\rm g}/3}\right) \tag{4.32}$$

Using this we can get the expression for energy dissipation $D(R)$

$$\begin{aligned} D\left(R\right) &= \frac{R^2}{2}\nu\Sigma\left(\frac{\partial\Omega}{\partial R}\right)^2 \\ &= \frac{3}{8}\frac{\dot{M}}{\pi}\frac{GM}{R}\left(\frac{1}{R-R_{\rm g}} - \frac{3^{3/2}R_{\rm g}^{1/2}}{2R^{3/2}}\right)\left(\frac{(R-R_{\rm g})^2}{R-R_{\rm g}/3}\right) \end{aligned} \tag{4.33}$$

Using this we can get then the expression for midplane temperature

$$\begin{aligned} T_{\rm c}^4 &= \frac{3\tau}{4\sigma}D(R) \\ &= \frac{27}{32}\frac{\tau}{\sigma}\nu\Sigma\frac{GM}{R}\frac{(R-R_{\rm g}/3)^2}{(R-R_{\rm g})^4}, \end{aligned} \tag{4.34}$$

where $\tau = \kappa\Sigma/2$ and $\kappa = 0.348\ \mathrm{cm}^2\ \mathrm{g}^{-1}$ is the electron scattering opacity.

To get the height of the accretion disc, we again repeat the considerations outlined in (Frank et al. 2002). Taking the Euler equation:

$$\rho\frac{\partial\mathbf{v}}{\partial t} + \rho\mathbf{v}\cdot\Delta\mathbf{v} = -\Delta P + \mathbf{f}_{\rm g}, \tag{4.35}$$

where $\mathbf{f}_g$ is the force density due to gravitation, we assume hydrostatic equilibrium in the z direction and neglect the velocity terms arriving at:

$$\frac{\partial}{\partial z}P = \rho\frac{\partial}{\partial z}\phi = \rho\frac{\partial}{\partial z}\left(-\frac{GM}{(R^2+z^2)^{1/2}-R_{\rm g}}\right) \tag{4.36}$$

completing the partial derivative on the right hand side and moving ρ to the left we get

$$\frac{1}{\rho}\frac{\partial}{\partial z}P = \frac{\mathrm{G}Mz}{(R^2+z^2)^{1/2}\left[(R^2+z^2)^{1/2}-R_{\rm g}\right]^2}. \tag{4.37}$$

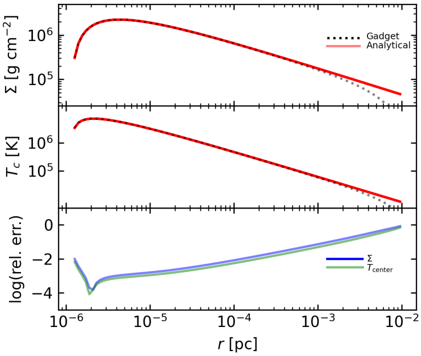

Figure 4.4: A comparison between the expected analytical (red) and model (dotted black) radial structure of the accretion disc. The top and middle panels show the surface density Σ and the central disc temperature T_c. The bottom panel shows the relative deviation from the analytical solution ($\log|\Sigma_\mathrm{model}/\Sigma_\mathrm{expected} - 1|$ in blue and the same for T_c in green). Deviations are larger closer to the disc boundaries.

Following the argumentation from Frank et al. (2002): if the scale height in z direction is H, then $\frac{\partial P}{\partial z} \sim \frac{P}{H}$ and z can be replaced with H in the equations. The thin disc assumption gives $H \ll R$; using $P \sim \rho c_\mathrm{s}^2$ we get our final expression for H:

$$H = c_\mathrm{s}\,(R - R_\mathrm{g})\left(\frac{R}{GM}\right)^{1/2}, \tag{4.38}$$

where the speed of sound c_s is given by:

$$c_\mathrm{s} = T_\mathrm{c}^4\left(\frac{k\gamma}{m_\mathrm{p}\mu}\right)^{1/2}, \tag{4.39}$$

with the mean molecular weight $\mu = 0.63$ and $\gamma = 5/3$. k is the Boltzmann constant.

4.2.3 Consistency and convergence

In our accretion disc model, the disc evolution is set to tend towards the standard quasi-steady thin α-accretion disc, but at each step, some mass distribution is added to the disc, depending on the properties of the accreted gas particles. Therefore, we still need to investigate whether the specific implementation in `Gadget` works as intended, as there are new considerations to do with the distribution of particles with spatial extent and mass.

First, we check if we get the expected result if we feed the accretion disc at a constant rate. We know that after some time, the disc should approach a steady state, that is, the disc's mass remains constant as does the rate of SMBH feeding and matter escaping via the outer boundary. To find the analytically expected result for comparison, we solve equations for the surface density Σ:

$$\Sigma = \left(\frac{64}{729}\frac{\mathrm{G}M\sigma_{\mathrm{SB}}}{R\kappa}\right)^{1/5}\left(\frac{\dot{M}}{\pi}\right)^{3/5}\left(\frac{1}{R-R_{\mathrm{g}}}-\frac{3^{3/2}R_{\mathrm{g}}^{1/2}}{2R^{3/2}}\right)^{3/5}\cdot$$
$$\cdot\left(\frac{3m_{\mathrm{p}}\mu}{5\alpha k(R-R_{\mathrm{g}})}\right)^{4/5}\left(\frac{(R-R_{\mathrm{g}})^2}{R-R_{\mathrm{g}}/3}\right), \quad (4.40)$$

where m_{p} is the proton mass and k is the Boltzmann constant, and the central temperature T_{c}:

$$T_{\mathrm{c}} = \left[\frac{9}{64}\frac{\kappa\Sigma}{\sigma_{\mathrm{SB}}}\frac{\dot{M}}{\pi}\frac{\mathrm{G}M_{\mathrm{BH}}}{R}\left(\frac{1}{R-R_{\mathrm{g}}}-\frac{3^{3/2}R_{\mathrm{g}}^{1/2}}{2R^{3/2}}\right)\frac{R-R_{\mathrm{g}}/3}{(R-R_{\mathrm{g}})^2}\right]^{1/4}. \quad (4.41)$$

Now we input the SMBH mass M_{BH} and SMBH accretion rate $\dot{M}$ from the model into equations (4.40) and (4.41) to get the radial structure of a steadily accreting disc as expected for the given parameters and plot it together with the radial structure obtained via model calculations in Fig. 4.4. The upper two panels show surface density Σ and central temperature T_{c}, respectively. The red curves represent the analytical results for the given disc parameters, while the dotted line shows results taken from a `Gadget` simulation. The bottom panel shows the relative deviation from the analytical solution for both the surface density (blue) and the central temperature (green). We can see, that both the central temperature and the surface density deviate more from the analytical solution the closer they get to the disc boundaries, but the agreement is generally very good; even the relatively large deviation at the outer boundary is relatively unimportant as it generates a negligible portion of the whole luminosity. However, if we were to implement the matter escaping the disc greater care should be taken in addressing the outer boundary specifically. This is discussed more in Section 4.4.3.

Now we shift focus to how the radius at which an SPH particle might be accreted, together with its extent, might affect the evolution of the disc. We use the angular momentum of a swallowed particle to determine its circularization radius R_{circ}. We then centre the particle's mass contribution on it, and the numerical smoothing length parameter h is used to represent the spatial extent of a particle's contribution. The contribution to each annulus is scaled by a kernel function, thus h plays a somewhat similar role as it does in the SPH formulation of hydrodynamics. To isolate just the effect of R_{circ} and h we again setup an artificially simple simulation with a constant inflow of gas and a fixed set of R_{circ} and h. [2]. The rate of disc feeding is similar to what is expected in a retrograde collision scaled to the mass of our system (3.9), with $\sim 10^5\ \mathrm{M}_{\odot}$ of gas

[2]An implementation of this model in `Python` is freely available in `https://github.com/Caradryan/accretiondisc`

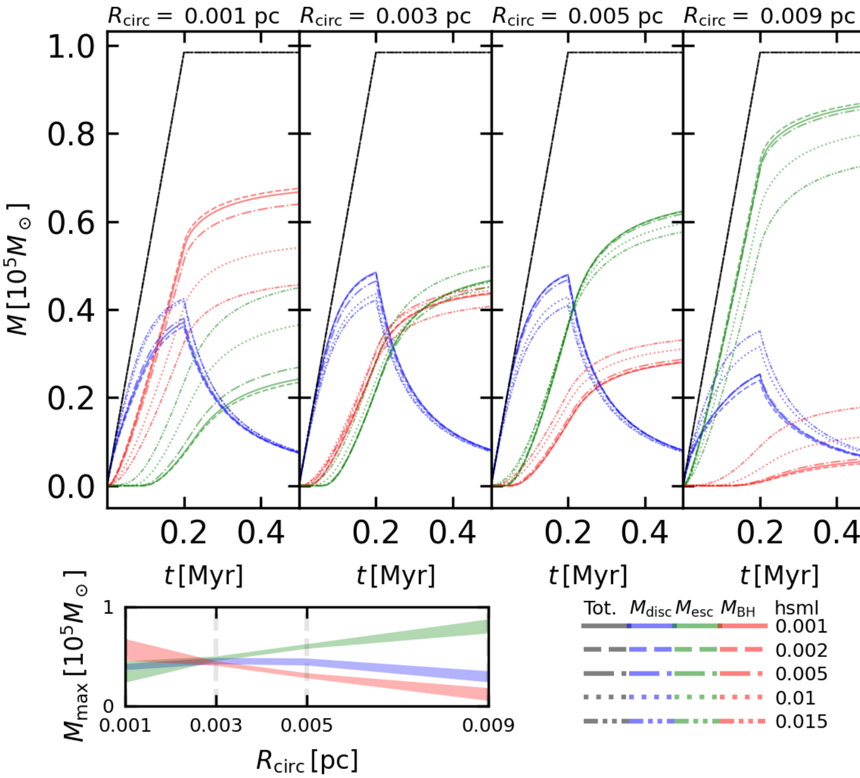

Figure 4.5: The injected mass (black), mass in the disc (blue), mass fed to the SMBH (red) and mass escaping the disc (green) over time, depending on the injection radius ($R_{\rm circ}$, values given at the top of each of the four main panels) and smoothing length h (different line styles, values given at the bottom right). The small graph on the bottom shows the peak disc mass (blue) and total mass accreted by the SMBH (red) and escaping through the outer boundary (green), as functions of $R_{\rm circ}$, with the width of the line corresponding to the variation due to the different chosen values of h.

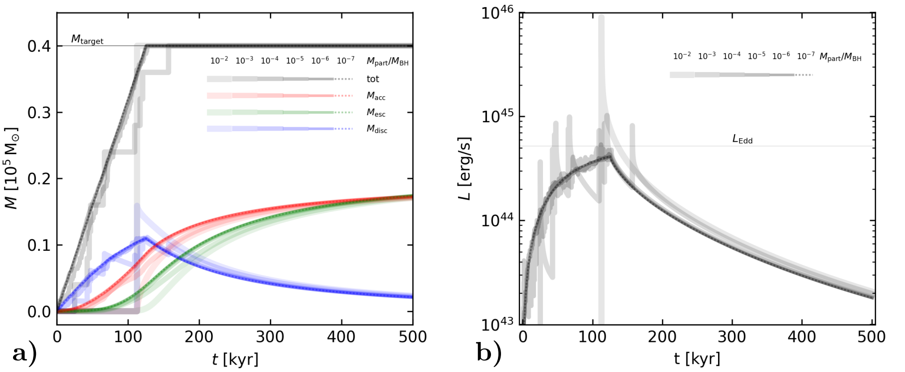

Figure 4.6: a) the injected mass (black), mass in the disc (blue), mass fed to the SMBH (red) and mass escaping the disc (green) over time, depending on the portion size of the injected matter. **b)** the luminosity of the accretion disc over time, depending on the portion size of the injected matter.

added to the accretion disc over a period of 200 kyr at a constant average rate of $\dot{M}_{\rm input} = 0.5\,{\rm M}_\odot\,{\rm yr}^{-1}$. The resulting growth curves of the accretion disc (blue), the black hole (red) and the escaping matter (green) are shown in Fig. 4.5. Each of the four subplots at the top shows results of simulations with a different fixed $R_{\rm circ}$ value, while different line styles correspond to different values of h. Here we clearly see several trends, which are all quite intuitive. First, the closer to the centre a particle is fed to the disc, the more material ends up feeding the SMBH, and conversely, the further out the particle is inserted, the more mass escapes the disc via the outer boundary. The smoothing parameter h, in this case, acts to soften this effect, as higher values allow for more matter to be placed in the middle annuli of the disc (Note the dash-double-dot line in Fig. 4.5).

In addition to the spatial resolution that depends on smoothing length, the mass resolution may also impact our accretion disc. To test this, we again performed a set of simulations with the `Python` version of our code aimed to emulate the swallowing of SPH particles with different masses. We fix the feeding radius $R_{\rm circ} = 0.003$ pc and the smoothing length $h = 0.01$ pc and only vary the mass of a single injected portion. The portion masses for these runs are chosen in proportion to the mass of the SMBH and are incremented by an order of magnitude in each run, from $M_{\rm part}/M_{\rm BH} = 10^{-7}$, up to $M_{\rm part}/M_{\rm BH} = 10^{-2}$ (the first corresponding to the ratio in the SPH simulations). We set a target mass to be fed over 125 kyr, which is a quarter of the total simulation time. The target mass $4 \times 10^4{\rm M}_\odot$, the same as a single portion in the run with $M_{\rm part}/M_{\rm BH} = 10^{-2}$. The results are shown in Fig. 4.6(a). As expected, simulations with more massive particles produced a step-like total mass growth curve (black) and spikier accretion disc mass (blue), however, both the SMBH accreted (red) and escaped (green) evolved rather smoothly. Despite the clearly different accretion histories, the total mass in each component converges over longer timescales; the mass of accreted particles becomes less significant compared to the amount already in the disc and when mass injection ends the disc settles into a steady decay. However, as shown in Fig. 4.6(b) on the right, sudden increases in disc mass due to the accretion of massive particles lead to luminosity spikes, which are highly super-Eddington but short-lived. This suggests that a limit on luminosity is necessary if very massive particles are used in the hydrodynamical simulation. At the same time, the accretion disc of the scale used in these runs (~ 0.01 pc) is probably too small for simulations that would also make use of particles as massive as used in the tests. The fact that parameters converge even in this limiting case suggests that over the longer timescales relevant to larger simulations the undesired short bursts of accretion should average out. We discuss the applicability of our model to large-scale simulations in Section 4.4.4.

In general, care should be taken when choosing the spatial resolution of the main simulation, as it could result in an artificially lower accretion disc mass and/or excessive instantaneous feeding/escape. Choosing a sink radius much larger than approximately the intended accretion disc size may also result in accretion of matter with larger than intended angular momentum and matter accumulation in the furthest parts of an unphysically large accretion disc. Our prescription does not account for the possible fragmentation and star formation at the outskirts of the disc; we leave this topic for further research.

4.3 Results

We ran 12 simulations in total: four with (FB) and four without (nFB) feedback using our ADP method `ringcode`, plus four runs with feedback using an instantaneous accretion prescription (INST). In the latter group, we set the radiative efficiency to the usual value $\eta = 0.1$, calculate the luminosity using $L = \eta \dot{M}_{\rm BH} c^2$ and limit it by the Eddington limit. Note that since the matter fed to the disc is assumed to be instantaneously transported to the SMBH in the INST case, the nFB disc feeding rate would correspond to the SMBH accretion rate in an INST run without feedback. This makes the additional four runs of INST without feedback redundant. The four simulations in each group differ only stochastically, with the cloud and ring initialized from different particle distributions. These stochastic variations allow us to test the robustness of our findings and identify which differences are due to the accretion methods rather than random initial conditions. The key results are summarized in table 4.1.

All simulations exhibit qualitatively similar behaviour, with one clear outlier, `FBr2` (bottom panel in Fig. 4.10), in which the initial system was almost

Run	FB	$E_{\rm tot.o}$	$E_{\rm tot.i}$	$t_{\rm Edd}$	$t_{\rm stop}$	$M_{\rm acc.tot.}$	$M_{\rm acc.bh.}$	$M_{\rm acc.esc.}$	$M_{\rm peak.disc.}$
		10^{57} erg	10^{55} erg	kyr		$10^5\mathrm{M}_\odot$			
nFBr0	off	5.3	-	98	-	1.17	0.44	0.60	0.42
nFBr1	off	5.3	-	163	-	1.18	0.45	0.62	0.41
nFBr2	off	5.0	-	137	-	1.10	0.41	0.58	0.46
nFBr3	off	5.9	-	145	-	1.29	0.48	0.68	0.46
FBr0	on	2.5	7.3	0	181	0.55	0.21	0.28	0.32
FBr1	on	3.2	9.2	3	276	0.69	0.26	0.35	0.32
FBr2	on	3.3	9.7	66	207	0.71	0.28	0.37	0.39
FBr3	on	3.2	9.1	32	219	0.69	0.26	0.35	0.37
INSTr0	on	3.3	15.9	107	-	0.44	0.44	-	-
INSTr1	on	3.4	16.3	117	-	0.63	0.63	-	-
INSTr2	on	3.5	16.5	140	-	0.68	0.68	-	-
INSTr3	on	3.5	16.8	142	-	0.63	0.63	-	-

Table 4.1: Main results of all simulations. All values are calculated at $t = 500$ kyr. The FB column shows whether feedback is turned on in the run. The total energy generated by the accretion disc or sink particle is $E_{\rm tot.o}$ and the total energy absorbed by the surrounding gas is $E_{\rm tot.i}$ (note that $\eta = 0.1$ for the INST runs). $t_{\rm Edd}$ is the time spent at or over the Eddington luminosity and $t_{\rm stop}$ is the time at which the central cavity appears and the disc accretion fully stops. The total accreted mass is given by $M_{\rm acc.tot.}$, total mass fed to the SMBH is $M_{\rm acc.bh.}$, the total amount of mass escaping via the outer disc boundary is $M_{\rm acc.esc.}$ and the maximum amount of matter contained in the accretion disc is $M_{\rm peak.esc.}$.

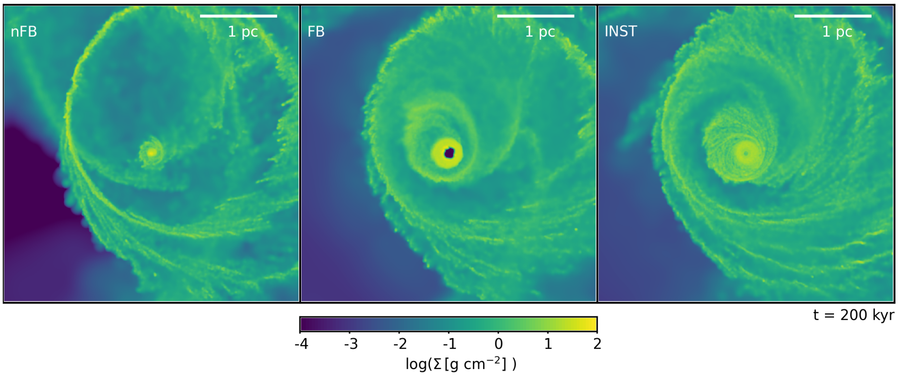

Figure 4.7: Density maps of the zoomed-in 4 pc region in `nFBr0`, `FBr0` and `INSTr0` runs at time $t = 200$ kyr. Clear differences are already apparent - a well-defined central disc aligned with the xy-plane in simulations with feedback contrasts with the more compact and misaligned central disc in the nFB run. The central cavity is also already present in the FB run.

completely cleared out (we will touch on that more Section 4.4.1). In general, the system evolves as expected, similarly to the retrograde case in Chapter 3, but with a couple of small differences due to the changes in initial conditions and the inclusion of more complicated physics (self-gravity, cooling, etc.). The collision occurs about 40 kyr after the start of the simulation. At this time, due to initial turbulence seeding, the cloud and the ring already consist of clumps and filaments. A portion of the cloud bypasses the ring entirely, later returning as an elongated stream, but a more significant portion impacts the torus in the direction opposite to its rotation causing significant angular momentum loss in the gas. Slowed-down gas quickly moves inwards feeding the accretion disc particle, with the disc accretion rate exceeding the Eddington mass accretion rate of the SMBH by almost an order of magnitude. Note that this is distinct from the feeding of the SMBH in the FB and nFB runs. Later on, a central disc/ring system forms within approximately the central parsec, surrounded by a larger ring that is still settling by $t = 500$ kyr. However, some identifiable differences between simulation sets appear after a few tens of kyr following the initial collision.

The most apparent differences are illustrated by density maps of the zoomed-in system (Fig. 4.7). The Figure shows a single representative run from each set at $t = 200$ kyr; around this time a central cavity becomes clearly apparent in the FB runs. At this point, the nFB run has a more compact ($r_{\rm out} \sim 0.1$ pc) central structure which is slightly warped in the centre. In contrast, both FB and INST produce a more extended central structure ($r_{\rm out} \gtrsim 0.2$ pc), with a central cavity appearing only in FB runs. Over time the differences in the extent of the central structure seem to mostly disappear

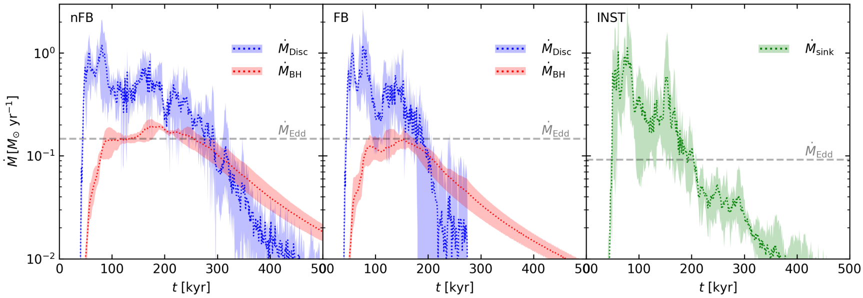

Figure 4.8: Accretion disc (blue) and SMBH (red) accretion rates in nFB (left) and FB (middle) runs and sink accretion rate in the INST runs (right). The dotted lines are the average rates in each set, while the filled regions show the effect of stochastic variations in each set. The grey horizontal dashed line shows the Eddington mass accretion rate $\dot{M}_{\rm Edd} = L_{\rm Edd}\eta^{-1}c^{-2}$

but the nFB central discs remain more warped and central cavities in the FB runs become even more pronounced.

A comparison between accretion rates in all three sets of runs is shown in Fig. 4.8, where nFB, FB and INST are in the three panels in order. The blue in nFB and FB runs corresponds to the accretion disc feeding rate, while red shows the SMBH feeding rate; in the INST case, green shows the feeding rate on to the SMBH sink particle, so it represents both sink accretion and SMBH feeding. In all cases, the dotted lines are the mean values of the four simulations in the set, and the filled regions encompass the range of variations in the four simulations. We can see that accretion onto the disc/sink particle varies by a factor of two or more on timescales < 10 kyr, which is due to the chaotic nature of clumpy matter infall. In contrast, the disc-mediated feeding of the SMBH is relatively smooth and slightly delayed in time. In FB runs, the feeding of the disc comes to an abrupt stop between $\sim 180 - 280$ kyr, which can be tied to the appearance of central cavities, while in the nFB runs the disc particle is still being fed after this time at a gradually decreasing rate. The feeding of the SMBH sink particle continues also in the INST runs. This reassures us that the cavity is not present and the central disc continues to be connected to the sink particle over a similar timespan as in the nFB runs. However, the accretion rate diminishes after the initial peaks, meaning that the regulating effects of feedback are not entirely absent.

We now further examine the nFB and FB runs. In Fig. 4.9(a) we show how the accreted gas is distributed within the ADP. Here, the total amount of gas swallowed by the sink particle is shown in black, while the amount of matter feeding the SMBH and escaping via the outer boundary are shown in red and green respectively. We can see the disc itself (blue lines) is far from empty at the end of the rapid accretion stage, so the feeding of the SMBH continues for ~ 200 kyr more even after the central region is cleared of gas (in the FB runs).

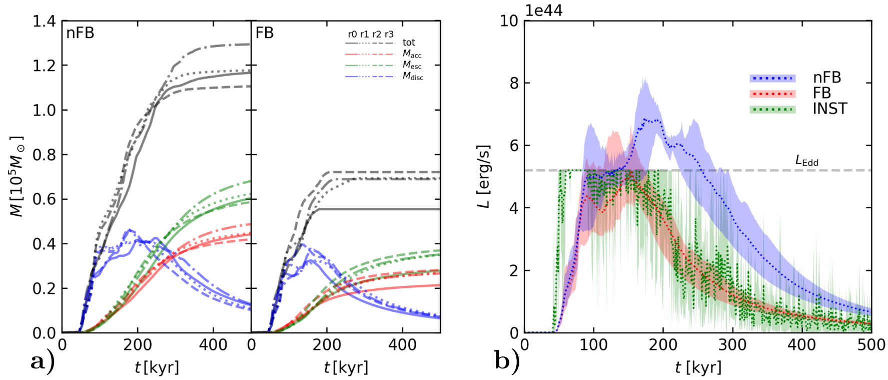

Figure 4.9: a) mass growth curves of mass accreted by the accretion disc particle (black), mass contained within the accretion disc (blue), mass added to the SMBH (red) and mass that escapes the disc via the outer boundary (green). The left-hand panel shows results for the nFB simulations while the right-hand panel shows results for FB simulations. Different line styles represent different realizations. **b)** accretion disc luminosity over time. Dotted curves show the mean in a set of four runs, while the filled regions show the variation found among runs in a set. The Eddington limit is shown by the gray dashed line.

In total, the lack of regulating feedback resulted in nFB models accreting about twice the amount of gas. Between $\sim 1.1 \times 10^5 \mathrm{M}_\odot$ and $\sim 1.3 \times 10^5 \mathrm{M}_\odot$ feeds the disc particle in the nFB runs; this is a significant fraction of the initial gas mass ($\sim 2 \times 10^5 \mathrm{M}_\odot$). More than a third of this mass ends up feeding the SMBH and about a half escapes the disc via the outer boundary (Fig. 4.9(a)). Similar proportions are found in the FB runs, with the total amount of accretion onto the ADP reduced by about half. The commonality between these proportions in all runs suggests that the stochasticity and the relatively chaotic dynamics of the surrounding gas have little effect on the accretion disc itself. We explore how the escaping gas might affect the system (sec. Section 4.4.3) in the Discussion. Note also, that the nFB set of SPH simulations show results somewhat similar to those of steady accretion between $R_{\mathrm{circ}} = 0.003$ pc and $R_{\mathrm{circ}} = 0.005$ pc (Fig. 4.5) meaning that few accreted particles had very small or very large angular momenta. This being the case, we can also infer from Fig. 4.5 that our chosen value for the minimum smoothing length $h_{\mathrm{min}} = 0.01$ pc had limited effect on the results: while some of the matter was put directly into the SMBH and the outer boundary, the amount was not overwhelming. In fact, even a significantly larger value $h = 0.015$ pc in the idealised tests did not have an impact larger than the stochastic variability between SPH simulations.

The evolution of luminosity in the three simulation sets is shown in Fig. 4.9(b). After accretion stalls, luminosity decreases. This is especially evident when compared with the nominal luminosity in the nFB run[3]. Luminosity in INST simulations is highly variable, or it could also be called noisy, as it follows the variations of accretion onto the sink particle. This variability is partially numerical in nature and should decrease somewhat with better resolution (i.e. larger $N_{\rm ngb}$, smaller $m_{\rm sph}$). Conversely, the evolution of disc luminosity in both FB and nFB is relatively smooth, since it follows the feeding of the SMBH; the radiative efficiency stays nearly constant at $\eta \approx 6.3$ % during the period of activity. Accretion disc luminosities reach super-Eddington values in all except one FB run. Feedback significantly reduces gas infall, thus the super-Eddington phases are not sustained for long and the peak luminosity is less than $1.3\,L_{\rm Edd}$ ($1.6\,L_{\rm Edd}$ in nFB). We note that currently, we do not account for any disc reconfiguration that might occur due to locally super-Eddington accretion. This is a drawback since that might happen on significantly shorter timescales dynamical timescale outside the disc; the effect would not build up and the larger scales, outside the accretion disc, might not get significantly super-Eddington feedback. Our simple model also neglects any mass loss from the disc due to super-Eddington luminosity. These shortcomings will be addressed in the future as we investigate the nature of self-regulation of accretion and feedback.

The disc has a collimating effect on the isotropically emitted SMBH wind. This leads to a conical outflow (Fig. 4.11). The total energy produced by the accretion disc in the FB runs is between 2.5×10^{57} erg and 3×10^{57} erg, but only a fraction of this energy is absorbed by the surrounding ISM in accordance with eq. (4.5), so the actual energy injected to the ISM in our simulation is about 7.8×10^{55} erg to 10.3×10^{55} erg. This value is still a few orders of magnitude higher than the estimate for the progenitor event of the 430-pc radio bubbles (7×10^{52} erg; Heywood et al. 2019). It also exceeds the energy contained within the *Fermi* bubbles by at least a factor of a few ($\sim 10^{54-55}$ erg; Su et al. 2010). In all cases except one, SMBH winds are not strong enough to completely disrupt the system, leaving an intact central disc and a surrounding ring system, just with a pronounced central cavity (we address this in more detail in Section 4.4.1). As the system evolves, more and more of the background gas is removed and the opening angle of the cone increases. The same general behaviour describes the INST runs. The luminosity is artificially capped at the Eddington value but since the accretion efficiency is set to a fiducial value of $\eta_{\rm INST} = 0.1$ they produce approximately twice the amount of energy ($\eta_{\rm INST}/\eta_{\rm FB} \simeq 1.6$). Also, as there is no delay between accretion and luminosity peaks in INST runs, the effect of feedback is near immediate.

By $t = 500$ kyr the outer portion of the central disc and the surrounding inner filaments/rings are aligned with the xy-plane within a few degrees in all

[3]Note that in the nFB simulations, we compute the luminosity of the accretion disc, but do not generate feedback particles, thus it has no effect on the surrounding gas.

runs, while the inner portion of the central disc is somewhat warped - the disc rotational plane shifts up to 50° in nFB and up to 20° in INST. A transient misaligned ($\sim 20^\circ$) disc is present in two FB runs. It is possible that the SMBH wind pressure on the central disc helps to keep it within the same rotational plane. In the run `FBr2` feedback pushes out all the gas except for a segment of the inner disc (Fig. 4.10; bottom). Interestingly, the total energy ejected as wind (table 4.1) is similar to that in the other runs, but the simulation spends more time in the super-Eddington regime as shown by the luminosity functions of all simulations in Fig. 4.12. Overall, at least for luminosities $L > 0.5L_{\rm Edd}$, the variation of the initial particle distribution is less important in determining the luminosity function than the differences between the accretion and/or feedback prescriptions. Another interesting aspect is that the total energy radiated as feedback is considerably larger in the INST simulations; curiously, this does not result in a complete disruption of the initial system as it does in `FBr2` or even in the creation of central cavities. It appears that sporadic bursty feedback is far less efficient at ejecting the gas and stopping further SMBH accretion than continuous energy injection, even at a milder rate.

4.3.1 A comment on performance

An important aspect of any numerical method is its computational cost. Although we did not do rigorous benchmarking, we compared the time that our different simulations take to run. On average it takes about 160 wall-clock hours to calculate each nFB run and about 140 wall-clock hours to calculate each FB run up to $t = 500$ kyr on 32 CPUs (for comparison, INST runs took slightly longer, 148 wall-clock hours, on the same system and setup). In both cases the time spent on accretion disc calculations is almost negligible: on average, the fraction of time spent on tasks directly related to the disc is $\sim 0.6\%$. Interestingly, the significant amount of time spent on calculating the interactions between feedback packets and gas particles in the FB runs ($\sim 32\%$ on average) is more than offset by the time saved when a large number of particles that would otherwise require very small time-steps are pushed out of the centre, resulting in quicker calculations.

4.4 Discussion

4.4.1 Chaotic nature of model evolution

All simulations with feedback produce qualitatively similar results regarding the large-scale morphology of the system. Stochastic variations primarily affect the smaller-scale central features, such as the central cavity and the precise shape and size of the central disc/ring structures. However, a more careful

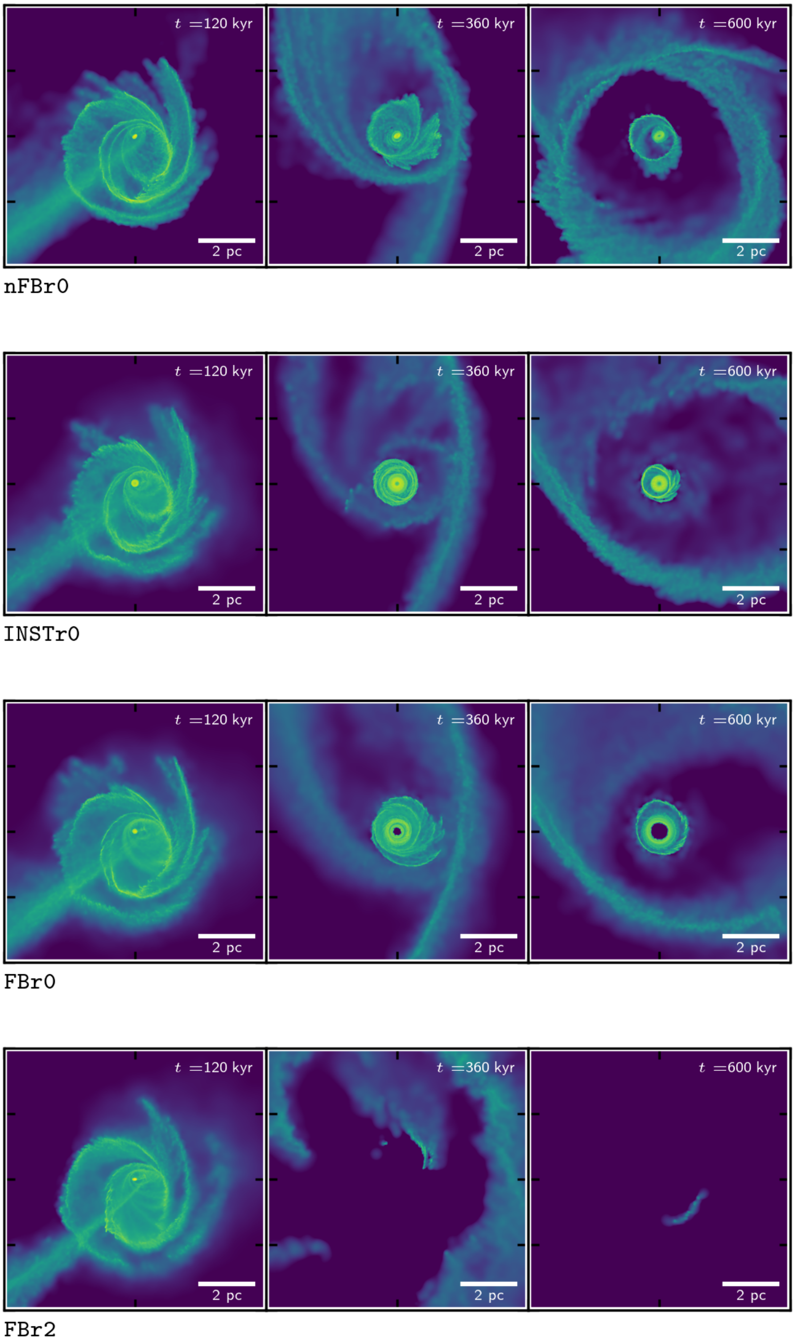

Figure 4.10: Density maps of showing the evolution of 4 representative simulations, from top to bottom: `nFBr0`, `INSTr0`, `FBr2` and `FBr2`

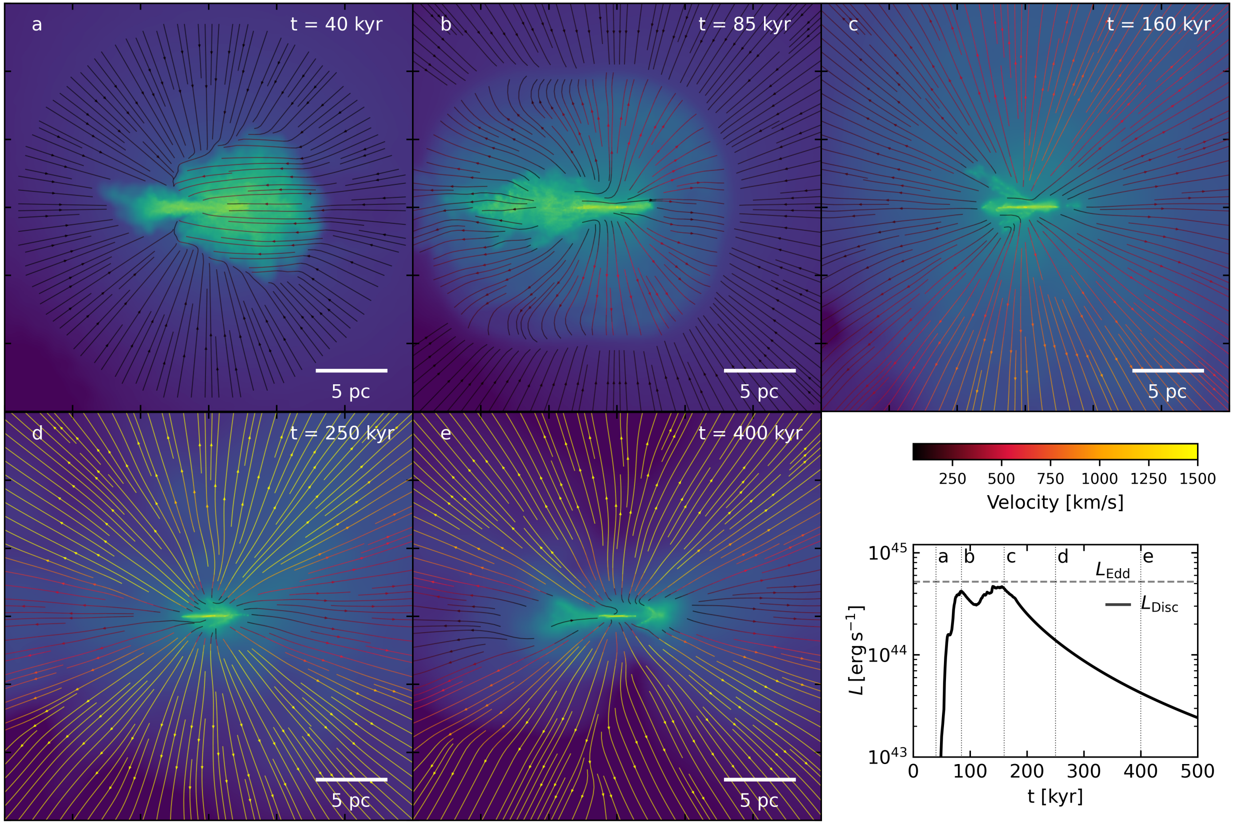

Figure 4.11: Surface density maps at various times during the run `FBr0`. The view is from the side of the initial ring plane. The change in luminosity over time is shown at the bottom right, along with the droplines corresponding to the times of the density map. Vectors show direction of gas movement, their length proportional to logarithm of gas velocity.

inspection reveals evidence of chaotic behaviour. For example, only simulation `FBr2` almost completely clears the central few parsecs of gas during the AGN event. The case is especially intriguing as there are no significant differences in the total accreted mass or total injected energy, which are both only $\sim 3\%$ larger than in other FB runs (table 4.1).

The main difference is that the `FBr2` feeds the disc at a relatively consistent rate for over 100 kyr. This can be seen in Fig. 4.9(a) - the black curves show the total mass injected into the disc. `FBr0` and `FBr1` runs both have a significant dip in disc accretion rate at ~ 100 kyr while `FBr3` somewhat lags behind the other runs. The consistent rate of feeding allows `FBr2` to maintain $L_{\rm disc} \geq L_{\rm Edd}$ for a longer period of time (table 4.1). However, this is clearly not the full explanation as illustrated by the significantly less extreme run `FBr3`. The latter also has significantly less gas remaining in the central 5 pc at $t = 500$ kyr when compared with the remaining two FB runs, but more interestingly, `FBr3` is also on average slightly less energetic than its two less extreme counterparts but sustains a super-Eddington luminosity for a significantly longer period of $\sim$ 32 kyr. We conclude that sustaining some critical luminosity is more important than the total energy injection for the removal of gas from the centre. This is consistent with the results of INST simulations. There we put an artificial cap at $L_{\rm AGN} = L_{\rm Edd}$ and no run resulted in significant gas removal from the centre. On the other hand, we have a counterexample with the runs `FBr0` and `FBr1`. Even though `FBr1` has a higher luminosity for the majority of the activity phase and the luminosity in `FBr0` never exceeds the Eddington limit, the central cavity in `FBr0` is more pronounced.

We investigated whether the heating and cooling prescription could explain the differences observed within the central parsec between runs. A consistently high luminosity could theoretically maintain a higher temperature of the surrounding gas, making it easier for feedback to expel it. Broadly, we expect three phases of gas to exist: the cold phase in the densest regions, cooling down to $\sim$ 20 K; the warm phase, remaining at approximately $\sim 10^4$ K in dense regions even under the influence of feedback; the hot phase ($T \gg 10^4$ K)usually representing the diffuse gas. The simplest case is the nFB run. Here, the denser gas simply cools down to $\sim$ 20 K after the collision and only the diffuse surroundings maintain the warm phase in line with the UV background. In both FB and INST runs, during the early AGN phase, the majority of most of the gas maintains a warm phase. In fact, INST runs show slightly more hot-phase gas in the surroundings, while also showing slightly more cold gas with $r > 0.5$ pc. However, in both FB and INST sets the central $r < 0.1$ pc is filled with similarly hot gas. Some cold clumps appear at $r \sim 0.1$ pc in the INST runs potentially due to more noisy luminosity or the lower peak luminosity. However, the inner $r < 0.1$ pc remains filled with hot gas. In FB runs, as the gas is evacuated from the central system, the outer sections of the central

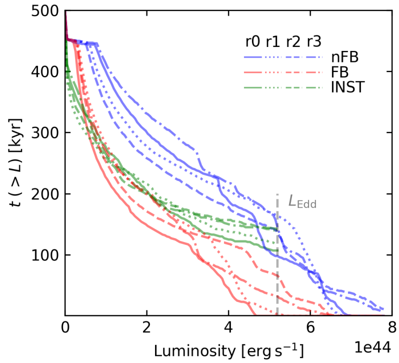

Figure 4.12: AGN luminosity functions in nFB (blue), FB (red) and INST (green) simulations. The Eddington limit is shown by the vertical gray dashed line.

disc begin to cool, but most of the inner section maintains the warm phase. In contrast, as luminosity diminishes, discs in INST systems quickly cool down, maintaining the warm/hot phase only within the inner $r < 0.1$ pc (which is by now empty in the FB runs). The cold clumps present closer to the SMBH might absorb more of the energy and are harder to push away; this may be a way to explain why the similar phase gas is not removed from the $r < 0.1$ pc in the INST runs.

Additionally, similarly to what was done in Section 3.3.6, we measure the weight of the disc and compare it with the outward force of the AGN wind pressure in each simulation with feedback (Zubovas et al. 2011). We take the disc's height to be the full width at half maximum in the density field perpendicular to the disc's radius. Again, we see no significant differences between FB runs - the outward force acting on the disc always outgrows the disc's weight, initially at the centre, and gradually pushes out the gas, producing the central cavity. Conversely, in INST runs the outward force never outgrows the weight of the disc.

In light of the above, we conclude that the INST runs do not clear out the innermost region due to a combination of lower peak luminosity and the near-instant effect of feedback. That is, the lack of delay between accretion and feedback injection leads to some of the feedback being wasted on the dense infalling matter. It is difficult to determine precisely why the outlier `FBr2` saw such strong feedback without invoking stochastics. In any case, the results show that the morphology of the resultant system is very sensitive to the interplay between feeding and feedback. This highlights potential risks in relying on fixed arbitrary parameters, such as a constant $t_{\rm visc}$, in feedback simulations, as small variations may lead to drastically different system evolution.

4.4.2 Accretion parameter tuning

One of the main advantages of our approach is that it gives consistent results that are less reliant on free parameters, but this comes at the cost of simplicity and a small increase in computational cost. For example, we do not select a specific viscous timescale $t_{\rm visc}$ or radius of gas accretion (although we need to specify the outer radius of the disc). As previously illustrated, the choice of these parameters might sometimes determine the outcome of a simulation as even a small increase in luminosity may result in significant changes in chaotic systems Section 4.4.1.

We can indirectly check how well a simpler approach would recreate the accretion evolution seen in our results by inputting the accretion data from the nFB simulation `nFBr0` into simpler two-stage accretion disc particle method (DP). We cannot use `FB` simulations for this because feedback has an effect on the dynamical evolution of the simulation. A convenient prescription for the rate of SMBH accretion that depends only on parameters readily available in `nFBr0` data is given by (Power et al. 2011a):

$$\dot{M}_{\rm BH} = \min\left[M_{\rm disc}/t_{\rm visc}, \dot{M}_{\rm Edd}\right], \tag{4.42}$$

where $M_{\rm disc}$ is the accretion disc mass, $t_{\rm visc}$ is an arbitrarily chosen constant viscous timescale and $\dot{M}_{\rm Edd}$ is the Eddington mass accretion rate. Note that $M_{\rm disc}$ used here is not equal to the disc mass in nFB run; instead, $M_{\rm disc}$ is given by the rate of sink accretion, subtracting the mass added to the SMBH using the prescription (4.42).

We use a set of four `Python` scripts that describe the evolution of the black hole and the gas reservoir coupled to it. In addition to the Eddington-limited model, we run scripts with no limits and one with an additional limit on the maximum allowed accretion disc mass according to the gravitational stability criterion (Pringle 1981):

$$M_{\rm disc,max} \approx \frac{H}{R} M_{\rm BH}, \tag{4.43}$$

where the disc height-radius ratio is taken to be a constant $H/R = 0.002$, typical for a thin disc.

We show the results of this procedure in Fig. 4.13. The blue and red curves represent the rate of disc and SMBH feeding, respectively, from the simulation `nFBr0`. The green lines represent the DP calculations with different choices of $t_{\rm visc}$. A disc evolution that most resembles the SMBH feeding in the `nFBr0` simulation is marked in black; when calculating it, we weigh the whole 500 kyr duration evenly. The bottom panel shows how the closest DP calculations compare with the variable $t_{\rm visc} = M_{\rm disc}/M_{\dot{\rm M}_{\rm BH}}$ calculated from `nFBr0`. The `No Limit` approach seems to work best for the ~ 200 kyr period where the variable $t_{\rm visc}$ remains approximately constant while overestimating the feeding in later stages. Applying the luminosity and/or disc mass limits substantially reduces the best-fitting $t_{\rm visc}$ which also reduces the time lag between disc and SMBH feeding. We note that even if the evolution seen in the main simulation could be approximated, the 'correct' $t_{\rm visc}$ is not known *a priori* and could be difficult to deduce as it corresponds to relatively small feeding radii $R_{\rm feed} \sim 2-5\times10^{-4}$ pc. These values are at least a factor a few lower than the $R_{\rm circ} \sim 10^{-3}$ pc of the majority of the accreted particles in the hydrodynamical simulations. This means that correcting only for angular momentum would not be enough to reproduce accretion disc results obtained with `ringcode` method.

4.4.3 Star formation on the disc outskirts

Over the induced activity period about half of matter added to the accretion disc particle escapes through the outer boundary (Fig. 4.9(a); left - green). At the moment, simulations just track the amount of matter escaping over time; it is no longer taken into account when calculating the evolution of the accretion disc nor returned to the main hydrodynamical simulation. Neglecting this 'lost mass' allows us not to complicate the calculations, but it is worthwhile to consider the possible interaction between this gas and the rest of the gas close to the SMBH as we plan to do when improving the prescription in the future. In particular, accounting for this gas in the hydrodynamical simulation may lead to either additional SMBH accretion, additional star formation in the centre, or both. The additional mass may also result in suppression of feedback, which would suppress the formation of central cavities.

First, we consider how interactions between the gas escaping the accretion disc and the surrounding material can produce additional accretion. Gas escaping via the outer boundary has $R_{\rm circ} \sim 0.01$ pc, therefore needs only a small reduction in angular momentum to get accreted back, so adding this gas to the hydro simulation can result in additional accretion as it collides with infalling material. Although the majority of mass escapes the disc in the later stages of the AGN episode, the peak escape rate occurs at about the same time as central cavities appear in the FB runs, when the central disc structure is somewhat settled. Additional gas might even prevent central cavities from forming, as the total mass of gas escaping via the outer boundary ($\sim 10^4\,{\rm M}_\odot$) is comparable to the total mass contained within the central few parsecs.

We can also envision a scenario, similar to the one described in Hobbs et al. (2011), in which this escaping gas provides an additional barrier to accretion as the mixing of different angular momentum gas creates a peaked angular momentum distribution and a pronounced ring with $r > 0.01$ pc. So the escaping matter might extend the AGN episode by providing some additional material to the accretion disc, but it might also create a more dense environment around the SMBH, maybe leading to star formation.

The main obstacle to star formation in the vicinity of the SMBH is the tidal force in the region where SMBH potential dominates ($r < 0.8$ pc in our case). As a first approximation, to allow for star formation, the density in a given

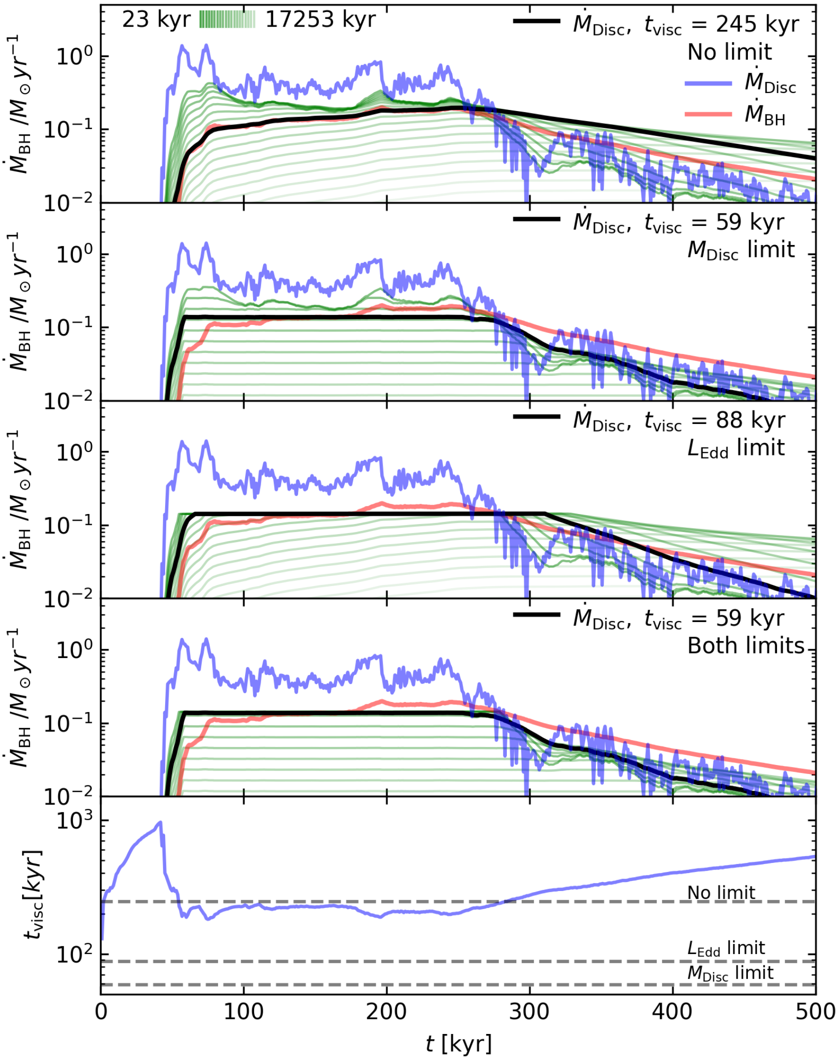

Figure 4.13: Results of applying a different two-stage accretion prescription to the data of the simulation `nFBr0`. Green lines represent calculations with different choices of the $t_{\rm visc}$ parameter, blue lines show the accretion onto the accretion disc particle, red - onto the SMBH using our accretion disc prescription, while the black curve is the best fitting two-stage prescription result. A plot of $t_{\rm visc} = M_{\rm disc}/\dot{M}_{\rm BH}$ is shown in the bottom panel; only the *no limit* two-stage model corresponds with the timescales found in the `ringcode` model for a period of ~ 200 kyr.

region has to exceed the tidal density $\rho_{\rm tidal}$:

$$\rho_{\rm esc} \gtrsim \rho_{\rm tidal} \simeq \frac{3M_{\rm BH}}{4\pi R^3}, \tag{4.44}$$

where $\rho_{\rm esc} = M_{\rm esc}/V$ is the density of the escaping gas, while V is the volume of the region containing the gas. We can very roughly estimate where star formation might occur due in the escaped gas if we assume that all the escaped matter stays within this volume. The upper density estimate can be found by assuming that all the gas stays within a wedge-shaped disc of angle:

$$\alpha = \arctan\left(\frac{2H_{\rm max}}{R_{\rm max}}\right), \tag{4.45}$$

here $R_{\rm max}$is the radius where the accretion disc is at its maximum height $H_{\rm max}$. We can use $\pi/2-\alpha$ to define a cone sector of a sphere; then the angle subtended by the disc is 4π minus the angle of the conical sector. Thus the tidal escaping gas density is given by:

$$\rho_{\rm esc} = \frac{M_{\rm esc}}{V_{\rm sphere} - 2V_{\rm sector}} = \frac{3M_{\rm esc}}{4\pi R^3 \cos\left(\pi/2 - \alpha\right)}. \tag{4.46}$$

In our simulations, the value of α is very small, of order 10^{-3}. In this case, $\rho_{\rm esc}$ is larger than $\rho_{\rm tidal}$ at $R < 1$ pc after enough matter escapes the disc ($t = 180$ kyr in FB simulations). Admittedly, this is an extreme case. Density is greatly reduced if we allow for even a small variation of the accretion disc plane. Consider a small angle β by which the accretion disc tilts. If we assume that the disc oscillates quickly enough compared with its viscous timescale, we expect that this effectively results in matter distributing over a larger volume defined by a larger wedge angle $\bar{\alpha} = \alpha + \beta$. Angles as small as $\beta \gtrsim 0.25°$ result in density low enough that star formation is no longer possible, even if all of the matter escaping the disc throughout the 500 kyr duration of the FB simulations accumulates within the specified volume.

Since discs that allow for star formation appear to be very thin, an interesting aspect to consider is the required spatial resolution in order to be able to track star formation around the SMBH in an SPH simulation. For simplicity, consider that the minimum resolvable height of the disc is the minimum smoothing length of an SPH particle in a given simulation: $H(R) \sim h_{\rm min}$. At radii below some threshold, where the disc is unresolved in the z-direction, its height remains constant and the volume can be approximated by a cylinder, giving a modified expression for $\rho_{\rm esc}$:

$$\rho_{\rm esc} = \frac{M_{\rm esc}}{\pi R^2 H}. \tag{4.47}$$

Equating this with the tidal density we get we get the maximum height required that still allows the disc to reach the tidal density at a given radius:

$$H_{\max} = \frac{4}{3}\frac{M_{\rm esc}}{M_{\rm BH}}R. \tag{4.48}$$

In our simulations, this value is

$$H_{\rm max,FB} \sim 0.013R; \qquad H_{\rm max,nFB} \simeq 0.02R, \tag{4.49}$$

where the differences arises due to differences in $M_{\rm esc}$. Given that our simulations have $h_{\min} = 0.01$ pc, we see that they would not be able to resolve star formation closer than $R \sim 0.5 - 0.8$ pc from the SMBH.

4.4.4 Applicability to larger scales

So far, we only applied our accretion disc prescription in a system where the spatial resolution is comparable to the size of the accretion disc, but it should be possible to apply the same approach to larger scales. Salas et al. (2021) performed simulations of the central molecular zone (CMZ) with turbulence driving. They suggest that turbulence results in a quasi-continuous inflow of matter towards the centre; they estimate the effective viscosity ν using the α-accretion disc theory and find it consistent with Sormani et al. (2018) models of nuclear rings present in the central ~ 1 kpc of galaxies, where viscosity due to turbulence is included as a free parameter. This suggests that the accretion disc grid can be extended outward in a straightforward manner up to the scales of at least tens of parsecs, where circumnuclear discs and/or rings are found. But extending the disc this far may be unnecessary since parsec-scale resolutions are common in modern galaxy simulations; therefore, extending the sub-resolution grid out to ~ 1 pc should be sufficient. However, this would require assuming a continuous disc in the centre, which is clearly not the case in many circumstances (eg. current GC, cf. Ferrière (2012), or the results of our FB simulations). In addition, an overly large sink radius would result in the smoothing out of even relatively large perturbations, leading to relatively smooth and long but weak periods of AGN activity. Some of the downsides of this extension may be circumvented by applying more stringent accretion criteria or, possibly, modifying the evolution equation itself, by accounting for disc instabilities and turbulence. Given that the current prescription requires very little computational power to process, some complications to the underlying model will not reduce its applicability from a processing power standpoint.

Another interesting possibility is a combination of our accretion disc method with a method applicable to larger scales. For example, Anglés-Alcázar et al. (2016) apply and extend an analytical model of mass transport due to gravitational torques developed by Hopkins & Quataert (2011) to determine BH accretion in cosmological simulations:

$$\dot{M}_{\rm BH} = (1 - \eta) \times \dot{M}_{\rm Torque}, \tag{4.50}$$

where $\dot{M}_{\rm Torque}$ is the mass transport due to the local properties of gas in the unresolved central region. The model is intended to be used in cosmological and other large-scale simulations; it describes the inflow of matter from scales of $0.1 - 1$ kpc down to the SMBH (sub-parsec) scales. It would be interesting to estimate $\dot{M}_{\rm disc}$ following the same formalism, especially in large-scale simulations with temporal resolution fine enough for the delay of feedback to have a meaningful impact.

4.5 Conclusions

We developed a simple 1D accretion disc prescription coupled to the SMBH sink particle in `Gadget-3` in order to increase the realism of black hole accretion and feedback. The prescription is based on the α-thin accretion disc model of Shakura & Sunyaev (1973), but uses the Paczyński-Wiita potential (Paczyński & Wiita 1980). We assume that the disc is stable and tends towards a quasi-steady state after each mass injection. We tested the prescription by simulating a retrograde collision between a torus-shaped ring surrounding an SMBH and an infalling cloud in an environment similar to the Galactic Centre. We run three sets of four simulations: with feedback from our accretion disc (FB), without feedback (nFB) and with instantaneous accretion and feedback (INST). The disruption of the initial system results in an AGN phase lasting a couple hundred kyr. Feedback reduces the total accreted mass in both sets of feedback simulations ($M_{\rm acc.tot} \sim 6 \times 10^4\,{\rm M}_\odot$) when compared with runs without feedback ($M_{\rm acc.tot} \sim 1.2 \times 10^5\,{\rm M}_\odot$) by about a half.

The major differences between simulations with instantaneous accretion and those with our accretion disc prescription are:

- The growth rate of the SMBH, $\dot{M}_{\rm BH}$, is reduced and spread more evenly over time in the accretion disc prescription simulations; the change in luminosity $L_{\rm disc}$ closely follows $\dot{M}_{\rm BH}$.
- Radiation from the disc carries away $\eta \sim 6.25\%$ of the rest mass energy of infalling matter, which is expected in the Paczyński-Wiita potential and within 10% of the expected value from the relativistic Schwarzschild solution.
- Feedback in the FB simulations expels gas from the central $0.1 - 1$ pc region, producing a central cavity. This is not reproduced in INST runs, although there the aggregate energy input into the gas is higher by a factor $\sim 1.5 - 2$.

- A significant amount of matter escapes via the outer boundary of the accretion disc; we neglect this in our current simulations.

While improvements are necessary, we show that the current implementation of the accretion disc sub-grid prescription `ringcode` works consistently while requiring negligible additional computational power. It provides robust results that differ significantly from those obtained using the instantaneous feeding prescription and are not replicable by simple delay using a single timescale. Our approach relies less on free parameters, most importantly the viscous timescale used to artificially delay the SMBH feedback. Thus, our accretion disc prescription should be especially useful in simulations of galactic nuclei on scales of tens of parsecs, where numerous questions about the interplay between feeding and feedback and their link to star formation remain unanswered.

Chapter 5

Feedback in inhomogeneous medium on kilo-parsec scales[1]

In previous chapters, we have demonstrated how an AGN event can begin. We leaned on a relatively well-studied system around Sgr A* to have a clear comparison with observations and other studies. Even in these relatively simple systems, we got very disparate results among various simulations when considering the effect of feedback on the dense/clumpy central rings (Section 4.4.1). Complexity is not necessarily confined to the central few parsecs - the larger kilo-parsec scales also feature clumpy cold gas and are far from totally uniform. Given that a significant amount of our understanding about the imprint an AGN leaves in galaxy evolution comes from larger scales, where large-scale outflows can be observed, we should endeavour to consider these complexities carefully.

Observed supermassive black hole (SMBH) scaling relations such as the $M_{\rm BH} - \sigma$ (Ferrarese & Merritt 2000; Gültekin et al. 2009; McConnell & Ma 2013; Kormendy & Ho 2013; Bennert et al. 2021) and $M_{\rm BH} - M_{\rm b}$ (Häring & Rix 2004; McConnell & Ma 2013; Kormendy & Ho 2013) relations provide indirect evidence that feedback from active galactic nuclei (AGN) has an impact on the evolution of the host galaxy. More direct observational evidence comes in the form of wide-angle cold gas outflows that extend up to ~ 10 kpc from the nucleus (Spence et al. 2016), with mass outflow rates of up to $\sim 1000\ {\rm M}_\odot\ {\rm yr}^{-1}$, momentum flow rates of up to $\sim 50 L_{\rm AGN}/c$ and energy flow rates of $\sim 0.05 - 10\% L_{\rm AGN}$ (Feruglio et al. 2010; Rupke & Veilleux 2011; Sturm et al. 2011; Maiolino et al. 2012; Cicone et al. 2014, 2015; Tombesi et al. 2015; González-Alfonso et al. 2017; Fiore et al. 2017; Fluetsch et al. 2019; Lutz et al. 2020).

In addition to the large-scale outflows, many active galaxies show evidence of fast nuclear winds with velocities ~ 0.1 c (Pounds et al. 2003b,a; Tombesi

[1] The content of this chapter is based on K. Zubovas, M. Tartėnas, M. Bourne, Astronomy & Astrophysics, **691**, A151 (2024)

et al. 2010a,b, 2013) derived from blue-shifted lines observed in the X-ray band which have subsequently been dubbed ultra-fast outflows (UFOs). Their kinetic power is comparable to that of the large-scale outflows, suggesting a possible physical connection between the two.

Several theoretical models explaining the presence of outflows exist, such as jet-driven cocoons (Gaibler et al. 2012; Bourne & Yang 2023; Talbot et al. 2022, 2024), AGN radiation pressure effects on dusty gas (Ishibashi & Fabian 2015; Thompson et al. 2015; Costa et al. 2018) and AGN wind-driven outflows (Costa et al. 2014; King & Pounds 2015). This last framework provides a connection between UFOs and large-scale outflows by showing that UFOs arise as winds from the AGN accretion disc (King 2010a) that subsequently shock against the interstellar medium (ISM) and reach temperatures of $\sim 10^{10}$ K (e.g., King 2003; Zubovas & King 2012a; Faucher-Giguère & Quataert 2012). The subsequent evolution depends strongly on whether the shocked wind bubble cools efficiently. If it does, then only the wind momentum is transferred to the surrounding gas (e.g., King 2003, 2005; Nayakshin 2014). Then the condition for the wind to be able to push away most of the surrounding gas translates into the SMBH mass $M_{\rm BH} \propto \sigma^4$, close to the observed relation (King 2010b; Zubovas & King 2012b). Alternatively, if most of the shocked wind energy is available to drive the ISM, a fast, massive large-scale outflow develops with properties very similar to those observed (Zubovas & King 2012a; Faucher-Giguère & Quataert 2012).

In several galaxies, UFOs and large-scale outflows have been discovered simultaneously (e.g., Feruglio et al. 2015; Tombesi et al. 2015; Veilleux et al. 2017). Although in some cases, the energy rates of the two components match almost exactly (e.g., in Mrk 231, cf. Feruglio et al. 2010, 2015), typically there is a significant discrepancy between the two values (Marasco et al. 2020). There are two primary explanations for this. The first involves AGN luminosity variations over the dynamical timescale of the outflow, $t_{\rm flow} \sim R/v_{\rm out} \sim 1 R_{\rm kpc} v_8^{-1}$ Myr, where $v_8 \equiv v_{\rm out}/1000$ km s^{-1}. Since outflow properties cannot change on timescales much shorter than dynamical, it follows that they correlate better with the average AGN luminosity over that time (Zubovas & Nardini 2020). Individual AGN episodes should not last longer than a few times 10^5 yr (King & Nixon 2015; Schawinski et al. 2015), so the instantaneous luminosity we observe is generally not representative of the long-term average. UFO properties, on the other hand, change on much shorter timescales of years or less (King & Pounds 2015) and so trace the AGN luminosity much more closely. The inclusion of this variability in models reproduces the scatter of large-scale outflow properties when compared against present-day AGN luminosity (Zubovas & Nardini 2020; Zubovas et al. 2022).

The second possible explanation of the variation of outflow properties with regard to UFO and/or AGN properties is uneven coupling in different galaxies.

Generally, the ISM exhibits clumping on various scales, with cold dense clouds and filaments embedded in a more diffuse hot component. In this case, most of the shocked wind energy can escape via paths of least resistance (Wagner et al. 2013; Nayakshin 2014; Zubovas & Nayakshin 2014; Bourne et al. 2014; Bieri et al. 2017), i.e. the low-density channels in the ISM, leaving the cold gas in its wake exposed mostly to the wind momentum. In fact, the fraction of wind energy affecting different clumps encompasses the whole continuum from zero to unity (Zubovas & Nayakshin 2014). Many clumps can be compressed by the passage of the outflow, enhancing star formation (Laužikas & Zubovas 2024) facilitating their infall and reducing the effective cross-section of dense clumps exposed to the wind (Bourne et al. 2014). This scenario also helps explain a particular shortcoming of the more idealised, spherically symmetric, wind-driven outflow model. Within that formulation, a momentum-driven outflow can only form if the shocked wind cools efficiently, mainly via the inverse Compton effect (King 2003). The transition between efficient and inefficient cooling should occur on scales of several hundred parsecs; however, the expected signature of radiative cooling on these scales is not observed (Bourne & Nayakshin 2013). In addition, when one considers that the shocked wind plasma is likely two-temperature, with protons carrying most of the energy, it becomes clear that inverse Compton cooling is very inefficient (Faucher-Giguère & Quataert 2012) and so energy-driven outflows should form very close to the SMBH, clearing gas from the galaxy and preventing the SMBH from growing. The possibility of both momentum- and energy-driven outflows to exist affecting different phases of the gas eliminates this issue.

While the behaviour of dense gas in multiphase outflows has received some attention, the large-scale properties of outflows launched in multiphase media remain relatively unexplored. In particular, it is uncertain whether the global properties - the kinetic powers, momentum and mass outflow rates - of the large-scale outflows produced in such systems agree with observational results. Intuitively, we would expect that the dense material which comprises the majority of the outflowing mass should move with lower velocities than predicted in the spherically symmetric scenario, with a corresponding decrease in momentum and energy rates and corresponding loading factors. This picture is complicated by the generally non-linear heating and cooling processes which lead to the outflowing gas changing phase as the outflow evolves (Zubovas & King 2014; Richings & Faucher-Giguère 2018b,a). Although early detections of massive outflows (Feruglio et al. 2010; Sturm et al. 2011; Rupke & Veilleux 2011; Maiolino et al. 2012) generally agreed quite well with the spherically symmetric prediction (Cicone et al. 2014), recent larger outflow samples show much larger scatter around these predictions, primarily toward lower values for a given AGN luminosity (Fluetsch et al. 2019; Lutz et al. 2020).

In this Chapter, we use numerical simulations of idealised systems to quantify the distribution and evolution of three major outflow parameters - mass outflow rate, momentum loading factor and energy loading factor - in both smooth and turbulent ISM, with and without gas cooling. We show that turbulence by itself does not impact the global parameters, i.e. the energy injected by the AGN couples equally well to smooth and clumpy gas distributions. Cooling, on the other hand, has a profound effect, even though we assume that the shocked AGN wind remains adiabatic. The effect of cooling is intertwined with that of gas clumpiness and shock heating by the outflow: in smooth systems, cooling reduces the outflow energy rate by 1-2 orders of magnitude, with higher AGN luminosity leading to less efficient cooling; in turbulent systems, the effect is mitigated, since some gas can be heated to very high temperatures where cooling is inefficient. In general, the mass outflow rates, momentum and energy loading factors we obtain in simulations with both turbulence and cooling agree quite well with corresponding values of real outflows, and the differences in the host gas density structure go a long way in explaining the observed variety of loading factors.

5.1 Analytical arguments and models

We already introduced the concept of spherical wind as AGN feedback in Section 1.2.1. The expansion of energy-driven outflows in a homogeneous medium has been detailed in several papers, including reviews by King & Pounds (2015) and Zubovas & King (2019); here we briefly summarise the main results before considering how we would expect the results to change in an inhomogeneous, clumpy gas distribution. First, it is assumed that the SMBH has reached its formal M_σ mass (King 2005)

$$M_\sigma = \frac{f_c \kappa}{\pi G^2}\sigma^4 = 3.7 \times 10^8 \left(\frac{\sigma}{200 \text{ km s}^{-1}}\right)^4 \text{M}_\odot, \tag{5.1}$$

where $f_c = 0.16$ is the cosmological baryon fraction, $\kappa = 0.4$ cm^2 g^{-1} is the electron scattering opacity and σ_{200} is the bulge velocity dispersion in units of 200 km s^{-1}. Secondly, feedback is Eddington-limited and the wind has momentum and kinetic energy rates of

$$\dot{p}_\text{w} = \frac{L_\text{Edd}}{c} \tag{5.2}$$

and

$$\dot{E}_\text{w} = \frac{\eta}{2} L_\text{Edd}. \tag{5.3}$$

In the regime in which the wind shock is unable to cool efficiently, i.e. the energy-driven regime, Zubovas & King (2012a) show that most of the wind energy is transferred to the kinetic energy of the outflow such that

$$\frac{1}{2}\dot{M}_{\rm out}v_{\rm out}^2 \simeq \frac{1}{2}\dot{M}_{\rm w}v_{\rm w}^2 \tag{5.4}$$

and hence

$$\dot{p}_{\rm out} = \dot{p}_{\rm w}\left(\frac{\dot{M}_{\rm out}}{\dot{M}_{\rm w}}\right)^{1/2} = \frac{L_{\rm Edd}}{c}f_{\rm L}^{1/2}, \tag{5.5}$$

where the AGN wind mass loading ratio

$$f_{\rm L} = \frac{\dot{M}_{\rm out}}{\dot{M}_{\rm w}} = \left(\frac{2\eta_{\rm r}c}{3\sigma}\right)^{4/3}\left(\frac{f_{\rm g}}{f_{\rm c}}\right)^{2/3}\frac{l^{1/3}}{\dot{m}}. \tag{5.6}$$

In this equation, $f_{\rm g}$ and $f_{\rm c}$ are the gas fraction and cosmological baryon fraction, respectively, $\eta_{\rm r}$ is the radiative efficiency of accretion, $l = L_{\rm AGN}/L_{\rm Edd}$ and $\dot{m} = \dot{M}_{\rm w}/\dot{M}_{\rm Edd}$. For typical galaxy and wind parameters, assuming $f_{\rm g} = f_{\rm c}$, $f_{\rm L} \sim 400$, and so momentum boosts of ~ 20 and mass outflow rates of several times $10^2 - 10^3 {\rm M}_{\odot}$ ${\rm yr}^{-1}$ can be reached.

An important point to note is that the model of Zubovas & King (2012a) assumes that all of the gas is swept up into the outflow. However, let us now assume that the ISM can be split into hot diffuse and cold dense components. We define the parameter

$$\eta_{\rm hot} = \frac{f_{\rm g} - f_{\rm cold}}{f_{\rm g}} \tag{5.7}$$

as the fraction of gas in the hot phase. Further, if we assume that only the hot phase can be easily swept up in the energy-driven outflow with the cold high-density clumps being left largely intact (e.g. Bourne et al. 2014), we can define the hot gas mass loading factor as

$$f_{\rm L,hot} = \left(\frac{f_{\rm g,hot}}{f_{\rm g}}\right)^{2/3} f_{\rm L} = \eta_{\rm hot}^{2/3} f_{\rm L}. \tag{5.8}$$

Replacing $f_{\rm L}$ with $f_{\rm L,hot}$ in the above analysis provides an analytical expectation that when the ISM is clumpy, with large fractions of the gas content contained in dense cold clumps, mass outflow rates and momentum boosts should be considerably tempered when compared with spherically symmetric calculations that assume a homogeneous gas distribution. It is important to note that there is, however, a degeneracy between $\eta_{\rm hot}$ and $f_{\rm g}$ and it is also likely that $\eta_{\rm hot}$ is a (possibly complicated) function of $f_{\rm g}$, with gas-rich systems likely being more clumpy and hence having smaller values of $\eta_{\rm hot}$. Further, as pointed out in Nayakshin (2014), from the cooling function of Sutherland & Dopita (1993), the hot gas fraction can be given as $\eta_{\rm hot} \sim 2.5 \times 10^{-3}\sigma_{200}^{5/2}R_{\rm kpc}Z^{-0.6}$, where Z is metallicity in solar units and $R_{\rm kpc}$ is the radial position within the host galaxy. As a result, more massive, larger and/or less metal-rich galaxies should have larger hot gas fractions. This also suggests that as outflows move to larger radii, the mass loading and momentum boosts should increase. However, reality is likely different from the simple picture painted here; this analysis assumes an isothermal gas density distribution, which is only an approximation to the true gas distribution in galaxies. On top of this, the outflow itself will impact $\eta_{\rm hot}$ as it propagates, through a combination of ablating and disrupting dense gas clouds and/or compressing gas to high densities as it is swept up. As such, we expect $f_{\rm L}$ to be a complicated function of feedback and galaxy properties.

5.2 Numerical simulations

While analytical models provide physical intuition, they can take us only so far and as such we now turn to numerical simulations. We adopt a similar set-up and methodology to that of simulations previously presented in Bourne et al. (2015), Zubovas et al. (2016) and Zubovas & Maskeliūnas (2023). A modified version of the hydrodynamical code `Gadget-3` (Springel 2005), which incorporates the SPHS (Read et al. 2010; Read & Hayfield 2012) flavour of SPH and the Wendland kernel (Wendland 1995; Dehnen & Aly 2012) is used for the simulations. The code employs adaptive hydrodynamical smoothing and gravitational softening lengths; the neighbour number is $N_{\rm ngb} = 100$. The SPH particle mass is $m_{\rm SPH} = 940$ M$_\odot$.

Since we are interested in understanding how outflow properties are affected by a more realistic gas density distribution, we adopt a two-step approach to making the simulation more realistic. The first step is the creation of turbulent initial conditions. This splits simulations into two groups of that we label `Smth` for smooth and `Turb` for turbulent. The second step is moving from an adiabatic equation of state, as assumed in the analytical calculations, to one with a realistic radiative cooling prescription; this further splits the simulations into adiabatic (labelled `Adia`) and cooling (labelled `Cool`). Below we describe this in more detail.

5.2.1 Initial conditions

In `smooth` simulations, the gas is smoothly distributed in a thick shell between $r_{\rm in} = 0.1$ kpc and $r_{\rm out} = 1$ kpc. The density falls with radius as $\rho \propto r^{-2}$ and the total mass is $M_{\rm gas} = 9.4\times10^8M_\odot$, tracked with $N = 10^6$ SPH particles. We neglect the self-gravity of the gas to avoid spurious fragmentation of dense clumps. The shell is embedded in a static singular isothermal sphere background potential with a 1D velocity dispersion of $\sigma_{\rm b} = 142$ km s^{-1}, corresponding to a background mass $M_{\rm b} = 9.4 \times 10^9$ M$_\odot$. Finally, we fix a SMBH-representing sink of mass $M_{\rm BH} = M_\sigma\left(\sigma_{\rm b}\right) = 10^8$ M$_\odot$ at the centre of the simulation domain. SMBH may swallow particles that fall closer than $r_{\rm acc} = 0.01$ kpc, however, this does not represent physically meaningful accretion in this case and only assures there is no unresolved dense clump at the centre.

In the 'turbulent' simulations, the extent of the gas shell is the same, but it is given a turbulent density distribution. To achieve this, we run a 'development' simulation which is identical to the 'smooth' simulations except for the following differences. The gas shell initially extends between $r_{\rm in,d} = 0.01$ kpc and $r_{\rm out} = 1$ kpc, has a total mass larger by a factor ~ 1.4 and is given a turbulent velocity field. Turbulence is generated using the same method as in Chapter 3, introduced by Dubinski et al. (1995) and Hobbs et al. (2011), which produces a divergence-free turbulent velocity spectrum. The initial characteristic velocity is $\sigma_{\rm t} = \sigma_{\rm b}\,(1 + M_{\rm gas}/M_{\rm b})^{1/2} = 149\ {\rm km\,s^{-1}}$. After 1 Myr, we stop the simulation and remove the gas in the central $r_{\rm in} = 0.1$ kpc. The leftover shell now contains $N \simeq 10^6$ particles within $r_{\rm out} = 1$ kpc that we use as the initial conditions for the 'turbulent' simulations. We repeat this process four times with different random seeds and perform simulations with the four sets of initial conditions. The background potential and BH particle properties in the `development` and `turbulent` simulations are identical to those of the `smooth` simulations.

5.2.2 Gas thermodynamics

In the adiabatic simulations, the initial gas temperature is set to the virial temperature of the background gravitational potential, $T \sim 9.3 \times 10^5$ K; we checked that using a lower initial temperature makes no difference to our results.

In the simulations with radiative cooling, we use a combination of two sub-resolution prescriptions, described in more detail in Section 2.2.1. In brief, below temperatures of 10^4 K, we adopt the function of Mashchenko et al. (2008), which allows gas to cool to 20 K. This cooling function is designed to incorporate the effects of atomic, molecular and dust-mediated cooling in Solar-metallicity gas. This means cooling is particularly efficient; together with the adiabatic simulations, our setup brackets a large range of 'interesting' cooling regimes. Above 10^4 K, we use the prescription of Sazonov et al. (2005), which models the heating and cooling of optically thin gas due to a typical AGN radiation field. We modify this function by neglecting the effect of Compton cooling, a change appropriate for the expected two-temperature plasma nature of the hottest outflowing gas (see Faucher-Giguère & Quataert 2012; Bourne & Nayakshin 2013). The optically thin approximation is unrealistic for the densest clumps, and so our simulations over-predict the heating rate in these regions and hence under-predict the total mass of cold gas. However, in terms of global outflow properties this has a negligible effect (Zubovas & Bourne 2017).

5.2.3 AGN episode and feedback injection

In all simulations, an AGN is turned on at the start and allowed to continue for the duration of the simulation, until the gas is cleared from the central kiloparsec or falls into the SMBH particle. We run simulations with different AGN luminosities, labelled as `L#`, where `#` refers to the luminosity in units of the Eddington luminosity $L_{\rm Edd} = 1.26 \times 10^{46}$ erg s^{-1}. Our fiducial simulations are `L1`, i.e. they have $L_{\rm AGN} = L_{\rm Edd}$, but we also check result dependence on luminosity by running `L0.3` simulations, i.e. with $L_{\rm AGN} = 0.3 L_{\rm Edd}$. We also run four control simulations without an AGN. The AGN affects the gas in two ways: by heating (described in 5.2.2 above) and by producing feedback in the form of a fast wind which we track using a novel grid-based scheme.

The `gridWind` method works by propagating the AGN wind effect on a static grid which allows for a quick coupling with cospatial particles using a spatial hash-like method and a sorted distance matrix. Spatial hashing is used widely outside astronomy (e.g. in collision detection and computer vision; Hastings & Mesit 2005; Teschner et al. 2003; Dong et al. 2021) and was suggested as an effective algorithm for friends-of-friends group finding in astrophysical simulations (Creasey 2018; however, this has been contested by Springel et al. 2021).

We use a modified version of `SREAG` grid with rectangular cells (Malkin 2019)[2]. To construct the grid, we subdivide the sphere's surface into latitudinal strips of a constant $\Delta\theta = \pi / N_{\rm strip}$. Each of these strips is then subdivided into a number rectangular cells $N_\Phi(\theta)$:

$$N_\Phi(\theta) = \left\lfloor \frac{2\pi \cos(b(\theta))}{\Delta\theta} \right\rceil, \text{with} \tag{5.9}$$

$$b(\theta) = \left\lfloor \frac{\theta}{\Delta\theta} \right\rfloor \Delta\theta + \Delta\theta/2 - \pi/2. \tag{5.10}$$

Here $\lfloor x \rfloor$ is the floor function and $\lfloor x \rceil$ denotes rounding to the nearest integer and θ is the central latitude of each strip. Now the longitudinal size of each rectangular cell for a given strip is $\Delta\phi(\theta) = 2\pi / N_\Phi(\theta)$. This results in a deviation of cell area of ± 1 % from the mean except for the two polar strips, where the deviation is about 5 %; this is taken into account when distributing feedback.

We can quickly determine grid indices (n_r, n_θ, n_ϕ) for SPH particles:

$$n_r = \lfloor r_{\rm p} / \Delta r \rfloor, \tag{5.11}$$

$$n_\theta = \lfloor \theta_{\rm p} / \Delta\theta \rfloor, \tag{5.12}$$

$$n_\phi = \lfloor \phi_{\rm p} / \Delta\phi(\theta) \rfloor, \tag{5.13}$$

[2] Another alternative would be to use the established `healpy` (Górski et al. 2005), which we intend to do in the future.

where $r_{\rm p}, \theta_{\rm p}, \phi_{\rm p}$ are SPH particle's spherical coordinates, $\Delta r, \Delta\theta, \Delta\phi$ are the respective grid step sizes. In practice, we derive a more practical set of indices for use in flattened arrays for each shell $n_{\rm shell}$ and the whole spherical volume $n_{\rm sphere}$:

$$n_{\rm shell} = n_{\phi} + \sum_{k=0}^{n_{\theta}} N_{\phi}(\theta), \tag{5.14}$$

$$n_{\rm sphere} = n_{\rm r} N_{\rm shell} + n_{\rm shell}, \tag{5.15}$$

where $N_{\rm shell}$ is the number of cells in each shell. In this work we use $N_{\rm strip} = 64$, which corresponds to $N_{\rm shell} = 5216$.

We use a simple discrete-step approach for wind propagation. We first inject wind into the 0-th shell in proportion to the total energy determined by $L_{\rm AGN}$ and the SMBH timestep weighted by the area of the cell. We assume that AGN wind travels radially outwards at a constant velocity $v_{\rm wind} = 0.1$c (King 2003, 2010b). We couple the SMBH and wind timesteps applying the additional limit, $\Delta t < C\Delta r / v_{\rm wind}$, where $C = 0.4$ is a Courant-type factor, to SMBH particle (i.e. particle accretion) and wind propagation.

Feedback is distributed to SPH particles in proportion to those particles' contribution to the overall density field at the centre of the grid cell. As each SPH particle has spatial extent expressed as the smoothing length h, we use a pre-calculated sorted distance matrix to quickly move over the nearest neighbouring cells. To prevent unnecessary iteration we check that the distance from each cell centre is not greater than h. We found that in practice, the radial extent of each particle over different shells can be safely neglected, greatly improving performance. This is safe as long as only make use of the relative ratio between the particles contribution to and the overall density field. Each wind variable - in our case, energy and momentum - is transferred independently. In the case of momentum injection, if the particle position is outside the cell in question, momentum is injected in the direction of the cell rather than the particle.

5.2.3.1 Momentum-only wind test

To better illustrate the viability of our approach we compare the `gridWind` to the virtual particle method (Nayakshin et al. 2009) previously used in Chapter 4. Here we follow the setup of Nayakshin et al. (2009) - a luminous source is placed at the centre of a unitary periodic box containing isothermal gas of constant density. Feedback is injected into the surrounding medium in the form of outward momentum resulting in an expanding central cavity. By equating the rate of change of momentum of the expanding cavityto the momentum input

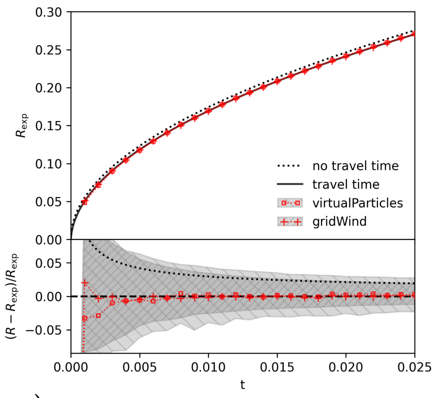

a)

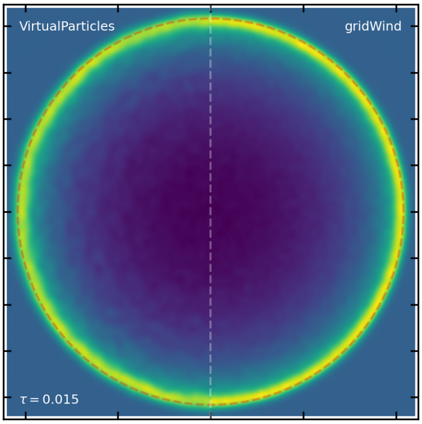

b)

Figure 5.1: a) a sphere expanding into uniform isothermal gas due to momentum injection. Bottom panel shows the deviation from analitical solution, with shaded areas corresponding to the width at half maximum from the density peak. **b)** density maps of the resultant spheres. the red dashed line shows the expected radius.

from the luminous source:

$$\frac{d}{dt}\left[\left(\frac{4}{3}\pi R^3 \rho_0\right)\dot{R}\right] = \frac{L}{c}, \tag{5.16}$$

the radius of the resultant central cavity at a given time $R(t)$ can be estimated:

$$R(t) = \left(\frac{3L}{2\pi c \rho_0}\right)^{1/4} t^{1/2}, \tag{5.17}$$

where L is the luminosity of the central source, c is the speed of light and ρ_0 is the initial density. A more complex estimate takes into account the finite velocity of the wind v and the restoring force due to external pressure.

$$\left[\left(\frac{4}{3}\pi R^3 \rho_0\right)\dot{R}\right] = \frac{L}{c}\left(t - \frac{R}{v}\right) - 4\pi R^2 \rho c_\mathrm{s}^2 t, \tag{5.18}$$

where c_s is the speed of sound. This expression is solved for $R(t)$ numerically. The momentum injection test allows us to check whether our method reproduces the expected evolution of a sphere expanding due to ionizing radiation from a central source. In addition, since the medium is homogeneous, it provides good conditions to understand systematic errors.

For the test we used $N_\mathrm{sph} = 1\times10^6$ particles. For `gridWind` we used $N_\mathrm{strip} = 64$, corresponding to $N_\mathrm{shell} = 5216$ (same as the main set of simulations) and the number of radial shells $N_\mathrm{r} = 200$, with $\Delta r = 0.0025$ which is of the same order as the minimum smoothing length $h = 0.001$. For virtual particles we used reasonably good resolution with $p_\gamma = 0.5$. The key results are shown in Fig. 5.1(a) and Fig. 5.1(b). `gridWind` shows good agreement with expectations, as the density peak follows the expected trajectory outlined by (5.18), except for the initial couple steps, where the front still contains a very small number of particles. Looking at the Fig. 5.1(b) we can see that `gridWind` results in a slightly smoother density distribution. Another advantage of `gridWind` is its computational performance. It finished the simulation ~ 80 times faster; the discrepancy would only increase with better SPH resolution.

5.2.4 List of simulations

A summary of main simulation parameters and salient results is given in table 5.1. The first column gives the simulation name, the next three give the main parameters encoded in the name: the type of gas distribution (smooth or turbulent), presence of radiative cooling (yes or no) and the AGN luminosity. The subsequent columns give the primary results, in the 'turbulent' case averaged over variations in the initial conditions. These are, in order, outflow velocity, mass outflow rate, momentum loading factor and energy loading factor. These values are averaged over the extent of the outflow, with the first (second) value in the last three columns using $\tau_{\rm AGN}$ ($\tau_{r/v}$) when averaging; see eq. (5.24) and text below it for the precise definitions used. All values are evaluated at $t = 0.5$ Myr, when the outflow has already developed but hasn't yet broken out of the initial shell even in the turbulent simulations. The bottom two rows of the table show analytical predictions for the main results, based on equations in Zubovas & King (2012a), using either the velocity of the contact discontinuity (lower) or the outer shock (higher) for calculations. Note that the analytically estimated values are upper limits, since the velocity calculation depends on the assumption that $v_{\rm out} \gg \sigma_{\rm b}$ which allows us to ignore one of the terms in the equation of motion (Zubovas & King 2012a) and the other quantities are calculated using this $v_{\rm out}$ estimate.

5.3 Results

5.3.1 Defining the loading factors

Before focusing on any specific simulation, we describe the process of determining the mass outflow rate $\dot{M}_{\rm out}$, the momentum loading factor $\dot{p}_{\rm out}c/L_{\rm AGN}$ and the energy loading factor $\dot{E}_{\rm out}/L_{\rm AGN}$ as these will be relevant for all subsequent analysis runs. First, the radial profiles are determined by summing up

Run	gas distribution	cooling?	L_{AGN} (erg s^{-1})	v_{out} (km s^{-1})	$\dot{M}_{\mathrm{out}}$ (M$_\odot$ yr^{-1})	$\dot{p}_{\mathrm{out}}c/L_{\mathrm{AGN}}$	$\dot{E}_{\mathrm{k,out}}/L_{\mathrm{AGN}}$ ($\times 10^{-3}$)
SmthAdiaL0.3	smooth	no	3.78×10^{45}	350	642 (348)	11.3 (6.1)	7.64 (4.14)
SmthAdiaL1.0	smooth	no	1.26×10^{46}	582	966 (671)	8.44 (5.86)	9.34 (6.49)
SmthCoolL0.3	smooth	yes	3.78×10^{45}	96.2	229 (166)	1.1 (0.8)	0.20 (0.15)
SmthCoolL1.0	smooth	yes	1.26×10^{46}	304	485 (402)	2.21 (1.83)	1.23 (1.02)
TurbAdiaL0.3	turbulent	no	3.78×10^{45}	312	641 (313)	10 (4.89)	8.70 (4.26)
TurbAdiaL1.0	turbulent	no	1.26×10^{46}	556	1030 (630)	8.64 (5.26)	11.22 (6.83)
TurbCoolL0.3	turbulent	yes	3.78×10^{45}	140	116 (23.3)	0.817 (0.164)	0.78 (0.16)
TurbCoolL1.0	turbulent	yes	1.26×10^{46}	297	710 (309)	3.18 (1.38)	3.38 (1.47)
analytical-L0.3	-	-	3.78×10^{45}	590 – 790	565 – 760	17 – 30	0.016 – 0.04
analytical-L1.0	-	-	1.26×10^{46}	885 – 1180	850 – 1130	11 – 20	0.017 – 0.039

Table 5.1: Summary of simulations, including key results. The first column shows the simulation name, the second - the type of gas distribution used, the third - the presence or absence of radiative cooling, while the fourth shows the AGN luminosity. The subsequent columns show the results: mass-weighted outflow velocity, time-averaged mass outflow rate, momentum and energy loading factors. In the final three columns, the first value is evaluated assuming $\tau = \tau_{\mathrm{AGN}}$, while the one in parentheses assumes $\tau = \tau_{r/v}$. All results evaluated at $t = 0.5$ Myr (see text for reasoning). Two rows at the bottom show the analytical predictions for the main results, based on Zubovas & King (2012a). The lower velocity is that of the contact discontinuity, while the higher corresponds to the outer shock; other parameter ranges correspond to these two velocities.

relevant particle properties over thin shells:

$$\dot{M}_{\rm out}(r)\Delta r = \sum_i m_i v_{{\rm rad},i}, \tag{5.19}$$

$$\dot{p}_{\rm out}(r)\Delta r = \sum_i m_i v_{{\rm rad},i}^2, \tag{5.20}$$

and

$$\dot{E}_{\rm k,out}(r)\Delta r = \sum_i \frac{1}{2} m_i v_{{\rm rad},i}^3, \tag{5.21}$$

where m_i and $v_{{\rm rad},i}$ are the mass and radial velocity of the ith particle, and the sum is performed over all outflowing particles in the radial bin between r and $r+\Delta r$; we use $\Delta r = 0.005$ kpc throughout, but the results are insensitive to the precise value as long as $\Delta r \ll 0.1$ kpc. We consider a particle to be outflowing if $v_{\rm rad,i} > 10$ km s^{-1}; the slightly above zero value is chosen to exclude just nominally outflowing particles, whose outwards velocity is due to stochastic scatter. This has little effect on the final result in practice. A more substantial correction requires us to calculate the radial profiles for each corresponding control ($L_{\rm AGN} = 0$) simulation. The final result, free of spurious gas motions, is then obtained by subtracting the values of the control simulation; in practice, this is only relevant for the `turbulent` simulations where gas turbulence results in spurious outflowing motions.

The total momentum of the outflow can then be calculated by integrating over radius, which in practice is done by summing over each shell r_i

$$p_{\rm out} = \int_r \dot{M}_{\rm out}\left(r\right) {\rm d}r \approx \sum_i \dot{M}_{{\rm out},i}\left(r\right) \Delta r, \tag{5.22}$$

and the same is done when calculating the total energy:

$$E_{\rm out} \approx \frac{1}{2} \sum_r \dot{p}_{\rm out}\left(r\right) \Delta r \approx \sum_i \dot{p}_{{\rm out},i}\left(r\right) \Delta r, . \tag{5.23}$$

We also define the global radially- and time-averaged values of outflow properties. The mass flow rate is given by

$$\dot{M}_{\rm out,ave} = \frac{M_{\rm out,corr}}{\tau_{\rm out}} = \frac{M_{\rm out} - M_{\rm out,L0}}{\tau_{\rm out}}, \tag{5.24}$$

where $M_{\rm out,corr}$ is the total outflowing mass corrected for spurious motions by subtracting its value in the corresponding control simulation and $\tau_{\rm out}$ is the age of the outflow. Importantly, the timescale $\tau_{\rm out}$ can be based on:

- **Simulation**: $\tau_{\rm out} = \tau_{\rm AGN} = t$, i.e. we use the real age of the outflow which is equal to the time since the start of the simulation.

- **Observation**: $\tau_{\rm out}$ is set the is defined using a common observational estimate for the flow time $\tau_{\rm out} = \tau_{r/v} = R_{\rm out}/v_{\rm out}$, where $R_{\rm out}$ and $v_{\rm out}$ are the radial extent and velocity of the outflow.

This distinction is important to consider, as observers do not have direct knowledge about the lifetime of the outflow. The exact values used for $R_{\rm out}$ and $v_{\rm out}$ can vary between studies and depend upon what assumptions are made about the outflow properties. Such ideas have already been discussed extensively in the literature (see, e.g., Rupke et al. 2005; Cicone et al. 2014; Veilleux et al. 2017), including the addition of numerical factors to take the outflow geometry into account (e.g. Maiolino et al. 2012) and the decomposition of the outflow into individual 'clumps' (e.g. Cicone et al. 2015; Bischetti et al. 2019). For the simple homogeneous case in which all gas is swept into a shell, $R_{\rm out}$ and $v_{\rm out}$ could simply be set to the shell radius and velocity. However, here we have two factors to consider: firstly, in the 'turbulent' simulations we do not have a simple, single-velocity thin-shell outflow, and secondly, our ISM shell has an initial inner cavity with $r_{\rm in} = 100$ pc. Therefore, we set $R_{\rm out} = \overline{r}_{\rm out} - r_{\rm in}$ and $v_{\rm out} = \overline{v}_{\rm out}$, which are the mass-weighted average outflow radius (corrected for the shell inner edge) and radial velocity, respectively. Finally, the averaged momentum and energy rates are then calculated as

$$\dot{p}_{\rm out,ave} = \dot{M}_{\rm out,ave}\overline{v}_{\rm out} \tag{5.25}$$

$$\dot{E}_{\rm out,ave} = \frac{1}{2}\dot{M}_{\rm out,ave}\overline{v^2}_{\rm out}, \tag{5.26}$$

respectively, where $\overline{v^2}$ is the mass-weighted average squared radial velocity.

5.3.2 Gas morphology and outflow rates

We start by describing the morphology and loading factors of each set of simulations in turn in Sections 5.3.2.1–5.3.2.4. The representative evolution of a run from each set is also shown in density map slices (Fig. 5.2). The specific differences in stochastically varied turbulent runs do not impact the general trend much. The evolution of the outflow properties is described in Section 5.3.2.5 and we finish this section by considering the 'average' outflow properties and the aggregate effect of cooling in Section 5.3.2.6.

5.3.2.1 Smooth adiabatic simulations

The evolution of `SmthAdiaL1.0` is shown in Fig. 5.2(a). As expected, the outflow expands spherically symmetrically, with minor variations only due to finite particle number. The peak density, which corresponds approximately to the contact discontinuity, quickly reaches a velocity $v_{\rm c.d.} \simeq 700$ km s^{-1}, while the outer edge expands with a velocity $v_{\rm out} \simeq 900$ km s^{-1}. These values

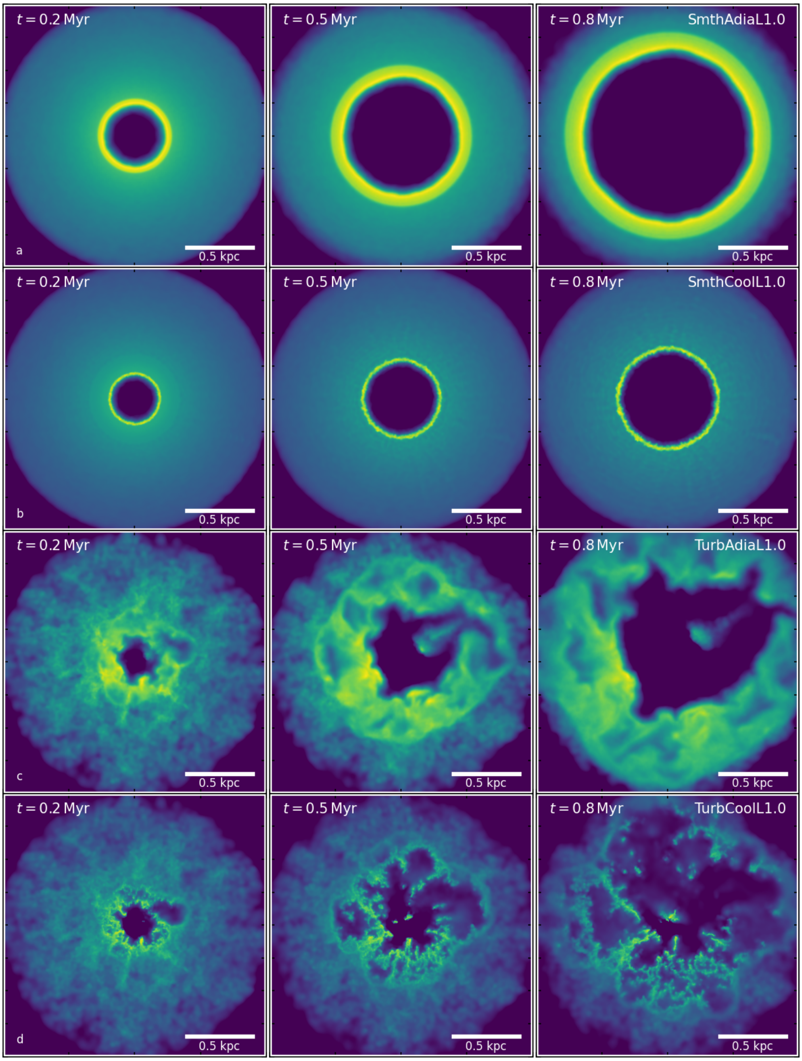

Figure 5.2: Gas density integrated through a 0.1 kpc thick slice in (from top to bottom) `SmthAdiaL1.0` (a), `SmthCoolL1.0` (b), `TurbAdiaL1.0` (c) and `TurbCoolL1.0` (d). The three panels show, from left to right, $t = 0.2$ Myr, $t = 0.5$ Myr and $t = 0.8$ Myr; brighter colours represent higher gas density.

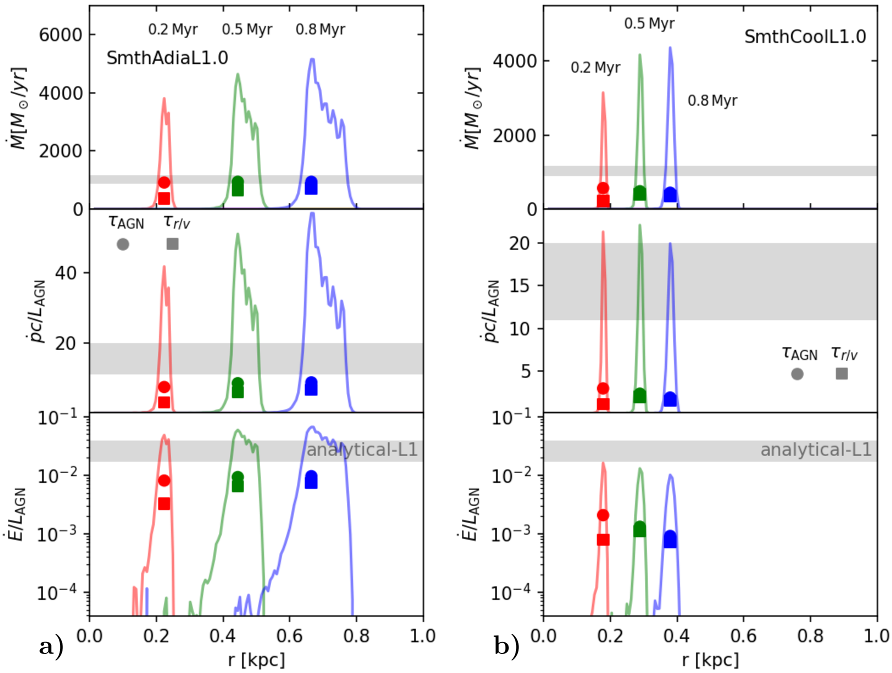

Figure 5.3: **a)** radial profiles of mass outflow rate (top), momentum loading factor (middle) and energy loading factor (bottom) in simulations `SmthAdiaL1.0` (solid lines and dark points) and `SmthAdiaL0.3` (dashed lines and faint points) at $t = 0.2$ Myr (red), $t = 0.5$ Myr (green) and $t = 0.8$ Myr (blue). Lines show the radial profiles calculated using equations 4.4, 4.5 and 4.6, the latter two converted into loading factors. Points show the globally averaged values calculated using τ_{AGN} (circles) and $\tau_{r/v}$ (squares). Grey shaded areas show the range of analytical estimates. **b)** same but for the SmthCoolL1.0 simulation.

are lower than the analytical estimate by $\sim 20\%$. Two effects account for this discrepancy; the first one relates to the applicability of the analytical description, while the second arises because of the numerical method used. First, the analytical estimate, as mentioned, is an upper limit; a more detailed integration of the equation of motion, relaxing the assumption that only the outflow velocity is relevant, gives a value several percent lower, pushing the estimate closer. A larger effect is due to how we are modelling feedback itself. The simulation does not treat the AGN wind hydrodynamically. That is, the wind only directly injects momentum, which is directed outwards, and energy, which is not directed. As the gas moves outwards, the cavity left behind does not provide pressure support, so the outflow cavity is filled by backflow from the shocked gas. This further reduces the energy available to push it outward. We found the total thermal energy of the gas contained in this hot bubble is

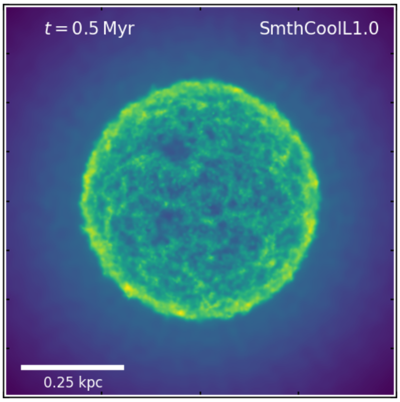

Figure 5.4: Gas density integrated throughout the simulation volume in simulation `SmthCoolL1.0` at $t = 0.5$ Myr.

$\sim 50\%$ of the total injected energy; reducing the energy injection by a factor of two in the analytical calculation brings the velocity estimate into agreement with the simulated one. Interestingly, the mass-weighted velocity, given in table 5.1, is even lower, $\overline{v}_{\rm out} = 582$ km s^{-1}.This happens because the velocity of the density peak is the highest that the gas reaches, while the velocity of the outer edge is the shockwave velocity which does not correspond to real particle motion. Instead, there are particles getting accelerated toward $v_{\rm c.d.}$ but still having lower velocities, and they bring the average velocity down.

Fig. 5.3(a) shows the radial profiles of mass outflow rate (top) and momentum and energy loading factors (middle and bottom, respectively) in the `SmthAdiaL1.0` simulation at three times: $t = 0.2$ Myr (red), $t = 0.5$ Myr (green) and $t = 0.8$ Myr (blue). These correspond to the times shown in Fig. 5.2. Each radial profile shows a single strong peak with a width increasing with time, from ~ 50 pc at $t = 0.2$ Myr to almost 200 pc at $t = 0.8$ Myr; again, this is expected and can be intuited from the density map The peaks are significantly higher than the analytical estimates, however we must keep in mind that they represent values estimated in very narrow radial shells. The globally averaged values, shown by individual circles (for estimates using $\tau_{\rm AGN}$) and squares (for estimates using $\tau_{r/v}$), essentially agree with the analytical estimates, when accounting for the lower outflow velocity. The trend of values estimated using $\tau_{r/v}$ being lower than those estimated using the real outflow age is present throughout all simulations, as shown below (Section 5.3.2.5); we discuss the implications of this in Section 5.4.2.

Outflow expansion in the `SmthAdiaL0.3` simulation is qualitatively identical to that of `SmthAdiaL1.0`. Again, the velocity is lower than the analytical estimate ($\overline{v}_{\rm out} = 350$ km s^{-1}, $v_{\rm c.d.} \simeq 400$ km s^{-1}), for the same reasons as presented above.

5.3.2.2 Smooth cooling simulations

The main feature distinguishing Cooling from Adiabatic simulations is the extent to which cooling allows matter to clump up, which is illustrated clearly when we integrate the density throughout the simulation volume, as shown in Fig. 5.4.

In Fig. 5.2(b) we show the density distribution of the outflow in simulation `SmthCoolL1.0` as it evolves. Comparing these plots with the same for `SmthAdiaL1.0`, we can immediately see that the cooling outflow expands more slowly, with an average velocity ~ 300 km s^{-1}, and that the expanding region is confined to a narrower, < 50 pc thick, shell. The first difference occurs because the gas in the diffuse outflow cavity cools down and provides less push to the outflowing gas. The second difference occurs because the outflowing gas itself cools down and is compressed into a thinner shell by its own motion. That is, the pressure support is less efficient at keeping this region from compressing. This compressed shell also starts to fragment; this can be seen more clearly when we integrate the density throughout the simulation volume, as shown in Fig. 5.4. Unlike in similar simulations performed in Nayakshin (2014), the density variations across the shell are not very large: the ratio between top 5% and bottom 5% of density values does not exceed 100. This difference is due to the lack of self-gravity in our setup. Note also, that the density contrast was not large enough to produce anisotropic outflows, as those seen in the simulations with additional clumps due to turbulence.

The overall weaker state of the outflow is even more evident when looking at the radial profiles (Fig. 5.3(b)). All three integrated parameters have lower values than in the adiabatic simulation. Although the peak values of $\dot{M}$ are only slightly lower, the globally integrated values are about twice smaller than those in the adiabatic simulation. This happens because, as mentioned above, the outflow shell is much thinner than in the adiabatic simulation. As a result, even though the instantaneous mass flow rate through a given surface is large, the value integrated over the thickness of the shell is lower. The difference is starker for the other parameters and at later times: momentum loading is ~ 3.5 times lower at $t = 0.5$ Myr, while energy loading is ~ 8 times lower.

Outflow expansion in simulation `SmthCoolL0.3` proceeds along the same lines as in `SmthCoolL1.0`. The velocity is $\sim$ 3 times lower than in `SmthCoolL1.0`, in contrast to the ~ 1.5 ratio between velocities in the two adiabatic simulations. This happens because at a lower initial velocity, gas in the outflow is heated to lower temperatures where cooling is more efficient. As a result, the fractional loss of energy in this simulation is greater than in the `SmthCoolL1.0`. The momentum loading factor is actually below unity, so such an outflow, if observed, would be interpreted as being driven by only the AGN wind momentum.

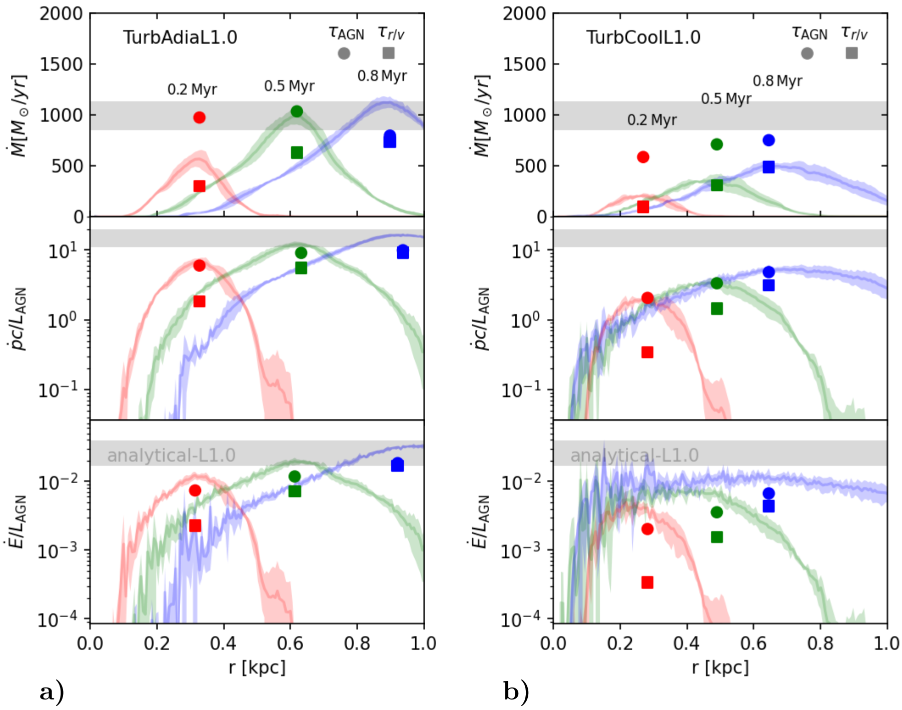

Figure 5.5: **a)** same as Figure 5.3(a) but for the `TurbAdiaL1.0` simulation. Shaded areas show standard deviation from a sample of four simulations differing only by the random seed used to generate turbulence. **b)** same but for `TurbCoolL1.0` simulation.

5.3.2.3 Turbulent adiabatic simulations

Turning now to the turbulent adiabatic simulations, we show the evolution of the density distribution in Fig. 5.2(c). While we can clearly see an expanding outflow, its shape is much more irregular, with different densities along the edge anti-correlated with outflow distance from the AGN. By $t = 0.5$ Myr, the outflow reaches the edge of the initial gas distribution at one point; later on, this becomes the site of a champagne outflow extending to very large distances. Radial profiles (Fig. 5.5(a)) echo the same result: we no longer see a clear sharp peak, but a very widely distributed outflow region. In these plots, the shaded area around each line represents the standard deviation from the mean of the results in four simulations, identical except for a different random seed used to generate the turbulent velocity field (see Section 5.2.1). The position of maximum mass outflow rate (and, similarly, the maximum momentum and energy loading factors) moves with higher velocity than in the smooth simulations, extending out to almost ~ 0.9 kpc by ~ 0.8 Myr, giving a radial velocity of

~ 1000 km s^{-1}. However, the large amounts of dense gas behind the peak reduce the average velocity to essentially the same as in the smooth simulation. Qualitatively, the same results are visible at other times and in both `L1` and `L0.3` simulations.

Simulation `TurbAdiaL0.3` evolves essentially in the same way as `TurbAdiaL1.0`, except the blowout phase starts around $t = 0.8$ Myr. The radial profiles are also very similar, and the integrated quantities show basically the same evolution as the higher-luminosity run, with loading factors being very similar to those in the corresponding `smooth` simulation.

5.3.2.4 Turbulent cooling simulations

Finally, we arrive at the `TurbCoolL1.0` simulation which has both a turbulent density distribution and gas cooling. Globally, the shape of the outflow (Fig. 5.2(d)) is similar to that of the `TurbAdiaL1.0` simulation, but the cooling outflow has much finer features and higher density contrasts, exceeding four orders of magnitude at distances $0.2 - 0.4$ kpc, compared to a ratio of ~ 50 outside the outflow. Multiple outflowing lobes are visible, separated by dense gas filaments. The average velocity is approximately twice lower than in the `TurbAdiaL1.0` simulation, but slightly higher than in `SmthCoolL1.0`. This happens because the diffuse gas can be pushed away very efficiently, creating a tail of particles with very high radial velocities $\left(v > 1000\,\mathrm{km\,s^{-1}}\right)$ while a significant fraction of cold gas is kept from collapsing to the centre very rapidly. The radial distributions of $\dot{M}_{\rm out}$ and loading factors (Fig. 5.5(b)) emphasize this: outflowing material is distributed in a very broad shell, ranging from ~ 0.25 kpc to > 1 kpc at $t = 0.8$ Myr, for example. The values of mass flow rate and momentum loading have visible peaks, while the energy loading factor is distributed almost uniformly with radius. The averaged values are a factor $\sim 1.5 - 3$ lower than analytical estimates.

In simulation `TurbCoolL0.3`, the features of the `TurbCoolL1.0` are even more pronounced. Density ratios are higher, velocity lower, and the radial distribution of the three parameters almost uniform between the AGN and the outer edge of the outflow. Curiously, this means that the mass flow rate and momentum loading factor in the `TurbCoolL0.3` simulation are lower than in the `SmthCoolL0.3`, reversing the trend seen when comparing other `smooth` and `turbulent` analogues.

5.3.2.5 Time evolution of average outflow properties

Now that we described each simulation set in detail, we turn to the evolution of average outflow properties. In the `SmthAdiaL1.0` simulations, the $\tau_{\rm AGN}$-evaluations tend to settle to approximately constant values by $t = 0.2$ Myr (Fig. 5.6(a), teal lines); evaluations using $\tau_{r/v}$ follow the same trend just take

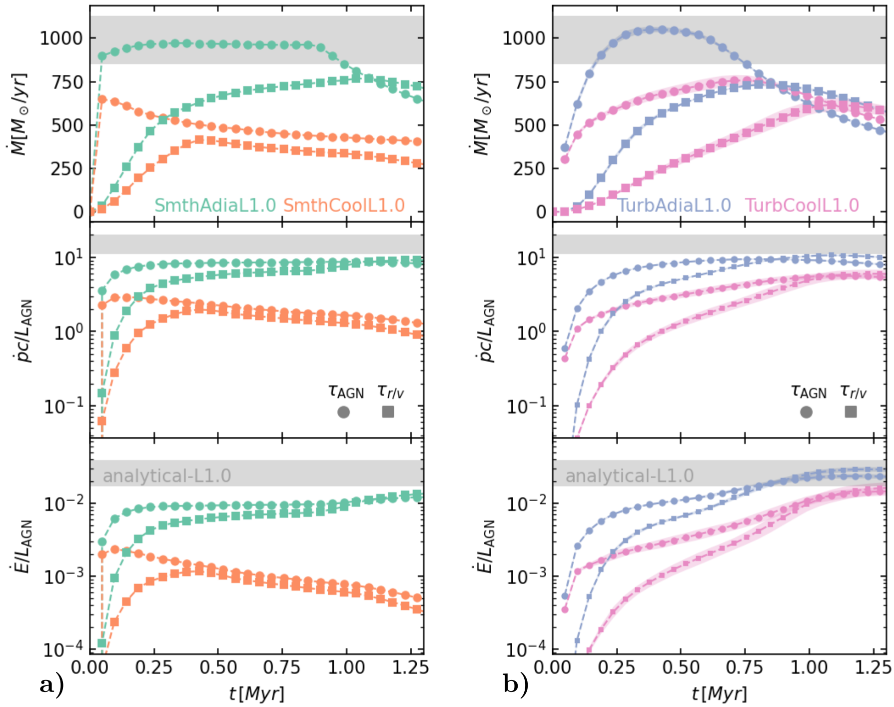

Figure 5.6: a) evolution of the averaged mass outflow rate (top), momentum (middle) and energy loading factors (bottom) in the `smooth L1.0` simulations with time. Teal and orange lines show estimates of the adiabatic and cooling simulations, respectively. Circles show estimates using $\tau_{\rm AGN}$, squares - using $\tau_{r/v}$. **b)** same , but for the `turbulent` simulations. Violet colour now reflects the adiabatic simulation, while magenta shows the cooling one.

longer ($0.3 - 0.4$ Myr) to reach the plateau. Once the outflow clears the initial gas shell, the mass outflow rate begins to decrease roughly as t^{-1}, because the total outflowing mass remains the same, while $\tau_{\rm AGN}$ keeps increasing. Due to a corresponding increase in outflow velocity, the momentum loading factor hardly changes and energy loading increases somewhat as they are proportional to higher powers of velocity respectively ((4.4)-(4.6)). This happens because there is less work is needed to inflate the gas, so a larger fraction of the input energy is retained as kinetic energy of the outflow. In the SmthCoolL1.0 simulations (orange lines), all parameters continuously decrease as ever more energy is radiated away.

In the `TurbAdiaL1.0` simulations (Fig. 5.6(b), violet lines), the $\tau_{\rm AGN}$-evaluated mass outflow rate reaches a peak at $t \sim 0.3 - 0.5$ Myr and begins to decrease as soon as the outflow reaches the edge of the initial shell, eventually settling on the same t^{-1} trend. The momentum loading factor stays essentially constant, while the energy loading increases as the outflow clears the shell, as in the 'smooth' simulations. The $\tau_{r/v}$-evaluated values evolve with a delay, much like their 'smooth' counterparts, and are still growing by $t \sim 0.7$ Myr. At this late stage, the velocity increases significantly as ever more of the outflow begins expanding into vacuum. This leads to the $\tau_{r/v}$-estimated values overtaking the $\tau_{\rm AGN}$-estimated ones at $t \simeq 0.8$ Myr and to the energy loading factor increasing significantly. Interestingly, the averaged values[3] of all parameters are in remarkable agreement between the smooth and turbulent adiabatic simulations. At late times, when parts of the outflow expand beyond $R_{\rm out}$, the average velocity begins increasing, while mass and momentum rates start to decrease and energy rate stays flat (see also Section 5.3.2.5 below). This, however, is an artifact of the initial conditions. It is also important to note, that when we no longer have a single uniform central cavity, the energy loss due to backflow could be somewhat reduces as expanding hot gas has something to push against. The slight increase in energy loading seems to confirm this.

The `TurbCoolL1.0` simulation evolution (Fig. 5.6(b), magenta lines) is remarkably different from the corresponding `smooth` simulation. Despite energy being radiated away, all parameters keep increasing with time up to ~ 0.75 (1) Myr for the $\tau_{\rm AGN}$ ($\tau_{r/v}$) evaluation. At later times, as the outflow escapes the initial shell, mass outflow rates begin to decrease, but momentum loading stays approximately constant, while energy loading keeps increasing. This happens because outflowing gas has a broad temperature distribution, meaning that cold gas contributes to significant mass outflow rate, the energy rate (and energy loading factor) is completely dominated by the hot gas, which cools inefficiently. We describe this in more detail in Section 5.3.3 below.

5.3.2.6 Global effect of turbulence and cooling

For ease of comparison, at a glance, of the effects of cooling, turbulence and both combined on the outflow properties, we plot the average values of the relevant parameters at $t = 0.5$ Myr in Figure 5.7. As in earlier plots, circles show values obtained using $\tau_{\rm AGN}$, while squares show those obtained using $\tau_{r/v}$. As noted above, there is virtually no difference between the `SmthAdiaL1.0` and `TurbAdiaL1.0` simulations or between the `SmthAdiaL0.3` and `TurbAdiaL0.3` ones, i.e. the addition of turbulence has no detrimental effect on the coupling efficiency of AGN wind momentum and energy to the surrounding ISM. Even though the energy is distributed in a much wider shell in the turbulent simulations, the total injected energy remains the same. In fact, turbulence increases the kinetic energy slightly, because there is more diffuse high-velocity gas in those simulations.

[3]These values are the same in simulations with different turbulence seeds, despite the considerable range covered by the shaded areas.

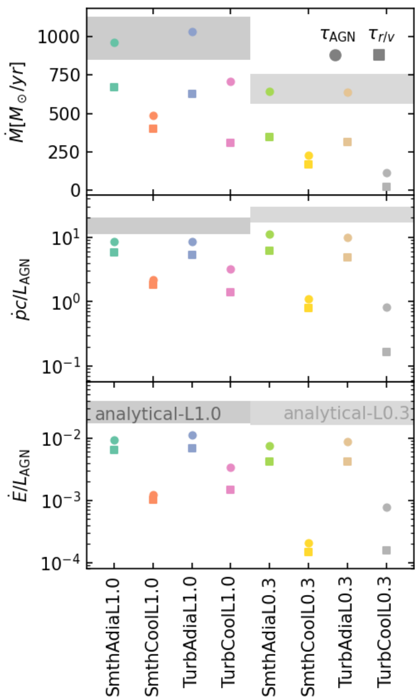

Figure 5.7: Values of mass outflow rate (top), momentum (middle) and energy loading factors (bottom) in all four `L1` and `L0.3` simulations at $t = 0.5$ Myr. Grey area is the analytical prediction.

When we compare the results of simulations with cooling, a curious pattern emerges: the `TurbCoolL1.0` simulation has significantly higher $\tau_{\rm AGN}$-evaluated values of all parameters than `SmthCoolL1.0`. Cooling in the smooth simulation is particularly effective because all of the outflowing material is compressed into a thin and dense shell, while in the turbulent simulations, a lot of the outflowing material remains diffuse and so cools inefficiently. However, in the `L0.3` simulations, the trend is reversed for mass and momentum outflow rates: the addition of turbulence leads to a decrease because lower AGN luminosity leads to less hot gas being produced and cooling is overall more efficient. In other words, AGN luminosity is insufficient to heat gas to temperatures where cooling becomes inefficient even in the diffuse gas.

Overall, the combined effect of turbulence and cooling, when compared with the smooth adiabatic setup, results in a reduction of the mass outflow rate by $\sim 25\%$ ($\sim 80\%$), the momentum loading factor by $\sim 60\%$ ($\sim 93\%$) and the energy loading factor by $\sim 63\%$ ($\sim 90\%$) in the `L1` (`L0.3`) simulations at $t = 0.5$ Myr. The difference in temporal evolution means that the reduction is greater at earlier times but becomes less significant as the outflow evolves.

Run	phase	temperature range	v_{out} $(\mathrm{km\ s^{-1}})$	$\dot{M}_{\mathrm{out}}$ $(\mathrm{M_\odot\ yr^{-1}})$	$\dot{p}_{\mathrm{out}}c/L_{\mathrm{AGN}}$	$\dot{E}_{\mathrm{k,out}}/L_{\mathrm{AGN}}$ $(\times 10^{-3})$	f_{esc} %
TurbCoolL0.3	cold	$< 3 \times 10^4$ K	91.4	92 (11.1)	0.42 (0.05)	0.13 (0.02)	0.0012
TurbCoolL0.3	intermediate	3×10^4 K - 10^7 K	221	9.2 (4.9)	0.1 (0.05)	0.06 (0.03)	0.54
TurbCoolL0.3	hot	$> 10^7$ K	603	15 (33)	0.45 (0.99)	0.95 (2.1)	21
TurbCoolL1.0	cold	$< 3 \times 10^4$ K	209	495 (160)	1.55 (0.50)	0.83 (0.27)	0.19
TurbCoolL1.0	intermediate	3×10^4 K - 10^7 K	316	93 (35)	0.44 (0.16)	0.33 (0.12)	3.4
TurbCoolL1.0	hot	$> 10^7$ K	691	122 (114)	1.27 (1.19)	2.42 (2.26)	34

Table 5.2: Properties of multiphase gas in the `turbulent` simulations with cooling. The first column shows the simulation name, the second and third give the name and temperature range of the gas phase. The subsequent columns show the results: mass-weighted outflow velocity, time-averaged mass outflow rate, momentum and energy loading factors, fraction of gas reaching escape velocity (eq. (5.27)). All numbers estimated as in table 5.1.

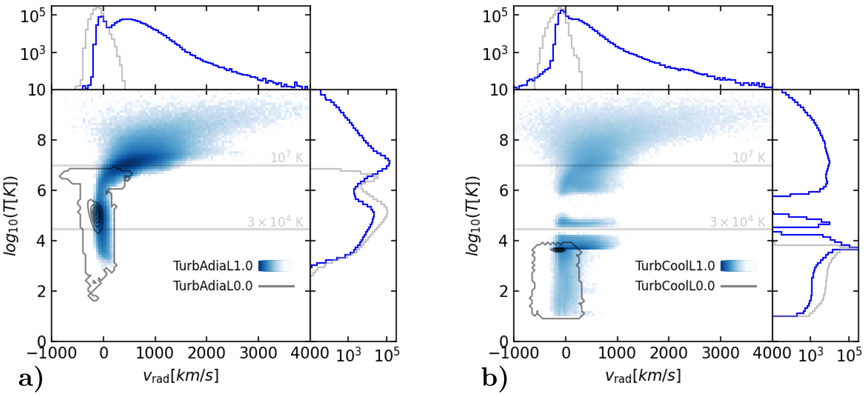

Figure 5.8: a) two-dimensional histograms of gas temperature (vertical axis) against radial velocity (horizontal axis) for `TurbAdiaL1.0` simulation. Grey contours show corresponding control simulation data. Grey horizontal lines show the criteria for labelling gas as *cold*, *intermediate* or *hot* . **b)** same, but for `TurbCoolL1.0` simulation.

5.3.3 Gas phase distribution

To better understand how AGN feedback couples with the gas and to connect our findings to observations of multiphase outflows, we separately examine the key outflow properties of cold, warm, and hot gas phases. Our focus is primarily on the results from the `turbulent` simulations with cooling, with occasional comparisons to other simulations when relevant. The key results are summarised in table 5.2.

In Fig. 5.8, we show two-dimensional histograms of gas temperature and radial velocity in the four `turbulent` simulations: `TurbAdiaL1.0` ((a), blue points and lines), `TurbCoolL1.0` (b) and their corresponding control simulations (grey contours and lines). Gas with temperatures below 10^4 K exists essentially only in the cooling simulations; we choose a significant drop in particle numbers at $T = 3 \times 10^4$ K in the `TurbCoolL1.0` simulation to delineate cold gas. Gas with temperatures above 10^7 K exists only in simulations with an AGN; it represents significantly shock-heated gas and we use this temperature to distinguish hot gas. We show these limits with grey horizontal lines in the histograms.

We plot the mass outflow rates, momentum and energy loading factors of gas of the three phases in the `TurbCoolL1.0` simulation at $t = 0.5$ Myr in Fig. 5.9 and give the averaged values in table 5.2. The cold gas dominates the mass outflow rate at distances $0.2 - 0.6$ kpc from the nucleus, while hot gas becomes dominant further out. The mass budget is also dominated by cold gas, which comprises $\sim 70\%$ of the total, followed by hot gas at $\sim 20\%$. As

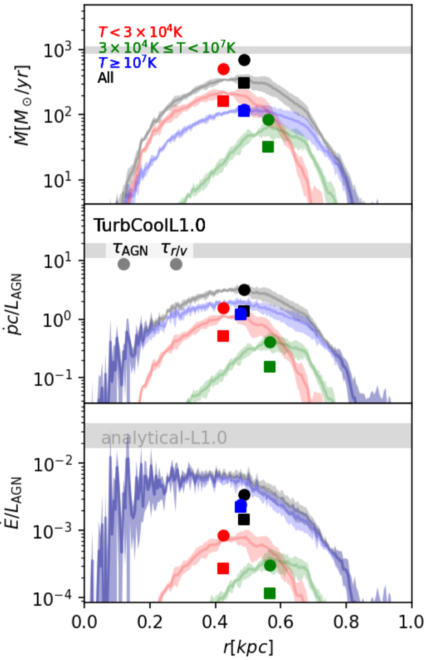

Figure 5.9: Radial profiles of mass outflow rate (top), momentum (middle) and energy loading factors (bottom) of cold (red lines and points), warm (green) and hot (blue) gas in simulation TurbCoolL1.0 at t = 0.5 Myr. The total values are shown in black.

expected, hot gas becomes more important when one considers momentum and especially energy loading: the momentum loading factors of hot and cold gas are comparable, while the energy loading factor of the hot gas is several times higher than that of the cold.

The radial velocities of gas of different phases show remarkable differences. In the adiabatic simulation, cold gas has a narrow velocity distribution peaking around zero, with maximum velocities $v_{\mathrm{c,max}} \simeq \pm 2\sigma_{\mathrm{b}}$. This represents gas that the outflow hasn't reached yet. Gas above 10^6 K shows increased radial velocities, but warm gas has maximum velocities ~ 1500 km s^{-1}. Hot gas contains material that has escaped from the initial gas shell and so moves with the highest velocities exceeding even 4000 km s^{-1}. In the TurbCoolL1.0 simulation, there is cold outflowing gas as well, but its velocity does not exceed 1000 km s^{-1}; the same is true for the warm gas. Conversely, the hot gas still has very high radial velocities. It is interesting to compare gas velocities with the escape velocity from the simulated galaxy; for a singular isothermal sphere, the escape velocity to infinity isn't well defined; instead, we choose $r_{\mathrm{esc}} = 100$ kpc as a proxy. Then the escape velocity becomes

$$v_{\mathrm{esc}} = 2\sigma_{\mathrm{b}} \left(1 + \ln\left(r_{\mathrm{esc}}/r\right)\right)^{1/2}, \tag{5.27}$$

where r is the current radial coordinate of the particle. For initial distances

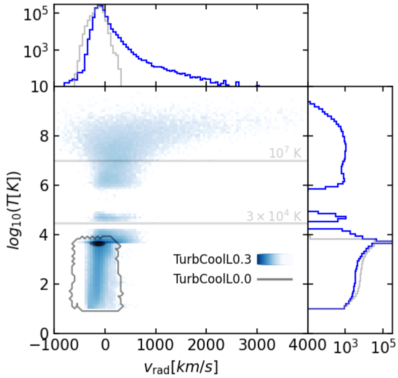

Figure 5.10: Same as Fig. 5.8, but for the `TurbCoolL0.3` simulation.

$0.1 < r < 1$ kpc from the nucleus, the escape velocity range is $4.7\sigma_{\rm b} < v_{\rm esc} < 5.6\sigma_{\rm b}$ or 667 km s$^{-1} < v_{\rm esc} <$ 795 km s^{-1}. The fraction of all gas that exceeds this velocity at 0.5 Myr is 3.6%; this number increases to 12% by 0.8 Myr. However, the fraction of escaping cold gas is only 0.19%, increasing to 0.77%. This is consistent with observational results showing that only a small fraction of outflowing material has enough kinetic energy to escape the host galaxy (Fluetsch et al. 2019). On the other hand, more than 1/3 of hot gas is escaping at 0.5 Myr, increasing to half by 0.8 Myr, reinforcing the point that most of the injected AGN energy is carried away by the hot phase.

The distribution of gas temperatures and velocities in the `TurbCoolL0.3` simulation is qualitatively very similar to that in `TurbCoolL1.0` (Fig. 5.10). There is less hot gas, but it still dominates the energy budget. The mean velocities, especially of the cold component, are lower. However, when we look at the velocities required to escape the galaxy, the picture is very different. Only 0.28% of gas is escaping at $t = 0.5$ Myr, 10 times less than in the higher-luminosity simulation; this number stays essentially the same at 0.8 Myr, suggesting that further energy input is not enough to unbind any more of the gas. When we consider only the cold gas, the escaping fraction is 1.2×10^{-5}, two orders of magnitude lower than in TurbCoolL1.0; by 0.8 Myr, it has increased to 1.1×10^{-4}, still a factor ~ 70 lower than in the higher luminosity run. The fraction of escaping warm gas also increases by almost an order of magnitude, from 0.54% to 4.7%, while the fraction of hot gas increases only a little, from 21% to 27%. This trend of increasing escaping gas fraction with luminosity suggests that there is a threshold, probably around $L = L_{\rm Edd}$, where even cold gas can be efficiently pushed away by an outflow. Such behaviour agrees with previous simulations (Zubovas & Nayakshin 2014) and represents a way to establish the $M - \sigma$ relation in the absence of efficient cooling of the shocked AGN wind (Faucher-Giguère & Quataert 2012).

5.4 Discussion

5.4.1 Comparison with real outflows

In our `turbulent` simulations with cooling, the cold gas phase dominates the mass budget, comprising 80% (70%) of the mass outflow rate in the `L0.3` (`L1`) simulation. The momentum loading factors of cold gas are comparable to those of the hot, while the energy loading is dominated by the hot component (see table 5.2). Furthermore, the hot phase moves with 3-6 times higher velocity and so extends further out - the average radius is $\sim 15\%$ higher at $t = 0.5$ Myr (Fig. 5.9). Looking at the compilations of outflow data from Fiore et al. (2017), Fluetsch et al. (2019) and Lutz et al. (2020), we see that our results qualitatively agree with real outflow parameters. Quantitatively, some discrepancies are present. Real ionized outflows typically have higher velocities, $\overline{v}_{\rm ion} \sim 1100$ km s^{-1}, and so do molecular ones, $\overline{v}_{\rm mol} \sim 450$ km s^{-1}. Both velocities correlate with AGN luminosity; at $L_{\rm AGN} \sim (0.3 - 1) \times 10^{46}$ erg s^{-1}, the mean ionized outflow velocity is the same, while that of molecular outflows is even higher, at ~ 650 km s^{-1}. Molecular outflows are observed to have on average higher mass outflow rates at $L_{\rm AGN} \sim 10^{46}$ erg s^{-1} and momentum loading factors, while the energy loading factors are comparable between the two phases. On the other hand, in the few objects where several outflow phases have been detected simultaneously, the molecular phase is dominant both in terms of mass and energy (Fluetsch et al. 2021). Finally, ionized outflows tend to be observed at higher distances of several kpc, while molecular gas is more commonly found in the central kiloparsec, even at $L_{\rm AGN} \sim 10^{46}$ erg s^{-1}. So our simulations are underestimating all outflow velocities, but the cold gas velocity is underestimated more; simultaneously, the radial extent of the hot outflow component is underestimated while its mass content is (slightly) overestimated. The reason for the discrepancy of the hot component properties may be the lack of hydrodynamic AGN wind. Because of this, the hot gas phase in our simulations extends inward to the AGN, filling the region that, in reality, is taken up by the shocked wind. On the other hand, this effect is significantly harder to quantify, and likely somewhat weaker, in turbulent runs. Furthermore, we do not model the halo gas, which is comparatively very diffuse and would contribute to the hot phase of the outflow. The lack of rapidly moving cold gas may be a consequence of our assumption that the gas is optically thin and the neglect of gas self-gravity. This makes cooling less efficient and precludes the precipitation of cold dense clumps from outflowing hot gas (Nayakshin & Zubovas 2012; Zubovas et al. 2013).

Our simulated outflow properties generally have rather clear dependence on AGN luminosity. In particular, mean outflow velocities in `L1.0` simulations are 1.6-2 times higher than in `L0.3`, except for the `SmthCool` simulations, where the ratio is 3.16. The mass outflow rates also differ by a factor 1.5-2.1, except for `TurbCool`, where the ratio is an exceptional 6.1. This can be compared with the analytical expectation $v_{\rm out} \propto L_{\rm AGN}^{1/3}$, which gives $v_{\rm L1.0}/v_{\rm L0.3} \simeq 1.5$. The mass outflow rate ratio in the adiabatic simulations agrees with the expectation, while the velocity ratio is only slightly higher, most likely due to the presence of hot gas filling the outflow cavity, which is fractionally more important in the `L0.3` runs. When cooling is introduced, the lower-luminosity AGN heats the gas to lower temperatures, leading to more efficient cooling and greater difference between the analytical estimate and simulated properties.

Observationally, outflow velocity scales roughly as $L^{0.16-0.29}$ (Fiore et al. 2017), i.e. the relationship is flatter than analytical estimate and much more discrepant with our results. The mass outflow rate, on the other hand, has a steeper dependence on luminosity: $\dot{M}_{\rm out} \propto L^{0.76-1.29}$ (Fiore et al. 2017); this is also discrepant with our results, as it predicts a difference by a factor $2.5-4.7$. Understanding why the two relationships differ so much helps explain their difference from the simulated results too. In our analytical estimate,

$$v_{\rm out} \propto f_{\rm g}^{-1/3} \sigma_{\rm b}^{-2/3} L_{\rm AGN}^{1/3}, \tag{5.28}$$

while the mass outflow rate

$$\dot{M}_{\rm out} \propto f_{\rm g} \sigma_{\rm b}^2 v_{\rm out} \propto f_{\rm g}^{2/3} \sigma_{\rm b}^{4/3} L_{\rm AGN}^{1/3}. \tag{5.29}$$

In our earlier calculations, we assumed that the only difference between the high- and low-$L_{\rm AGN}$ systems is the AGN luminosity. In reality, the gas velocity dispersion, which is closely related to the galaxy and SMBH masses, has a systematic dependence on $L_{\rm AGN}$, and the gas fraction may also have such a dependence. Assuming that $\sigma_{\rm b} \propto M_{\rm BH}^{1/4} \propto \left(L_{\rm AGN}/l\right)^{1/4}$, where $l \equiv L_{\rm AGN}/L_{\rm Edd}$ is the Eddington ratio, we find

$$v_{\rm out} \propto f_{\rm g}^{-1/3} L_{\rm AGN}^{1/6}, \tag{5.30}$$

while the mass outflow rate

$$\dot{M}_{\rm out} \propto f_{\rm g}^{2/3} L_{\rm AGN}^{2/3}. \tag{5.31}$$

We see that even without any correlation between $f_{\rm g}$ and $L_{\rm AGN}$, we recover almost exactly the observed correlations $v_{\rm out} \propto L_{\rm AGN}^{0.16}$ and $\dot{M}_{\rm out} \propto L_{\rm AGN}^{0.66}$. So the observed correlations can be explained if the different AGN have the same distribution of Eddington ratios, and the luminosity difference arises from the difference in SMBH (and host galaxy) masses, an aspect we don't cover in our simulations. As the number of outflow observations with known SMBH masses increases, it will be interesting to check whether the relationship between out-

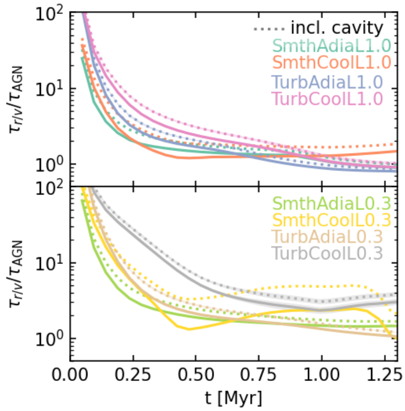

Figure 5.11: Ratio of the two outflow age estimates, $\tau_{r/v}/\tau_{\rm AGN}$, as function of time in all simulations. Dotted lines are calculated without accounting for the presence of the initial cavity in the gas distribution.

flows in galaxies differing only in AGN Eddington ratio follows our simulated results (and analytical predictions) more closely than the whole population.

5.4.2 Determining outflow properties from observations

Throughout our simulations, the average outflow properties estimated using $\tau_{r/v}$ are almost always higher than those estimated using $\tau_{\rm AGN}$. In Fig. 5.11, we plot the ratio of these two timescale estimates as a function of time for all eight non-control simulations. The solid lines correspond to the actual $\tau_{r/v}$ used when estimating outflow parameters, while dotted lines correspond to the ratio $\overline{R}_{\rm out}/\overline{v}_{\rm out}$, i.e. ignoring the presence of the central cavity at the start of the simulation. We see that initially, $\tau_{r/v}$ can be more than an order of magnitude higher than $\tau_{\rm AGN}$ (i.e. the real age of the outflow), and generally remains higher throughout the simulations. Only when the outflow breaks out of the initial gas shell, at $t > 0.8$ Myr in simulations SmthAdiaL1.0, TurbAdiaL1.0 and TurbCoolL1.0, does the ratio drop below unity. This means that using the commonly adopted equation $\dot{M}_{\rm out} = M_{\rm out} v_{\rm out}/R_{\rm out}$ provides mass outflow estimates that are up to several times too small. The discrepancy is higher when the AGN luminosity is lower and when the outflow is younger, i.e. closer to the nucleus. This estimate is sometimes multiplied by a factor of a few, which would bring it into agreement with the real value, however this multiplication is usually done when trying to account for different outflow geometries (e.g. Cicone et al. 2014; González-Alfonso et al. 2017).

5.4.3 Establishing the $M - \sigma$ relation

One of the reasons why cooling is much more efficient in the low-luminosity turbulent simulations is the presence of dense gas clumps. While the clumps get slightly heated by the outflow, they cool down quickly and remain resilient to the feedback. They can subsequently fall on to the SMBH and continue feeding and growing it. By $t = 0.5$ Myr, $\sim 85\%$ of the cold gas is falling inward and this number is essentially unchanged by $t = 0.8$ Myr. In the high-luminosity simulation, the total mass of such clumps is much smaller - $\sim 45\%$ at $t = 0.5$ Myr and only $\sim 13\%$ at $t = 0.8$ Myr. While we don't have simulations with higher luminosity, we expect this trend to continue: cold gas clumps will be pushed away, heated and dispersed ever more efficiently as the AGN luminosity increases. This confirms a way to establish the $M - \sigma$ relation without having explicitly momentum-driven outflows (King 2010b), as predicted by considering the two-temperature nature of the shocked wind plasma (Faucher-Giguère & Quataert 2012). At low luminosities, the cold dense clumps, resilient to heating and evaporation, are not pushed by the high-energy outflow and continue feeding the SMBH. As the luminosity increases, the wind momentum becomes high enough to push the dense clumps away, as is happening in the `TurbCoolL1.0` simulation. Then the SMBH feeding stops and its mass is established as given by the momentum-driven wind formalism (King 2010b). This has been shown before in idealised simulations with global density gradients (Zubovas & Nayakshin 2014), but here we see the same process working on smaller density inhomogeneities.

5.4.4 Implementation of AGN feedback in numerical simulations

As we noted in Section 5.3.2.1, the lack of hydrodynamic realisation of an AGN wind leads to a reduction in outflow energy by a factor ~ 2. The precise reduction is lower in simulations with turbulence and in simulations with higher luminosity, but these dependencies appear weak; there may also be a dependence on gas density. This issue is almost certainly important for cosmological simulations which typically implement AGN feedback as simple injection of kinetic and/or thermal energy into the surrounding gas (e.g. Booth & Schaye 2009; Vogelsberger et al. 2014; Tremmel et al. 2017; Davé et al. 2019; Nelson et al. 2019a). As the outflow bubble expands in those simulations, the lack of pressure from the presumably extreme hot shocked wind or a thermalising jet leads to a backflow, leaving less energy to push the gas outward, much like in our simulations.

We envision a few ways to mitigate this issue. The numerically most straightforward way is to double the formal AGN feedback efficiency. However, this would merely mask the problem and would not account for the possible influence of gas density, outflow size and shape. A more realistic solution would be to add a pressure term to the SMBH particle, with the value of this pressure directly proportional to total injected AGN feedback energy and inversely proportional to the volume of the shocked wind/jet cavity. The injected energy should be modified by cooling, which becomes important once

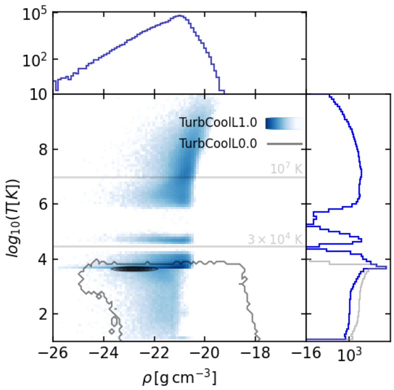

Figure 5.12: Same as Figure 5.8, but here showing the relationship between gas temperature and density.

the AGN luminosity decreases and the wind energy is no longer maintained. The volume of the cavity can be approximated by using the distance to the gas particles neighbouring the SMBH in SPH simulations, and by considering a density threshold in grid-based ones. A drawback of this approach is that the pressure is necessarily isotropic and cannot account for such effects as outflow breakout through low-density channels. A more detailed and anisotropic solution would be to track wind pressure using the same grid that is being used for feedback injection (see Section 5.2.3). That way, shocked wind properties can be tracked in each direction independently, providing a continuous push to the gas particles at the inner edge of the outflow cavity.

Of course, the best way of eliminating the problem is to actually treat the wind hydrodynamically. This has been done in `AREPO` moving-mesh simulations, where the quasi-relativistic wind is injected into cells neighbouring the SMBH particle (Costa et al. 2020a), as well as for jet feedback in galactic (Bourne & Sijacki 2017; Talbot et al. 2022, 2024; Ehlert et al. 2023) and cosmological (Bourne et al. 2019; Bourne & Sijacki 2021), by using novel refinement techniques. In general, improvements of numerical resolution around supermassive black holes (Curtis & Sijacki 2015; Hopkins et al. 2024a) can pave the way to detailed treatments of extreme gas in their vicinity and lead to better prescriptions for making feedback and its effects more realistic (Curtis & Sijacki 2016; Bourne & Sijacki 2017; Koudmani et al. 2019; Talbot et al. 2021).

Another aspect of our results relevant to larger scale simulations is connected to the spatial resolution. We showed that the uneven density distribution arising due to turbulence interacts with cooling in a non-trivial way. Depending on the AGN luminosity, the clumpiness of gas can either enhance or suppress mass and momentum rates of the outflow. The connection relies on the gas temperature distribution: diffuse hot gas cools inefficiently, while dense gas can radiate away injected energy very rapidly. In addition to AGN luminosity, the connection almost certainly depends on average gas density and level of turbulence, which determines the typical ratio of densities at a given distance from the nucleus. These results echo the conclusion of Bourne et al. (2015) that low-resolution simulations are better at destroying galaxies via AGN feedback, because more even density distribution does not allow injected energy to escape. Cosmological simulations usually cannot resolve gas with density exceeding $n_{\rm H} \sim 100$ cm^{-3} (e.g. Nelson et al. 2019a), corresponding to $\rho \sim 10^{-22}$ g cm^{-3}, which is lower than the *average* gas density in the central parts of our simulated shell. As the simulation evolves, most of the cold gas, but also some warm and even hot gas attain higher densities (see Fig. 5.12). As a result, cosmological simulations may overpredict the amount of hot gas in outflows and underpredict the cooling rate of outflowing gas. Even dedicated smaller-scale simulations may be underpredicting the mass of cold dense gas (e.g. Nuza et al. 2014; Valentini et al. 2017). At the same time, cosmological simulations generally don't resolve gas of very low density either, overpredicting the cooling rate.

There are two common approaches to mitigate this issue. The first, preventing gas particles that receive AGN feedback injection from cooling for a while (e.g. Tremmel et al. 2017, 2019), does not capture the nuances of this process, leading to an unrealistic distribution of different gas phases. The second method, accumulating AGN feedback energy for a significant period of time (e.g. 25 Myr, cf. Henden et al. 2018) before injecting it into the gas in one explosive event, misses the gradual development of outflows. Potentially the best way to reduce this problem is to use multiphase particles (Springel & Hernquist 2003; Murante et al. 2010; Valentini et al. 2017), where each particle (or cell in a grid-based method) is assumed to contain gas of two or three phases, each with distinct temperature and density. Furthermore, improved numerical resolution around shocks and other density discontinuities (Bennett & Sijacki 2020) can help better track the evolution of multiphase gas within an outflow.

5.4.5 Model caveats

In this chapter, we presented numerical simulations capturing the effect and interplay of turbulence and cooling of AGN wind-driven outflows. For this reason, our simulations are heavily idealised. While their results can be used to interpret real outflow data and improve large-scale numerical simulations (as outlined above), numerous improvements are possible.

First of all, in real galaxies, even the central spheroid usually has some angular momentum, which facilitates outflow escape via the polar directions (Zubovas & Nayakshin 2012, 2014; Curtis & Sijacki 2016). This is enhanced further by the presence of a disc. Another effect collimating the large-scale feedback may be small-scale anisotropies, i.e. the conical geometry of the AGN wind (Proga & Kallman 2004; Nardini et al. 2015; Luminari et al. 2018). The wind geometry in any particular source is highly uncertain and so would be another free parameter in our simulations. In general, the polar direction of the accretion disc need not line up with the polar direction of the galaxy (as evidenced by the directions of observed AGN jets, Kinney et al. 2000) and the interplay between collimation on different spatial scales can lead to further complexities in outflow geometry.

We neglected gas self-gravity in these simulations, which precludes the formation of very dense clumps and stars. Star formation consumes some material and so reduces the mass outflow rate; simultaneously, stellar feedback may combine with AGN feedback to enhance the energy of outflows.

The cooling function we adopted is also simplified by assuming constant Solar metallicity of the gas. It is well known that more metal-rich gas cools more quickly (Costa et al. 2015) and so will preferentially precipitate out of the outflow. This should lead to formation of high velocity, high density, cold, metal-rich gas (Zubovas & King 2014; Richings & Faucher-Giguère 2018b,a). The assumption that gas is optically thin also leads to unrealistically inefficient cooling of dense clumps. These clumps may efficiently transport metal-rich gas to galactic outskirts, the circumgalactic or even intergalactic medium, affecting the chemical evolution of the galaxy and its environment.

Finally, our assumption of constant AGN luminosity is unrealistic. Both observations (Schawinski et al. 2015) and analytical arguments (King & Nixon 2015) suggest that individual AGN episodes should last only ~ 0.1 Myr, although they may be clustered into longer phases of enhanced activity (Hopkins et al. 2007; Zubovas et al. 2022). This finding is corroborated by numerical simulations of realistic accretion of interstellar gas clouds (Alig et al. 2011) and as shown in Chapters 3 and 4. A *flickering* AGN would interact with gas cooling in a non-linear way, because the cooling timescale of some gas is shorter than the expected downtime between successive AGN episodes, while the hot gas would stay hot throughout.

5.5 Summary

In this Chapter, we presented the results of hydrodynamical simulations of AGN wind-driven outflows in idealised galaxy bulges, focusing on the effects of turbulence, cooling and their interplay on the major properties of the outflows: the mass outflow rate, momentum and energy loading factors. Our main results are the following:

- Simulations of smoothly distributed gas under an adiabatic equation of state produce spherically symmetric outflows with properties in general agreement with analytical expectations, except that a significant fraction of the injected energy remains in the outflow cavity where the shocked AGN wind would be in reality; this leads to outflows being slower, having lower momentum and energy than predicted.

- The addition of turbulence has almost no effect on the coupling between AGN wind and the gas; in fact, the outflows become slightly more energetic in the turbulent simulations.

- Cooling, on the other hand, has a significant effect, reducing the outflow energy by 1-2 orders of magnitude in the simulations with smoothly distributed gas and by up to one order of magnitude in the turbulent simulations.

- The interplay between cooling and turbulence is not straightforward and depends on AGN luminosity: in simulations with $L_{\rm AGN} = L_{\rm Edd}$, turbulence mitigates cooling by allowing for a large amount of gas to be heated to very high temperatures where cooling is inefficient, while in simulations with $L_{\rm AGN} = 0.3L_{\rm Edd}$, turbulence enhances the effect of cooling on the mass and momentum rates by creating dense gas clumps that are resilient to feedback and can maintain their density by cooling. The destruction of such clumps in the higher luminosity simulations can lead to the establishment of the $M - \sigma$ relation.

- In the most realistic simulation - with both turbulence and cooling - cold gas dominates the mass outflow rate, both cold and hot gas have similar momentum rates, while the energy rate is dominated by the hot gas. The hot gas has a significantly higher velocity and is distributed further out than the cold. This agrees qualitatively with the properties of observed outflows.

- As outflows evolve and break out from the initial gas shell, their velocity increases while mass outflow rate decreases; the combined effect leads to an increase in the kinetic energy rate.

- Estimates of average mass outflow rates obtained using the common observational prescription $\dot{M}_{\rm out} = M_{\rm out} v_{\rm out} R_{\rm out}^{-1}$ almost always underestimates the true values obtained by dividing the total outflowing mass by the age of the outflow. The discrepancy is typically only by a factor < 2, but can be much higher when the outflow is young. Estimates of momentum and energy rates are similarly lower.

Conclusions

In this thesis we investigated SMBH feeding and the effect of the resultant feedback on the surrounding ISM. For this we used a suite of idealised `Gadget-3` SPH hydrodynamical simulations designed to isolate specific problems. We use the first two sets of simulations to investigate an idealised representation of the centre of our own Galaxy - the several-parsec-wide system of Sgr A* and the surrounding CNR. The choice of the system is motivated by a number of evidence several pieces of evidence suggesting past AGN phases (*Fermi*, *eRosita* bubbles, 430-pc radio bubbles, *X-ray chimneys* etc.). We investigate whether a collision between the CNR and an infalling MC could trigger an AGN event capable of producing such structures. We also stress that similar circumnuclear structures are likely in other galaxies and feeding of the central regions is observed there, therefore the outlined scenario can be applied to other galaxies. In the third set of simulations we investigated how the unevenness and cooling of the ISM affect the formation and evolution of large-scale outflows. In the following paragraphs we will briefly summarize our findings before presenting conclusions.

In Chapter 3 we investigate a scenario of a MC collision with already present CNR surrounding Sgr A*. The modelled system is highly idealised - we disregard self-gravity and cooling is described by the simple β-cooling prescription dependent only on the dynamical timescale. Due to these choices, the dynamics should not depend strongly on the gas mass of the system and our results should be scalable by up to two orders of magnitude. We calculated collisions with 13 different collision angles incrementing by 15° from zero to 180°, where collision angle represents the angle between the orbital angular momenta of the CNR and the cloud. Each collision was realised 4 times with stochastically varied initial conditions.

System evolution is in line with intuition with larger collision angles resulting in more significant disruptions of the initial system and significant feeding of the SMBH with about half of the initial system gas mass fed to the SMBH in the most extreme cases, which would be enough for to fuel a significant AGN episode. However, there is a relatively small range of high angles that would result in significant SMBH feeding - a more common occurrence would be a lower angle collision leading to a very similar but more massive CNR. This means that chaotic accretion from larger scales is likely to increase mass stored in the vicinity of the SMBH up until a more uncommon event triggers an AGN event. We estimate that this could occur on average once per $60 - 140$ Myr, although smaller-scale activity could happen more often. To better estimate the amount of energy that would be released during and an AGN outburst, we input the SMBH feeding data from our simulations to an accretion disc model. Here we find that the luminosity evolution is sensitive to the free parameter of viscous timescale $t_{\rm visc}$. While we found that feedback was unlikely to fully disperse the initial system, it still highlights the importance of modelling accretion with more care.

The sensitivity to the free parameter $t_{\rm visc}$ and the importance of on-the-fly accretion modelling when feedback is in effect was a strong motivation to create `ringcode` (Chapter 4) - a method to model SMBH accretion via standard 1D accretion disc model directly in the hydrodynamical code by solving the viscous diffusion equation describing the disc evolution. We tested our new approach in a very similar, but less idealised system, opting to only model the most extreme retrograde CNR-MC collision which results in a significant AGN episode. This time we turned on self-gravity and opted for a more detailed cooling/heating prescription that takes into account the luminosity of the SMBH. We performed three sets of four stochastically different simulations: one set with `ringcode` enabled `FB`, one of instantaneous accretion, but feedback limited to $L_{\rm Edd}$ `INST` and a control set `nFB` without feedback injection, but still calculating the accretion disc parameters.

We found that in `FB` simulations feedback had a more profound effect on the system than in `INST`. In all cases feedback cleared out the central region suppressing further SMBH accretion thus demonstrating self-regulation; in one case the system was completely destroyed. Conversely, the nominally stronger feedback in `INST` simulations did not clear out a central cavity thus the feeding of the SMBH ceased more gradually. This discrepancy is likely due to a combined effect of an artificial luminosity limit and the loss of energy due the accretion of dense clumps in the innermost regions of the disc. In any case, since only a single simulation resulted in the clearing out of the entire system, the results here somewhat reinforce the conclusions of the previous simpler models, where we found that feedback is unlikely to completely disrupt the CNR and it is possible for the dense structure to remain while simultaneously having a bright AGN episode and coincident star formation. We also found that the CNR somewhat collimated the outflow resulting in a wide conical shape.

Finally, in Chapter 5, we investigated the evolution of large-scale outflows produced by an AGN in a clumpy/cooling ISM. We designed the simulation to specifically isolate the effects of clumping due to turbulence, cooling or both. In addition, we developed a new more computationally efficient feedback injection scheme windGrid, which propagates wind on a static grid and employs spatial-hashing-like techniques to locate the ISM-wind interactions.

We calculated four sets of models. SmthAdia is a smooth and adiabatic system, SmthCool is a smooth system that is allowed to cool in the same manner as in Chapter 4. Similarly, we have TurbAdia and TurbCool sets, with clumpy initial conditions generated by a turbulent velocity field that are adiabatic or allowed to cool, respectively. There are significant morphological differences between outflows in each set. In SmthAdia the outflow expands spherically, slightly slower than analytically predicted. Allowing gas to cool in this case results in an overall weaker outflow with a narrower front, however, the clumping due to cooling is not significant enough to create anisotropy in the outflow. This is in contrast to both turbulent simulations, where the outflows are not spherical, with hot gas escaping through the least dense regions between clumps. Interestingly, this collimation results in an 'on average' as powerful outflows in the adiabatic case as in the SmthAdia runs. In TurbCool models, cold gas dominates the mass outflow rate; warm and hot phases have similar momentum loading factors, but energy loading factor is dominated by the hot phase - qualitatively in line with observations. Significantly, the typical observational estimate for the mass outflow rate $\dot{M}_{\rm out} = M_{\rm out} v_{\rm out} R_{\rm out}^{-1}$ is about two times lower than one determined using the actual lifetime of the AGN. momentum and energy loading factors are similarly lower.

Differences in AGN luminosity also have an effect on the overall evolution of the system. In $L_{\rm AGN} = L_{\rm Edd}$ case the diffuse gas in the gaps between clumps is heated enough for an outflow to form, but this is not the case in $L_{\rm AGN} = 0.3 L_{\rm Edd}$. Again we find that it is significantly harder to push out dense gas, which is in a somewhat tenuous agreement, considering the differences in scale, with our previous simulations presented in Chapter 4.

Briefly, our conclusions can be summarized as follows:

1. The result of a CNR-MC collision strongly depends on the collision angle γ with three scenarios regarding the morphological evolution of the system. Collisions with angles $\gamma \leq 105°$ result in the CNR increasing in size and mass, with minimal mass transfer to the central part of the system; collisions with steeper $\gamma > 105°$ result in an increased transport of gas toward the centre, where it forms a warped disc and feeds the central SMBH; The steepest collisions, $\gamma > 150°$, result in significant feeding of the SMBH; up to half of the initial gas mass is fed to the SMBH in the most extreme cases.

2. The range of non-AGN-inducing collision angles is five times greater than the range of AGN-inducing angles. Together with the fact that more prograde collisions are more likely, this suggests that the CNR should grow substantially before a significant enough collision results in significant dis-

ruption and an AGN phase, supporting the CNR-limit cycle hypothesis.

3. The new accretion disc particle method `ringcode` produces robust results. The prescription allows the SMBH to grow more smoothly and to directly link feedback to the standard accretion disc model in which luminosity closely follows the actual feeding rate of the SMBH, which is delayed with respect to the feeding rate of the accretion disc.

4. Feedback in simulations using `ringcode` expels gas from the central $0.1-1$ pc region around the SMBH, producing a central cavity. Self-regulation of black hole accretion occurs naturally with high luminosities suppressing SMBH feeding.

5. The `gridWind` feedback injection scheme efficiently distributes feedback, however an accounting of hydrodynamical pressure from feedback is required to prevent energy loss to backflow.

6. The cooling of dense gas clumps significantly reduces the outflow energy by 1-2 orders of magnitude in the simulations with smoothly distributed gas and by up to one order of magnitude in the turbulent simulations compared to analytical predictions. Clumping without cooling produce a collimating effect which results slightly more energetic in outflows.

7. The common observational estimates of the mass outflow rate, momentum and energy loading factors are potentially underestimated by a factor of two.

8. All models indicate that dense gas is significantly harder to clear out; even significant AGN phases reaching luminosities $\sim L_{\rm Edd}$ cannot be assumed to completely clear out the densest material from SMBH surroundings. The presence of dense material could make star formation possible even during an AGN phase.

Future outlook

With our models of CNR-MC collisions in the vicinity of Sgr A* we suggest that CNR is expected to grow via these interactions until one causes an AGN outburst. However, here we are extrapolating from singular events. An ideal obvious extension of our setup would be to actually model a time period long enough for multiple such occurrences, hopefully determining the expected duty cycle. There are a few similar models already (e.g. Tress et al. 2020; Moon et al. 2023), however they disregard feedback from SMBH and are generally more focused on the CMZ-scale rings. A slightly smaller, < 100 pc, setup could use the data describing the gas inflow from the larger scales. The reduced scope would allow us to use a more detailed sub-grid prescription for accretion, like ringcode, and couple it to a realistic AGN wind injection method, like BOLA (Costa et al. 2020b). Making use of the moving mesh Arepo code Springel (2010) could be especially interesting as it provides a way to self-consistently inject the material that escapes the accretion disc back into the main simulation; this is a formidable challenge in SPH. A similar model may also be generalised for more galaxies as we have increasingly robust estimates for feeding rates from larger scales via dust lanes (e.g. Sormani et al. 2023) and from circumnuclear environments inwards towards the SMBH (e.g. Combes 2019; Audibert et al. 2019).

The methods developed for this work, ringcode and gridWind are robust and can be applied to other hydrodynamical codes. ringcode can be extended to track the direction and warping of the disc plane. The inclusion of these effects should help us to better understand how collimated feedback affects the surrounding gas. It may also be possible to extend the model to different regimes of accretion, similarly to Koudmani et al. (2024). We also intend to improve gridWind by including an approximation for the hydrodynamical pressure of the shocked AGN wind and improving its memory usage. Interestingly, the static grid used for wind propagation may also be used to store a coarse-grained representation of the overall density field - this can be used to apply more consistent shielding.

Our exploration of the kiloparsec-scale outflow could be significantly improved by running simulations with a wider range and denser sampling of AGN luminosity. The dependence of outflow phases on AGN luminosity and the details of the cooling prescription are a straightforward step and a likely target for a future publication. It would also be relatively simple to vary the geometry of feedback injection. Since we noticed that clumps created by turbulence provide a collimating effect, it would be interesting to check whether this collimation is increased or reduced by the addition of a sub-resolution prescription for collimating the wind on the scales of the accretion disc.

We plan to address most of these caveats in future works, gradually building up a realistic picture of SMBH accretion and feedback from kiloparsec down to sub-parsec scales. This will enhance our understanding of accretion, real outflows and the interplay between inflowing and outflowing gas. We also expect this work to lead to improvements of the sub-resolution prescriptions used in large-scale numerical simulations.

Santrauka

Įvadas

Galaktikų centruose vykstantis centrinių supermasyvių juodųjų skylių (SMBH) maitinimas, akrecija, suformuoja galingus vėjus ir/arba čiurkšles, gebančias išstumti ženklią dalį aplinkinių dujų ir suformuoti tėkmes (King & Pounds 2015). Šiuo būdu nereguliarūs SMBH maitinimo ir grįžtamojo ryšio ciklai susieja galaktikos (kiloparsekų ir daugiau) bei SMBH (tipiškai parsekai ir mažiau) mastelius (Gaspari et al. 2020). Akreciją palaiko iš didesnių mastelių į galaktikų centrus krentanti medžaga.

Galaktikos skersėse esančios dulkių juostos yra vienas pagrindinių kanalų, kuriuo dujos priartėja prie centro (Sellwood & Wilkinson 1993). Įvertinus dulkių juostose esančių dujų kiekį ir kinematiką, galima įvertinti ir tikėtiną centro maitinimo mastą. Pavyzdžiui, Sormani & Barnes (2019) nustatė tikėtiną Paukščių Tako (PT) Centrinės molekulinės zonos (CMZ) maitinimo spartą ateinantiems ~ 10 mln. m., kuri vidutiniškai siekia apie $3\,\mathrm{M}_{\odot}\,\mathrm{m.}^{-1}$. Kiek vėliau Sormani et al. (2023) įvertinto dujų pernašą ir NGC 1097 - joje per 40 mln. m. centras bus maitinamas $\sim\ 3\,\mathrm{M}_{\odot}\,\mathrm{m.}^{-1}$ sparta. Įdomu tai, kad abi nustatytos spartos gerokai svyruoja trumpesniais laikotarpiais. Šios dulkių juostomis įkrentančios dujos formuoja aplinkbranduolinius žiedus (Combes 2019). Šias dinamiškas struktūras, su mažesniais SMBH masteliais jungia įvairios vijos ir debesys (Combes et al. 2014; Audibert et al. 2019, 2021). Šios vijos bei debesys gali per sąlyginai trumpą laiką (per vieną apsisukimą, ~ 10 mln. m.) prarasti reikšmingą judesio kiekio momento dalį ir taip priartėti prie SMBH (Combes 2019). Šiuos stebėjimų rezultatus patvirtina ir detalūs modeliai įtraukiantys vis daugiau fizikinių procesų (žvaigždžių grįžtamasis ryšys, dujų savigravitacija, magnetiniai laukai ir kt.) (pvz. Tress et al. 2020, 2024; Moon et al. 2023). Mūsų Galaktikoje, CMZ (šimtų parsekų dydžio žiedą) su keliais centriniais parsekais irgi jungia sudėtingas vijų ir molekulinių debesų tinklas. Aplinkbranduolinis žiedas (CNR; kelių parsekų dydžio žiedas) galimai veikia kaip tarpinė dujų stotelė, kuri tik susidarius palankioms sąlygoms kvaziperiodiškai pamaitina SMBH ir sukelia aktyvumo epizodą (Hsieh et al. 2017; Bryant & Krabbe 2021).

Mūsų Galaktikoje stebimas ne vienas epizodiško aktyvumo padarinys. Nors šiuo metu ir neaktyvi, ji svarbi aktyviųjų galaktikos branduolių (AGN) tyrimuose (Ponti et al. 2013a). Galaktikos centro aktyvumas yra tikėtiniausias *Fermi* ir *eRosita* burbulų paaiškinimas (Zubovas & Nayakshin 2012). Šie burbulai - milžiniškos dvipolės struktūros, iškilusios atitinkamai $\sim$ 10 kpc ir $\sim$ 15 kpc iš Galaktikos centro (GC), statmenai Galaktikos disko plokštumai (Su et al. 2010; Predehl et al. 2020). Taipogi, CMZ stebima sustiprėjusi SiO emisija rodo Galaktikos centro aktyvumą kiek arčiau mūsų dienų, prieš $\sim$ 0.1 mln. m. (Takekawa et al. 2024). Tikėtina, kad šis epizodas buvo gerokai silpnesnis, tačiau pajėgus suformuoti šimtų parsekų mastelio „Rentgeno kaminus“ ir 430 pc aukščio radijo burbulus (Ponti et al. 2019; Heywood et al. 2019). Kiek seniau aptikti kelių šimtų metų senumo rentgeno aktyvumo aidai (Koyama et al. 1996; Revnivtsev et al. 2004; Ponti et al. 2013a). Būtent dėl aktyvumo padarinių stebimųįvairiuose masteliuose ir dėl tikėtino jų epizodiškumo, mūsų Galaktika yra puiki laboratorija tirti kvaziperiodišką SMBH maitinimą bei jo sukelto grįžtamojo ryšio padarinius (Zubovas & Nayakshin 2012).

Deja, mes negalime nuosekliai milijonus metų stebėti tos pačios galaktikos dinaminės evoliucijos. Šią spragą užpildome lipdydami bendrą paveikslą iš įvairių galaktikų, stebimų skirtinguose panašios evoliucijos etapuose ir remdamiesi vis sudėtingesniais skaitmeniniais modeliais. Galaktikos skersės modelis, pateiktas Tress et al. (2020) ir Tress et al. (2024), gerai atitinka CMZ maitinimo greičio įverčius (Sormani & Barnes 2019; Su et al. 2024). Autoriai taip pat parodo, kad žvaigždžių grįžtamasis ryšys ir dujų savigravitacija yra svarbūs veiksniai, lemiantys dujų judėjimą iš CMZ link SMBH. Idealizuotas Salas et al. (2021) CMZ modelis iliustruoja turbulencijos vaidmenį. Centrinių $\sim$ 10 pc modeliai rodo, kad įkrentančios dujos formuoja CNR primenančią struktūrą (Mapelli & Trani 2015; Trani et al. 2018). 2 skyriuje parodyta, jog dujos, susiduriančios su centre jau esančiu CNR, dažniausiai (priklausomai nuo kritimo kampo) prie jo prisijungia, tačiau gali ir sukelti AGN epizodą. Naujai į CNR įsiliejusios dujos, galbūt ir AGN vėjo slėgis, gali skatinti žvaigždžių formavimąsi arti SMBH. Tačiau norint nuosekliai ištirti sąveiką tarp maitinančių dujų bei grįžtamojo ryšio, subraiškinis akrecijos modelis turi nuosekliai įvertinti ne tik šviesio mastą, bet ir paveikti dujas teisingomis laiko skalėmis. Tokio modelio implementaciją demonstruoju 3 skyriuje. AGN vėjo sąveika su tarpžvaigždine terpe (ISM) dažnai remiasi analitiniais sferinio vėjo modeliais, neatsižvelgiančiais į netolygų dujų pasiskirstymą ir padidėjusius energijos nuostolius greičiau vėstančiuose tankiuose gumuluose. Didelio masto modeliuose dažnai neatsižvelgiama į šias detales dėl per mažos modelių skyros. 4 skyriuje parodome, kad šie veiksniai svarbūs kiloparsekų dydžio tėkmėse ir gali paveikti jų parametrų įverčius.

Darbo tikslas ir uždaviniai

Šiuo darbu siekiu pagerinti mūsų supratimą apie sąveiką tarp juodųjų skylių maitinimo ir grįžtamojo ryšio bei nustatyti šių reiškinių poveikį centrinėms dujų sankaupoms aplink SMBH. Tam naudoju idealizuotus, konkrečius aspektus izoliuoti skirtus, parsekų ir kiloparsekų mastelio modelius. Įvardintiems tikslams pasiekti iškėliau šiuos uždavinius:

- Nustatyti, kaip dujų morfologija centriniuose parsekuose priklauso nuo įkrentančios medžiagos savybių, pasitelkus idealizuotą PT CNR regiono modelį.
- Sukurti realistišką subraiškinį SMBH akrecijos sekimo hidrodinaminiuose modeliuose metodą ir nustatyti, kaip pasikeitusios laiko skalės ir/arba aktyvumo mastas pakeičia grįžtamojo ryšio poveikį SMBH supančiai medžiagai.
- Sukurti skaitmeniškai efektyvų AGN grįžtamojo ryšio injekcijos metodą.
- Ištirti AGN tėkmių plitimą vėsioje ir netolygioje ISM ir įvertinti, kaip dėl šių efektų įtraukimo pakinta AGN vėjo poveikio ISM našumas.

Pagrindiniai rezultatai ir ginami teiginiai

1. Dujų žiedų formavimasis kelių parsekų masteliais galaktikų centruose yra galimas kvaziperiodinio Galaktikos aktyvumo paaiškinimas.
2. Ar konkretus įkrentančio debesies susidūrimas su jau egzistuojančiu CNR sukels aktyvumo epizodą, priklauso nuo įtekančios medžiagos parametrų. Medžiagos kiekis, pamaitinantis SMBH, nuo kritimo kampo priklauso laipsniškai; priešpriešiniai susidūrimai sudaro sąlygas SMBH praryti apie pusę pradinės sistemos dujų masės.
3. Sukurtas subraiškinis SMBH akrecijos įvertinimo metodas patikslinantis AGN epizodo raidą; metodas pagrįstas tiesioginiu standartinio plono akrecinio disko modelio sprendimo įtraukimu.
4. AGN vėjas gali sukelti didelio mastelio tėkmes, nesunaikindamas tankiausių struktūrų centriniuose parsekuose, tuo pačiu metu galimas ir žvaigždžių ir tėkmių formavimasis ar SMBH maitinimas, išskyrus pačius šviesiausius AGN.
5. Dujų netolygumai ir juose vykstantis vėsimas sumažina grįžtamojo ryšio poveikį ISM; nustatyti 1-2 eilėmis mažesni judesio kiekio bei energijos apkrovos faktoriai nei taikant tipinį analitinį sferinį AGN vėjo modelį.

Autoriaus indėlis

Autorius sukūrė naujus subraiškinius metodus skirtus sekti SMBH akreciją ir grįžtamojo ryšio injekciją. Autorius sukūrė ir suskaičiavimo visas skaitmeninių modelių, naudojamų šiame darbe, realizacijas, apdorojo bei atliko duomenų analizę ir interpretaciją. Autorius parašė straipsnius, kurių pagrindu parašyti skyriai 2 ir 3. Autorius reikšmingai prisidėjo prie 4 skyrių grindžiančio straipsnio teksto.

1 skyrius

Supermasyvios juodosios skylės galaktikų centruose: maitinimas ir grįžtamasis ryšys

Tikėtina, kad daugumos galaktikų centruose egzistuoja supermasyvios juodosios skylės (SMBH) (Lynden-Bell 1969; Kormendy & Richstone 1995; Magorrian et al. 1998; Merritt & Ferrarese 2001a). Idėją, jog bene kiekviename galaktikos centre yra SMBH, kuri auga dėl akrecijos išpopuliarino Soltan (1982), pasirėmęs kvazarų šviesio funkcija (dabar tai žinoma Soltan'o argumento pavadinimu). Visgi, nors tipiškos jų masės ($10^6 - 10^{10}\mathrm{M}_\odot$) atrodo milžiniškos palyginus su žvaigždžių masėmis, jų gravitacija dominuoja tik sąlyginai mažame tūryje. Pavyzdžiui Paukščių Tako (PT) Galaktikos Centre (GC) esanti SMBH, Sgr A*, dominuoja tik (Peißker et al. 2024):

$$r_{\mathrm{inf}} \sim \frac{GM_{\mathrm{SgrA^*}}}{\sigma_\star^2} \sim 1.7 \left(\frac{M_{\mathrm{SgrA^*}}}{4\times 10^6 \mathrm{M}_\odot}\right) \left(\frac{\sigma_\star}{100\,\mathrm{km\,s^{-1}}}\right)^{-2} \mathrm{pc}, \tag{1.1}$$

kur $M_{\mathrm{SgrA^*}}$ yra Sgr A* masė, o $\sigma_\star$ - žvaigždžių greičių dispersija centriniuose parsekuose. Intuityviai tai suteikia pagrindo abejoti SMBH įtaką galaktikų evoliucijai. Tačiau prie SMBH priartėjus pakankamam kiekiui medžiagos, SMBH kompaktiškumas, kai visa ši masė susitelkia spinduliu nedaug didesniu nei Schwarzschild'o ($r_\mathrm{s} \sim 2GM/c^2$), sudaro sąlygas formuotis akreciniams diskams. Šios struktūros ne tik maitina SMBH, bet ir efektyviai išlaisvina dalį prisijungtos medžiagos gravitacinės potencinės energijos itin greitų vėjų ar čiurkšlių pavidalu. Šie reiškiniai, vadinami SMBH grįžtamuoju ryšiu, leidžia paskleisti šią išlaisvintą energiją toli už SMBH gravitacinės įtakos ribų.

Tai, kad SMBH kuriamas grįžtamasis ryšys gali reikšmingai paveikti ir galaktikos mastelius paprastai King & Pounds (2015) iliustruoja parodydamas kiek energijos išlaisvinama, jeigu SMBH užauga iki $M-\sigma$ masės dėl akrecijos:

$$\Delta E \approx \eta M_{\rm BH} c^2 \approx 2 \times 10^{61} \frac{M_{\rm BH}}{10^8 {\rm M}_\odot}\,{\rm erg}, \tag{1.2}$$

čia tipiškai $\eta \approx 0.1$; ši energija gerokai didesnė nei gravitacinė ryšio energija centriniuose galaktikų telkiniuose:

$$E_{\rm bulge} \sim 8 \times 10^{58} \frac{M_{\rm BH}}{10^8 {\rm M}_\odot} \left(\frac{\sigma}{200\,{\rm km\,s^{-1}}}\right)^2 {\rm erg}, \tag{1.3}$$

kur $M_{\rm BH}$ ir σ yra SMBH masė ir centrinio telkinio greičių dispersija masteliuojamos į tipines vertes, $10^8\,{\rm M}_\odot$ ir 200 km s^{-1} atitinkamai. Taigi, neabejotina, kad išlaisvinamos energijos pakanka reikšmingam poveikiui. Visgi svarbu atkreipti dėmesį ne tik į bendrą išlaisvintos energijos kiekį, bet ir jos perdavimo aplinkai pobūdį.

Šiame darbe susitelksiu į grįžtamąjį ryšį, kuris pasireiškia akrecinio disko kuriamo greito, sferiško vėjo pavidalu. Toks vėjas gali pasiekti $\sim 0.1c$ greitį (Pounds et al. 2003b,a; Tombesi et al. 2010a,b). Vėjo greitis yra vienas esminių parametrų nulemiančių grįžtamojo ryšio poveikį, nes temperatūra, kurią vėjo medžiaga pasiekia atsimušusi į aplinkines galaktikos dujas, stipriai priklauso nuo greičio: $T_{\rm shock} \approx 10^{10} (v/30000\,{\rm km\,s^{-1}})^2$ K. Jeigu pasiekiama temperatūra $T > 10^9$ K, tai vėsimas nebėra efektyvus ir karštas burbulas efektyviai plečiasi atlikdamas beveik adiabatišką darbą. Taip formuojasi energijos varomos tėkmės. Priešingu atveju, kai šiluminė energija efektyviai išspinduliuojama ir nepadeda formuoti dujų tėkmės, sąlygos tinkamos judesio kiekio-varymo režimui. King (2003, 2005) parodė, kad judesio kiekio varymo režime sferiškas vėjas sustabdo akreciją pasiekus SMBH masę, atitinkančią $M-\sigma$ (Gebhardt et al. 2000; Ferrarese & Merritt 2000; Kormendy & Ho 2013) sąryšį, tačiau būtent energijos varymas sukuria milžiniškas tėkmes, stebimas mūsų ir kitose galaktikose.

Taigi, SMBH kuriamas grįžtamasis ryšys pakankamai stiprus paveikti galaktikos mastelius. Visgi, reikia nepamiršti ir to, kad stipriam aktyvumui palaikyti būtini milžiniški maitinančios medžiagos kiekiai. Tai, kiek medžiagos reikės aktyvumui palaikyti, galime grubiai įvertinti remdamiesi ribinis šviesiu $L_{\rm Edd}$. Šis šviesis atitinka balansą tarp į išorę nukreiptos spinduliuos jėgos ir į vidų nukreiptos gravitacijos, todėl $L > L_{\rm Edd}$ lemtų medžiagos nustūmimą ir maitinimo stabdymą.

$$\begin{aligned} L_{\rm Edd} &\approx 1.3 \times 10^{38}\,(M_{\rm BH}/{\rm M}_\odot)\,{\rm erg\,s^{-1}} \\ \dot{M}_{\rm Edd} &= \frac{L_{\rm Edd}}{c^2 \eta} \approx 2.4 \times 10^{-8}\,(M_{\rm BH}/{\rm M}_\odot)\,{\rm M}_\odot {\rm yr}^{-1}. \end{aligned} \tag{1.4}$$

Į šią išraišką įsistatę palyginti mažos masės SMBH Sgr A*masės vertę, gauname, jog tipiškos trukmės ($\sim$ 0.1 mln. m. (Zubovas et al. 2022)), epizodą palaikyti reikėtų $\sim 10^5\,M_\odot$.

SMBH maitinimą sukelia tiek galaktikų susiliejimai, tiek galaktikos viduje vykstantys, sekuliarūs, procesai (pvz.: Lin et al. 2023; Martin et al. 2018; McAlpine et al. 2020; Smethurst et al. 2021, 2022). Tikėtina, jog sekuliarūs procesai atsakingi už didesnę maitinimo dalį (Garland et al. 2024). Šiame darbe susitelksiu būtent į tokius procesus. Tiek stebėjimai, tiek modeliai rodo, jog medžiaga gali keliauti centro link dėl dinaminių nestabilumų, tokių kaip galaktikose dažnai stebimos skersės (Sellwood & Wilkinson 1993; Maciejewski et al. 2002; Tress et al. 2020; Sormani & Barnes 2019; Sormani et al. 2023). Tokią išvadą netiesiogiai patvirtina ir tai, jog didesnė proporcija skersėtų galaktikų yra ir aktyvios (Agüero et al. 2016; Garland et al. 2023, 2024). Skersė gali efektyviai transportuoti dujas centro link, iš kiloparsekų ligi šimtų parsekų. Stebėjimai rodo, kad dujos nesustoja šimtų parsekų dydžio aplinkbranduoliniuose žieduose - dujų judėjimas bent iki $\sim$ 10 pc stebimas NGC 613, NGC 1808, o sujungimas su centru stebimas ir Circinus, bei NGC 1097 (Audibert et al. 2017; Combes 2019; Prieto et al. 2019a; Kolcu et al. 2023).

Dujų judėjimas skersės dulkių juostomis iki centrinės molekulinės zonos (CMZ) bei jos sąsaja su aplinkbranduoliniu žiedu (CNR)[4] stebimi ir mūsų Galaktikoje. Be to, PT įvairiuose masteliuose stebimi ir paskirų aktyvumo tarpsnių palikti pėdsakai (Sarkar 2024). Ko gero geriausiai žinomi $\sim$ 10 kpc *Fermi* burbulai, skleidžiantys γ spinduliuotę, bei $\sim$ 14 kpc rentgeno *eRosita* burbulai (Su et al. 2010; Predehl et al. 2020). Tokius burbulus pajėgtų išpūsti ir žvaigždžių grįžtamasis ryšis (Sarkar et al. 2015; Miller & Bregman 2016), tačiau per ilgesnį laiko tarpą ($\sim$ 30 mln. m.) negu įvertintas iš burbulų kinematikos ($6-9$ mln. m.) (Bordoloi et al. 2017). Be šių milžiniškų struktūrų, stebimi ir kiek mažesni, šimtų parsekų dydžio rentgeno kaminai, bei radijo burbulai (Heywood et al. 2019; Ponti et al. 2019). Taip pat jau gana ilgą laiką žinoma apie GC stebimus rentgeno aidus, bylojančius apie tikėtiną trumpą aktyvumo epizodą, vykusį prieš kelis šimtus metų (Koyama et al. 1996; Revnivtsev et al. 2004; Marin et al. 2023), o neseniai kiek didesniais CMZ masteliais buvo aptikta ir didesnė SiO emisija pasklidusi taip, jog tikėtina yra susijusi su padidėjusiu Sgr A*aktyvumu prieš 0.1 mln. m..

Būtent tai, kad PT aktyvumo padariniai stebimi įvairiuose masteliuose, be to, palyginti detaliai išskiriamos smulkios centro struktūros, galimai palaikančios protarpinius aktyvumos epizodus, daro PT puikiu taikiniu AGN tyrimams, nors šiuo metu Galaktika ir nėra aktyvi (Genzel et al. 2010).

[4]Paukščių take, $\sim$ 100 pc žiedas vadinamas CMZ, ne aplinkbranduoliniu žiedu. Pastarasis pavadinimas, skirtingai nei dažnai naudojama kitų galaktikų kontekste, naudojamas apibūdinti $\sim$ 4 pc žiedą, supantį Sgr A*.

1.1 Akrecijos bei grįžtamojo ryšio modeliavimas

Šiame darbe galaktikų centruose judančios dujos modeliuojamos pasitelkus skaitinius metodus. Konkrečiau, naudojamas išskleistųjų dalelių hidrodinamikos (SPH) (Lucy 1977; Gingold & Monaghan 1977) pagrindu sukurtas kodas `Gadget-3`, kuris yra modifikuota ir išplėsta `Gadget-2` (Springel 2005) versija. SPH yra *Lagranžinis* kodas, kuriame tolydūs laukai modeliuojame paskiromis, medžiagos dalį atitinkančiomis, dalelėmis. Esminė tokį lauko diskretizavimą aprašanti lygtis:

$$f(\mathbf{r}) \approx \sum_{i}^{N_{\rm ngb}} \frac{m_i}{\rho_i} f(\mathbf{r}_i) W(\mathbf{r}-\mathbf{r}_i, h_i), \tag{1.5}$$

kur f, tai lauko vertė vertinimo vietoje $\mathbf{r}$ (šiuo atveju ir *pagrindinės* dalelės pozicija). m_i, ρ_i ir r_i tai kaimyninių dalelių masė, tankis ir pozicija atitinkamai. Lauko vertė gaunama susumavus visų skleidimo atstumu h_i esančių dalelių įtaką. Šių dalelių įtaka silpnėja didėjant atstumui nuo taško $\mathbf{r}$ priklausomai nuo svertinės funkcijos $W(\mathbf{r}, h)$. Įprastai, tinkamas kaimynių skaičius priklauso nuo pasitinktos $W(\mathbf{r}, h)$ funkcijos. Šiame darbe naudojama Wendland C^2 (Wendland 1995; Dehnen & Aly 2012) funkcija, kuri dera su mūsų naudojama SPH algoritmo versija SPHS. Šis SPH variantas, sukurtas Read & Hayfield (2012), leidžia adaptyviai įvesti dirbtinę klampą Π_{ij} tik ten, kur ji būtina. Dirbtinė klampa padeda nesusidaryti daugiareikšmiams sprendiniams, dalelėms priartėjus itin arti viena kitos - ši problema itin reikšminga smūginėse bangose, kai dalelės sustumiamos arti viena kitos. Galiausiai, ši klampa pridedama į entropijos tvermės pagrindu išvestą SPH judėjimo lygtį (sekant Read et al. (2010)):

$$\frac{\mathrm{d}v_i}{\mathrm{d}t} = -\sum_{j=1}^{N} m_j \left(\frac{P_i}{\rho_i^2} + \frac{P_j}{\rho_j^2} + \Pi_{ij} \right) \nabla_i \bar{W}_{ij}, \tag{1.6}$$

kur slėgis P gaunamas pasinaudojus išraiška:

$$P = A(s)\rho^{\gamma}, \tag{1.7}$$

čia $A(s)$ yra entropijos funkcija priklausanti nuo entropijos s, γ yra adiabatinis indeksas, o $\bar{W}_{ij} = W(\mathbf{r}_{ij}, h_i)/2 + W(\mathbf{r}_{ji}, h_j)/2$.

Modelyje taip pat reikia atsižvelgti gravitaciją. `Gadget-3` gravitacija yra skaidoma į savigravitaciją ir į *išorinę* gravitaciją. Pastaroji yra skaitmeniškai efektyviai įvedama pasitelkus *išorinį* potencialą. Sunkiau įvertinti savigravitaciją - tai kaip kiekviena dalelė veikia viena kitą. Paprastai skaičiuojant kiekvienos dalelių poros tarpusavio sąveikas, algoritmo skaičiavimo trukmė augtų kaip N^2 ir didelės skyros modeliai taptų praktiškai neįmanomi. Šią problemą `Gadget` (Springel 2005) sprendžia medžio algoritmas. Šis metodas leidžia sugrupuoti toli esančias ar mažai atskiros įtakos darančias daleles ir skaičiuoti tik bendrą jų poveikį; taip algoritmo skaičiavimo trukmė auga proporcingai $N\log(N)$. Žinoma, tai įveda tam tikrų netikslumų, tačiau šie yra įvertinami, o leistinas jų dydis pasirenkamas modelio skaičiavimo pradžioje.

Tam, kad išvengtume nepagrįstai staigių pokyčių, svarbu tinkamai diskretizuoti ir laiko eigą. Teoriškai, modelis veiktų itin gerai, jeigu būtų parenkami vienodi, pakankamai trumpi, laiko žingsniai visoms dalelėms. Tačiau toks sprendimas labai sulėtintų kodo veikimą, todėl apribotų įmanomą pasiekti skyrą. Dėl to `Gadget` naudojami adaptyvūs laiko žingsniai, tipiškai trumpesni tankiose srityse ar greitai judančiose dujose. Praktiškai kode tai implementuota laiko žingsnio vertinimo kriterijais, iš kurių rinkinio visada pasirenkamas mažiausias. Standartinė `Gadget` laiko žingsnio skaičiavimo išraiška yra:

$$\Delta t_i = \min\left[\Delta t_{\max}, \left(\frac{2\eta\epsilon}{|a_i|}\right), \frac{Ch_i}{\max_j(v_{ij}^{\mathrm{sig}})}\right], \tag{1.8}$$

kur trys nariai atitinkamai reiškia įverčius atsižvelgiant į pasirinktą maksimumą ($\Delta t_{\max}$) ir gravitacines ar hidrodinamines sąveikas atitinkamai. Gravitacijos naryje η yra integravimo tikslumo parametras, ϵ yra gravitacijos glotninimo ilgis, o a - gravitacijos kuriamas pagreitis. Hidrodinamikos sąveikos naryje C yra Courant'o faktorius, o v_{ij}^{sig} yra signalo greitis. Šis pagrindinių kriterijų rinkinys dažnai praplečiamas; pilnas rinkinys tipiškai didesnis, kai modelyje dalyvauja skirtingų tipų dalelės. Šiame darbe pristatomuose modeliuose visoms dalelėms taikomas papildomas dalelių laiko žingsnių ilgių ribojimas pagal Saitoh & Makino (2009) - užtikrinama, kad kaimyninių dalelių laiko žingsniai negalėtų skirtis daugiau nei 4 kartus. Nustačius kaip dalelės veikiamos gravitacijos bei hidrodinaminių sąveikų, jų pozicija ir greitis keičiami pasitelkiant Kick-Drift-Kick (KDK) *šuoliuojantį* algoritmą.

Mano darbe taip pat pasitelkiami vadinamieji subraiškiniai metodai. Jais aprašomi procesai, kurių (praktiškai) neįmanoma tiesiogiai išskirti modelyje, tačiau šių procesų padariniai svarbūs. Konkrečiai pristatomuose darbuose svarbiausi iš jų:

- Dalelių vėsimas - energijos nuostoliai dėl įvairių tiesiogiai nemodeliuojamų procesų. Šiame darbe naudojami tiek labai paprasti variantai, izoterminis, β-cooling (Meru & Bate 2011), tiek sudėtingesni, aprašantys kaitinimą dėl AGN spinduliuotės, vėsimą per metalų smulkiosios struktūros linijas, fotoelektrinį kaitinimą, *Bremsstrahlung* ir *Compton* kaitinimą/vėsimą (Bakes & Tielens 1994; Sazonov et al. 2005; Mashchenko et al. 2008).

- SMBH akrecija - akreciniai srautai nėra išskiriami ir šiame darbe aprašomi naudojant akrecinio disko dalelės metodą iš Power et al. (2011a) bei mūsų sukurtą `ringcode` metodą pristatomą 3 skyriuje.

- Grįžtamasis ryšys - grįžtamasis ryšys įvedamas naudojant virtualiųjų dalelių metodą pagal Nayakshin et al. (2009) arba mūsų sukurtą `windGrid` pristatomą 4 skyriuje

2 skyrius

Protarpinis SMBH maitinimas chaotiškai įkrentančiomis dujomis

Aplink Sgr A*, stebimas CNR (Lau et al. 2013). Hidrodinaminiai modeliai rodo, kad ši, ~ 2 pc nuo centro nutolusi, struktūra galėtų susiformuoti iš priartėjusio ir išardyto molekulinio debesies (MC) (Mapelli & Trani 2015; Trani et al. 2018). Ryšys tarp CNR ir galaktikos aktyvumo nėra akivaizdus - šiuo metu dujos juda maždaug apskritiminėmis orbitomis ir SMBH beveik nemaitinama (Marrone et al. 2007; Ferrière 2012). Tačiau nesunku įsivaizduoti scenarijų, kai į jau esamą CNR įkrenta naujas MC (Liu et al. 2012; Hsieh et al. 2017; Tress et al. 2020). Sistemos perturbacijos smarkumas turėtų priklausyti nuo įkrentančio MC parametrų. Pakankamai išdarkyta sistema galbūt ir pamaitintų SMBH, kas sukeltų AGN epizodą. Šio darbo esmė yra ištirti, kokie susidūrimai galėtų sukelti AGN epizodą, bei įvertinti šio scenarijaus tikėtinumą.

2.1 Skaitmeninio modelio aprašas

Susidūrimą modeliuojame pasitelkią hibridinį N-kūnų ir SPH kodą `Gadget-3` (Springel 2005). Naudojame adaptyvią dirbtinę klampą (SPHS; Read & Hayfield 2012) ir Wendland C^2 svertinę funkciją (Dehnen & Aly 2012), kuriai tinkamas kaimynių skaičius $N_{\rm ngb} = 100$. Modelius sudaro $N_{\rm part} = 5 \times 10^5$ dalelių, kurių masės $m_{\rm SPH} = 0.04\,{\rm M}_{\odot}$; modelyje išskiriama masė: $M_{\rm res} = N_{\rm ngb} m_{\rm SPH} = 4\,{\rm M}_{\odot}$.

Mūsų idealizuotą modelį sudaro trys pagrindiniai elementai:

- **Supermasyvi juodoji skylė**: jos pradinė masė $M_{\rm BH} = 4 \times 10^6, {\rm M}_{\odot}$ (Boehle et al. 2016), yra fiksuota centre. SMBH prisijungia gravitaciškai susietas daleles, priartėjusias arčiau nei $r_{\text{sink}} = 0.01$ pc.

- **Aplinkbranduolinis žiedas**: CNR modeliuojamas pradžioje kaip toro formos žiedas su vidiniu $R_{\text{in}} = 1.5$ pc ir išoriniu $R_{\text{out}} = 4$ pc spinduliais. Pradinei CNR masei pasirinkta mažesnis stebėjimais grįstas vertinimas $M_{\text{ring}} = 10^4\,\mathrm{M}_\odot$ (Christopher et al. 2005; Ferrière 2012).

- **Įkrentantis molekulinis debesis**: paprastumo dėlei, pagrindiniuose modeliuose MC masė tokia pati, kaip CNR: $M_{\text{cl}} = M_{\text{ring}} = 10^4\,\mathrm{M}_\odot$, o jo spindulys $r_{\text{cl}} = 1$ pc. Debesis padėtas 6 pc nuo susidūrimo vietos.

Dujos juda SMBH bei izoterminiame išoriniame potenciale (formuojamo nemodeliuojamų žvaigždžių ir kt.):

$$\phi = -\frac{\mathrm{G}M_{\text{BH}}}{r} + 2\sigma^2 \log\frac{r}{r_0}. \tag{2.1}$$

Čia izoterminį potencialą apibūdina centrinė greičių dispersija $\sigma = 100$ km s^{-1}; r_0 - didelė pasirenkama konstanta. Izoterminio potencialo apimama masė $M_{\text{enc}} = M_{\text{BH}}$ ties $R_{\text{enc}} = 0.8$ pc. Pradinis CNR dalelių greitis lygus apskritiminio judėjimo greičiui ir yra tarp $v_{\text{R1.5}} \sim 181$ km s^{-1} ties vidiniu kraštu ir $v_{\text{R4}} \sim 160$ km s^{-1} ties išoriniu. MC debesies greitis $v_{\text{cl}} = 220$ km s^{-1} atitinka parabolinio judėjimo greitį ties pradiniu debesies centro nuotoliu. Be orbitinių greičių, MC ir CNR dalelėms suteikiama greičiai ir turbulencijos greičio lauko dedamoji. Greičių laukas generuojamas remiantis Dubinski et al. (1995), su greičio amplitude $\sigma_{\text{turb}} = 37.5$ km s^{-1}. Turbulencija modelyje nėra papildomai palaikoma. Taip pat modelyje išjungta savigravitacija ir naudojamas β-cooling (Meru & Bate 2011) vėsimas. Tai reikšmingai supaprastina mūsų modelį, tačiau leidžia ir ekstrapoliuoti rezultatus didesnei bendrai sistemos masei, nes dinaminė sistemos evoliucija nuo jos nepriklauso. Pradiniai dalelių greičiai suskaičiuojami pritaikius (2.1).

Iš viso suskaičiuoti 52 susidūrimo scenarijai, su skirtingais susidūrimo kampais bei stochastine variacija dėl atsitiktinai generuojamos turbulencijos ir pradinių dalelių pozicijų.

2.2 Rezultatai ir diskusija

Debesis iki žiedo keliauja ~ 20 tūkst. m., šio laiko pakanka susiformuoti vijoms ir gumulams dėl įvestos turbulencijos dedamosios. 2.1. pav. iliustruoja tipišką sistemos evoliuciją su kritimo kampais $\gamma = 15^\circ$ (viršuje) $\gamma = 165^\circ$ (apačioje) ir gerai iliustruoja esminius šių sistemų tarpusavio skirtumus. Esant mažam kritimo kampui, pradinė sistema yra perturbuojama, bet nesunaikinama - įkritęs MC prisijungia prie žiedo. Situacija daug įdomesnė, kai debesies judėjimas

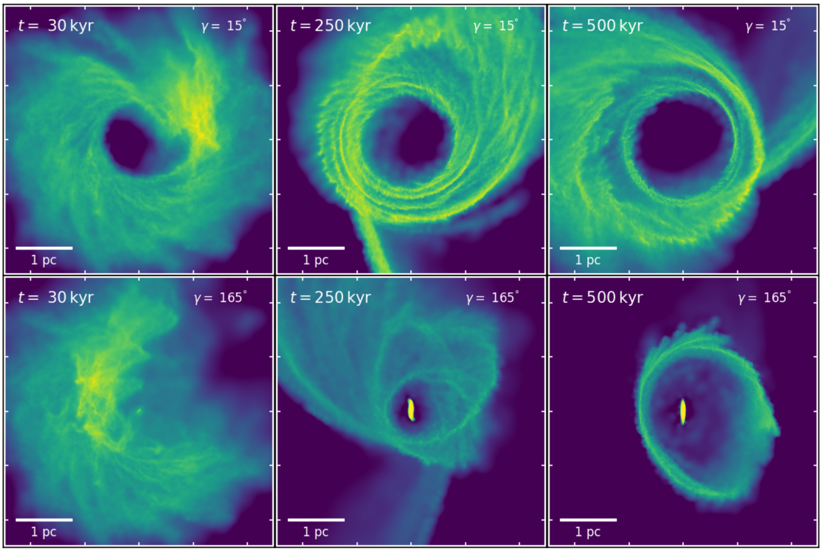

2.1 pav.: modelių raida po žiedo sukimosi kryptimi vykusio susidūrimo (viršuje) ir priešinga kryptimi vykusio susidūrimo (apačioje).

priešingas CNR sukimuisi. Šiuo atveju pradinė sistema beveik visiškai išardoma ir susiformuoja nauja. Ji dažnai susideda iš disko, kuris yra SMBH įtakos sferoje, ir žiedo, esančio kiek toliau. Tipiškai žiedai sukasi toje pačioje plokštumoje, kaip sukosi CNR, tačiau centriniai diskai - nebūtinai. Šie rezultatai iš esmės dera su CNR formavimo modeliais iš (Mapelli & Trani 2015) ir (Trani et al. 2018).

Nuosekliau sistemos evoliucijos priklausomybė nuo kritimo kampo įvertinta priskyrus dujas atitinkamai žiedui arba centriniam diskui. Grafike pav. 2.2 vaizduojamas dujų apskritimizacijos spindulys, o pav. 2.2b vaizduojama struktūrose sukaupta masė. Spalvomis išskiriamos skirtingų struktūrų savybės. Visos dujos vaizduojamos pilkai, žiedas raudonai, centrinis diskas žaliai. Nuspalvintos sritys rodo didžiausias/mažiausias vertes, gautas stochastiškai skirtinguose modeliuose. Čia aiškiai matome, jog didesnis kampas lemia didesnę masės koncentraciją centre. Juoda linija vaizduoja CNR-MC sąveikos dalį κ, kuris parodo maždaug kokia dalis žiedo sąveikaus su debesiu pirminio susidūrimo metu. ši turi minimumą, kai MC greičio projekcija CNR plokštumoje artimiausia jo orbitiniam greičiui. Kaip ir tikėtasi, bendrai sistemos dujos formuoja tuo didesnes struktūras, kuo ši sąveika mažesnė. Masės grafike matyti, jog didėjant kampui, vis didesnė dalis medžiagos telkiasi būtent centriniame diske, ar net pamaitina SMBH (pilka sritis). Galima daryti išvadą, kad susidūrimai iki maždaug $\gamma = 150°$ nesukelia reikšmingo SMBH maitinimo vietoje suformuodami panašaus mastelio masyvesnę sistemą. Būtent šis rezul-

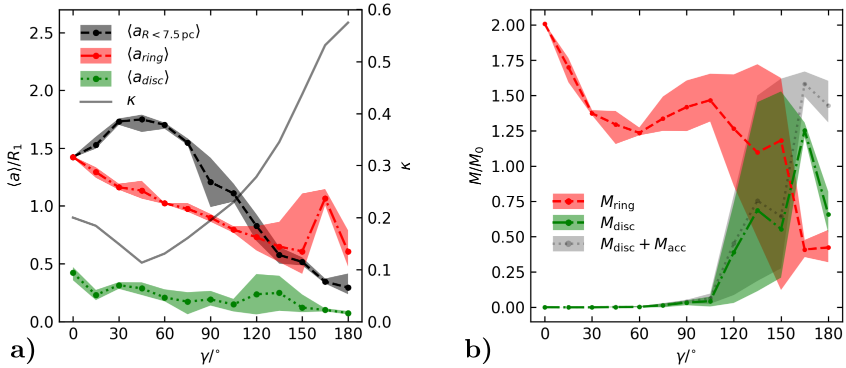

2.2 pav.: **a)** vidutinis apskritimizacijos spindulys po 0.5 mln. m. priklausomai nuo susidūrimo kampo γ. Juoda linija žymimos vidutinės vertės visoms dujos centriniuose 7.5 pc; raudonai - žiedui priskirtos dujos; žaliai - centriniui diskui priskirtos dujos. Atitinkama spalva užspalvintos didžiausios/mažiausios vertės nustatytos stochastiškai skirtinguose modelių realizacijose. Pilka ištisinė linija žymi CNR-MC sąveikos ilgio parameratą κ, kurio vertė rodo kokia dalis CNR tiesiogiai sąveikavo su MC pirminio susidūrimo metu. **b)** vidutinė masė sukaupta atitinkamoje struktūroje priklausomai nuo susidūrimo kampo γ. Raudona - žiedui priskirtos dujos; žaliai - centriniui diskui priskirtos dujos; pilka - su centrinio disko ir SMBH prarytos masės.

tatas pagrindžia vadinamąją CNR ribinio ciklo teoriją, kuri teigia, kad paskiri medžiagos įkritimo į centrą epizodai gali suformuoti CNR primenančias struktūras kurios, auga ligi pakankamai stipraus susidūrimo, sukeliančio naują AGN epizodą.

Taip pat įvertinome potencialą SMBH aplinkoje formuotis žvaigždėms. Tiesiogiai žvaigždėdaros nesekame (skyra modelyje būtų per maža) todėl analizę parėmėme Toomre Q parametru (Toomre 1964),

$$Q = \left(\frac{GM}{r^3} + \frac{2\sigma^2}{r^2} \right) \frac{c_{\mathrm{s}}}{\pi G \Sigma}, \tag{2.2}$$

kur $Q < 1$ rodo gravitaciškai nestabilų diską/žiedą. Nestabilios sritys formavosi tik keliuose modeliuose su $150° \leq \gamma \leq 165°$, tačiau padidinus pradinę sistemos masę kelis kartus savigravitacija taptų svarbi ir galėtų vykti žvaigždėdara.

Nustatę, kiek medžiagos prisijungė centrinė SMBH, galime įvertinti tikėtiną AGN epizodo šviesį. Grafike 2.3a pav. parodoma visa modeliuoto laiko metu SMBH praryta masė. Atmetus modelius, kuriuose medžiagos praryta mažiau, nei modelyje išskiriama masė ir pritaikius *bootstrapping* algoritmą, nustatyta eksponentinė priklausomybė:

$$\log M_{\mathrm{acc}}/M_0 \approx 2.34^{+0.14}_{-0.15} \times 10^{-2} \gamma - 4.34^{+0.22}_{-0.19} \tag{2.3}$$

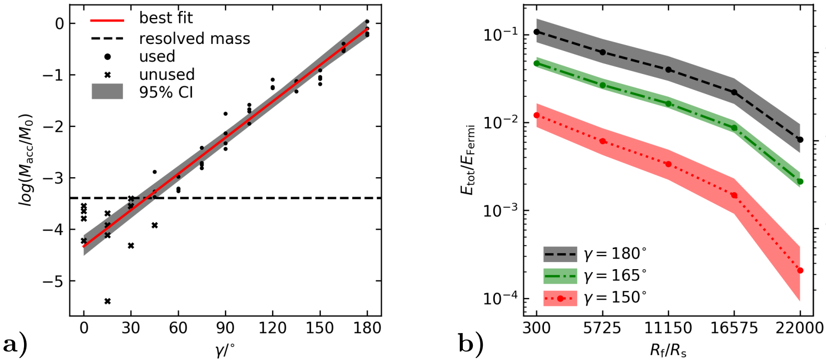

2.3 pav.: **a)** visa SMBH per 0.5 mln. m. praryta masė. Taškai žymi skirtingose realizacijose gautas vertes. Horizontali brūkšninė linija žymi modelio skyros ribą - žemiau esantys taškai nenaudoti funkcijos derinime. Raudona linija rodo geriausiai derančią funkciją (2.3), pilkai pažymėtas 95% patikimumo intervalas. **b)** Aktyvumo metu išlaisvinta energija priklausomai nuo akrecinio disko maitinimo spindulio (klampos laiko skalės) trijuose modeliuose rinkiniuose su didžiausiu SMBH prarytos medžiagos kiekiu; užspalvintos sritys žymi didžiausias/mažiausias vertes tarp stochastiškai skirtingų modelių realizacijų.

Energijos kiekį, išlaisvintą AGN epizodo metu, galime įvertinti panaudoję:

$$E_{\rm tot} = \eta c^2 M_{\rm acc} = 1.8 \times 10^{57} \eta_{0.1} M_4 \text{erg}, \tag{2.4}$$

kur $\eta \equiv 0.1\eta_{0.1}$ yra akrecijos efektyvumas, o $M_{\rm acc} \equiv 10^4 M_4\,{\rm M_\odot}$ - bendra praryta masė. Šios lygties pakanka grubiam įvertinimui. Tuo tarpu 2.3b pav. pateikti rezultatai atsižvelgia į medžiagos judėjimą standartiniame akreciniame diske. Šis vertinimas atliktas pateikus maitinimo duomenis atskiram difuzijos lygtimi grįstam akrecinio disko modeliui (Shakura & Sunyaev 1973; Frank et al. 2002). Grafike 2.3b pav. rodomi tik modeliai, kur vyko ženkli akrecija - $\gamma >= 150°$. Išlaisvintos energijos kiekis reikšmingai priklauso ir nuo pasirinkto akrecinio disko maitinimo spindulio $R_{\rm f}$. Didėjant maitinimo spinduliui $R_{\rm f}$ išlaisvinamos energijos kiekis mažėja, nes dalis medžiagos pabėga per akrecinio disko išorinį kraštą. Nuoseklesnis akrecinio disko įtraukimas demonstruojamas 3 skyriuje. Grafike mes lyginame išlaisvintą energiją su *Fermi* burbulams išpūsti reikalinga pagal $E_{\rm Fermi} = 1.6 \times 10^{58}$ erg (Zubovas & Nayakshin 2012), visgi verta pastebėti du dalykus. Pirma, Zubovas & Nayakshin (2012) gana aukštas vertinimas, Sarkar (2024) apžvalgoje rasime ir gerokai mažesnių skaičių. Antra - kaip jau minėjau, mūsų modelio dinamika nepriklauso nuo dujų kuriamos gravitacijos. Tai reiškia, kad šiuos rezultatus galima ekstrapoliuoti ir masyvesniems MC ar CNR, kas lemtų atitinkamai ir stipresnį AGN epizodą.

Pritaikę žaislinį CMZ modelį, įvertinome, kad CNR augimo greitis $\dot{M}_{\rm CNR} \sim (4.3 - 6.0) \times 10^{-2}\,{\rm M_\odot\,m.^{-1}}$, kas yra daugiau nei $\dot{M}_{\rm min} \sim 2 \times 10^{-3}\,{\rm M_\odot\,m.^{-1}}$

(Hsieh et al. 2017) nustatytas stebėjimais, tačiau tik porą kartų skiriasi nuo verčių paremtų detaliais CMZ modeliais (Tress et al. 2020, 2024). Tuo pačiu įvertinome, kad AGN epizodas, išpučiantis Fermi burbulus, vyktų kas $60-140$ mln. m., tačiau mažesni epizodai vyktų dažniau.

Nors šiame modelyje tiesiogiai nesekėme grįžtamojo ryšio, sekdami Zubovas et al. (2011) parodėme, kad net ir stipriausio aktyvumo metu sistema greičiausiai nebus visiškai suardyta, nes jos sunkis keliomis eilėmis didesnis, nei į išorę veikiantis grįžtamojo ryšio slėgio jėga. Didesnė pradinė sistemos masė tik dar labiau padidintų sunkį, todėl tikėtina, kad CNR sistema veiktų kaip kolimuojantis elementas, nukreipiantis vėją mažesnio pasipriešinimo keliu (Zubovas & Nayakshin 2014).

2.3 Apibendrinimas

Šiame tyrime parodžiau, kad susidūrimas tarp CNR ir įkrentančio molekulinio debesies gali sukelti aktyvumo epizodą, tačiau sistemos evoliucija smarkiai priklauso nuo susidūrimo kampo γ - kampo tarp žiedo ir debesies orbitinių judesio kiekio vektorių:

- Debesiui krentant mažesniu nei $\gamma \leq 105°$ kampu, pradinė sistema nežymiai perturbuojama; susiformuoja naujas, masyvesnis ir nežymiai didesnis CNR.
- Susidūrimai, kuomet debesies judėjimas priešingas žiedo sukimuisi ($\gamma > 105°$) reiškmingai perturbuoja sistemą; nauja sistema labiau koncentruota centre.
- Ekstremaliu atveju, $\gamma > 150°$, iki pusės pradinės sistemos masės pamaitina SMBH; tokio maitinimo pakaktų palaikyti reikšmingą aktyvumo epizodą.

Šie sistemų raidos skirtumai dera su CNR ribinio ciklo hipoteze. Prie SMBH kvaziperiodiškai priartėjančios dujos (Hsieh et al. 2017; Tress et al. 2020), tikėtina, arba suformuoja CNR (Mapelli & Trani 2016; Trani et al. 2018), arba prisijungia prie jau esančios CNR sistemos. Retais atvejais, iš didesnių mastelių įkrentantis debesis su CNR susiduria priešinga jo sukimuisi kryptimi; toks susidūrimas galėtų vykti kartą kas $60-140$ mln. m. ir, tikėtina, sukeltų reikšmingą aktyvumo epizodą.

3 skyrius

Nuoseklus akrecijos įtraukimas hidrodinaminiuose modeliuose

Apžvalgoje minėjau, kad tipiškai akrecija modeliuose įtraukiama kaip subraiškinis modulis. Ko gero arčiausiai standartinio galime laikyti vadinamąjį Bondi metodą (Springel et al. 2005) ar jo variacijas, paremtą klasikiniu Bondi-Hoyle-Lyttleton sferiškai simetriško akrecijos srauto sprendiniu (Hoyle & Lyttleton 1939; Bondi & Hoyle 1944; Bondi 1952). Šis metodas puikiai tinka didelio masto modeliams, nes akrecijos sparta priklauso nuo dujų savybių santykinai toli nuo pačios SMBH. Įvertinus, kiek dujų bus praryta per tam tikrą laiko tarpą, iš aplinkos pašalinamas atitinkamas dalelių kiekis, palaikant masės tvermę. Nors šis metodas dėl nerealistiškų prielaidų gali pervertinti ar nuvertinti akrecijos spartą (Hobbs et al. 2012; Negri & Volonteri 2017), tipiškai problemas stengiamasi spręsti įvairiais empiriškai grįstomis pataisomis (Springel et al. 2005; Booth & Schaye 2009; Rosas-Guevara et al. 2015; Schaye et al. 2015).

Į problemą iš kitos pusės žiūrima taikant *dviejų žingsnių* metodus. Šiuo atveju gravitaciškai, ar kitaip, susieta medžiaga pirma prijungiama prie SMBH ir akrecinį diską atitinkančios dalelės, ir tik tuomet pagal jų savybes skaičiuojama akrecijos sparta. Toks metodas atsižvelgia į prie SMBH priartėjusios medžiagos savybes, tačiau būtina išskirti palyginti mažus, su akrecinių diskų išoriniais kraštais palyginamus, mastelius. Prijungus daleles prie SMBH+akrecinio disko dalelės, tolesnis akrecijos modeliavimas gali būti sąlyginai paprastas, kur medžiaga užlaikoma akrecinį diską atitinkančiame rezervuare ir maitinama SMBH pagal pasirinktą laiko skalę (Power et al. 2011a; Hopkins 2015). Sudėtingesni moduliai, kaip Koudmani et al. (2024), leidžia atsižvelgti į įvairių tipų akrecinius srautus tame pačiame modelyje.

Šio darbo tikslas yra patobulinti SMBH akrecijos vertinimą į hidrodinaminį modelį įtraukiant standartinio plono akrecinio disko modelį (Shakura & Sunyaev 1973; Pringle 1981; Frank et al. 2002), nuosekliai sekamą viso mode-

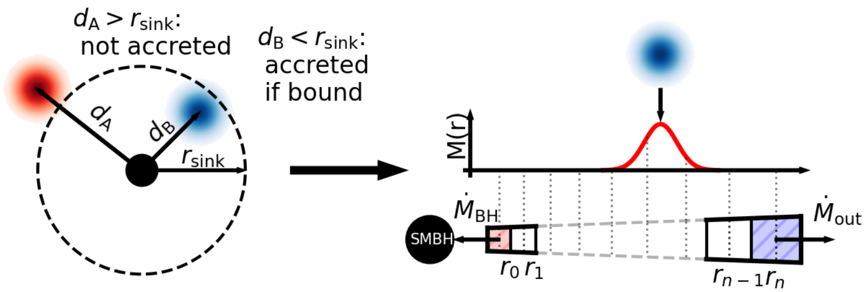

3.1 pav.: `ringcode` ADP metodo schema. Dalelėms priartėjus prie SMBH arčiau nei r_{sink} tikrinama ar dalelė gravitaciškai susieta su SMBH ir ar jos cirkuliarizacijos spindulys yra akrecinio disko ribose. Jeigu taip, dalelė šalinama iš hidrodinaminio modelio ir prijungiama prie akrecinio disko. Dalelės medžiaga tolygiai padalijama per diską sudarančius žiedelius priklausomai nuo jos dydžio ir skleidimo funkcijos.

liuojamo laiko metu. Skirtingai nei alternatyvose, naudojamasi ne jau žinomu disko sprendiniu, bet skaitmeniškai sprendžiama 1D disko difuzijos lygtis, todėl metodas nominaliai nepriklauso nuo iš anksto parenkamų parametrų, kaip akrecijos spindulys ar klampos laiko skalė. Šiame darbe metodas implementuotas `Gadget-3` SPH modelyje.

3.1 Skaitmeninio modelio aprašas

Šio darbo tikslas yra ištirti SMBH akreciją, todėl fizikinę sistema pasirinkome labai panašią į modeliuotą praeitame skyriuje. Tiek dujų žiedo, tiek įkrentančio debesies masė padidintos 10 kartų, todėl $m_{\text{SPH}} = 0.4\,\text{M}_\odot$; modelyje išskiriama masė: $M_{\text{res}} = N_{\text{neigh}} m_{\text{SPH}} = 40\,\text{M}_\odot$. Modelį sudaro šie elementai:

- **Supermasyvi juodoji skylė**, kurios pradinė masė $M_{\text{BH}} = 4 \times 10^6\,\text{M}_\odot$ (Boehle et al. 2016), yra fiksuota centre. SMBH prisijungia gravitaciškai susietas daleles, priartėjusias arčiau nei $r_{\text{sink}} = 0.01$ pc ir perduoda susietam su akrecinio disko modeliui (žr. žemiau).

- **Aplinkbranduolinis žiedas**: CNR modeliuojamas kaip pradžioje toro formos žiedas su vidiniu $R_{\text{in}} = 1.5$ pc ir išoriniu $R_{\text{out}} = 4$ pc spinduliais. Pradinė CNR masė dešimt kartų didesnė nei 2 skyriuje - $M_{\text{ring}} = 10^5\,\text{M}_\odot$ - pakankama sistemai pasiekti Edingtono šviesį.

- **Įkrentantis molekulinis debesis**: Debesies masė padidinta tiek pat, dešimt kartų, $M_{cl} = M_{ring} = 10^5\,\text{M}_\odot$. Kartu padidintas ir debesies spindulys $r_{\text{cl}} = 3$ pc. Debesis padėtas 12 pc nuo susidūrimo vietos.

- **Foninės dujos**: 25 parsekų spindulio sferą aplink SMBH užpildėme

$M_{\rm bg} = 1.2 \times 10^3\,{\rm M}_\odot$ foninių dujų. Šias dujas sudaro $N_{\rm bg} \approx 3 \times 10^5$dalelių, ir jų masė 100 kartų mažesnė, nei CNR ar MC sudarančių. Šios dujos skirtos tik sekti grįžtamojo ryšio injekciją.

Dujos juda tame pačiame SMBH ir izoterminio fono kuriamame potenciale, todėl pradiniai dujų greičiai skaičiuojami analogiškai pritaikius išraišką (2.1) ir pridėjus tą pačią turbulencijos dedamąją, kaip ir 2 skyriuje. Taigi, pradinis CNR greitis atitinka apskritiminę orbitą ir yra tarp $v_{\rm R1.5} \sim 181$ km s^{-1} ties vidiniu kraštu ir $v_{\rm R4} \sim 160$ km s^{-1} ties išoriniu. MC debesies greitis $v_{\rm cl} = 220$ km s^{-1}, debesis krenta priešinga žiedo sukimosi kryptimi.

Į dujų kaitimą ar vėsimą šiame modelyje atsižvelgiama detaliau, nes norime įvertinti grįžtamojo ryšio poveikį. Dujų vėsimas tarp 20 K ir 10^4 K aprašomas empirine funkcija iš Mashchenko et al. (2008), kuri atsižvelgia į C, N, O, Fe, S, and Si metastabilias linijas. Laikoma, dujų metalingumas lygus Saulės metalingumui. Karštesnes nei 10^4 K dujas aprašome sekdami Sazonov et al. (2005). Šis receptas įveda AGN spinduliuotės kaitinimo dedamąją, bei atsižvelgia į laisvųjų elektronų spinduliuotės ir Komptono efektus. Be šių, modelyje taip pat yra foninis fotoelektinis kaitinimas sekant Bakes & Tielens (1994), tačiau praktiškai jis turi itin mažą įtaką mūsų rezultatams.

Mūsų modelyje taip pat naudojamas žvaigždžių formavimosi algoritmas, stochastiškai verčiantis daleles žvaigždinėmis, jei jų tankis didesnis nei Jeans ir potvyniniai tankiai. Tikimybė transformuoti dalelę apskaičiuojama palyginant dalelės kolapsavimo dėl gravitacijos laiko skalę su jos laiko žingsniu modelyje. Visgi modelio skyra nėra pakankama tikroviškam žvaigždėdaros modeliavimui arti prie SMBH.

Laikome, kad grįžtamasis ryšys modelyje yra sferinio AGN vėjo pavidalo (pvz. King & Pounds 2015). Pats vėjas yra modeliuojamas naudojant virtualias daleles (Nayakshin et al. 2009). Žinant akrecinio disko šviesį, kiekvieno SMBH žingsnio metu sukuriamas proporcingas virtualiųjų dalelių, nešančių energiją bei judesio kiekį, skaičius. Šios dalelės juda atsitiktinai parinktomis trajektorijomis iš centro tipišku AGN vėjo greičiu $v_\gamma = 0.1c$. Tuomet, šių virtualiųjų dalelių poveikis dalelėms yra perduodamas proporcingai jų indėliui į tankio lauką virtualios dalelės pozicijoje. Pavyzdžiui, i-tosios SPH dalelės judesio kiekis $\mathbf{p}_{\gamma,i}$ pakinta pagal:

$$\Delta\mathbf{p}_{\gamma,i} = \frac{\rho_i(\mathbf{r})}{\rho(\mathbf{r})}\Delta\mathbf{p}_\gamma, \tag{3.1}$$

kur $\rho_i(\mathbf{r})$, tai - dalelės tankis ties virtualia dalele, $\rho(\mathbf{r})$ bendras tankis toje pat vietoj, o $\Delta\mathbf{p}_\gamma$ - virtualios dalelės nešamas judesio kiekis. Analogiškai perduodama ir energija.

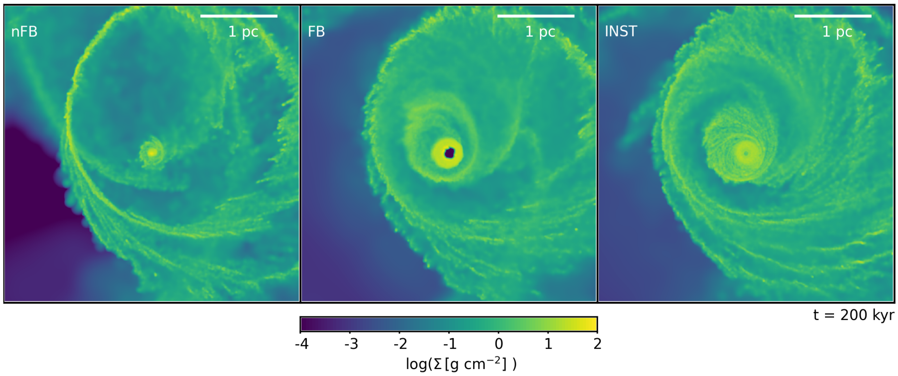

3.2 pav.: 4 pc regiono tankio žemėlapiai `nFBr0`, `FBr0` ir `INSTr0` praėjus $t = 200$ tūkst. m.. Modeliuose su įjungtu grįžtamuoju ryšiu centrinis diskas didesnis ir dera su xy-plokštuma; modelyje be grįžtamojo ryšio diskas smulkesnis ir kreivesnis. Taip pat, `FB` modeliuose su `ringcode` formuojasi centrinė ertmė; analogiškos tuštumos nesiformuoja `INST`.

3.2 Akrecinio disko dalelė

Šio darbo pagrindas yra naujas akrecinio disko dalelės metodas. Jis nuosekliai susieja pagrindinį hidrodinaminį modelį su kartu sprendžiamu 1D standartiniu plono akrecinio disko modeliu. Modelio schema pavaizduota 3.1 pav.. Akrecinis diskas susideda iš pasirinkto skaičiaus žiedų. Vidinis žiedas padedamas artimiausios stabilios apskritiminės orbitos (ISCO) viduje. Tai - sritis, kur apskritiminės orbitos nebeįmanomos ir galime laikyti, jog medžiaga iškart įkrenta į SMBH. Diską sudarančių žiedų spinduliai logaritmiškai auga išorės link. Išorinis disko kraštas/spindulys - labiau dirbtinis pasirinkimas, šiame darbe suderintas su SMBH dalelės akrecijos spinduliu.

Kaip būdinga ir akrecijos dalelių metodams, metode apibrėžiamos sąlygos, kada priartėjusi dalelė prijungiama prie disko (Power et al. 2011a). Mūsų atveju iškyla papildoma komplikacija, nes diskas nebėra tik abstraktus maitinimą pristabdantis konteineris - maitinimas priklauso nuo to, kurioje vietoje prie disko prisijungia medžiaga. Į šią problemą mes atsižvelgiame apskaičiuodami apskritimizacijos spindulį $R_{\rm circ} = J^2_{\rm part}/(GM_{\rm BH})$, kur $J_{\rm part}$ yra SPH dalelės judesio kiekio momentas masės vienetui. Tuomet mes panaudojame pačios SPH dalelės skleidimo spindulį ir padaliname medžiagą per visus jos apimamus žiedukus, indėlį pasverdami pagal skleidimo funkcijos vertę ties žieduko viduriu, su prielaida, kad šis prisijungimas ir disko persikonfigūravimas vyksta greičiau nei dinaminė laiko skalė.

Run	FB	$E_{\rm tot.o}$	$E_{\rm tot.i}$	$t_{\rm Edd}$	$t_{\rm stop}$	$M_{\rm acc.tot.}$	$M_{\rm acc.bh.}$	$M_{\rm acc.esc.}$	$M_{\rm peak.disc.}$
		10^{57} erg	10^{55} erg	tūkst. m.		$10^5 M_\odot$			
`nFBr0`	off	5.3	-	98	-	1.17	0.44	0.60	0.42
`nFBr1`	off	5.3	-	163	-	1.18	0.45	0.62	0.41
`nFBr2`	off	5.0	-	137	-	1.10	0.41	0.58	0.46
`nFBr3`	off	5.9	-	145	-	1.29	0.48	0.68	0.46
`FBr0`	on	2.5	7.3	0	181	0.55	0.21	0.28	0.32
`FBr1`	on	3.2	9.2	3	276	0.69	0.26	0.35	0.32
`FBr2`	on	3.3	9.7	66	207	0.71	0.28	0.37	0.39
`FBr3`	on	3.2	9.1	32	219	0.69	0.26	0.35	0.37
`INSTr0`	on	3.3	15.9	107	-	0.44	0.44	-	-
`INSTr1`	on	3.4	16.3	117	-	0.63	0.63	-	-
`INSTr2`	on	3.5	16.5	140	-	0.68	0.68	-	-
`INSTr3`	on	3.5	16.8	142	-	0.63	0.63	-	-

3.1 lentelė: Pagrindiniai rezultatai praėjus $t = 500$ tūkst. m.. „Run“ stulpelyje realizacijos pavadinimas; „FB“ - ar įjungiamas grįžtamasis ryšys. Tolesni stulpeliai rodo įvarių skaičiavimų rezultatus. $E_{\rm tot.o}$ rodo akrecinio disko išlaisvintą energiją, $E_{\rm tot.i}$ rodo ISM absorbuotą energiją (`INST` modeliuose $\eta = 0.1$). $t_{\rm Edd}$ yra laiko tarpas praleistas su viršedingtoniniu šviesiu, $t_{\rm stop}$ - centrinės ertmės susiformavimo (atitinkamai akrecinio disko maitinimo sustabdymo) laiką. $M_{\rm acc.tot.}$ nurodo visą prie akrecinio disko prijungtą masę, $M_{\rm acc.bh.}$ rodo SMBH prarytą masę, $M_{\rm acc.esc.}$ rodo iš akrecinio disko pabėgusią masę ir $M_{\rm peak.esc.}$ nurodo didžiausią akrecinio disko masę pasiektą masę.

Disko evoliuciją aprašo difuzijos lygtis:

$$\frac{\partial \Sigma}{\partial t} = \frac{3}{R}\frac{\partial}{\partial R}\left[\frac{(R-R_{\rm g})^2}{R^{1/2}(R-3R_{\rm g})}\frac{\partial}{\partial R}\left(\nu \Sigma R^{3/2}\frac{R-\frac{1}{3}R_{\rm g}}{(R-R_{\rm g})^2}\right)\right]; \tag{3.2}$$

išvesta pritaikius Paczyński-Wiita (PW) gravitacinį potencialą (Paczyński & Wiita 1980), kuris leidžia gerai atkurti kai kuriuos reliatyvistinius efektus, nesprendžiant pilnų reliatyvumo teorijos lygčių:

$$\phi = \frac{-GM_{\rm BH}}{R-R_{\rm g}}, \tag{3.3}$$

Čia R, tai - atstumas nuo centro, o $R_{\rm g}$ tai - Schwarzschild spindulys. Klampa ν apibrėžta standartiniu α parametrizavimu - $\nu = \alpha c_{\rm s} H$, kur $c_{\rm s}$ yra garso greitis, H yra disko aukštis ir $\alpha = 0.1$ (tipiška vertė) (Shakura & Sunyaev 1973).

Lygtis 3.2 yra sprendžiama skaitmeniškai. Laiko žingsniai yra parenkami adaptyviai, pirmiausia atsižvelgiant į klampą:

$$\Delta t_{\rm est} = {\rm C} \min\left[\Delta t_i\right] = {\rm C}\min\left[\frac{\Delta R_i^2}{\nu_i}\right], \tag{3.4}$$

kur Courant'o faktorius C = 0.01. Po šio vertinimo laiko žingsnis pakoreguojamas užtikrinant sinchronizaciją tarp akrecinio disko dalelės ir disko, tai yra, užtikrinama, kad būtų išpildytos abi salygos: $\Delta t n_{\rm steps} = \Delta t_{\rm sink}$ ir $\Delta t < \Delta t_{\rm est}$.

Turint akrecinio disko būseną galime suskaičiuoti ir kiekvieno jį sudarančio žieduko šviesį:

$$L(R) = 2\pi\left[D\left(R_{\rm out}\right)R_{\rm out} + D\left(R_{\rm in}\right)R_{\rm in}\right]\left(R_{\rm out} - R_{\rm in}\right), \tag{3.5}$$

kur $R_{\rm in}$ ir $R_{\rm out}$ yra atitinkamai kiekvieno žieduko vidiniai ir išoriniai spinduliai. $D(R)$ yra klampos sukelti energijos nuostoliai:

$$D(R) = \frac{3}{8}\frac{\dot{M}}{\pi}\frac{GM_{\rm BH}}{R}\left(\frac{1}{R-R_{\rm g}} - \frac{3^{3/2}R_{\rm g}^{1/2}}{2R^{3/2}}\right)\frac{\left(R-R_{\rm g}\right)^2}{R-\frac{1}{3}R_{\rm g}}. \tag{3.6}$$

Akrecinio disko šviesis tuomet yra kiekvieno iš sudarančių žiedukų šviesių suma. Proporcingai šiam parenkamas grįžtamojo ryšio stiprumas. Šio akrecinio disko spinduliuotės efektyvumas artimas teorinei PW disko vertei $\eta \sim 6.25\%$ (Paczyński & Wiita 1980).

3.3 Rezultatai ir diskusija

Pagrindiniai skaičiavimų rezultatai apibendrinti 3.1 lentelėje. Iš viso suskaičiuoti trijų tipų modeliai: a) `nFB` - modeliai be grįžtamojo ryšio, tačiau akrecija sekama su akrecinio disko dalele, b) `FB` - modeliai su akrecinio disko dalelės

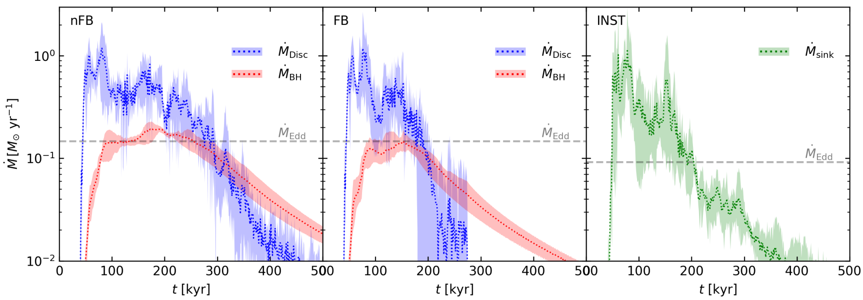

3.3 pav.: Akrecijos disko (mėlyna) ir SMBH (raudona) akrecijos spartos `nFB` (kairėje) ir `FB` (viduryje) modeliuose. Akrecijos sparta `INST` modelyje (dešinėje). linijos nurodo vidutines vertes, užspalvintos sritys - diažiausias/mažiausias vertes tarp stochastiškai skirtingų modelių realizacijų. Pilka horizontali punktyrinė linija rodo Eddington'o akrecijos spartą $\dot{M}_{\rm Edd} = L_{\rm Edd}\eta^{-1}c^{-2}$

kuriamu grįžtamuoju ryšiu ir c) `INST` - modeliai, kuriuose praryta medžiaga iš karto maitina SMBH, o šviesis yra dirbtinai ribojamas iki $L_{\rm Edd}$. Šis ribojimas būtinas, nes tiesioginis SMBH maitinimas lemia nepagrįstai aukštas momentines šviesio vertes. Kiekvienu atveju skaičiuotos keturios realizacijos su skirtingais pradiniais dalelių pasiskirstymais bei turbulencijos lauku.

Esminiai skirtumai tarp šių trijų modelių tipų atsiskleidžia grafike 3.2 pav.. Čia vaizduojami centriniai keli parsekai žiūrint iš viršaus į xy plokštumą. Modeliuose `nFB` tipiškai formuojasi labiau koncentruoti centriniai diskai, nei `INST`. Tuo tarpu `FB` stebima ir atsivėrusi skylė centre. Vienu atveju, `FBr2`, centrinė sistema beveik visiškai suardoma. Šis skirtumas tarp modelių matomas ir akrecijos spartų grafike 3.3 pav., kur tiek `nFB`, tiek `INST` modeliuose akrecinio disko maitinimas (mėlyna ir žalia linijos) vyksta visą modeliuojamą laiką, kai `nFB` įvyksta savireguliacija: čia geriau dvitaškis tolygus šviesis, šiek tiek viršijęs $L_{\rm Edd}$ (be dirbtinio ribojimo) greitai sustabdo tolesnę akreciją, o tolesnis SMBH maitinimas (raudona) vyksta iš akreciniame diske jau sukauptos medžiagos.

Grįžtamajam ryšiui nepristabdžius akrecijos, diską iš viso pamaitina maždaug dvigubai daugiau medžiagos (3.4a pav.). Apie trečdalis šios pamaitina SMBH, tačiau didesnė dalis palieka diską per išorinį kraštą. Šiuo metu mūsų modelis į tai neatsižvelgia - mažo skaičiaus paskirų dujų dalelių grąžinimas į modelį galėtų sukelti nefiziškus netolygumus. Tačiau iš principo toks medžiagos sugrįžimas įmanomas ir galėtų sukelti papildomą akreciją šiai išmestai medžiagai sąveikaujant su aplinkinėmis dujomis, ar net sudaryti pagrindą žvaigždėdarai. Čia svarbu paminėti, kad nemaža dalis medžiagos per kraštą pabėga ir dėl dalelių prijungimo prie akrecinio disko schemos - nemažai medžiagos iškart atsiduria prie išorinio krašto. Ši problema geriausiai sprendžiama keliant modelio skyrą, taip leidžiant dalelėms įgyti mažesnius skleidimo spindulius. Šiuo atveju tai reiškia, kad modelis nuvertina bendrą akreciją ir šviesio vertes galima

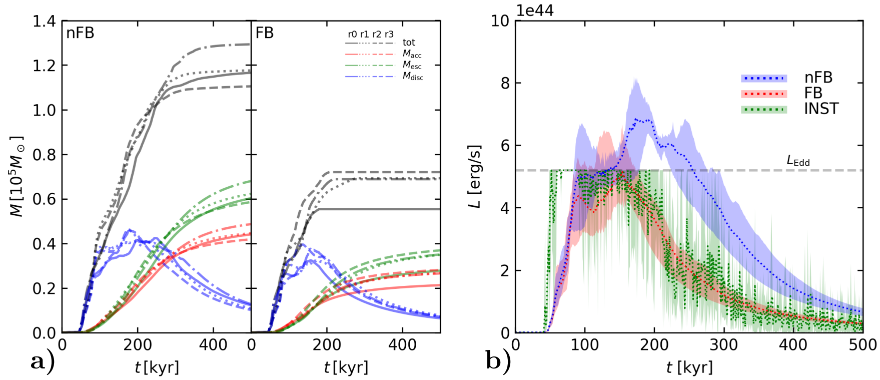

3.4 pav.: **a)** masės augimo kreivės `nFB` (kairėje) ir `FB` (dešinėje) modeliuose. juodai - visa akrecinio disko dalelės prisijungta masė; mėlynai - akrecinio disko masė; raudona - SMBH praryta masė; žalia - iš akrecinio disko pabėgusi masė. Skirtingų stilių linijos rodos rezultatus stochastiškai skirtingose modelių realizacijose. **b)** akrecinio disko šviesio kitimas laike. Užspalvintos linijos rodo didžiausias/mažiausias vertes stochastiškai skirtingose modelių realizacijose. horizontali linija rodo Eddington'o šviesį.

laikyti konservatyviomis.

Šviesio kitimas laike pavaizduotas 3.4b pav.. Esminis skirtumas tarp aktyvumo `FB` ir menamo aktyvumo `nFB`, tai - jų intensyvumas. `nFB` nėra reguliuojančio grįžtamojo ryšio poveikio, todėl akrecinis diskas maitinamas ilgiau, atitinkamai aktyvumas epizodas vyksta ilgiau ir yra stipresnis. Įdomiau yra pastebėti aiškią delsą `FB` modelyje lyginant su `INST`. Ši delsa atsiranda dėl medžiagos judėjimo akreciniu disku. Taip pat `INST` akrecija daug triukšmingesnė. Bendrai energijos daugiau išlaisvinta `INST` modeliuose, tačiau paradoksaliai juose centrai nėra ištuštinami. Šitai geriausiai aiškina tai, jog `INST` atveju grįžtamasis ryšys akimirksniu perduodamas energiją, dalį jos perduoda ir tankiems gumulams. Šie ir greitai vėsta ir potencialiai yra iškart praryjami SMBH, dėl ko dalis grįžtamojo ryšio nėra efektyviai panaudojama medžiagai stumti nuo centro. kartu, dėl L_{Edd} ribojimo, judesio kiekio injekcijos nepakanka tankioms dujoms nustumti.

Įvertinome, kaip šviesio evoliuciją galėtų atkurti paprastesni akrecinio disko dalelės modeliai pagal Power et al. (2011a). Rezultatai pateikti grafike 3.5, čia akrecijos rezultatai įvedami į atskirą akrecinio disko dalės modelį. Naudojami kontrolinio `nFB` modelių rezultatai, nes kituose dujų dinamika yra jau paveikta grįžtamojo ryšio, kuris kistų priklausomai nuo pasirinktų akrecinio disko dalelės parametrų. Juodosios skylės akrecija šiame modelyje aprašoma pagal:

$$\dot{M}_{\mathrm{BH}} = \min\left[M_{\mathrm{disc}}/t_{\mathrm{visc}}, \dot{M}_{\mathrm{Edd}}\right], \qquad (3.7)$$

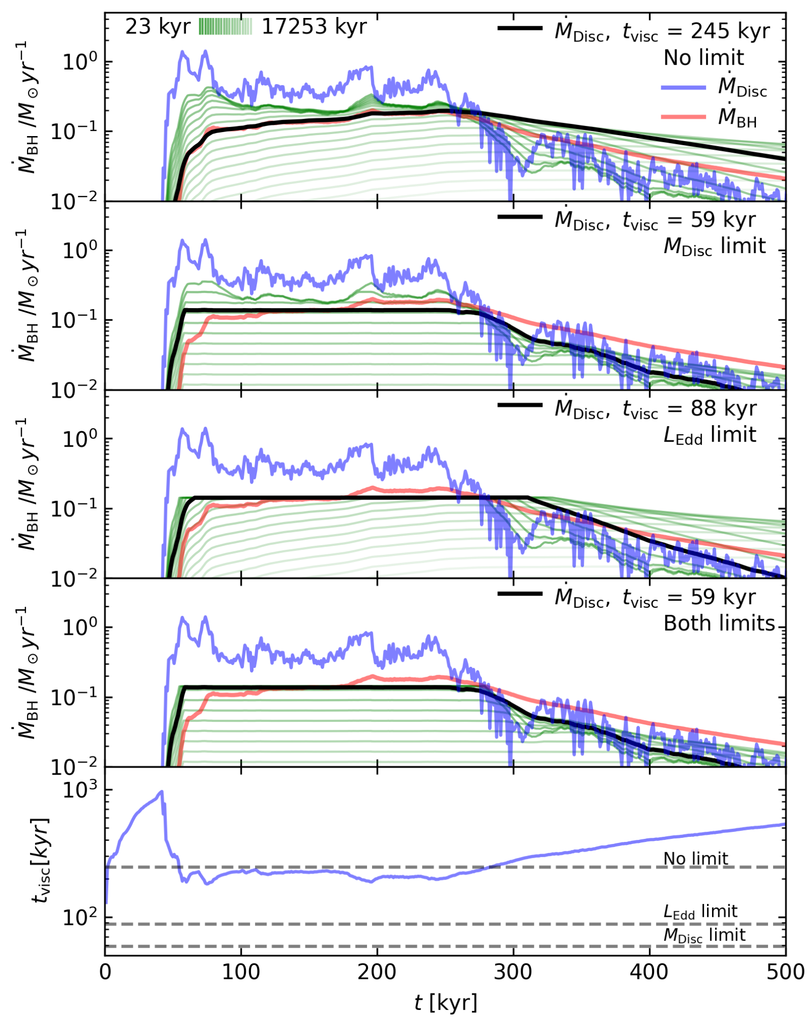

3.5 pav.: Skirtingų „dviejų žingsnių“ akrecijos metodų palyginimas su `ringcode` naudojant `nFBr0` modelio duomenis. Mėlyna ir raudona linijos rodo `nFBr0` modelyje nustatytas, atitinkamai, akrecinio disko ir SMBH maitinimo spartas. Blyškėjančios žalios linijos rodo skaičiavimus su didėjančiomis klampos laiko skalės $t_{\rm visc}$ vertėmis. Juoda linija rodo geriausiai derantį variantą. Apačioje pavaizduotas `nFBr0` modelyje nustatytas klampos laiko skalės $t_{\rm visc} = M_{\rm disc}/\dot{M}_{\rm BH}$ kitimas laike bei geriausiai atitikus iš „dviejų žingsnių“ variantų pastovios $t_{\rm visc}$ vertės.

kur $M_{\rm disc}$ tai yra disko masė suskaičiuota iš akrecijos spartos `nFBr0` modelyje, $t_{\rm visc}$ tai - klampos laiko skalė. Papildomai patikriname modelius ir be Edingtono akrecijos spartos ribojimo $\dot{M}_{\rm Edd}$ bei pritaikę maksimalią stabilią disko masę pagal Pringle (1981):

$$M_{\rm disc,max} \approx \frac{H}{R} M_{\rm BH}, \tag{3.8}$$

kur $H/R = 0.002$.

Grafike 3.5 pav. matome, kad parinkus tinkamą klampos laiko skalę galime atkurti pakankamai uždelstą SMBH maitinimo spartą, tačiau sunku atkurti maitinimo spartą vėlesnėse evoliucijos stadijose. Visgi esminė problema yra ta, kad *teisinga* $t_{\rm visc}$ vertė nėra žinoma prieš pradedant skaičiavimus, o įvertinimas būtų itin sudėtingas. Apatinis grafikas rodo, jog laiko skalė diske kinta, todėl skirtingus disko maitinimo rėžimus derėtų aprašysi skirtingomis ir nebūtinai pastoviomis klampos laiko skalėmis. Gautą tinkamiausią laiko skalę atitinkantis maitinimo spindulys $R_{\rm feed} \sim 2 - 5 \times 10^{-4}$ pc - gerokai mažesnis nei akrecinio disko dalelės akrecijos spindulys 0.01 pc, ar vidutinis praryjamų dalelių apskritimizacijos spindulys $R_{\rm circ} \sim 10^{-3}$ pc. Tai taip pat reiškia, kad atsižvelgimas į dujų judesio kiekio momentą nebūtų pakankamas kriterijus.

3.4 Apibendrinimas

Šiame darbe pristatytas naujas SMBH akrecijos aprašymas, implementuotas hidrodinaminio modeliavimo kode `Gadget-3`. Metodas pagrįstas tiesioginiu 1D standartinio α-parametrizacijos plono akrecinio disko (Shakura & Sunyaev 1973) skliaustai, su Paczyński-Wiita potencialiu (Paczyński & Wiita 1980) sprendimu. Akrecinis diskas prijungtas prie SMBH reprezentuojančios dalelės. Metodas išbandytas jį pritaikius modelyje, kuriame SMBH sparčiai maitinama (panašiame į nagrinėtą 2 skyriuje) po susidūrimo tarp CNR bei jo sukimuisi priešingai judančio MC. Iš viso suskaičiuota 12 realizacijų: keturiose naudotas `FB`, keturiose akrecija vyksta akimirksniu `INST`. Dar keturi, be grįžtamojo ryšio, laikomi kontroliniais `nFB`. Sudsidūrimas stipriai perturbuoja pradinę sistemą, sukelia aktyvumo epizodą; `FB` modeliuose SMBH pamaitinama $M_{\rm acc.tot} \sim 6 \times 10^4\,{\rm M}_\odot$ - perpus mažiau nei `nFB`, $M_{\rm acc.tot} \sim 1.2 \times 10^5\,{\rm M}_\odot$.

- Pritaikius akrecinio disko dalelės metodą SMBH augimo sparta $\dot{M}_{\rm BH}$ sumažėja ir tolygiau pasiskirsto laike; šviesio pokyčiai artimai seka SMBH maitinimo spartą.

- Spinduliuotė išlaisvina $\eta \sim 6.25\%$ įkrentančių dujų rimties masės energijos, kaip ir tikėtasi naudojant Paczyński-Wiita potencialuią; vertė gaunama netaikant dirbtinių ribojimų.

- AGN vėjas `FB` modeliuose pašalina dujas iš centrinių $0.1 - 1$ pc, taip sustabdydamas tolesnę akreciją; daugiau energijos į aplinką išleidę `INST` modeliai to neatkartoja, tikėtina, dėl dirbtinio šviesio ribojimo ir grįžtamojo ryšio nuostolių akrecijai.

- Nors didelis šviesis, $L > 0.3L_{\mathrm{Edd}}$, buvo ~ 0.1 mln. m., centrinė sistema pilnai išardyta tik viename modelyje, `FBr2`.

4 skyrius

Vėjo poveikis netolygiame centriniame telkinyje

Praeituose modeliuose nagrinėjome SMBH maitinimą, bei grįžtamąjį ryšį sąlyginai gerai suprantamoje ~ 10 pc sistemoje panašioje į stebimą mūsų GC (pvz.: Genzel et al. 2010; Ferrière 2012; Bryant & Krabbe 2021). Visgi vienas pagrindinių tiesioginių grįžtamojo ryšio padarinių yra tėkmės, stebimos kiloparsekų masteliuose (Spence et al. 2016). Šios tėkmės galimai susijusios ir su ultra-greitomis (UFO), $v_{\rm w} \sim 0.1$ c pasiekiančiomis, tėkmėmis, aptinkamomis labai arti AGN (Pounds et al. 2003b,a; Tombesi et al. 2010a,b, 2013), nešančiomis panašią kinetinę energiją. Šias tėkmes gali paaiškinti ne vienas teorinis modelis, iš kurių dažniausiai sutinkami yra čiurkšlės (Gaibler et al. 2012; Bourne & Yang 2023; Talbot et al. 2022, 2024), spinduliuotės slėgio poveikis dulkėms (Ishibashi & Fabian 2015; Thompson et al. 2015; Costa et al. 2018) bei AGN vėjas (Costa et al. 2014; King & Pounds 2015).

Įvade minėjome, jog AGN vėjas, priklausomai nuo smūginėje bangoje pasiekiamos temperatūros, gali veikti energijos ar judesio kiekio varymo režimuose. Energijos varymas daug efektyviau kuria tėkmes, nes plėtimuisi naudojamas ne tik judesio kiekis, bet ir karštų dujų plėtimosi darbas (e.g., King 2003; Zubovas & King 2012a; Faucher-Giguère & Quataert 2012; Costa et al. 2014). Tačiau šiuose standartiniuose modeliuose laikomasi prielaidos, jog dujos išsidėsčiusios sferiškai ir tolygiai. Pirminiai stebėjimai gerai atitiko ir šį itin idealizuotą paveikslą - rasti, kaip ir prognozuota, aiškūs sąryšiai tarp AGN šviesio ir tėkmės greičio, masės pernašos spartos, judesio kiekio bei kinetinės galios (Cicone et al. 2014). Tačiau naujesniuose stebimą mūsų GC matomas vis didesnis tėkmių savybių verčių išsibarstymas, esant vienodam AGN šviesiui, ypač žemesnių verčių link (Fluetsch et al. 2019; Lutz et al. 2020). Tai parodo, kad realybė sudėtingesnė ir ISM gumuluotumas gali sudaryti sąlygas energijos ir judesio kiekio varymo režimams veikti vienu metu skirtingose, tą pačią tėkmę sudarančių dujų, fazėse. Intuityviai, sutankėjimų atsiradimas turėtų tiesiog sumažinti AGN vėjo poveikį, visgi ISM vėsimas/kaitimas yra sudėtingas netiesinis procesas ir norint tėkmių evoliuciją išnagrinėti detaliai, tenka pasitelkti ir skaitmeninius modelius.

4.1 Skaitmeninio modelio aprašas

Šiame darbe nagrinėjamas AGN vėjo kuriamos tėkmės plitimas idealizuotoje sferinėje sistemoje - keliuose centriniuose galaktikos kiloparsekuose. Modeliai skirti izoliuoti pokyčius tėkmių evoliucijoje, atsiradusius įtraukus vėsimą ir/arba ISM netolygumą (sukuriamą pradinės turbulencijos).

Skaičiavome dvi modelių grupes - tolygius pavadinome `Smth`, o turbulentiškus `Turb`. Abiem atvejais pradinė dujų masė $M_{\rm gas} \sim 9.4 \times 10^8 {\rm M}_\odot$, o dalelių skaičius $N \sim 10^6$. Dujos išsidėsčiusios sferiškai, tarp $r_{\rm in} = 0.1$ kpc ir $r_{\rm out} = 1$ kpc, jų tankis mažėja didėjant atstumui nuo centro, pagal sąryšį $\rho \propto r^{-2}$. Centre taip pat padėta SMBH atitinkanti dalelė, kurios masė atitinka M-σ saryšį $M_{\rm BH} = M_\sigma\left(\sigma_{\rm b}\right) = 10^8$ ${\rm M}_\odot$; ši praryja daleles priartėjusias prie jos arčiau nei $r_{\rm acc} = 0.01$ kpc, tačiau šiuose modeliuose realistiškos akrecijos nemodeliuojame, todėl ši sąlyga fizikinės prasmės neturi. `Smth` modeliuose taip pat išjungiame dujų savigravitaciją siekdami išvengti papildomų netolygumų formavimosi. `Turb` modeliuose įvedamas pradinis turbulencijos greičių laukas su charakteristiniu greičiu $\sigma_{\rm t} = 149$ km s^{-1} $= \sigma_{\rm b}\left(1 + M_{\rm gas}/M_{\rm b}\right)^{1/2}$, kur $M_{\rm b}$ yra centrinio telkinio masė, aprašytas pagal Dubinski et al. (1995) ir Hobbs et al. (2011). `Turb` modeliai inicijuojami su didesniu medžiagos kiekiu nei `Smth` (maždaug $N_{\rm turb} \sim 1.4N$), nes modeliui leidžiame nusistovėti 1 mln. m. ir per šį laiką dalis medžiagos palieka modeliuojamą tūrį. Modeliui nusistovėjus atrenkame daleles tarp $r_{\rm in} = 0.1$ kpc ir $r_{\rm out} = 1$ kpc; dalelių skaičius artimas $N \simeq 10^6$. `Turb` skaičiuojame keturias tokias realizacijas, kad įvertintume atsitiktinių variacijų turbulentiškame greičių lauke įtaką.

Taip pat modelius skirstome į adiabatiškus `Adia` ir vėstančius/kaistančius `Cool`. Dujų, kurių temperatūra $T < 10^4$ K vėsimą aprašome Mashchenko et al. (2008) vėsimo funkcija, apimančia atominius, molekulinius ir dujinius vėsimo procesus Saulės metalingumo ISM. Aukštesnėse temperatūrose naudojame Sazonov et al. (2005) AGN kuriamo spinduliuotės lauko aprašymą mažo optinio gylio aplinkoje. Optinio gylio prielaida netiksli tankiose dujose - jos perteklinai kaitinamos, todėl susidaro mažiau tankių gumulų. Tačiau bendras šio neatitikimo poveikis vidutinėms tėkmių savybėms nėra didelis (Zubovas & Bourne 2017).

Skaičiavome kelių šviesių modelius: $L = L_{\rm Edd} = 1.26 \times 10^{46}$ erg s^{-1}, $L = 0.3 L_{\rm Edd}$ ir kontrolinius $L = 0$. Grįžtamasis ryšys perduodamas aplinkai naudojant naują, autoriaus sukurtą, `gridWind` metodą. Šio metodo esmė - gretutinė statiška gardelė, kuria propaguojamas vėjas. Kadangi turime sferiškai plintantį vėją, sferiška gardelė aprašoma pagal Malkin (2019), tačiau be nežymios θ modifikacijos. Vėjo sąveikos su ISM sritis nustatoma pasitelkus į *Spatial-hashing* panašų metodą. Konkrečiai, kiekviena dalelė, bei gardelės taškas, be savo realios pozicijos, turi ir indeksus, nurodančius priskyrimą atitinkamai gardelės ląstelei (r, θ, ϕ):

$$r = \lfloor r_{\mathrm{p}} / \Delta r \rfloor , \tag{4.1}$$

$$\theta = \lfloor \theta_{\mathrm{p}} / \Delta \theta \rfloor , \tag{4.2}$$

$$\phi = \lfloor \phi_{\mathrm{p}} / \Delta \phi(\theta) \rfloor , \tag{4.3}$$

kur $r_{\mathrm{p}}, \theta_{\mathrm{p}}, \phi_{\mathrm{p}}$ yra SPH dalelės sferinės koordinatės, $\Delta r, \Delta\theta, \Delta\phi$- gardelės lastelių dydžiai, o $\lfloor x \rfloor$ - *grindų* funkcija. Pastoviu, $v_{\mathrm{wind}} = 0.1$c, greičiu judantis vėjas (King 2003, 2010b) perduoda savo judesio kiekį ir energiją atskirai dalelėms, proporcingai jų indėliui į bendrą tankio lauką atitinkamoje ląstelėje. Paveiktų dalelių laiko žingsniai nedaugiau keturis kartus viršija vėjo laiko žingsnius parenkamus pagal $C\Delta r / v_{\mathrm{wind}}$, kur $C = 0.4$, kriterijų.

4.2 Rezultatai ir diskusija

Pagrindiniai rezultatai pateikti 4.1 lentelėje. Pirma, naudinga paprastai apžvelgti tipinę sistemų evoliuciją ir esminius skirtumus tarp jų. tankio žemėlapiuose 4.1 pav. parodyti ploni, 0.1 kpc, kiekvieno tipo `L1.0` modelių pjūviai ties $t = 0.2$ mln. m., $t = 0.5$ mln. m. ir $t = 0.8$ mln. m. atitinkamai iš kairės į dešinę. Viršutinėse dviejose eilutėse rodomi `Smth` modeliai , apatinėse - `Turb`. `SmthAdia` modelis vystosi kaip ir tikėtasi - tėkmė plinta sferiškai; atsiranda salyginai plonas smūginės bangos regionas. Visgi, tėkmė plinta ~ 20 % lėčiau nei numato analitinis Zubovas & King (2012a) modelis, $\overline{v}_{\mathrm{out}} = 582$ km s^{-1}. To priežastys žinomos, ir galioja kituose modeliuose. Pirma, analitinis sprendinys yra viršutinė riba - detalesnis sprendimas vertinimą sumažintų keletą procentų. Antra, AGN vėjas nėra modeliuojamas hidrodinamiškai, todėl centrinę ertmę užpildo karštos retos dujos; taip iki ~ 50 % šiluminės energijos nenaudojama efektyviam tėkmės plėtimui. `SmthCool` modelyje dėl vėsimo medžiaga sukrenta į smulkesnes struktūras. Šitai galioja tiek tėkmės frontui, kuris pastebimai plonesnis už `SmthAdia`, tiek už tėkmės esančioms dujoms. Tačiau tankio kontrastai mažesni, nei Nayakshin (2014), dėl savigravitacijos neįtraukimo. `SmthCool` taip pat gerokai mažesnis tėkmės vidutinis greitis ~ 300 km s^{-1} maždaug perpus mažesnis, nei `SmthAdia`. `TurbAdia` modelyje pranyksta tvarkingas sferiškas plitimas - vietoje to didesni tankio kontrastai lemia tėkmių judėjimą mažesnio pasipriešinimo plonesnis ir fragmentiškų tėkmių formavimąsį. Šiose tėkmese dujų greičiai didesni, nei `SmthAdia` ir siekia iki ~ 1000 km s^{-1}, tačiau lėčiau slenkančios tankios dujos greičių vidurkį gerokai sumažina. `TurbCool` dėl vėsimo dujos gali sukurti dar ryškesnius vėsimas sukuria dar ryškesnius dujų tankio

Run	gas distribution	cooling?	$L_{\rm AGN}$ $\left(\rm erg\ s^{-1}\right)$	$v_{\rm out}$ $\left(\rm km\ s^{-1}\right)$	$\dot{M}_{\rm out}$ $\left(\rm M_\odot\ m.^{-1}\right)$	$\dot{p}_{\rm out}c/L_{\rm AGN}$	$\dot{E}_{\rm k,out}/L_{\rm AGN}$ $\left(\times 10^{-3}\right)$
SmthAdiaL0.3	smooth	no	3.78×10^{45}	350	642 (348)	11.3 (6.1)	7.64 (4.14)
SmthAdiaL1.0	smooth	no	1.26×10^{46}	582	966 (671)	8.44 (5.86)	9.34 (6.49)
SmthCoolL0.3	smooth	yes	3.78×10^{45}	96.2	229 (166)	1.1 (0.8)	0.20 (0.15)
SmthCoolL1.0	smooth	yes	1.26×10^{46}	304	485 (402)	2.21 (1.83)	1.23 (1.02)
TurbAdiaL0.3	turbulent	no	3.78×10^{45}	312	641 (313)	10 (4.89)	8.70 (4.26)
TurbAdiaL1.0	turbulent	no	1.26×10^{46}	556	1030 (630)	8.64 (5.26)	11.22 (6.83)
TurbCoolL0.3	turbulent	yes	3.78×10^{45}	140	116 (23.3)	0.817 (0.164)	0.78 (0.16)
TurbCoolL1.0	turbulent	yes	1.26×10^{46}	297	710 (309)	3.18 (1.38)	3.38 (1.47)
analytical-L0.3	-	-	3.78×10^{45}	$590 - 790$	$565 - 760$	$17 - 30$	$0.016 - 0.04$
analytical-L1.0	-	-	1.26×10^{46}	$885 - 1180$	$850 - 1130$	$11 - 20$	$0.017 - 0.039$

4.1 lentelė: pagrindiniai modelių rezultatai. pirmi keturi stulpeliai nusako modelio parametrus: Run - modelio pavadinimas; gas distribution - dujų pasiskirstymo tipas; cooling? - ar įjungtas vėsimas; $L_{\rm AGN}$ - pasirinktas AGN šviesis. Toliau seka vidutinės pagrindinių vertintų parametrų vertės: pagal masę pasvertas tėkmės greitis, masės tėkmės sparta, judesio kiekio ir energijos apkrovos faktorių vertės. Šiuose stulpeliuose pirmoji vertė apskaičiuota naudojant tikrąjį AGN gyvavimo laiką, o antroji - stebėjimų $\tau = \tau_{r/v}$. Dvi apatinės eilutės rodo analitinių modelių rezultatus pagal Zubovas & King (2012a). Žemesnis greitis apskaičiuotas atitinkamai susidūrimo srityje, o didesnis - išorinėje smūginėje bangoje; atitinkamai ir stulpeliuose parametruose.

kontrastus; tankis varijuoja keturiomis eilėmis, palyginti su 50 kartų už tėkmės ribų tuo tarpu už tėkmės ribų - iki 50 kartų. Kokybiškai, tėkmių morfologija atrodo panaši į `TurbAdia`, tačiau tėkmės mažesnės bei turi smulkesnių struktūrų.

Toliau nagrinėjant tėkmių savybes pravartu suskaičiuoti masės pernašos spartą ir judesio kiekio bei energijos apkrovos faktorius, kurie apibrėžiami kaip šių tėkmės savybių santykiai su atitinkamomis AGN spinduliuotės lauko savybių vertėmis. Šių radialinius profilius galime įvertinti nagrinėdami siaurus, mūsų atveju pasirinkta $\Delta r = 0.005$ kpc, sferinius kevalus. Tuomet:

$$\dot{M}_{\rm out}(r)\Delta r = \sum_i m_i v_{{\rm rad},i}, \tag{4.4}$$

$$\dot{p}_{\rm out}(r)\Delta r = \sum_i m_i v_{{\rm rad},i}^2, \tag{4.5}$$

ir

$$\dot{E}_{\rm k,out}(r)\Delta r = \sum_i \frac{1}{2} m_i v_{{\rm rad},i}^3, \tag{4.6}$$

kur m_i ir $v_{{\rm rad},i}$ yra, atitinkamai, i-tosios dalelės masė ir greitis. Skaičiuojant atrenkamos dalelės, kurios priklauso tėkmei, jų greitis $v_{\rm rad} > 10$ km s^{-1}. Taip pat kontrolinis modelis `L0` panaudotas atmesti turbulencijos įneštą greičio komponentą. Visą tėkmės nešamą judesio kiekį ir energiją tuomet galima suskaičiuoti sumuojant radialiai.

Skaičiuojant laike ir radialiai vidurkintas vertes, naudojamas masės srautas:

$$\dot{M}_{\rm out,ave} = \frac{M_{\rm out,corr}}{\tau_{\rm out}} = \frac{M_{\rm out} - M_{\rm out,L0}}{\tau_{\rm out}}, \tag{4.7}$$

$M_{\rm out,corr}$ yra masės srautas atmetus judesius, kurių nesukėlė tėkmė, įvertintas pasitelkus kontrolinį modelį. Tačiau aktyvumo laikas, $\tau_{\rm out}$, nėra tiesiogiai stebimas parametras. Dažnai stebėjimuose šis parametras įvertinamas su $\tau_{r/v} = R_{\rm out}/v_{\rm out}$, tačiau tarp darbų apibrėžimai ir prielaidos gali skirtis (Rupke et al. 2005; Cicone et al. 2014; Veilleux et al. 2017). Taip pat siūloma geriau atsižvelgti į geometriją (e.g. Maiolino et al. 2012) ar išdalinti tėkmę į paskirus gumulus (e.g. Cicone et al. 2015; Bischetti et al. 2019). Mes atsižvelgiame į tai, kad mūsų modeliuose skaičiavimų pradžioje jau yra $r_{\rm in} = 100$ pc ertmė, todėl $R_{\rm out} = \overline{r}_{\rm out} - r_{\rm in}$ ir $v_{\rm out} = \overline{v}_{\rm out}$. Svarbu paminėti, kad net gana idealizuotuose pradinėse sąlygose, `Turb` modeliuose nėra vieno konkretaus tėkmės tankų frontą atitinkančio kevalo (žr. 4.1 pav.).

Radialinių masės pernašos bei apkrovos faktorių vidutinių verčių raida pavaizduota 4.2 pav.. `SmthAdia` modeliuose, beveik visą sekamą laiką, su $\tau_{\rm AGN}$ nustatytos vertės didesnės. Po pradinio staigaus šuolio, vertės kurį laiką kinta lėtai kol tėkmė pasiekia pradinio dujų kiauto kraštą. Tuomet, dėl to, kad tėkmė nebepasipildo nauja mase ir jos greitis didėja, stebimas masės srauto

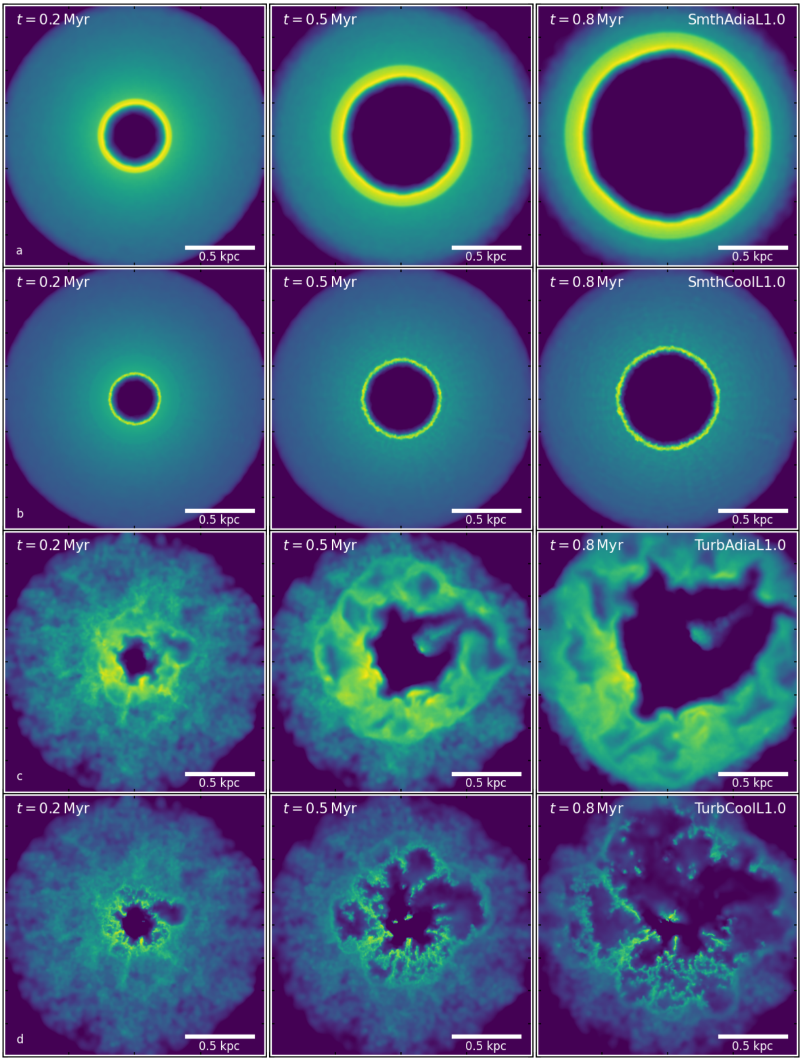

4.1 pav.: Dujų tankis integruotas per 0.1 kpc gylio pjūvį. Stulpeliai iš kairės į dešinę atitinką didesnį praėjusį laiką, $t = 0.2$ mln. m., $t = 0.5$ mln. m. ir $t = 0.8$ mln. m. atitinkamai; ryškesnės spalvos reiškia didesnį dujų tankį.

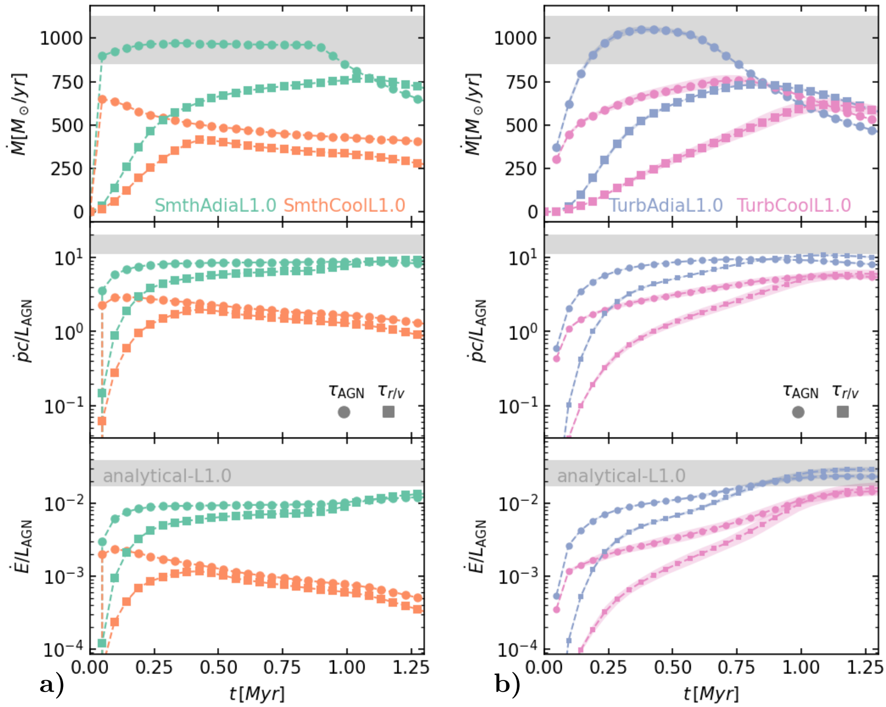

4.2 pav.: **a)** vidutinių tėkmės masės pernašos spartų (viršuje), judesio kiekio ir energijos apkrovos faktorių (atitinkamai viduryje ir apačioje) verčių kitimas laike `Smth` modeliuose. Apskritimai rodo vertes gautas su $\tau_{\rm AGN}$, o kvadratukai - $\tau_{r/v}$. Pilkai užspalvintos sritys rodo analitinių skaičiavimų rezultatus. **b)** tas pat, bet `Turb` modeliuose.

mažėjimas t^{-1}, tuo pačiu judesio kiekis beveik nekinta, o energija auga (ji proporcinga greičio kvadratui). Vėstančiuose modeliuose `SmthCool` po pirminio šuolio parametrai nuosekliai mažėja dėl energijos nuostolių. `TurbAdia` modeliuose tėkmė sąlyginai greitai prasiveržia pro pradinę sferą, todėl masės srautas pradeda mažėti anksčiau. `TurbCool` modelyje parametrai lėtai auga iki pat $\sim$ 0.75 (1) mln. m., vertinant pagal $\tau_{\rm AGN}$ ($\tau_{r/v}$). Taip nutinka dėl to, kad šiuose aiškiai atsiskiria tankios/vėsios ir retos/karštos dujų fazės.

Rezultatai apibendrinti grafike 4.3 pav.. Jame taip pat parodyti ir `L0.3` modelių rezultatai. Bendras turbulencijos ir vėsimo efektas sumažina masės srautą $\sim$ 25% ($\sim$ 80%), judesio kiekio apkrovos faktorių $\sim$ 60% ($\sim$ 93%) ir energijos apkrovos faktorių $\sim$ 63% ($\sim$ 90%) atitinkamai `L1` (`L0.3`) modeliuose ties $t = 0.5$ mln. m.. Tai kad judesio kiekio apkrovos faktorius `L0.3` modeliuose krenta žemiau vieneto, reiškia, kad šios tėkmės būtų atrodo tarsi varomos tik judesio kiekio. Bendrai, nors mūsų modeliai kokybiškai dera su stebėjimais, visgi nuvertina tiek molekulinių, tiek karštų retų dujų greičius (Fiore et al. 2017;

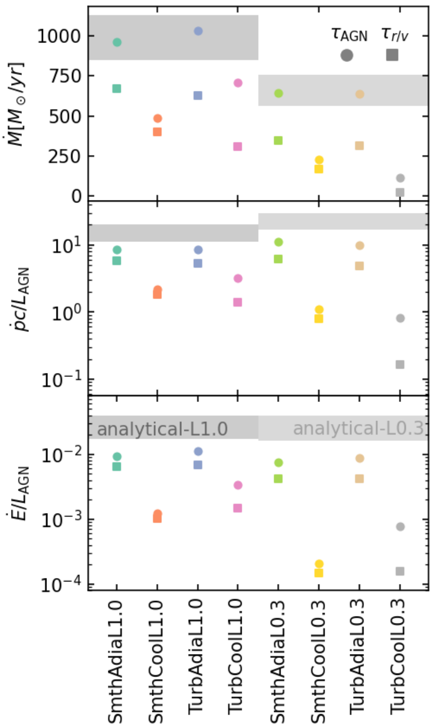

4.3. pav.: Masės pernašos sparta (viršuje), judesio kiekio apkrovos faktorius (viduryje) ir energijos apkrovos faktorius (apačioje) visiems modeliams ties t = 0.5 mln. m.. Pilkai užspalvintos sritys rodo analitinių skaičiavimų rezultatus.

Fluetsch et al. 2019; Lutz et al. 2020), kur jonizuotų dujų tėkmių greičiai siekia $\overline{v}_{\rm ion} \sim 1100$ km s^{-1}, o molekulinių - $\overline{v}_{\rm mol} \sim 450$ km s^{-1}. Greičiai koreliuoja su šviesiu ir ties aukštesnėmis $L_{\rm AGN} \sim (0.3-1) \times 10^{46}$ erg s^{-1} rėžių vertėmis, molekulinių srautų greičiai gali siekti ir ~ 650 km s^{-1}. Šiuos skirtumus dalinai paaiškina keli mūsų idealizuoto modelio supaprastinimai. Pirmiausia, mūsų vėsimo receptas daro prielaidą, jog dujos optiškai retos. Ši prielaida akivaizdžiai klaidinga tankiuose gumuluose, dėl ko vėsimas, tikėtina, yra nepagrįstai greitas. Prie šio efekto prisideda ir dujų savigravitacijos neįtraukimas - šis leidžia geriau izoliuoti būtent vėsimo/turbulencijos efektus, tačiau kartu su efektyviu vėsimu, tikėtina, mažina fragmentaciją tėkmėse, ką matome modeliuose, kuriuose savigravitacija įjungta (Nayakshin & Zubovas 2012; Zubovas et al. 2013). Galiausiai, svarbus aspektas yra vėjo hidrodinamikos nemodeliavimas. Ši problema greičiausiai svarbi ir kosmologiniuose modeliuose, kur AGN grįžtamasis ryšys aprašomas tiesiogine kinetinės ar šiluminės energijos injekcija kaimynėms (e.g. Booth & Schaye 2009; Vogelsberger et al. 2014; Tremmel et al. 2017; Davé et al. 2019; Nelson et al. 2019a). Yra skaitmeninių modelių, kuriuose šios problemos nėra, pavyzdžiui Costa et al. (2020a) sukūrė `BOLA` metodą ir jį implementavo judančios adaptyvios gardelės kode `AREPO`. Šiuo atveju vyksta pačio vėjo injekcija arti SMBH. Tačiau šią problemą verta nagrinėti ir SPH modeliuose. Paprasčiausias problemos apėjimas būtų skaitinio faktoriaus, sustiprinančio vėjo poveikį, įvedimas. Taip pat, naudojant mūsų grįžtamojo ryšio aprašymą, vėjo savybes galima aprašyti analitiškai iki vėjo/ISM sąveikos srities. Tokiu būdu į slėgį būtų galima atsižvelgti teisingai ir anizotropiškų tėkmių atveju.

Iš stebėjimų taip pat nustatyta, kad tėkmių greičiai priklauso nuo AGN šviesio kaip $L^{0.16-0.29}$, o masės srautas $\dot{M}_{\rm out} \propto L^{0.76-1.29}$ (Fiore et al. 2017) - šios nedera su mūsų rezultatais ar analitiniais vertinimais. Tačiau tarus, jog $\sigma_{\rm b} \propto M_{\rm BH}^{1/4} \propto (L_{\rm AGN}/l)^{1/4}$, kur $l \equiv L_{\rm AGN}/L_{\rm Edd}$ yra Eddington'o santykis, randame modifikuotą analitinę išraišką greičiui:

$$v_{\rm out} \propto f_{\rm g}^{-1/3} L_{\rm AGN}^{1/6}, \tag{4.8}$$

ir masės srautui:

$$\dot{M}_{\rm out} \propto f_{\rm g}^{2/3} L_{\rm AGN}^{2/3}, \tag{4.9}$$

taigi priartėjame prie nustatytų verčių neatsižvelgę į tikėtiną $f_{\rm g}$ koreliaciją su AGN šviesiu. Į šį aspektą bus įdomu atsižvelgti detaliau netolimoje ateityje, kai bus daugiau tėkmių stebėjimų galaktikose su nustatytomis SMBH masėmis.

4.3 Apibendrinimas

Šiame darbe išnagrinėta AGN tėkmių raidos priklausomybė nuo turbulencijos, vėsimo bei jų tarpusavio sąveikos idealizuotuose galaktikų centriniuose telkiniuose.

- Tėkmės adiabatiškose modeliuose be turbulencijos plinta sferiškai simetriškai, tačiau lėčiau nei numato analitinis modelis; taip nutinka todėl, kad AGN vėjas nėra nuosekliai sekamas hidrodinamiškai, todėl dalis šiluminės energijos išnaudojama centro užpildymui karštomis dujomis.

- Turbulencija be vėsimo nemažina vėjo poveikio ISM efektyvumo; vėjo poveikio sutelkimas karštose retose srityse padidina tėkmės kinetinę energiją.

- Vėsimas reikšmingai, keliomis eilėmis, sumažina tėkmės energiją.

- Modeliuose su vėsimu ir turbulencija, vėsios dujos dominuoja masės sraute, vėsios ir karštos turi panašų judesio kiekio apkrovos faktorių, tačiau karšta fazė dominuoja pagal energijos apkrovos faktorių; tai kokybiškai atitinka stebėjimus

- Tipiškai stebėjimuose naudojamas masės srauto įvertis $\dot{M}_{\rm out} = M_{\rm out} v_{\rm out} R_{\rm out}^{-1}$ apie du kartus mažesnis, nei tikrasis, skaičiuotas naudojant žinomą tikrąją AGN gyvavimo trukmę. Judesio kiekio, bei energijos apkrovos faktorių vertės atitinkamai mažesnės.

- Turbulencijos ir vėsimo poveikis tėkmės raidai priklauso ir nuo AGN šviesio. $L_{\mathrm{AGN}} = L_{\mathrm{Edd}}$ atveju turbulencijos sukelti netolygumai leidžia įkaitinti retas dujas, tačiau tai neįvyksta $L_{\mathrm{AGN}} = 0,3L_{\mathrm{Edd}}$ atveju. Vėsių tankių dujų gumulai gali atlaikyti silpnesnį AGN šviesį.

5 skyrius

Apibendrinimas ir išvados

Šiame darbe siekta ištirti SMBH akreciją bei grįžtamąjį ryšį galaktikų centruose. Tyrimui naudoti idealizuoti hidrodinaminiai modeliai ir siekta izoliuoti konkrečius su SMBH maitinimu, ir dėl jo atsirandančiu grįžtamuoju ryšiu susijusius galaktikų raidos aspektus. Pirmuose dvejuose darbuose pasirinkta nagrinėti sistemą, panašią į Paukščių Tako galaktikos centrą. Konkrečiai, modeliuoti susidūrimai tarp su Sgr A*siejamo SMBH supančio dujų žiedo, vadinamo CNR, ir įkrentančio dujų debesies. Šis pasirinkimas pagrįstas tuo, kad mūsų Galaktije yra stebimas ne vienas praeities aktyvumo požymis (*Fermi*, *eRosita* burbulai, 430-pc radijo burbulai, *rentgeno kaminai* ir pan.). Be to galima tiek stebėjimais, tiek modeliais pagrįstai teigti, jog Galaktikos centras bus aktyvus ir ateityje. Šis pasirinkimas leido priderinti modelius prie sąlyginai gerai suprantamos sistemos. Tuo pačiu, mūsų Galaktika iš esmės nėra kažkuo išskirtinė, todėl išvados nėra išskirtinai taikytinos tik jai.

Pirmiausia (2 skyriuje) nagrinėtas stipriai idealizuotas susidūrimas tarp CNR ir įkrentančio molekulinio debesies. Sąlyginai paprasta sistema buvo realizuota po 4 kartus su kiekvienu žiedo/debesies susidūrimo iš 12 pasirinktų susidūrimo kampo verčių. Kadangi CNR bei įkrentančio debesies masės nedominuoja gravitaciškai, pasirinkta išjungti dujų savigravitaciją, paliekant tik išorinį SMBH, žvaigždžių ir tamsiosios materijos kuriamą potencialą, bei taikyti sąlyginai paprastą vėsimo aprašymą, priklausantį nuo orbitinio dinaminio laiko. Dėl to, modelių dinaminė evoliucija nepriklauso nuo pasirinktos dujų masės. Modeliai inicijuoti pasirinkus minimalią CNR masę leistina pagal stebėjimus, todėl modelyje nustatytas SMBH maitinimo vertes galime laikyti apatine riba.

Sistemų raida atitinka intuiciją: didesnis susidūrimo kampas lėmė didesnę sistemos perturbaciją ir SMBH maitinimą. Visgi esminis rezultatas yra netiesioginis CNR ribinio ciklo hipotezės pagrindimas. Šiuose modeliuose aiškiai matosi, jog su CNR susidūrusios dujos dažniausiai prisijungia prie jau esamos struktūros, taip augindamos dujų rezervuarą. Reti priešpriešiniai susidūrimai, ar tiesiog žiedo nestabilumai, gali gali sukelti AGN epizodą. Tokie susidūrimai galėtų vykti kas $60 - 140$ mln. m..

SMBH maitinimo vertes panaudojome atskirame akrecinio disko modelyje, taip įvertinome ir galimo aktyvumo epizodo šviesio raidą, kuri stipriai priklauso nuo pasirenkamų laisvųjų parametrų.

Sekančiame darbe (2 skyrius) buvo sukurtas naujas subraiškinis SMBH akrecijos modulis. Šis paremtas nuosekliu 1D standartinio akrecinio disko modelio sprendimu kartu su pagrindiniu hidrodinaminiu modeliu. Modelis leidžia atsisakyti laisvųjų parametrų, kaip klampos laiko skalė, tipiškai naudojamų dirbtinai praskleisti/uždelsti SMBH maitinimą hidrodinaminiuose modeliuose.

Modelis pritaikytas detalesniam prieš tai nagrinėto Aplinkbranduolinio žiedo susidūrimo su molekuliniu debesiu inicijuoto AGN epizodo sprendimui. Šiuo atveju pasirinkta modeliuoti realistiškesnę sistemą, pritaikius detalų vėsimo/kaitinimo AGN aplinkoje aprašą. Nagrinėtos 4 stochastiškai skirtingos realizacijos modelių su akrecinio disko dalele aprašoma akrecija `FB`, akimirksniu vykstančia akrecija `INST` bei kontroliniai modeliai, kur sekama akrecija, tačiau nevyksta grįžtamojo ryšio injekcija `nFB`.

Visuose modeliuose susidūrimas lėmė reikšmingą SMBH maitinimą, bei iššauktą AGN epizodą. `FB` modeliuose AGN vėjas išstūmė dujas iš centrinės sistemos dalies, taip sustabdydamas tolesnę akreciją. Be dirbtinių ribojimų, dažnai taikomų tokiuose modeliuose, įvyko savireguliacija ir $L_{\rm Edd}$ riba buvo peržengta. `INST` modeliuose, tikėtina būtent dėl dirbtinio šviesio ribojimo ties $L_{\rm Edd}$ bei dėl energijos praradimų tankiuose prarytuose gumuluose dėl delsos nebuvimo, centrinė dalis ištuštinta nebuvo.

Tik vienoje realizacijoje, `FBr2`, centrinė sistema buvo beveik visiškai išardyta. Tai reiškia, kad grįžtamasis ryšys nebūtinai sustabdytų žvaigždėdarą ir SMBH aplinkoje.

Trečias modelių rinkinys (pristatomas 4 skyriuje) buvo skirtas išnagrinėti tėkmių raidą stipriai idealizuotame galaktikos centriniame telkinyje. Konkrečiai norėta izoliuoti turbulencijos, vėsimo bei jų tarpusavio sąveikos įtaką tėkmės raidai. Modelyje pritaikytas ir naujas grįžtamojo ryšio injekcijos metodas. Jame vėjas propaguojamas statiška gardele, dėl ko galima itin sparčiai nustatyti vėjo/ISM sąveikos sritis.

Tam kad izoliuotume paskirus efektus, nagrinėti 4 tipų modeliai. Paprasčiausiu atveju nagrinėta tolygi nevėstanti sistema (pavadinta `SmthAdia`). Atskirai vertiname vėsimo ir turbulencijos/gumuluotumo įtakas modeliuose `SmthCool` ir `TurbAdia`. O bendrą jų poveikį nagrinėjame `TurbCool` modeliuose. Tėkmės adiabatiškuose modeliuose be turbulencijos plinta sferiškai, tačiau lėčiau nei numato analitiniai modeliai. Turbulencija neįtraukus vėsimo sutelkia tėkmių poveikį retose karštose srityse. Vėsimas, savo ruožtu, reikšmingai, keliomis eilėmis, sumažina tėkmės energiją. Tą lemia šiluminiai nuostoliai vėstančiuose tankiuose gumuluose. Modeliuose su vėsimu ir turbulencija vėsios dujos dominuoja masės sraute, vėsios ir karštos turi panašų judesio kiekio apkrovos faktorių, tačiau karšta fazė dominuoja žiūrint į energijos apkrovos faktorių; tai kokybiškai atitinka stebėjimus stebėjimų rezultatus.

Tipiškai stebėjimuose naudojamas masės srauto įvertis $\dot{M}_{\rm out} = M_{\rm out} v_{\rm out} R_{\rm out}^{-1}$ apie du kartus mažesnis, nei tikrasis, skaičiuotas naudojant žinomą tikrąją AGN gyvavimo trukmę. Judesio kiekio bei energijos vertės taip pat atitinkamai mažesnės.

Turbulencijos ir vėsimo poveikis tėkmės raidai priklauso ir nuo AGN šviesio. $L_{\rm AGN} = L_{\rm Edd}$ atveju turbulencijos sukelti netolygumai leidžia įkaitinti retas dujas, tačiau tai neįvyksta $L_{\rm AGN} = 0.3 L_{\rm Edd}$ atveju. Vėsių tankių dujų gumulai gali atlaikyti silpnesnį AGN šviesį. Efektas gali būti dar stipresnis atsisakius klaidingos mažo optinio gylio prielaidos tankiuose gumuluose, bei modeliuojant didesne skyra. Bendrai tai bent dalinai dera ir su ankstesnio, mažesnio modelio rezultatais.

5.1 Išvados

1. CNR sistemos morfologijos raida po susidūrimo su MC priklauso nuo susidūrimo kampo: su $\gamma \leq 105°$, pradinė sistema nežymiai perturbuojama; susiformuoja naujas, masyvesnis ir nežymiai didesnis CNR; $\gamma > 105°$ reikšmingai perturbuoja sistemą, nauja sistema labiau koncentruota centre; ekstremaliu atveju, $\gamma > 150°$, iki pusės pradinės sistemos masės pamaitina SMBH; tokio maitinimo pakaktų palaikyti reikšmingą aktyvumo epizodą.

2. Kampų intervalas, nesukeliantis aktyvumo epizodo, penkis kartus didesnis nei kampų intervalas, sukeliantis aktyvumo epizodą. Tai reiškia, kad CNR masė galėtų reikšmingai išaugti iki priešpriešinio susidūrimo; tai dera su CNR ribinio ciklo hipoteze.

3. Naujas akrecinio disko dalelės metodas `ringcode` leidžia tolygiai maitinti SMBH. Taip pat, leidžia grįžtamąjį ryšį susieti su standartinio akrecinio disko modelio evoliucija, kur šviesis seka tikrąjį SMBH maitinimą, uždelstą laike palyginus su pačio disko maitinimu.

4. Grįžtamasis ryšys modeliuose, kuriuose naudotas `ringcode`, pašalina dujas iš centrinių $0.1-1$ pc, tokiu būdu sustabdomas tolesnis akrecinio disko maitinimas - vyksta savireguliacija.

5. `gridWind` grįžtamojo ryšio injekcijos schema efektyviai perduoda grįžtamojo ryšio poveikį aplinkai, tačiau būtina atsižvelgti į hidrodinaminį slėgį norint prislopinti energijos nuostolius.

6. Vėsimas tankiuose dujų gumuluose 1-2 eilėmis sumažina tėkmės energiją tolygiuose ir maždaug eile turbulentiškuose modeliuose. Dėl gumuluotumo turbulentiškame modelyje be vėsimo vyksta kolimacija, lemianti nežymiai didesnę tėkmės energiją.

7. Analizuojant stebėjimų duomenis nustatomos masės srauto, judesio kiekio bei energijos apkrovos faktorių vertės iki dviejų kartų per mažos dėl netikslaus tėkmės gyvavimo laiko įverčio.

8. Visi modeliai rodo, jog tankias dujas pašalinti iš galaktikos centro sunku; Net ir stiprus AGN aktyvumo epizodas, siekiantis $L_{\rm Edd}$, nebūtinai išstumia tankiausias dujas. Tokių dujų buvimas centriniuose regionuose gali sudaryti sąlygas žvaigždėdarai net ir AGN epizodo metu.

Bibliography

Abbott, B. P., Abbott, R., Abbott, T. D., et al. 2016a, Phys. Rev. Lett., 116, 061102

Abbott, B. P., Abbott, R., Abbott, T. D., et al. 2016b, Phys. Rev. Lett., 116, 241103

Abbott, B. P., Abbott, R., Abbott, T. D., et al. 2017, Phys. Rev. Lett., 119, 161101

Abbott, R., Abbott, T. D., Abraham, S., et al. 2020, Phys. Rev. Lett., 125, 101102

Abramowicz, M. A. 2009, A&A, 500, 213

Abramowicz, M. A., Czerny, B., Lasota, J. P., & Szuszkiewicz, E. 1988, ApJ, 332, 646

Abramowicz, M. A. & Fragile, P. C. 2013, Living Reviews in Relativity, 16, 1

Agüero, M. P., Díaz, R. J., & Dottori, H. 2016, International Journal of Astronomy and Astrophysics, 6, 219

Alig, C., Burkert, A., Johansson, P. H., & Schartmann, M. 2011, MNRAS, 412, 469

Alig, C., Schartmann, M., Burkert, A., & Dolag, K. 2013, ApJ, 771, 119

Anglés-Alcázar, D., Özel, F., & Davé, R. 2013, ApJ, 770, 5

Anglés-Alcázar, D., Davé, R., Faucher-Giguère, C.-A., Özel, F., & Hopkins, P. F. 2016, MNRAS, 464, 2840

Antonucci, R. 1993, ARA&A, 31, 473

Asmus, D. 2019, MNRAS, 489, 2177

Audibert, A., Combes, F., García-Burillo, S., et al. 2019, A&A, 632, A33

Audibert, A., Combes, F., García-Burillo, S., et al. 2021, A&A, 656, A60

Audibert, A., Combes, F., García-Burillo, S., & Salomé, P. 2017, FSPAS, 4, 58

Bakes, E. L. O. & Tielens, A. G. G. M. 1994, ApJ, 427, 822

Balbus, S. A. & Hawley, J. F. 1991, ApJ, 376, 214

Balick, B. & Brown, R. L. 1974, ApJ, 194, 265

Balsara, D. S. 1995, Journal of Computational Physics, 121, 357

Bambi, C. 2020, in Multifrequency Behaviour of High Energy Cosmic Sources - XIII. 3-8 June 2019. Palermo, 28

Bartko, H., Martins, F., Fritz, T. K., et al. 2009, ApJ, 697, 1741

Bartko, H., Martins, F., Trippe, S., et al. 2010, ApJ, 708, 834

Beckwith, K., Hawley, J. F., & Krolik, J. H. 2006, arXiv e-prints, astro

Begelman, M. C., Scepi, N., & Dexter, J. 2022, MNRAS, 511, 2040

Bennert, V. N., Treu, T., Ding, X., et al. 2021, ApJ, 921, 36

Bennett, J. S. & Sijacki, D. 2020, MNRAS, 499, 597

Bieri, R., Dubois, Y., Rosdahl, J., et al. 2017, MNRAS, 464, 1854

Binney, J., Gerhard, O. E., Stark, A. A., Bally, J., & Uchida, K. I. 1991, MNRAS, 252, 210

Bischetti, M., Piconcelli, E., Feruglio, C., et al. 2019, A&A, 628, A118

Bisnovatyi-Kogan, G. S. & Ruzmaikin, A. A. 1976, Ap&SS, 42, 401

Bland-Hawthorn, J., Maloney, P. R., Sutherland, R., et al. 2019, ApJ, 886, 45

Bland-Hawthorn, J., Maloney, P. R., Sutherland, R. S., & Madsen, G. J. 2013, ApJ, 778, 58

Blandford, R., Meier, D., & Readhead, A. 2019, ARA&A, 57, 467

Blandford, R. D. & McKee, C. F. 1982, ApJ, 255, 419

Blandford, R. D. & Znajek, R. L. 1977, MNRAS, 179, 433

Boehle, A., Ghez, A. M., Schödel, R., et al. 2016, ApJ, 830, 17

Bolton, C. T. 1972, Nature, 235, 271

Bondi, H. 1952, MNRAS, 112, 195

Bondi, H. & Hoyle, F. 1944, MNRAS, 104, 273

Bonnell, I. A. & Rice, W. K. M. 2008, Science, 321, 1060

Booth, C. M. & Schaye, J. 2009, MNRAS, 398, 53

Bordoloi, R., Fox, A. J., Lockman, F. J., et al. 2017, ApJ, 834, 191

Bourne, M. A., Fiacconi, D., Sijacki, D., Piotrowska, J. M., & Koudmani, S. 2024, MNRAS, 534, 3448–3477

Bourne, M. A. & Nayakshin, S. 2013, MNRAS, 436, 2346

Bourne, M. A., Nayakshin, S., & Hobbs, A. 2014, MNRAS, 441, 3055

Bourne, M. A. & Sijacki, D. 2017, MNRAS, 472, 4707

Bourne, M. A. & Sijacki, D. 2021, MNRAS, 506, 488

Bourne, M. A., Sijacki, D., & Puchwein, E. 2019, MNRAS, 490, 343

Bourne, M. A. & Yang, H.-Y. K. 2023, Galaxies, 11, 73

Bourne, M. A., Zubovas, K., & Nayakshin, S. 2015, MNRAS, 453, 1829

Bryant, A. & Krabbe, A. 2021, New A Rev., 93, 101630

Buchner, J. 2024, A&A, 689, L2

Burke, C. J., Shen, Y., Blaes, O., et al. 2021, Science, 373, 789

Busch, G., Eckart, A., Valencia-S., M., et al. 2017, A&A, 598, A55

Capellupo, D. M., Netzer, H., Lira, P., Trakhtenbrot, B., & Mejía-Restrepo, J. 2015, MNRAS, 446, 3427

Carter, B. 1971, Phys. Rev. Lett., 26, 331

Cattaneo, A., Faber, S. M., Binney, J., et al. 2009, Nature, 460, 213

Chandrasekhar, S. 1931, ApJ, 74, 81

Chang, C.-J. & Kiang, J.-F. 2024, Universe, 10, 279

Chen, S., Laor, A., Behar, E., et al. 2024, arXiv e-prints, arXiv:2408.15934

Christopher, M. H., Scoville, N. Z., Stolovy, S. R., & Yun, M. S. 2005, ApJ, 622, 346

Cicone, C., Maiolino, R., Gallerani, S., et al. 2015, A&A, 574, A14

Cicone, C., Maiolino, R., Sturm, E., et al. 2014, A&A, 562, A21

Ciotti, L., Lanzoni, B., & Volonteri, M. 2007, ApJ, 658, 65

Ciotti, L. & Ostriker, J. P. 2007, ApJ, 665, 1038

Ciotti, L., Pellegrini, S., Negri, A., & Ostriker, J. P. 2017, ApJ, 835, 15

Clarke, J. P., Wegg, C., Gerhard, O., et al. 2019, MNRAS, 489, 3519

Combes, F. 2019, arXiv e-prints, arXiv:1911.00707

Combes, F., García-Burillo, S., Casasola, V., et al. 2014, A&A, 565, A97

Cossins, P. J. 2010, PhD thesis, PhD Thesis, 2010

Costa, T., Pakmor, R., & Springel, V. 2020a, MNRAS, 497, 5229

Costa, T., Pakmor, R., & Springel, V. 2020b, MNRAS, 497, 5229

Costa, T., Rosdahl, J., Sijacki, D., & Haehnelt, M. G. 2018, MNRAS, 479, 2079

Costa, T., Sijacki, D., & Haehnelt, M. G. 2014, MNRAS, 444, 2355

Costa, T., Sijacki, D., & Haehnelt, M. G. 2015, MNRAS, 448, L30

Courant, R., Friedrichs, K., & Lewy, H. 1928, Mathematische Annalen, 100, 32

Crain, R. A., Schaye, J., Bower, R. G., et al. 2015, MNRAS, 450, 1937

Creasey, P. 2018, Astronomy and Computing, 25, 159

Cuadra, J., Armitage, P. J., Alexander, R. D., & Begelman, M. C. 2009, Monthly Notices of the Royal Astronomical Society, 393, 1423

Cuadra, J., Nayakshin, S., & Martins, F. 2008, MNRAS, 383, 458

Cullen, L. & Dehnen, W. 2010, MNRAS, 408, 669

Curd, B., Emami, R., Anantua, R., et al. 2023, MNRAS, 519, 2812

Curtis, M. & Sijacki, D. 2015, MNRAS, 454, 3445

Curtis, M. & Sijacki, D. 2016, MNRAS, 457, L34

Czerny, B. 2019, Universe, 5, 131

Czerny, B. & Naddaf, M. H. 2018, in Accretion Processes in Cosmic Sources - II, 6

Davé, R., Anglés-Alcázar, D., Narayanan, D., et al. 2019, MNRAS, 486, 2827

Dehnen, W. & Aly, H. 2012, MNRAS, 425, 1068

Dexter, J., Tchekhovskoy, A., Jiménez-Rosales, A., et al. 2020, MNRAS, 497, 4999

Di Matteo, T., Springel, V., & Hernquist, L. 2005, Nature, 433, 604

Do, T., Witzel, G., Gautam, A. K., et al. 2019, ApJ, 882, L27

Dong, W., Lao, Y., Kaess, M., & Koltun, V. 2021, arXiv e-prints, arXiv:2110.00511

Dubinski, J., Narayan, R., & Phillips, T. G. 1995, ApJ, 448, 226

Dubois, Y., Volonteri, M., Silk, J., Devriendt, J., & Slyz, A. 2014, MNRAS, 440, 2333

Eardley, D. M. & Press, W. H. 1975, ARA&A, 13, 381

Eckart, A. & Genzel, R. 1996, Nature, 383, 415

Edgar, R. 2004, New A Rev., 48, 843

Ehlert, K., Weinberger, R., Pfrommer, C., Pakmor, R., & Springel, V. 2023, MNRAS, 518, 4622

Einstein, A. 1915, Sitzungsberichte der Königlich Preußischen Akademie der Wissenschaften (Berlin), Seite 844-847., 844

Elías-Chávez, M., Longinotti, A. L., Krongold, Y., et al. 2024, MNRAS, 532, 1564

Event Horizon Telescope Collaboration, Akiyama, K., Alberdi, A., et al. 2022, ApJ, 930, L12

Event Horizon Telescope Collaboration, Akiyama, K., Alberdi, A., et al. 2019, ApJ, 875, L1

Fabian, A. C. 2012, ARA&A, 50, 455

Fabian, A. C., Iwasawa, K., Reynolds, C. S., & Young, A. J. 2000, PASP, 112, 1145

Faucher-Giguère, C.-A. & Quataert, E. 2012, MNRAS, 425, 605

Ferrarese, L. & Merritt, D. 2000, ApJ, 539, L9

Ferrière, K. 2012, A&A, 540, A50

Feruglio, C., Fiore, F., Carniani, S., et al. 2015, A&A, 583, A99

Feruglio, C., Maiolino, R., Piconcelli, E., et al. 2010, A&A, 518, L155+

Filloux, C., Durier, F., Pacheco, J. A. F., & Silk, J. 2010, International Journal of Modern Physics D, 19, 1233

Finkelstein, D. 1958, Physical Review, 110, 965

Fiore, F., Feruglio, C., Shankar, F., et al. 2017, A&A, 601, A143

Fluetsch, A., Maiolino, R., Carniani, S., et al. 2021, MNRAS, 505, 5753

Fluetsch, A., Maiolino, R., Carniani, S., et al. 2019, MNRAS, 483, 4586

Fox, A. J., Frazer, E. M., Bland-Hawthorn, J., et al. 2020, ApJ, 897, 23

Frank, J., King, A., & Raine, D. J. 2002, Accretion Power in Astrophysics: Third Edition

Fritz, T. K., Chatzopoulos, S., Gerhard, O., et al. 2016, ApJ, 821, 44

Gaburov, E., Johansen, A., & Levin, Y. 2012, ApJ, 758, 103

Gaibler, V., Khochfar, S., Krause, M., & Silk, J. 2012, MNRAS, 425, 438

Gammie, C. F. 2001, ApJ, 553, 174

García-Burillo, S., Alonso-Herrero, A., Ramos Almeida, C., et al. 2021, A&A, 652, A98

García-Burillo, S., Combes, F., Ramos Almeida, C., et al. 2019, A&A, 632, A61

García-Burillo, S., Combes, F., Schinnerer, E., Boone, F., & Hunt, L. K. 2005, A&A, 441, 1011

García-Burillo, S., Hicks, E. K. S., Alonso-Herrero, A., et al. 2024, A&A, 689, A347

Garland, I. L., Fahey, M. J., Simmons, B. D., et al. 2023, MNRAS, 522, 211

Garland, I. L., Walmsley, M., Silcock, M. S., et al. 2024, MNRAS, 532, 2320

Gaspari, M., Tombesi, F., & Cappi, M. 2020, Nature Astronomy, 4, 10

Gebhardt, K., Bender, R., Bower, G., et al. 2000, ApJ, 539, L13

Generozov, A., Nayakshin, S., & Madigan, A. M. 2022, MNRAS, 512, 4100

Genzel, R., Eisenhauer, F., & Gillessen, S. 2010, Reviews of Modern Physics, 82, 3121

Genzel, R., Watson, D. M., Crawford, M. K., & Townes, C. H. 1985, ApJ, 297, 766

Ghez, A. M., Duchêne, G., Matthews, K., et al. 2003, ApJ, 586, L127

Gillessen, S., Eisenhauer, F., Fritz, T. K., et al. 2009, ApJ, 707, L114

Gingold, R. A. & Monaghan, J. J. 1977, MNRAS, 181, 375

Goicoechea, J. R., Pety, J., Chapillon, E., et al. 2018, A&A, 618, A35

Gong, Y., Cao, Z., Gao, H., & Zhang, B. 2019, MNRAS, 488, 2722

González-Alfonso, E., Fischer, J., Spoon, H. W. W., et al. 2017, ApJ, 836, 11

Górski, K. M., Hivon, E., Banday, A. J., et al. 2005, ApJ, 622, 759

Gu, H.-P., Wang, H.-T., & Shao, L. 2024, Phys. Rev. D, 109, 024058

Guerra, J. A., Lopez-Rodriguez, E., Chuss, D. T., Butterfield, N. O., & Schmelz, J. T. 2023, AJ, 166, 37

Gültekin, K., Richstone, D. O., Gebhardt, K., et al. 2009, ApJ, 698, 198

Hankins, M., Lau, R., Cotera, A., et al. 2020, in American Astronomical Society Meeting Abstracts, Vol. 235, American Astronomical Society Meeting Abstracts #235, 336.02

Häring, N. & Rix, H.-W. 2004, ApJ, 604, L89

Harms, R. J., Ford, H. C., Tsvetanov, Z. I., et al. 1994, ApJ, 435, L35

Harris, C. R., Millman, K. J., van der Walt, S. J., et al. 2020, Nature, 585, 357

Harrison, C. M., Costa, T., Tadhunter, C. N., et al. 2018, Nature Astronomy, 2, 198

Harrison, C. M. & Ramos Almeida, C. 2024, Galaxies, 12, 17

Hastings, E. & Mesit, J. 2005, in , Vol. 3140., 9–17

Hawkins, M. R. S. 2002, MNRAS, 329, 76

He, Z., Liu, G., Wang, T., et al. 2022, Science Advances, 8, eabk3291

Heckman, T. M. & Best, P. N. 2014, ARA&A, 52, 589

Henden, N. A., Puchwein, E., Shen, S., & Sijacki, D. 2018, MNRAS, 479, 5385

Henshaw, J. D., Longmore, S. N., Kruijssen, J. M. D., et al. 2016, MNRAS, 457, 2675

Hewish, A., Bell, S. J., Pilkington, J. D. H., Scott, P. F., & Collins, R. A. 1968, Nature, 217, 709

Heywood, I., Camilo, F., Cotton, W. D., et al. 2019, Nature, 573, 235

Hickox, R. C. & Alexander, D. M. 2018, ARA&A, 56, 625

Hobbs, A. & Nayakshin, S. 2009, MNRAS, 394, 191

Hobbs, A., Nayakshin, S., Power, C., & King, A. 2011, MNRAS, 413, 2633

Hobbs, A., Power, C., Nayakshin, S., & King, A. R. 2012, MNRAS, 421, 3443

Hönig, S. F. 2019, ApJ, 884, 171

Hopkins, P. F. 2015, MNRAS, 450, 53

Hopkins, P. F., Grudic, M. Y., Su, K.-Y., et al. 2024a, The Open Journal of Astrophysics, 7, 18

Hopkins, P. F., Hernquist, L., Cox, T. J., Robertson, B., & Krause, E. 2007, ApJ, 669, 67

Hopkins, P. F., Kereš, D., Oñorbe, J., et al. 2014, MNRAS, 445, 581

Hopkins, P. F. & Quataert, E. 2011, MNRAS, 415, 1027

Hopkins, P. F., Squire, J., Quataert, E., et al. 2024b, The Open Journal of Astrophysics, 7, 20

Hopkins, P. F., Squire, J., Su, K.-Y., et al. 2024c, The Open Journal of Astrophysics, 7, 19

Hopkins, P. F., Torrey, P., Faucher-Giguère, C.-A., Quataert, E., & Murray, N. 2016, MNRAS, 458, 816

Hoyle, F. & Lyttleton, R. A. 1939, Proceedings of the Cambridge Philosophical Society, 35, 405

Hsieh, P.-Y., Koch, P. M., Ho, P. T. P., et al. 2017, ApJ, 847, 3

Hsieh, P.-Y., Koch, P. M., Kim, W.-T., et al. 2018, ApJ, 862, 150

Hunter, J. D. 2007, Computing in Science & Engineering, 9, 90

Ikeuchi, S. 1981, PASJ, 33, 211

Impellizzeri, C. M. V., Gallimore, J. F., Baum, S. A., et al. 2019, ApJ, 884, L28

Inayoshi, K., Visbal, E., & Haiman, Z. 2020, ARA&A, 58, 27

Iserlohe, C., Bryant, A., Krabbe, A., et al. 2019, ApJ, 885, 169

Ishibashi, W. & Fabian, A. C. 2015, MNRAS, 451, 93

Issaoun, S., Johnson, M. D., Blackburn, L., et al. 2019, ApJ, 871, 30

Izumi, T., Wada, K., Fukushige, R., Hamamura, S., & Kohno, K. 2018, ApJ, 867, 48

Jahnke, K. & Macciò, A. V. 2011, ApJ, 734, 92

Jovanović, P., Borka Jovanović, V., Borka, D., & Zakharov, A. F. 2024, Phys. Rev. D, 109, 064046

Kauffmann, J., Pillai, T., Zhang, Q., et al. 2017, A&A, 603, A89

Kawashima, T., Matsumoto, Y., & Matsumoto, R. 2017, PASJ, 69, 43

Kerr, R. P. 1963, Phys. Rev. Lett., 11, 237

Kerr, R. P. 2023, arXiv e-prints, arXiv:2312.00841

King, A. 2003, ApJ, 596, L27

King, A. 2005, ApJ, 635, L121

King, A. 2012, Mem. Soc. Astron. Italiana, 83, 466

King, A. & Nixon, C. 2015, MNRAS, 453, L46

King, A. & Pounds, K. 2015, ARA&A, 53, 115

King, A. R. 2010a, MNRAS, 408, L95

King, A. R. 2010b, MNRAS, 402, 1516

King, A. R. & Pringle, J. E. 2007, MNRAS, 377, L25

King, A. R., Zubovas, K., & Power, C. 2011, MNRAS, 415, L6

Kinney, A. L., Schmitt, H. R., Clarke, C. J., et al. 2000, ApJ, 537, 152

Kolcu, T., Maciejewski, W., Gadotti, D. A., et al. 2023, MNRAS, 524, 207

Kormendy, J. & Ho, L. C. 2013, ARA&A, 51, 511

Kormendy, J. & Richstone, D. 1995, ARA&A, 33, 581

Koudmani, S., Sijacki, D., Bourne, M. A., & Smith, M. C. 2019, MNRAS, 484, 2047

Koudmani, S., Somerville, R. S., Sijacki, D., et al. 2024, MNRAS, 532, 60–88

Koyama, K., Maeda, Y., Sonobe, T., et al. 1996, PASJ, 48, 249

Kruijssen, J. M. D., Dale, J. E., & Longmore, S. N. 2015, MNRAS, 447, 1059

Kruskal, M. D. 1960, Physical Review, 119, 1743

Kubota, A. & Done, C. 2018, MNRAS, 480, 1247

Laha, S., Reynolds, C. S., Reeves, J., et al. 2021, Nature Astronomy, 5, 13

Lahiri, S. K., Bhattacharya, K., Shaw, A., & Ramachandra, L. S. 2020, Journal of Computational Physics, 422, 109761

Lam, S. K., Pitrou, A., & Seibert, S. 2015, in Proceedings of the Second Workshop on the LLVM Compiler Infrastructure in HPC, LLVM '15 (New York, NY, USA: Association for Computing Machinery)

Lau, R. M., Herter, T. L., Morris, M. R., Becklin, E. E., & Adams, J. D. 2013, ApJ, 775, 37

Laužikas, M. & Zubovas, K. 2024, A&A, 690, A396

Lemaître, G. 1933, Annales de la Société Scientifique de Bruxelles, 53, 51

Levin, Y. & Beloborodov, A. M. 2003, ApJ, 590, L33

Li, Z., Shen, J., Gerhard, O., & Clarke, J. P. 2022, ApJ, 925, 71

Lin, C.-H., Chen, K.-J., & Hwang, C.-Y. 2023, ApJ, 952, 121

Liu, H. B., Hsieh, P.-Y., Ho, P. T. P., et al. 2012, ApJ, 756, 195

Lucas, W. E., Bonnell, I. A., Davies, M. B., & Rice, W. K. M. 2013, MNRAS, 433, 353

Lucy, L. B. 1977, AJ, 82, 1013

Luminari, A., Piconcelli, E., Tombesi, F., et al. 2018, A&A, 619, A149

Lutz, D., Sturm, E., Janssen, A., et al. 2020, A&A, 633, A134

Lynden-Bell, D. 1969, Nature, 223, 690

Lynden-Bell, D. & Pringle, J. E. 1974, MNRAS, 168, 603

Maciejewski, W., Teuben, P. J., Sparke, L. S., & Stone, J. M. 2002, MNRAS, 329, 502

Magorrian, J., Tremaine, S., Richstone, D., et al. 1998, AJ, 115, 2285

Maiolino, R., Gallerani, S., Neri, R., et al. 2012, MNRAS, 425, L66

Malkan, M. A. 1983, ApJ, 268, 582

Malkin, Z. 2019, A New Equal-area Isolatitudinal Grid on a Spherical Surface

Mapelli, M. & Trani, A. 2015, AA, 585

Mapelli, M. & Trani, A. A. 2016, A&A, 585, A161

Marasco, A., Cresci, G., Nardini, E., et al. 2020, A&A, 644, A15

Marin, F., Churazov, E., Khabibullin, I., et al. 2023, Nature, 619, 41

Marrone, D. P., Moran, J. M., Zhao, J.-H., & Rao, R. 2007, ApJ, 654, L57

Martin, G., Kaviraj, S., Volonteri, M., et al. 2018, MNRAS, 476, 2801

Mashchenko, S., Wadsley, J., & Couchman, H. M. P. 2008, Science, 319, 174

Matthews, T. A. & Sandage, A. R. 1963, ApJ, 138, 30

McAlpine, S., Harrison, C. M., Rosario, D. J., et al. 2020, MNRAS, 494, 5713

McConnell, N. J. & Ma, C.-P. 2013, ApJ, 764, 184

McKinley, B., Tingay, S. J., Gaspari, M., et al. 2021, arXiv e-prints, arXiv:2111.02683

Merritt, D. & Ferrarese, L. 2001a, MNRAS, 320, L30

Merritt, D. & Ferrarese, L. 2001b, in Astronomical Society of the Pacific Conference Series, Vol. 249, The Central Kiloparsec of Starbursts and AGN: The La Palma Connection, ed. J. H. Knapen, J. E. Beckman, I. Shlosman, & T. J. Mahoney, 335

Meru, F. & Bate, M. R. 2011, MNRAS, 411, L1

Michail, J. M., Yusef-Zadeh, F., Wardle, M., et al. 2024, ApJ, 971, 52

Mickaelian, A. M. 2015, Iranian Journal of Astronomy and Astrophysics, 2, 1

Miller, M. J. & Bregman, J. N. 2016, ApJ, 829, 9

Mingozzi, M., Cresci, G., Venturi, G., et al. 2019, A&A, 622, A146

Misner, C. W., Thorne, K. S., & Wheeler, J. A. 1973, Gravitation

Molinari, S., Bally, J., Noriega-Crespo, A., et al. 2011, ApJ, 735, L33

Monaghan, J. J. 1992, ARA&A, 30, 543

Monaghan, J. J. & Lattanzio, J. C. 1985, A&A, 149, 135

Montero-Castaño, M., Herrnstein, R. M., & Ho, P. T. P. 2009, ApJ, 695, 1477

Montgomery, C., Orchiston, W., & Whittingham, I. 2009, Journal of Astronomical History and Heritage, 12, 90

Moon, S., Kim, W.-T., Kim, C.-G., & Ostriker, E. C. 2023, ApJ, 946, 114

Morgan, C. W., Hyer, G. E., Bonvin, V., et al. 2018, ApJ, 869, 106

Morgan, C. W., Kochanek, C. S., Morgan, N. D., & Falco, E. E. 2010, ApJ, 712, 1129

Morris, M. & Serabyn, E. 1996, ARA&A, 34, 645

Murante, G., Monaco, P., Giovalli, M., Borgani, S., & Diaferio, A. 2010, MNRAS, 405, 1491

Murchikova, E. M., Phinney, E. S., Pancoast, A., & Blandford, R. D. 2019, Nature, 570, 83

Naddaf, M. H., Martinez-Aldama, M. L., Marziani, P., et al. 2023, A&A, 675, A43

Nagai, H., Onishi, K., Kawakatu, N., et al. 2019, ApJ, 883, 193

Narayan, R., Igumenshchev, I. V., & Abramowicz, M. A. 2003, PASJ, 55, L69

Narayan, R., Yi, I., & Mahadevan, R. 1996, A&AS, 120, 287

Nardini, E., Reeves, J. N., Gofford, J., et al. 2015, Science, 347, 860

Natarajan, P., Sigurdsson, S., & Silk, J. 1998, MNRAS, 298, 577

Nayakshin, S. 2014, MNRAS, 437, 2404

Nayakshin, S., Cha, S.-H., & Hobbs, A. 2009, MNRAS, 397, 1314

Nayakshin, S., Cuadra, J., & Springel, V. 2007, MNRAS, 379, 21

Nayakshin, S. & Zubovas, K. 2012, MNRAS, 427, 372

Nealon, R., Nixon, C., Price, D. J., & King, A. 2016, MNRAS, 455, L62

Negri, A. & Volonteri, M. 2017, MNRAS, 467, 3475

Nelson, D., Pillepich, A., Genel, S., et al. 2015, Astronomy and Computing, 13, 12

Nelson, D., Pillepich, A., Springel, V., et al. 2019a, MNRAS, 490, 3234

Nelson, D., Springel, V., Pillepich, A., et al. 2019b, Computational Astrophysics and Cosmology, 6, 2

Netzer, H. 2015, ARA&A, 53, 365

Newman, E. T., Couch, E., Chinnapared, K., et al. 1965, Journal of Mathematical Physics, 6, 918

Nobels, F. S. J., Schaye, J., Schaller, M., et al. 2024, MNRAS, 532, 3299

Nordström, G. 1918, Koninklijke Nederlandse Akademie van Wetenschappen Proceedings Series B Physical Sciences, 20, 1238

Novak, G. S., Ostriker, J. P., & Ciotti, L. 2011, ApJ, 737, 26

Novikov, I. D. & Thorne, K. S. 1973, in Black Holes (Les Astres Occlus), ed. C. Dewitt & B. S. Dewitt, 343–450

Nuza, S. E., Parisi, F., Scannapieco, C., et al. 2014, MNRAS, 441, 2593

Oka, T., Nagai, M., Kamegai, K., & Tanaka, K. 2011, ApJ, 732, 120

OpenAI. 2025, ChatGPT (January 2025 version), https://chat.openai.com, accessed January 2025

Oppenheimer, J. R. & Volkoff, G. M. 1939, Physical Review, 55, 374

Paczyński, B. & Wiita, P. J. 1980, A&A, 500, 203

Padovani, P., Alexander, D. M., Assef, R. J., et al. 2017, A&A Rev., 25, 2

Paumard, T., Ciurlo, A., Morris, M. R., Do, T., & Ghez, A. M. 2022, A&A, 664, A97

Paumard, T., Genzel, R., Martins, F., et al. 2006, ApJ, 643, 1011

Peißker, F., Zajaček, M., Labaj, M., et al. 2024, ApJ, 970, 74

Peng, C. Y. 2007, ApJ, 671, 1098

Penrose, R. 1965, Phys. Rev. Lett., 14, 57

Peterson, B. M. 2006, in Astronomical Society of the Pacific Conference Series, Vol. 360, AGN Variability from X-Rays to Radio Waves, ed. C. M. Gaskell, I. M. McHardy, B. M. Peterson, & S. G. Sergeev, 191

Pillepich, A., Nelson, D., Springel, V., et al. 2019, MNRAS, 490, 3196

Pillepich, A., Nelson, D., Truong, N., et al. 2021, MNRAS, 508, 4667

Pillepich, A., Springel, V., Nelson, D., et al. 2018, MNRAS, 473, 4077

Ponti, G., Hofmann, F., Churazov, E., et al. 2019, Nature, 567, 347

Ponti, G., Morris, M. R., Terrier, R., & Goldwurm, A. 2013a, in Astrophysics and Space Science Proceedings, Vol. 34, Cosmic Rays in Star-Forming Environments, ed. D. F. Torres & O. Reimer, 331

Ponti, G., Morris, M. R., Terrier, R., & Goldwurm, A. 2013b, in Cosmic Rays in Star-Forming Environments, ed. D. F. Torres & O. Reimer, Vol. 34, 331

Ponti, G., Terrier, R., Goldwurm, A., Belanger, G., & Trap, G. 2010, ApJ, 714, 732

Porth, O., Chatterjee, K., Narayan, R., et al. 2019, ApJS, 243, 26

Porth, O., Mizuno, Y., Younsi, Z., & Fromm, C. M. 2021, MNRAS, 502, 2023

Pounds, K. A., King, A. R., Page, K. L., & O'Brien, P. T. 2003a, MNRAS, 346, 1025

Pounds, K. A., Reeves, J. N., King, A. R., et al. 2003b, MNRAS, 345, 705

Power, C., Nayakshin, S., & King, A. 2011a, MNRAS, 412, 269

Power, C., Nayakshin, S., & King, A. 2011b, MNRAS, 412, 269

Predehl, P., Sunyaev, R. A., Becker, W., et al. 2020, Nature, 588, 227

Price, D. J. 2011, SPLASH: An Interactive Visualization Tool for Smoothed Particle Hydrodynamics Simulations, Astrophysics Source Code Library, record ascl:1103.004

Price, D. J. 2012, Journal of Computational Physics, 231, 759

Prieto, M., Fernandez-Ontiveros, J., Bruzual, G., et al. 2019a, MNRAS, 485, 3264

Prieto, M., Fernandez-Ontiveros, J., Bruzual, G., et al. 2019b, Monthly Notices of the Royal Astronomical Society, 485, 3264

Prieto, M. A., Fernandez-Ontiveros, J. A., Bruzual, G., et al. 2019, MNRAS, 485, 3264

Pringle, J. E. 1981, ARA&A, 19, 137

Proga, D. & Kallman, T. R. 2004, ApJ, 616, 688

Ramos Almeida, C. & Ricci, C. 2017, Nat As, 1, 679

Read, J. I. & Hayfield, T. 2012, MNRAS, 422, 3037

Read, J. I., Hayfield, T., & Agertz, O. 2010, MNRAS, 405, 1513

Reissner, H. 1916, Annalen der Physik, 355, 106

Revnivtsev, M. G., Churazov, E. M., Sazonov, S. Y., et al. 2004, A&A, 425, L49

Ricci, C., Ueda, Y., Paltani, S., et al. 2014, MNRAS, 441, 3622

Richings, A. J. & Faucher-Giguère, C.-A. 2018a, MNRAS, 478, 3100

Richings, A. J. & Faucher-Giguère, C.-A. 2018b, MNRAS, 474, 3673

Rindler, W. 1956, MNRAS, 116, 662

Rosas-Guevara, Y. M., Bower, R. G., Schaye, J., et al. 2015, Monthly Notices of the Royal Astronomical Society, 454, 1038

Rosswog, S. 2009, NAR, 53, 78

Rothschild, R. E., Boldt, E. A., Holt, S. S., & Serlemitsos, P. J. 1974, ApJ, 189, L13

Rowan-Robinson, M. 1977, ApJ, 213, 635

Rupke, D. S., Veilleux, S., & Sanders, D. B. 2005, ApJS, 160, 115

Rupke, D. S. N. & Veilleux, S. 2011, ApJ, 729, L27+

Saitoh, T. R. & Makino, J. 2009, ApJ, 697, L99

Salas, J. M., Morris, M. R., & Naoz, S. 2021, AJ, 161, 243

Salpeter, E. E. 1964, ApJ, 140, 796

Sanders, D. B., Soifer, B. T., Elias, J. H., Neugebauer, G., & Matthews, K. 1988, ApJ, 328, L35

Sarkar, K. C. 2024, A&A Rev., 32, 1

Sarkar, K. C., Nath, B. B., & Sharma, P. 2015, MNRAS, 453, 3827

Sato-Polito, G. & Zaldarriaga, M. 2024, arXiv e-prints, arXiv:2406.17010

Sazonov, S. Y., Ostriker, J. P., Ciotti, L., & Sunyaev, R. A. 2005, MNRAS, 358, 168

Schawinski, K., Koss, M., Berney, S., & Sartori, L. F. 2015, MNRAS, 451, 2517

Schaye, J., Crain, R. A., Bower, R. G., et al. 2015, MNRAS, 446, 521

Schmidt, M. 1963, Nature, 197, 1040

Schödel, R., Ott, T., Genzel, R., et al. 2002, Nature, 419, 694

Schwarzschild, K. 1916, Abh. Konigl. Preuss. Akad. Wissenschaften Jahre 1906,92, Berlin,1907, 189

Sellwood, J. A. & Wilkinson, A. 1993, Reports on Progress in Physics, 56, 173

Shakura, N. I. & Sunyaev, R. A. 1973, A&A, 24, 337

Shankar, F., Weinberg, D. H., & Miralda-Escudé, J. 2013, MNRAS, 428, 421

Shin, J., Kim, S. S., Baba, J., et al. 2017, ApJ, 841, 74

Sijacki, D., Vogelsberger, M., Genel, S., et al. 2015, MNRAS, 452, 575

Silk, J. & Rees, M. J. 1998, A&A, 331, L1

Smajić, S., Moser, L., Eckart, A., et al. 2015, A&A, 583, A104

Smethurst, R. J., Beckmann, R. S., Simmons, B. D., et al. 2022, arXiv e-prints, arXiv:2211.13677

Smethurst, R. J., Simmons, B. D., Coil, A., et al. 2021, MNRAS, 507, 3985

Smith, A. & Bromm, V. 2019, Contemporary Physics, 60, 111

Sofue, Y. 1995, PASJ, 47, 527

Soltan, A. 1982, MNRAS, 200, 115

Sormani, M. C. & Barnes, A. T. 2019, MNRAS, 484, 1213

Sormani, M. C., Barnes, A. T., Sun, J., et al. 2023, MNRAS, 523, 2918

Sormani, M. C., Gerhard, O., Portail, M., Vasiliev, E., & Clarke, J. 2022, MNRAS, 514, L1

Sormani, M. C., Sobacchi, E., Fragkoudi, F., et al. 2018, Monthly Notices of the Royal Astronomical Society, 481, 2

Sormani, M. C., Treß, R. G., Ridley, M., et al. 2018, MNRAS, 475, 2383

Spence, R. A. W., Zaurín, J. R., Tadhunter, C. N., et al. 2016, MNRAS, 459, L16

Springel, V. 2005, MNRAS, 364, 1105

Springel, V. 2010, MNRAS, 401, 791

Springel, V., Di Matteo, T., & Hernquist, L. 2005, MNRAS, 361, 776

Springel, V. & Hernquist, L. 2003, MNRAS, 339, 289

Springel, V., Pakmor, R., Zier, O., & Reinecke, M. 2021, MNRAS, 506, 2871

Steinborn, L. K., Dolag, K., Hirschmann, M., Prieto, M. A., & Remus, R.-S. 2015, MNRAS, 448, 1504

Storchi-Bergmann, T. 2014, in IAU Symposium, Vol. 303, The Galactic Center: Feeding and Feedback in a Normal Galactic Nucleus, ed. L. O. Sjouwerman, C. C. Lang, & J. Ott, 354–363

Stratton, F. J. M. and Smart, W. M. and Greaves, W. H. 1935, The Observatory, 58, 33

Sturm, E., González-Alfonso, E., Veilleux, S., et al. 2011, ApJ, 733, L16+

Su, M., Slatyer, T. R., & Finkbeiner, D. P. 2010, ApJ, 724, 1044

Su, Y., Zhang, S., Sun, Y., et al. 2024, ApJ, 971, L6

Sutherland, R. S. & Dopita, M. A. 1993, ApJS, 88, 253

Takekawa, S., Oka, T., Tsujimoto, S., et al. 2024, arXiv e-prints, arXiv:2408.09252

Talbot, R. Y., Bourne, M. A., & Sijacki, D. 2021, MNRAS, 504, 3619

Talbot, R. Y., Sijacki, D., & Bourne, M. A. 2022, Blandford-Znajek jets in galaxy formation simulations: exploring the diversity of outflows produced by spin-driven AGN jets in Seyfert galaxies

Talbot, R. Y., Sijacki, D., & Bourne, M. A. 2024, MNRAS, 528, 5432

Tartėnas, M. & Zubovas, K. 2020, MNRAS, 492, 603

Tartėnas, M. & Zubovas, K. 2022, MNRAS, 516, 2522

Teschner, M., Heidelberger, B., Müller, M., Pomerantes, D., & Gross, M. H. 2003, in International Symposium on Vision, Modeling, and Visualization

Thompson, R. 2014, pyGadgetReader: GADGET snapshot reader for python, Astrophysics Source Code Library

Thompson, T. A., Fabian, A. C., Quataert, E., & Murray, N. 2015, MNRAS, 449, 147

Tolman, R. C. 1939, Physical Review, 55, 364

Tombesi, F., Cappi, M., Reeves, J. N., et al. 2013, MNRAS, 430, 1102

Tombesi, F., Cappi, M., Reeves, J. N., et al. 2010a, A&A, 521, A57+

Tombesi, F., Meléndez, M., Veilleux, S., et al. 2015, Nature, 519, 436

Tombesi, F., Sambruna, R. M., Reeves, J. N., et al. 2010b, ApJ, 719, 700

Toomre, A. 1964, ApJ, 139, 1217

Torrey, P., Hopkins, P. F., Faucher-Giguère, C.-A., et al. 2020, MNRAS, 497, 5292

Trani, A. A., Mapelli, M., & Ballone, A. 2018, ApJ, 864, 17

Tremmel, M., Karcher, M., Governato, F., et al. 2017, MNRAS, 470, 1121

Tremmel, M., Quinn, T. R., Ricarte, A., et al. 2019, MNRAS, 483, 3336

Tress, R. G., Sormani, M. C., Girichidis, P., et al. 2024, arXiv e-prints, arXiv:2403.13048

Tress, R. G., Sormani, M. C., Glover, S. C. O., et al. 2020, MNRAS, 499, 4455

Tsuboi, M., Kitamura, Y., Miyoshi, M., et al. 2016, PASJ, 68, L7

Urry, C. M. & Padovani, P. 1995, PASP, 107, 803

Valentini, M., Murante, G., Borgani, S., et al. 2017, MNRAS, 470, 3167

Veilleux, S., Bolatto, A., Tombesi, F., et al. 2017, ApJ, 843, 18

Vogelsberger, M., Genel, S., Springel, V., et al. 2014, MNRAS, 444, 1518

von Fellenberg, S. D., Gillessen, S., Stadler, J., et al. 2022, ApJ, 932, L6

von Fellenberg, S. D., Witzel, G., Bauboeck, M., et al. 2024, A&A, 688, L12

Wagner, A. Y., Umemura, M., & Bicknell, G. V. 2013, ApJ, 763, L18

Wang, L.-F., Shao, Y., Zhang, J.-F., & Zhang, X. 2022, arXiv e-prints, arXiv:2201.00607

Wardle, M. & Yusef-Zadeh, F. 2008, ApJ, 683, L37

Wardle, M. & Yusef-Zadeh, F. 2014, ApJ, 787, L14

Webster, B. L. & Murdin, P. 1972, Nature, 235, 37

Wendland, H. 1995, Advances in computational Mathematics, 4, 389

Williams, J. & Mckee, C. 1997, ApJ, 476, 166

Witzel, G., Martinez, G., Hora, J., et al. 2018, ApJ, 863, 15

Yang, H. Y., Ruszkowski, M., & Zweibel, E. 2018, Galaxies, 6, 29

Yang, H. Y. K., Ruszkowski, M., & Zweibel, E. G. 2022, Nature Astronomy, 6, 584

Yelda, S., Ghez, A. M., Lu, J. R., et al. 2014, ApJ, 783, 131

Yonehara, A., Mineshige, S., Fukue, J., Umemura, M., & Turner, E. L. 1999, A&A, 343, 41

Zel'dovich, Y. B. 1964, Soviet Physics Doklady, 9, 195

Zhao, J.-H., Blundell, R., Moran, J. M., et al. 2010, ApJ, 723, 1097

Zubovas, K., Bialopetravičius, J., & Kazlauskaitė, M. 2022, MNRAS, 515, 1705

Zubovas, K. & Bourne, M. A. 2017, MNRAS, 468, 4956

Zubovas, K., Bourne, M. A., & Nayakshin, S. 2016, MNRAS, 457, 496

Zubovas, K. & King, A. 2012a, ApJ, 745, L34

Zubovas, K. & King, A. 2021, MNRAS, 501, 4289

Zubovas, K. & King, A. R. 2012b, MNRAS, 426, 2751

Zubovas, K. & King, A. R. 2014, MNRAS, 439, 400

Zubovas, K. & King, A. R. 2019, General Relativity and Gravitation, 51, 65

Zubovas, K., King, A. R., & Nayakshin, S. 2011, MNRAS, 415, L21

Zubovas, K. & Maskeliūnas, G. 2023, MNRAS, 524, 4819

Zubovas, K. & Nardini, E. 2020, MNRAS, 498, 3633

Zubovas, K. & Nayakshin, S. 2012, MNRAS, 424, 666

Zubovas, K. & Nayakshin, S. 2014, MNRAS, 440, 2625

Zubovas, K., Nayakshin, S., Sazonov, S., & Sunyaev, R. 2013, MNRAS, 431, 793

Zubovas, K., Tartėnas, M., & Bourne, M. A. 2024, A&A, 691, A151

Curriculum Vitae

Personal Information

Name:	Matas Tartėnas
Location:	Vilnius, Lithuania

Work Experience

Center for Physical Science and Technology, Department of Fundamental Research

2018 - now:	Junior researcher in projects: *The impact of outflows on star formation in their host galaxy* (MIP-17-78); *The long-term evolution of active galaxy outflows* (S-MIP-20-43); *The origin, evolution and impact of multiphase galactic outflows* (S-MIP-24-100).
2019.10 – 2020.04:	Trainee, student research project: "Modeling of an activity period and its effects in the Milky Way galaxy" (ESF Project No. 09.3.3-LMT-K-712-16-0283).
2018.10 – 2019.04:	Trainee, student research project: "Modeling of Supermassive Black Hole Accretion" (ESF Project No. 09.3.3-LMT-K-712-10-0062).
2018.07 – 2019.08:	Engineer, computer modeling and data analysis.

Education

2018 – 2020:	Master's in Theoretical Physics and Astrophysics, Vilnius University, Faculty of Physics.
2014 – 2018:	Bachelor's in Computational Physics and Modelling, Vilnius University.

Publications

1. Matas Tartėnas, Kastytis Zubovas, 'Feeding of active galactic nuclei by dynamical perturbations', *Monthly Notices of the Royal Astronomical Society*, Volume 492, Issue 1, February 2020, Pages 603–614, https://doi.org/10.1093/mnras/stz3484.

2. Matas Tartėnas, Kastytis Zubovas, 'Improving black hole accretion treatment in hydrodynamical simulations', *Monthly Notices of the Royal Astronomical Society*, Volume 516, Issue 2, October 2022, Pages 2522–2539, https://doi.org/10.1093/mnras/stac2330.

3. Kastytis Zubovas, Matas Tartėnas, Martin Albert Bourne, ‘The complex effect of gas cooling and turbulence on AGN-driven outflow properties’, *Astronomy & Astrophysics*, Volume 691, November 2024, A151, https://doi.org/10.1051/0004-6361/202451187

Highlight conferences

- **43rd Lithuanian National Conference on Physics, 2019:** Oral presentation: *Activity in the Galactic Centre Induced by a Cloud-Ring Collision.*
- **44th Lithuanian National Conference on Physics, 2021:** Oral presentation: *Improving Black Hole Accretion and Feedback in Numerical Simulations.*
- **European Astronomical Society Annual Meeting, 2024:** Oral presentation: *SMBH feeding by parsec-scale chaotic accretion over millions of years.*

Computer Skills

- Python, Bash, C/C++, R, Matlab, LaTeX

Languages

- Lithuanian (native), English (C1)

Volunteer Work

- **2019:** CMS International Masterclass, Moderator of students’ hands-on activity.
- **2014 – 2018:** Open Readings Conference, preparation and local organizing committee member (2016, 2018).
- **2018 – now:** Lituanicon, event preparation and activities.

Additional Information

- Participated in Student Science Fellowship activities, organizing lectures and documentary film evenings.
- Irregular attendee of a local sci-fi/fantasy book club.
- Recipient of the best master’s thesis prize in the natural sciences category from Lietuvos jaunųjų mokslininkų sąjunga (LJMS).
- Member of a local capoeira club.

NOTES

Vilnius University Press
9 Saulėtekio Ave., Building III, LT-10222 Vilnius
Email: info@leidykla.vu.lt, www.leidykla.vu.lt
bookshop.vu.lt, journals.vu.lt
Print run copies 15